LAWRENCE
LIVERMORE
NATIONAL
LABORATORY

UCRL-JRNL-225066

ENDF/B-VII.0: Next Generation Evaluated Nuclear Data Library for Nuclear Science and Technology

M. B. Chadwick, P. Oblozinsky, M. Herman, N. M. Greene, R. D. McKnight, D. L. Smith, P. G. Young, R. E. MacFarlane, G. M. Hale, R. C. Haight, S. Frankle, A. C. Kahler, T. Kawano, R. C. Little, D. G. Madland, P. Moller, R. Mosteller, P. Page, P. Talou, H. Trellue, M. White, W. B. Wilson, R. Arcilla, C. L. Dunford, S. F. Mughabghab, B. Pritychenko, D. Rochman, A. A. Sonzogni, C. Lubitz, T. H. Trumbull, J. Weinman, D. Brown, D. E. Cullen, D. Heinrichs, D. McNabb, H. Derrien, M. Dunn, N. M. Larson, L. C. Leal, A. D. Carlson, R. C. Block, B. Briggs, E. Cheng, H. Huria, K. Kozier, A. Courcelle, V. Pronyaev, S. C. van der Marck

October 6, 2006

Nuclear Data Sheets

Disclaimer

ENDF/B-VII.0: Next Generation Evaluated Nuclear Data Library for Nuclear Science and Technology

M.B. Chadwick,[1] P. Obložinský,[2*] M. Herman,[2] N.M. Greene,[6] R.D. McKnight,[3] D.L. Smith,[3]
P.G. Young,[1] R.E. MacFarlane,[1] G.M. Hale,[1] R.C. Haight,[1] S. Frankle,[1] A.C. Kahler,[1,12] T. Kawano,[1] R.C. Little,[1]
D.G. Madland,[1] P. Moller,[1] R. Mosteller,[1] P. Page,[1] P. Talou,[1] H. Trellue,[1] M. White,[1] W.B. Wilson,[1]
R. Arcilla,[2] C.L. Dunford,[2] S.F. Mughabghab,[2] B. Pritychenko,[2] D. Rochman,[2] A.A. Sonzogni,[2]
C. Lubitz,[4] T.H. Trumbull,[4] J. Weinman,[4]
D. Brown,[5] D.E. Cullen,[5] D. Heinrichs,[5] D. McNabb,[5]
H. Derrien,[6] M. Dunn,[6] N.M. Larson,[6] L.C. Leal,[6]
A.D. Carlson,[7] R.C. Block,[8] B. Briggs,[9] E. Cheng,[10] H. Huria,[11] K. Kozier,[13]
A. Courcelle,[14] V. Pronyaev,[15] S.C. van der Marck[16]
(CSEWG Collaboration)

[1] *Los Alamos National Laboratory, Los Alamos, NM 87545*
[2] *National Nuclear Data Center, Brookhaven National Laboratory, Upton, NY 11973-5000*
[3] *Argonne National Laboratory, 9700 South Cass Ave, Argonne, IL 60439-4842*
[4] *Knolls Atomic Power Laboratory, P.O. Box 1072, Schenectady, NY 12301-1072*
[5] *Lawrence Livermore National Laboratory, PO Box 808, Livermore, CA 94551-0808*
[6] *Oak Ridge National Laboratory, P.O. Box 2008, Oak Ridge, TN 37831-6171*
[7] *National Institute of Standards and Technology, Gaithersburg, MD 20899-8463*
[8] *Gaerttner LINAC Laboratory, Rensselaer Polytechnic Institute, Troy, NY 12180-3590*
[9] *Idaho National Laboratory, P.O. Box 1625, Idaho Falls, ID 83415-3860*
[10] *TSI Research Corp, 312 S. Cedros Ave, Solana Beach, CA 92067*
[11] *Westinghouse Electric Corp., 4350 Northern Pike, Monroeville, PA 15146*
[12] *Bettis Laboratory, P.O. Box 79, West Mifflin, PA 15122*
[13] *Atomic Energy of Canada Ltd., Chalk River, ON KOJ1JO, Canada*
[14] *Centre d'Études Nucléaires de Cadarache, F-13108 Saint-Paul lèz Durance, Cedex, France*
[15] *Institute for Physics and Power Engineering, Ploschad Bondarenko 1, 249 020 Obninsk, Russia and*
[16] *Nuclear Research and Consultancy Group, P.O. Box 25, NL-1755 ZG Petten,The Netherlands*

(Dated: October 2, 2006)

We describe the next generation general purpose Evaluated Nuclear Data File, ENDF/B-VII.0, of recommended nuclear data for advanced nuclear science and technology applications. The library, released by the U.S. Cross Section Evaluation Working Group (CSEWG) in December 2006, contains data primarily for reactions with incident neutrons, protons, and photons on almost 400 isotopes. The new evaluations are based on both experimental data and nuclear reaction theory predictions.

The principal advances over the previous ENDF/B-VI library are the following: (1) New cross sections for U, Pu, Th, Np and Am actinide isotopes, with improved performance in integral validation criticality and neutron transmission benchmark tests; (2) More precise standard cross sections for neutron reactions on H, ^{6}Li, ^{10}B, Au and for ^{235,238}U fission, developed by a collaboration with the IAEA and the OECD/NEA Working Party on Evaluation Cooperation (WPEC); (3) Improved thermal neutron scattering; (4) An extensive set of neutron cross sections on fission products developed through a WPEC collaboration; (5) A large suite of photonuclear reactions; (6) Extension of many neutron- and proton-induced reactions up to an energy of 150 MeV; (7) Many new light nucleus neutron and proton reactions; (8) Post-fission beta-delayed photon decay spectra; (9) New radioactive decay data; and (10) New methods developed to provide uncertainties and covariances, together with covariance evaluations for some sample cases.

The paper provides an overview of this library, consisting of 14 sublibraries in the same, ENDF-6 format, as the earlier ENDF/B-VI library. We describe each of the 14 sublibraries, focusing on neutron reactions. Extensive validation, using radiation transport codes to simulate measured critical assemblies, show major improvements: (a) The long-standing underprediction of low enriched U thermal assemblies is removed; (b) The ^{238}U, ^{208}Pb, and ^{9}Be reflector biases in fast systems are largely removed; (c) ENDF/B-VI.8 good agreement for simulations of highly enriched uranium assemblies is preserved; (d) The underprediction of fast criticality of ^{233,235}U and ^{239}Pu assemblies is removed; and (e) The intermediate spectrum critical assemblies are predicted more accurately.

We anticipate that the new library will play an important role in nuclear technology applications, including transport simulations supporting national security, nonproliferation, advanced reactor and fuel cycle concepts, criticality safety, medicine, space applications, nuclear astrophysics, and nuclear physics facility design. The ENDF/B-VII.0 library is archived at the National Nuclear Data Center, BNL. The complete library, or any part of it, may be retrieved from **www.nndc.bnl.gov**.

*) Corresponding author, electronic address: oblozinsky@bnl.gov

Contents

I. INTRODUCTION

In the United States, evaluated nuclear reaction data are made available to users in applied and basic nuclear science through the Evaluated Nuclear Data File (ENDF/B). The Cross Section Evaluation Group (CSEWG), which was founded in 1966 [1], is the organization that oversees the development of this database. It is comprised of members from national laboratories, universities, and industry. CSEWG also benefits from collaborative relationships with other national cross section evaluation projects that are coordinated through the OECD Nuclear Energy Agency (NEA, Paris) and the International Atomic Energy Agency (IAEA, Vienna).

In the period 2002 - 2006, during which the ENDF/B-VII.0 library was developed, CSEWG had the following organizational structure:

- CSEWG chair - Pavel Obložinský, BNL.
- CSEWG committee chairs - Mark Chadwick, LANL (evaluations), Maurice Greene, ORNL (formats and processing); Don Smith, ANL (measurements and basic physics), Dick McKnight, ANL (validation).
- ENDF database manager - Mike Herman, BNL (since March 2003, replaced V. McLane, BNL).

Major releases of the ENDF/B library are summarized in Table I. After an initial two-year release cycle, CSEWG moved to ever longer release cycles. Recent releases occured at widely-spaced intervals: ENDF/B-V was released in 1978, ENDF/B-VI in 1990, followed by this ENDF/B-VII.0 release in 2006. However, interim releases have occurred more frequently, containing certain cross section advances. Prior to the new ENDF/B-VII.0 library, the ENDF/B-VI library had upgrades embodied in eight releases, the last one occurring in October 2001 and referred to in the present paper as ENDF/B-VI.8 [2].

A comment should be made on the name of the ENDF/B library. The founding fathers of CSEWG envisioned the existence of two versions of the library [3]. The first one was called ENDF/A. It was intended to store partial evaluations, to be used to produce complete evaluations that were to be stored in the second library, ENDF/B. Although this concept has never been used in practice, the name ENDF/B has become an established trade mark for 40 years. In 2005, CSEWG re-established the idea of ENDF/A. This library is currently being used to store partial evaluations, many of them developed by LLNL for radiochemical applications. Also, it served as an interim storage for preliminary evaluations submitted to the new ENDF/B-VII library.

The cross section advances in the ENDF library support needs in a wide variety of applied technologies. Complete cross section evaluations are needed in radiation transport simulation codes that are used to model the neutronics, activation and nuclear transmutations, energy deposition and aborbed dose, *etc.* The applications include advanced reactor design, nuclear waste transmutation and fuel cycles, nuclear criticality safety, medical applications (isotope production, external beam therapy, *etc.*), nonproliferation and national security, space physics, radiation protection and shielding. Cross section data are also used to design physics facilities, especially target and shielding design, for example in the Spallation Neutron Source (SNS, at Oak Ridge), and in designs for a future Exotic Beam Accelerator. Nuclear astrophysics also uses cross sections in nucleosynthesis research.

TABLE I: Major releases of the ENDF/B library.

ENDF/B	I	II	III	IV	V	VI	VII
Year	1968	1970	1972	1974	1978	1990	2006

The work described in the present paper represents a coordinated effort for five years by researchers from many US institutions, organized by CSEWG. The principal advances were dictated by specific programmatic priorities set by our laboratories and by the Department of Energy (DOE). The DOE Office of Science, Office of Nuclear Physics' US Nuclear Data Program (USNDP, see www.nndc.bnl.gov/usndp) provided the bulk of the support for bringing the various capabilities developed at different laboratories together under CSEWG, and for the National Nuclear Data Center to maintain and archive the ENDF databases at Brookhaven National Laboratory. Most of the underlying research was supported by the DOE National Nuclear Security Agency's Advanced Simulation and Computing (ASC), Nuclear Criticality Safety, and Nonproliferation Research and Engineering programs, in addition to the Office of Science. The DOE Nuclear Energy (NE) office supported work related to advanced fuel cycles, and advanced reactors. Important support also came from the DOE Naval Reactor Laboratories, and from the National Institute for Standards and Technology (NIST).

The development of complete, evaluated cross section data files depends upon a variety of expertises: nuclear experimentation; nuclear theory and model predictions; statistical analysis; radiation transport physics; computer code and database development; processing of nuclear data; and fundamental and integral validation against experiments that include criticality and neutron transmission (shielding) measurements. This effort has brought together scientists from these different disciplines to create our new ENDF/B-VII.0 library.

A cross section library is developed not only for the purpose of providing accurate basic physics data, isotope-by-isotope, but also to perform well, as an ensemble, in applied simulations. This is particularly important for nuclear criticality applications, where for some critical assemblies the performance may depend sensitively upon ^{1}H, ^{16}O, ^{235,238}U, *etc.* data. Since all cross sections are known only to a certain level of precision, significant

attention was paid to ensure that the evaluated cross sections perform together well as a group in validation simulations of these critical assemblies. Such integral data testing is given in Section X.

The paper is organized as follows. Section II provides an overview of the library. There are 14 sublibraries and each sublibrary is briefly described. Afterwards, the most important sublibraries are described in more detail in the follow-up sections. Section III describes the neutron sublibrary. We start by describing the evaluation methodology. Then, we discuss new actinide cross section evaluations, for both major and minor actinides. Improving the actinide cross section evaluations has represented one of the largest efforts in the cross section measurement, modeling, and data evaluation community because of the requirements for new and more accurate actinide data coming from many applied nuclear technologies. One subsection is devoted to evaluations of neutron reactions on fission product targets that were entirely revised compared to those contained in ENDF/B-VI.8. Another subsection describes how a subset of the ENDF/B-VII.0 evaluations extend beyond the traditional upper energy of 20 MeV, up to 150 MeV. Section IV is devoted to the thermal neutron scattering sublibrary. Section V details the new ENDF/B-VII.0 neutron standard cross sections - these cross sections are known very precisely and are particularly important since other cross sections are often determined relative to these standards. Section VI describes the photonuclear cross section evaluations. Section VII describes evaluations for charged-particles. Section VIII is devoted to the radioactive decay data sublibrary. Section IX provides a summary of the remaining 5 sublibraries that have been taken over from ENDF/B-VI.8. Section X presents our integral data testing results for validating the accuracy of the database, especially in criticality and neutron transmission applications. Conclusions are given in Section XI. A summary of the ENDF-6 format and explanation of abbreviations is given in Appendix A. A complete list of evaluated materials in each sublibrary can be found in Appendix B.

II. OVERVIEW OF THE LIBRARY

A. Contents of ENDF/B-VII.0

The ENDF/B-VII.0 library contains 14 sublibraries as summarized in Table II. They are ordered according to NSUB, the identification number of the sublibrary defined by the ENDF-6 format [4]. The number of materials (isotopes or elements) are given both for the new (VII.0) and previous (VI.8) versions of the ENDF/B library. The total number of materials in ENDF/B-VII.0 has increased considerably, largely thanks to the new decay data sublibrary. Although the ENDF/B library is widely known for evaluated neutron cross sections, it is evident that the library contains a considerable amount of non-neutron data.

TABLE II: Contents of the ENDF/B-VII.0 library, with ENDF/B-VI.8 shown for comparison. NSUB stands for the sublibrary number in the ENDF-6 format. Given in the last two columns are the number of materials (isotopes or elements).

No.	NSUB	Sublibrary name	Short name	VII.0	VI.8
1	0	Photonuclear	g	163	-
2	3	Photo-atomic	photo	100	100
3	4	Radioactive decay	decay	3830	979
4	5	Spont. fis. yields	s/fpy	9	9
5	6	Atomic relaxation	ard	100	100
6	10	Neutron	n	393	328
7	11	Neutron fis.yields	n/fpy	31	31
8	12	Thermal scattering	tsl	20	15
9	19	Standards	std	8	8
10	113	Electro-atomic	e	100	100
11	10010	Proton	p	48	35
12	10020	Deuteron	d	5	2
13	10030	Triton	t	3	1
14	20030	^{3}He	he3	2	1
		Full library*		**4812**	**1709**

*) Detailed list of materials in ENDF/B-VII.0 can be found in Appendix B.

As discussed below, out of the total of 14 sublibraries, there are two new sublibraries, 7 sublibraries were considerably updated and extended, while the remaining 5 sublibraries were taken over from ENDF/B-VI.8 without any change:

1. The photonuclear sublibrary is entirely new. It contains evaluated cross sections for 163 materials (all isotopes) mostly up to 140 MeV. The sublibrary has been supplied by Los Alamos National Laboratory (LANL) and it is largely based on the IAEA-coordinated collaboration completed in 2000 [5]. This project mostly used the evaluation methodology and modeling tools for photonuclear reactions developed at LANL.

2. The photo-atomic sublibrary has been taken over from ENDF/B-VI.8. It contains data for photons from 10 eV up to 100 GeV interacting with atoms for 100 materials (all elements). The sublibrary has been supplied by Lawrence Livermore National Laboratory (LLNL).

3. The decay data sublibrary has been completely re-evaluated and considerably extended by the National Nuclear Data Center, Brookhaven National Laboratory (BNL).

4. The spontaneous fission yields were taken over from ENDF/B-VI.8. The data were supplied by LANL.

5. The atomic relaxation sublibrary was taken over from ENDF/B-VI.8. It contains data for 100 materials (all elements) supplied by LLNL.

6. The neutron reaction sublibrary represents the heart of the ENDF/B-VII.0 library. The sublibrary has been considerably updated and extended, with a number of entirely new evaluations. It contains 393 materials, including 390 isotopic evaluations and 3 elemental ones (C, V and Zn). These evaluations can be considered to be complete[1] since they contain data for all important reaction channels including energy spectra and angular distributions for use in neutronics calculations. Important improvements were made to the actinide nuclides by LANL, often in collaboration with ORNL. Evaluations in the fission product range (Z = 31 - 68) have been changed entirely. ENDF/B-VII.0 contains fission product evaluations for 219 materials, with 71 materials evaluated by BNL, 2 by LLNL, 1 by LANL-BNL and the remaining 145 materials produced by the international project (NEA WPEC). Of the 393 materials, about 2/3 of the evaluations are based upon recent important contributions from the U.S. evaluators. The remaining evaluations were adopted from other sources (mostly the JENDL-3.3 library). Livermore provided β-delayed γ-ray data for ^{235}U and ^{239}Pu, for the first time in ENDF/B.

7. Neutron fission yields were taken over from ENDF/B-VI.8. The data were supplied by LANL.

8. The thermal neutron scattering sublibrary contains thermal scattering-law data, largely supplied by LANL, with several important updates and extensions (some based on the work by Mattes, IKE Stuttgart, Germany [6]).

9. The neutron cross section standards sublibrary is new. Although standards traditionally constituted part of the ENDF/B library, in the past these data were stored on a tape with a specific tape number. As the concept of tapes has been abandoned in ENDF/B-VII.0 the neutron cross sections standards sublibrary (short name *std*, sublibrary number NSUB = 19), has been introduced. Out of 8 standards materials, 7 were newly evaluated, while ^{nat}C(n,n) was taken over from ENDF/B-VI.8. These new evaluations come from the international collaboration coordinated by the IAEA and NEA WPEC [7]; the US effort was led by NIST and LANL.

10. The electro-atomic sublibrary was taken over from ENDF/B-VI.8. It contains data for 100 materials (all elements) supplied by LLNL.

11. The proton-induced reactions were supplied by LANL, the data being mostly to 150 MeV. There are several updates and several new evaluations.

12. The deuteron-induced reactions were supplied by LANL. This sublibrary contains 5 evaluations.

13. The triton-induced reactions were supplied by LANL. This sublibrary contains 3 evaluations.

14. Reactions induced with ^{3}He were supplied by LANL. This sublibrary contains 2 evaluations.

The major US laboratory contributors to the ENDF/B-VII.0 library are summarized in Table III. A dominant contributor to the evaluations is LANL, who provided the many actinide evaluations in the neutron reaction sublibrary, almost all the evaluations in the neutron thermal scattering sublibrary, many photonuclear and all the charged particle evaluations. BNL contributed the decay data sublibrary and many fission product evaluations in the neutron sublibrary; ORNL contributed neutron resonances for several actinides of key importance; LLNL contributed 3 atomic sublibraries (carried over from previous evaluations), and NIST played the leading role in developing neutron cross section standards. BNL performed Phase 1 testing (data verification), and LANL was the leading laboratory in Phase 2 testing (data validation).

TABLE III: Major US laboratory contributors to the ENDF/B-VII.0 library.

Sublibrary/activity	**Major US contributors**
Neutron sublibrary	LANL, BNL, ORNL
Thermal scattering sublibrary	LANL
Standards sublibrary	NIST,LANL
Photonuclear sublibrary	LANL
Decay data sublibrary	BNL
Proton sublibrary	LANL
d, t, ^{3}He sublibraries	LANL
Fission yield sublibraries	LANL
Atomic data sublibraries	LLNL
Data verification	BNL
Data validation	LANL, KAPL, Bettis, ANL
Archival and dissemination	BNL

B. Processing, testing and dissemination

The ENDF/B-VII.0 library was issued in its basic format defined by the ENDF-6 Formats Manual [4]. For practical applications the library must be processed so that basic data are converted into formats suitable as input for applied codes such as the Monte Carlo transport code MCNP and the reactor licensing code SCALE [8]. Recommended processing codes for the ENDF/B-VII.0 library are as follows:

[1] The only exception is ^{253}Es that contains (n,γ) dosimetry cross sections.

TABLE IV: Testing versions of the ENDF/B-VII.0 library.

Version	Date	Comment
beta0	March 2005	1 sublibrary (neutron)
beta1	October 2005	11 sublibraries
beta2	April 2006	14 sublibraries
beta3	October 2006	Became VII.0 in December 2006

- LANL's processing code NJOY-99 [9, 10]. The code NJOY-99 can be obtained from RSICC [11], and also from NEA Data Bank [12], while patches are available at the LANL T-2 webpage [13].

- Two codes are available for processing of covariance data (MF=32) for the Reich-Moore formalism. The code ERRORJ [14], since recently a part of the ERROR module of the NJOY package, uses numerical methods for calculating sensitivities. The PUFF code [15], a module of the Oak Ridge processing code AMPX [16], uses analytical methods for calculating sensitivities.

In the period 2005-2006, several testing versions of the new library were issued, see Table IV. These beta versions have been tested, deficiencies were identified, and improved versions were issued. The last testing version was declared to be the official ENDF/B-VII.0 library. This complex process was important for the careful Quality Assurance (QA) procedure adopted by CSEWG. Each beta version was subject to two-step data testing: Phase 1 testing (data verification), and Phase 2 testing (integral data validation).

Data verification was performed by the National Nuclear Data Center, BNL as follows:

- Checking the whole library by a suite of ENDF-6 utility codes (CHECKR, FIZCON, PSYCHE) [17] for possible formatting problems and inconsistencies in physics.

- Processing of 4 sublibraries needed for neutronics calculations (photonuclear, neutron, thermal scattering and proton) by the processing code NJOY-99.161 to ensure that a processed library suitable for neutronics calculations can be produced.

- Use of the processed files by the Monte Carlo codes MCNP (photonuclear, neutron, thermal scattering) [18, 19] and MCNPX (proton) [20] in simple neutronics test calculations to ensure that neutronics calculations can be performed.

- Processing of covariance data was performed to ensure that multigroup data for applied calculations can be produced.

Data validation is a complex process described in considerable detail in Section X and we are not going to discuss it here.

The ENDF/B-VII.0 library was officially released in December 2006. Users should use the present document as the ENDF/B-VII.0 reference. The library is archived by the National Nuclear Data Center (NNDC) at BNL. The NNDC also disseminates these data, along with many other data, and provides user support [21]. One can download the whole library or any part of it from the NNDC web server, **www.nndc.bnl.gov**.

III. NEUTRON REACTION SUBLIBRARY

A. Evaluation methodology

Our evaluation methodology for neutron induced reactions consists of three distinctive parts. First, an evaluation starts with a careful analysis of pertinent experimental data. Second, the low energy region, including thermal energy, resolved resonances and unresolved resonances is treated by methods developed to analyze neutron resonances. Third, the fast neutron region is evaluated using methods based on nuclear reaction modeling calculations and experimental data. Our discussion will be concerned with these two latter parts.

1. Overview

Nuclear theory and modeling has played a central role in developing complete cross section evaluations. Complete evaluations, by which we mean representations that cover all incident projectile energies, and outgoing particle and photon energies and angular distributions, are needed for use in radiation transport, transmutation, and other types of application codes. Because experimental data have often been measured in only limited regions, nuclear reaction theory codes provide a powerful tool to interpolate and extrapolate from the measured data, and naturally incorporate constraints such as unitarity, and energy and momentum conservation.

The community has developed a number of reaction physics codes that have supported this work. They fall into the following categories:

- Hauser-Feshbach and preequilibrium, direct, and fission models, for use in modeling medium and heavy nucleus reactions (*e.g.*, for the actinides, and for fission product cross sections described in this work), notably the GNASH code (LANL, [22–24]), the code COH by Kawano (LANL, unpublished), and the EMPIRE code (BNL, [25]), which are often used in conjunction with coupled-channels optical model codes such as ECIS (CEA Cadarache, [26]),

- R-matrix codes for light nucleus reactions, and for lower incident energy reactions on heavier targets, notably the Oak Ridge SAMMY code [27] and the Los Alamos EDA code [28],

TABLE V: Summary of the evaluation codes used for new evaluations by U.S. national laboratories.

Lab	Resonance region	Fast neutron region	Primary application
LANL	-	GNASH, COH	Actinides
LANL	EDA	EDA	Light nuclei
BNL	Atlas	EMPIRE	Fission products
LLNL	-	EMPIRE	Dosimetry
ORNL	SAMMY	-	Actinides
LANL	-	ECIS	Actinides
BNL	-	ECIS	Fission products

- The Atlas code system [29] for analyzing neutron resonances in terms of multi-level Breit-Wigner formalism by Mughabghab at BNL to produce comprehensive evaluation of resonance parameters for the Atlas of Neutron Resonances [30].

While these approaches utilize modern developments in reaction theory - for example, multistep direct preequilibrium scattering, dispersive optical potentials, R-matrix theory, it is still the case that they rely to a high degree on phenomenology. This is appropriate given our goal to represent as accurately as possible the known measured nuclear reaction phenomena, and to have tools that can reliably interpolate and extrapolate to unmeasured regimes.

An exception to the more phenomenological models are the methods we have applied to study some of the light reactions, n+D and n+^{3}He, where more fundamental methods, such as Resonating Group Method (RGM) [31, 32], have directed our analysis of these systems. For such reactions, advances in high performance computing resources have enabled fully microscopic calculations to provide input to more phenomenological approaches such as R-matrix.

New evaluations for ENDF/B-VII.0 were produced by LANL (the fast region for many actinides and light nuclei), BNL (a large suite of fission products, both in the resonance and fast regions), ORNL (resonance region for several actinides and other materials) and LLNL (2 fission products). A summary of the codes used by U.S. laboratories for these new evaluations is given in Table V.

Fig. 1 qualitatively summarizes nuclear reaction models (and relative codes) as used in the ENDF/B-VII.0 evaluations for various combinations of mass number and incident energy. Levels in the very light nuclei are generally sparse and well isolated. This feature necessitates use of special few-body techniques that are feasible due to a limited number of nucleons in the system. We have used the explicit R-matrix theory, implemented in the Los Alamos code EDA, for evaluations of nuclides up to A=10 (with a few exceptions). This approach, although formally strict, relies on experimental input. In the most important cases, such as the standards, the R-matrix analysis was supported by microscopic RGM calculations

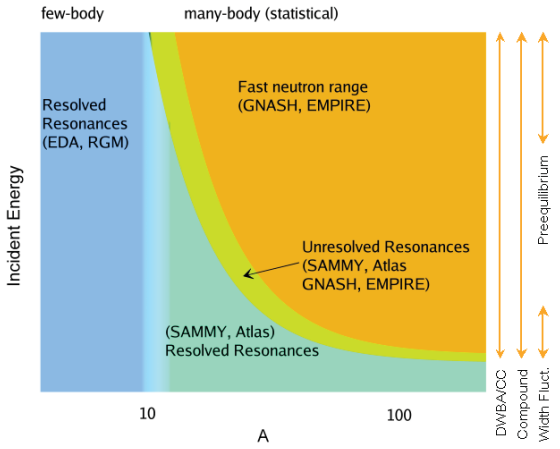

FIG. 1: Schematic representation depicting the use of various evaluation techniques and related codes (in brackets) depending on target mass and incident energy. Arrows to the right of the figure indicate major reaction mechanisms in the fast neutron range and their energy range of applicability.

that predicted high energy discrete levels (resonances) and their characteristics from the basic nucleon-nucleon interaction. In Fig. 1 the few-body regime is depicted as a vertical rectangle at the left of the picture. Note, that in this case the same methodology is applied throughout the whole energy range.

Increasing the number of nucleons in the target makes usage of few-body models impractical – the number of nuclear levels is too big to treat all of them explicitly. On the other hand, the large number of levels facilitates approaches that, to a certain extent, are built upon statistical assumptions. This "statistical regime" appears in Fig. 1 to the right of A$\sim$10, which happens to be a boundary between the usage of the two basic evaluation methodologies in ENDF/B-VII.0.

Contrary to the light nuclei, for which the same model is applied in the whole evaluated energy range, we have to deal with three distinct energy regions for heavier nuclei:

- resolved resonance region (including thermal neutrons),
- unresolved resonance region,
- fast neutron region.

Since the density of neutron resonances increases with A, the upper limit of the resolved resonance region decreases when moving to heavier nuclei. A neighboring region is known as the unresolved resonance region. Overlapping resonances usually produce quite smooth cross sections and there is no clear boundary between the unresolved and the fast neutron region. In many new evaluations in ENDF/B-VII.0 the energy of the first excited level in the target was adopted as an upper limit of the unresolved resonance region. Each of these three regions needs different techniques and different reaction modeling.

The resolved resonance region is a sort of no man's land in the sense that there is no theory capable of predicting individual resonances. The physics is far too complex for the microscopic few-body approach, while the practical importance of the region is such that we can not resort to a purely statistical treatment. Therefore, realistic evaluations require experimental data for neutron resonances. These data have to be analyzed with statistical methods to correct for likely loss of resonances that escaped experimental detection, and to assign individual resonance parameters. In ENDF/B-VII.0 the Reich-Moore approach derived from the R-matrix theory, as implemented in the Oak Ridge code SAMMY, was utilized for the important actinides. For about 150 fission product nuclei, the multilevel Breit-Wigner formalism, and statistical methods from the Atlas of Neutron Resonances [30] were used at BNL.

The unresolved region is a transitional region that could be treated with the methods from the resolved region as well as in the terms of the models used in the fast neutron region. Whenever possible, we prefer to extrapolate results of the resonance region analysis and adjust them to the available experimental cross sections in the unresolved resonance region, since such an approach improves the accuracy of self-shielding calculations.

The fast neutron region involves a whole suite of nuclear reaction models. Vertical arrows on the right hand side of Fig. 1 indicate energy ranges for the major mechanisms. All the models used in the fast neutron range have a strong statistical component resulting from the averaging over many resonances. This is true even for the direct reactions such as DWBA and Coupled Channels, which while providing cross sections for inelastic scattering to individual collective levels, still rely on the optical potential resulting, at least conceptually, from the averaging procedure. The Hauser-Feshbach formulation of the compound nucleus is a key model for any evaluation in the fast neutron region, although in the low energy range it must be corrected to account for the width fluctuation effects. At incident energies above 10 MeV, preequilibrium emission has to be taken into account and we implement a variety of semi-classical and quantum-mechanical models. All these are built into the two major nuclear reactions codes GNASH (Los Alamos) and EMPIRE (BNL) used for ENDF/B-VII.0 evaluations.

While most of the nuclear reaction models used for the evaluations are predominantly phenomenological, their usage involves a huge number of input parameters. These include nuclear masses, deformations, optical model potentials, level densities, discrete level schemes, fission barriers, and γ-ray strength functions to mention only the most important classes of parameters. The quality of this input is reflected in the performance of nuclear models and becomes critical if there are no or insufficient experimental data to constrain model calculations. Developement of the ENDF/B-VII.0 library largely benefited from the Reference Input Parameter Library (RIPL), an international project coordinated by the IAEA. The first phase of this project [33], under leadership of Ignatyuk (IPPE) and Obložinský (IAEA, currently at BNL), set up the framework by compiling huge numbers of model parameters. The second phase [34], led by Young (LANL) and Obložinský/Herman (IAEA, currently at BNL), standardized the format, extended and updated the database, and performed validation of the library. The third phase of the project, directed by Herman (BNL) and Capote (IAEA), is extending the library to charged particles and to nuclei off the stability line addressing issues not covered in the previous releases. The availability of such a comprehensive and consistent database was instrumental for the development of new evaluations for ENDF/B-VII.0.

2. Neutron resonances: R-matrix analysis

Two different approaches were used in the evaluations of neutron resonances. ORNL used its well known code SAMMY based on R-matrix fits to experimental cross section data. BNL used another method that is based on multi-level Breit-Wigner approach combined with statistical analysis of resonance parameters that were extracted from experimental cross section data.

a. Resolved resonance region. Several important resolved resonance region evaluations in ENDF/B-VII.0 were performed using the SAMMY software. In the resonance region, the cross-section structure is sufficiently complex to preclude the calculation of cross section data from first principles. As a result, high-resolution (in terms of cross-section and energy) measurements must be performed to obtain the complex data structure. Accelerator facilities such as the Oak Ridge Electron Linear Accelerator (ORELA) and the Rensselaer Polytechnic Institute (RPI) Gaerttner accelerator. are used to perform high-resolution cross-section measurements in the resonance region. Before the data can be transmitted to the user community, the experimental data must be analyzed using a state-of-the-art R-matrix analysis tool such as SAMMY. SAMMY combines multichannel multilevel R-matrix fits with corrections for experimental conditions to fit experimental data to theoretical calculations using generalized least squares fitting procedures. A brief discussion of the salient features of the SAMMY code is given here. The detailed explanation can be found in the SAMMY manual [27].

Theoretical cross sections in SAMMY are calculated via the Reich-Moore approximation to R-matrix theory. R-matrix channels are characterized by the two particles with spin i and I, the orbital angular l, the channel spin s (where $s = i + l$), and the total spin J (where $J = s + l$) and parity π. Those channels having the same J and π (the only two quantum numbers that are conserved) are collected in the same spin group. Resonances (which appear as peaks in the cross sections) are assigned to particular spin groups depending on their individual characteristics; initial assignments may be changed as

knowledge is gained during the evaluation process. The goal of the evaluation process is to determine those values for the resonance energy (peak position) and channel widths for each of the resonances that provide the best fit to the measured data.

Most types of energy differential data can be fitted with SAMMY, including but not necessarily limited to total cross section (fitted most efficiently in the form of transmission data), capture, fission, elastic, inelastic, (n,p), and (n,α). Energy and angle differential elastic, inelastic, or other reaction data can be fitted. Certain types of integral data (*e.g.*, resonance integrals) can also be included. Generally, all available and reliable data of all types are included for an evaluation.

For each experimental measurement, the physical circumstances of the measurement introduce modifications to the cross sections; these modifications can be significant and must be incorporated into the analysis process. For example, all experiments occur at finite temperature; Doppler broadening lessens the height and widens the base of the observed resonance peaks. SAMMY provides mathematical descriptions for a large number of experimental effects, the most important of which are listed here.

- Doppler broadening in SAMMY is accomplished via the free gas model or, on those rare occasions when solid state effects are seen, by a crystal lattice model.

- Resolution broadening occurs in time-of-flight experiments because of the finite distribution of locations and times at which the neutron is produced and the locations and times at which the exiting particle is detected. Available treatments in SAMMY range from simple (Gaussian distributions) to complex (individual descriptions of each component of the resolution function, convoluted to give realistic and accurate simulations of the experimental resolution).

- Many options exist for normalization and energy-dependent backgrounds.

- For capture measurements, the finite size of the sample can significantly alter the shape of the measured cross sections: It is possible for a neutron to be scattered one or more times inside the sample before it is finally captured. Because the neutron loses energy with each scattering, the measured cross section may appear to have another much smaller peak at higher incident energy than the actual resonance. In SAMMY, the single-scattering correction is simulated with a mathematical model that gives a highly accurate representation of the physical effect. (The accuracy has been determined both by comparison with experiment and by Monte Carlo calculations [35]). A relatively crude approximation for two or more scatterings give reasonably accurate shape and less accurate magnitudes; this higher-order correction is, however, of lesser importance in measurements.

- The multiple-scattering corrections described above for capture measurements can also be used for fission or other reaction data. However, it is generally not needed there.

- Many experiments utilize samples which are not isotopically pure; also, elements other than the one of interest may be in the sample, as chemical compounds or contaminants. It is often important that these multiple nuclides be treated during the analysis process, rather than experimentally subtracted during the measurement, because effects such as the multiple-scattering corrections are quite dependent on the actual composition of the sample.

The fitting process used in SAMMY is a form of generalized least squares. Multiple data sets are fitted at the same time, either simultaneously or, more often, sequentially with the resonance parameter values and the associated covariance matrix resulting from fitting to one data set used as input for the fitting another data set (a process that would be exactly equivalent to simultaneous fitting if the theoretical calculations were linear with respect to the fitting parameters).

Experimental uncertainties play an important role in the data-fitting process. Statistical uncertainties for each individual data point contribute to the experimental uncertainties, that is, to the diagonal elements of the data covariance matrix (DCM). However, an equally important contribution comes from the other measurement-related uncertainties, such as uncertainties in the experimental correction parameters described in the bullet list above, as well as from uncertainties involved in the data-reduction process. These common or systematic uncertainties cause significant correlations between all the data points in an individual measurement; that is, the covariance matrix associated with the experimental data from any given measurement is fully off-diagonal. In order to properly evaluate the cross section, these off-diagonal terms must not be neglected.

Treatment of fully off-diagonal DCMs in SAMMY is straightforward. Uncertainties in parameters for experimental corrections can simply be flagged to indicate that SAMMY should treat them as having a fixed value but include the effect of their uncertainties in the DCM [36]. The contribution of uncertainties arising in the data-reduction process itself can be determined by the experimentalist, and relevant information fed into the SAMMY code.

At no time is it necessary to actually generate, store, or invert a fully off-diagonal DCM. (For large data sets, such activities are prohibitively expensive, in terms of manpower time, computer time, and computer storage - a situation which explains why off-diagonal DCMs have seldom been used in the past.) Instead, the DCM is

TABLE VI: New evaluations in the resolved and unresolved resonance regions via SAMMY for ENDF/B-VII.0. MF=2 contains resonance parameters and MF=32 their covariances.

Resonance Region	Actinides	Other materials	MF=2 files	MF=32 files
Resolved	^{233,238}U, ^{232}Th,^{241}Pu	^{19}F,^{27}Al, ^{35,37}Cl	8	1*)
Unresolved	^{233,235}U	-	2	-

*) In addition to the direct SAMMY method discussed here, the retroactive SAMMY method was used to evaluate MF=32 for 8 isotopes of Gd, see Section III H 3.

inverted symbolically. When the resulting equations are inserted into the least-squares formulae, only relatively small and easily handled matrices occur. For details on this procedure, see [37].

The final product of a complete evaluation involving many data sets is a set of resonance parameters (including spin assignments for each resonance) and the associated resonance parameter covariance matrix (RPCM). Cross sections calculated from this set of resonance parameters (when properly corrected for experimental conditions) provide the best possible fit to all included data. The resonance parameters are reported in MF=2 file and in some cases the associated RPCM in MF=32 file.

The new actinide evaluations in ENDF/B-VII.0 performed with the SAMMY code include ^{233}U, ^{238}U, ^{232}Th and ^{241}Pu. The new evaluations with SAMMY for intermediate-mass nuclides include ^{19}F, ^{27}Al and ^{35,37}Cl. All these evaluations have data in MF=2 (resonance parameters), while MF=32 data (covariances of resonance parameters) are for ^{232}Th only. A summary of new evaluations by SAMMY is given in Table VI.

b. Unresolved resonance region. In the resolved resonance energy region, the experimental resolution is smaller that the width of the resonances. Consequently, individual resonances can be seen and resonance parameters can be extracted via cross section fitting using methodologies such as the R-matrix formalism and generalized-least-squares techniques in the code SAMMY.

In the unresolved resonance region, the situation is different. Fluctuations exist in the measured cross sections; however, they are smaller than those in the resolved range but are still important for correct calculation of the energy self-shielding of the cross sections. These fluctuations are due to unresolved multiplets of resonances for which it is not possible to determine parameters of individual resonances as can be done in the resolved region. The formalism used for cross section treatment in the unresolved region is therefore based on average values of physical quantities obtained in the resolved resonance range. Approximate values for statistical quantities such as average level spacings, strength-functions, widths, and other relevant parameters are determined from the resolved energy region and used as starting values for the unresolved evaluation.

The unresolved resonance formalism included in SAMMY is based on the methodology used in the statistical model code FITACS, developed by F. Fröhner [38]; details are found in the SAMMY manual. Values of the average parameters are found from fitting the calculated cross sections to experimental cross sections. The set of parameters that best reproduces the data cannot be reported directly to ENDF/B, because the ENDF-6 format uses a less rigorous single-level-Breit Wigner representation. SAMMY/FITACS parameters must therefore be converted into average widths before insertion into ENDF/B.

The new SAMMY unresolved-resonance region evaluations in ENDF/B-VII.0 are ^{233}U and ^{235}U, see Table VI.

3. Neutron resonances: BNL approach

A statistical analysis of neutron resonances was used by S. Mughabghab, BNL, to produce the well known BNL-325. Its 5^{th} edition was published in 2006 as the Atlas of Neutron Resonances: Resonance Parameters and Thermal Cross Sections [30], representing a considerable update to the 1981 [39] and 1984 editions of BNL-325 [40]. These latest thermal values and resonance parameters provided a basis for more than 150 new evaluations included in ENDF/B-VII.0. The resolved and unresolved resonance parameters are adopted from Ref. [30]. The methodology of the evaluation is described in some detail in a forthcoming paper [25].

Accurate knowledge of the thermal neutron fission and capture cross sections are of paramount importance. Because of this, considerable experimental as well as evaluation effort was expended in obtaining very precise and consistent constants at a neutron energy of 2200 m/sec (0.0253 eV). The parameters under consideration are the absorption (σ_a), fission (σ_f), and capture (σ_γ) cross sections. These quantities are interrelated by the following equation at energies below the inelastic threshold:

$$\sigma_a = \sigma_f + \sigma_\gamma \tag{1}$$

In addition, when the scattering cross section is known, the absorption cross section can be determined absolutely to a high degree of accuracy from a measurement of the total cross section by $\sigma_a = \sigma_t - \sigma_s$.

Thermal Capture Cross Sections. The capture cross section, σ_γ, for a single resonance at energy E_0, represented by the Breit-Wigner formalism, is given by:

$$\sigma_\gamma = \sigma_0 \frac{\Gamma_\gamma}{\Gamma} \left(\frac{E_0}{E}\right)^{1/2} \frac{1}{1+y^2} \tag{2}$$

where

$$y = \frac{2}{\Gamma}(E - E_0)$$

$$\sigma_0 = \frac{2.608 \times 10^6}{E_0(\text{eV})} \left(\frac{A+1}{A}\right)^2 \frac{g\Gamma_n}{\Gamma} \tag{3}$$

In this relation, Γ_n, Γ_γ and Γ are the scattering width, the radiative width, and total width of the resonance, respectively; σ_0 is the peak total cross section; A is the atomic mass number of the target nucleus; g is the statistical spin weight factor defined below.

If N s-wave resonances of a nucleus are located away from the thermal energy, then their contribution to the thermal capture cross section is given by the following expression:

$$\sigma_\gamma^0(E) = 2.608 \times 10^6 \left(\frac{A+1}{A}\right)^2 \sum_{j=1}^{N} \frac{g\Gamma_{nj}^0 \Gamma_{\gamma j}}{\Gamma_j^2 + 4(E - E_{0j})^2} \tag{4}$$

The spin-dependent scattering lengths, a_+ and a_-, associated with spin states $I + 1/2$ and $I - 1/2$, where I is the spin of the target nucleus, can be written as:

$$a_\pm = R' + \sum_{j=1}^{N} \frac{\lambda\!\!\!^{-}_j \Gamma_{nj}}{2(E - E_j) - i\Gamma_j} \tag{5}$$

where R' is the potential scattering length and $\lambda\!\!\!^{-}$ is De Broglie's wavelength divided by 2π. The summation is carried out over N s-wave resonances with the same spin.

The total coherent scattering length for non-zero spin target nuclei, is then the sum of the spin-dependent coherent scattering widths, a_+ and a_-, weighted by the spin statistical factor, g_+ and g_-:

$$a = g_+ a_+ + g_- a_-$$

where

$$g_+ = \frac{I+1}{2I+1} \qquad \text{and} \qquad g_- = \frac{I}{2I+1} \tag{6}$$

The coherent, incoherent, and total scattering cross sections can then be expressed in terms of the scattering lengths by the following relations:

$$\sigma_{coh} = 4\pi \left(g_+ a_+ + g_- a_-\right)^2 \tag{7}$$

$$\sigma_{inc}(\text{spin}) = 4\pi g_+ g_- (a_+ - a_-)^2 \tag{8}$$

$$\sigma_s = 4\pi \left(g_+ a_+^2 + g_- a_-^2\right)^2 \tag{9}$$

To calculate the capture cross section, coherent scattering amplitudes, and various spin-dependent scattering cross sections in terms of neutron-resonance parameters, the above relations, Eq. (2) to Eq. (9), were applied [30]. If the results of the calculated cross sections do not agree with measurements within the uncertainty limits, then one or two negative energy (bound) levels are invoked.

Thermal Fission Cross Sections. The fission cross section can be described as a sum over positive and negative energy resonance contributions. In the framework of the Breit-Wigner formalism, the fission cross section can be obtained from:

$$\sigma_{nf}(E_n) = \frac{2.608 \times 10^6}{(E_n)^{1/2}} \frac{A+1^2}{A} \sum_{j}^{N} \frac{g\Gamma_{nj}^0 \Gamma_{fj}}{\Gamma_j^2 + 4(E_n - E_j)^2} \tag{10}$$

$$\Gamma_j(E) = \Gamma_{nj}(E) + \Gamma_{\gamma j} + \Gamma_{fj}$$

Potential Scattering Length. The potential scattering length or radius, R', is an important parameter which is required in the calculation of scattering and total cross sections. In analogy with the coherent scattering length, R' is defined by the relation:

$$R' = -\lim_{k \to 0} \left(\frac{Re(\delta'_{OP})}{k}\right) \tag{11}$$

where Re means the real part and δ'_{0P} is the optical model s-wave phase shift.

In R-matrix theory the potential scattering radius is expressed by

$$R' = R(1 - R^\infty) \tag{12}$$

where R^∞ is related to the distant s-wave resonance contribution and is represented by

$$R^\infty = \sum_n \frac{{\gamma_n}^2}{E_n - E} \tag{13}$$

where the summation is carried out over the distant resonances. We note that R' can be determined to a high degree of accuracy from the measured coherent scattering amplitude by Eq.(5) when the resonance data is complete.

Resolved Resonance Region. The Bayesian approachis adopted in this evaluation to distinguish p-wave from s-wave resonances for cases where the orbital angular momentum, l, has not been determined from measurements. Even though there is a potential danger of incorrect assignment of l [41], the Bayesian approach was used in several cases in the past. The first investigators to apply Bayes' conditional probability for the determination of parities of ^{238}U resonances were Bollinger and Thomas [42]. Subsequently, Perkins and Gyullassy [43] and Oh *et al.* [29] extensively applied this procedure in the evaluation of resonance parameters.

For a resonance with a neutron width weighted by the spin statistical factor, $g\Gamma_n$, the probability that a resonance is a p-wave resonance is given according to Bayes' theorem of conditional probability by:

$$P(p|g\Gamma_n) = \left(1 + \frac{P(g\Gamma_n|s)\langle D_1\rangle}{P(g\Gamma_n|p)\langle D_0\rangle}\right)^{-1} \quad (14)$$

where $\langle D_1\rangle/\langle D_0\rangle$ is the level-spacing ratio for p- and s-wave resonances, and $P(g\Gamma_n|s)$ (or $P(g\Gamma_n|p)$) is the probability that the neutron width is $g\Gamma_n$ if the resonance is an s-wave (or p-wave) resonance.

Eq. (14) can be solved by taking into account the Porter and Thomas distribution [44] and assuming a (2J+1) law of the nuclear level density. The result is

$$P(p|g\Gamma_n) = \left(1 + \frac{D_1}{D_0}\sqrt{\frac{S_1P_1}{S_0P_0}}\frac{e^x}{A_{Il} + (1 - A_{Il})y}\right)^{-1} \quad (15)$$

where

$$x = \frac{g\Gamma_n}{2D_0\sqrt{E}}\left(\frac{1}{S_1P_1} - \frac{1}{S_0P_0}\right) \quad (16)$$

$$y = \sqrt{\frac{\pi g\Gamma_n}{2\sqrt{E}D_0S_1P_1}} \quad (17)$$

D_1/D_0=3, 9/4, 1/2 for I=0, 1/2, or larger than 1 respectively; and A_{Il}=1, 2/3, 1/2 for I=0, 1/2, or larger than 1 respectively. S_0 and S_1 are the s-wave and p-wave neutron strength functions, respectively, while P_0 and P_1 are the corresponding penetrabilities.

Figs. 2 and 3 illustrate the Porter-Thomas analysis as applied to the s- and p- wave resonances of ^{133}Cs. From this procedure, the average level spacings and strength functions for the s- and p- wave resonances are determined.

Figs. 4 and 5 show the evaluated capture cross sections for ^{133}Cs and ^{141}Pr, respectively, in the thermal and low energy resonance region and are compared with the available experimental data. The unresolved resonance region is extended up to the first excited level. At higher energies (fast neutrons), the evaluations were done by the code EMPIRE described below. We note that there is almost perfect match between the unresolved resonance region and the fast neutron region.

Unresolved Resonance Region. To describe the unresolved resonance region in the single-level Breit-Wigner formalism, the following paremeters are required: the average level spacing, D_l, the average reduced neutron widths $\langle g\Gamma_n^l\rangle$, the strength functions S_l, the average radiative widths, $\Gamma_{\gamma l}$, and R'.

After determination of l values for all resonances, the reduced neutron widths are analyzed in terms of Porter-Thomas distribution [44] (if the number of measured resonances is large enough for a statistical sample).

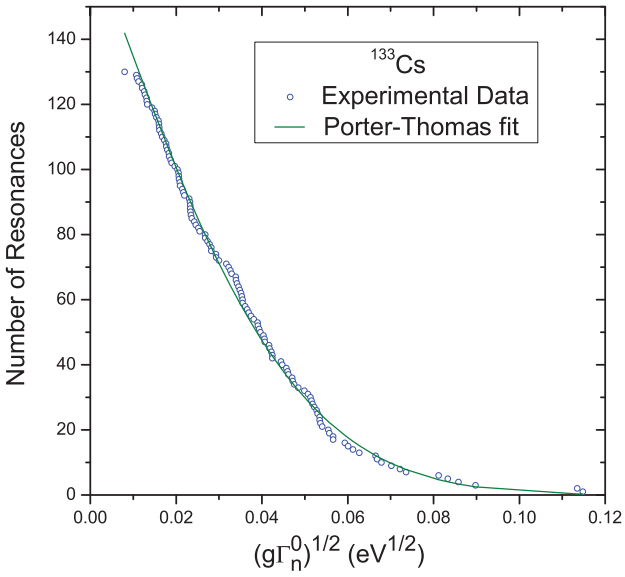

FIG. 2: Porter-Thomas distribution of reduced neutron widths, $g\Gamma_n^0$ for s-wave resonances of ^{133}Cs in the energy region below 3400 eV.

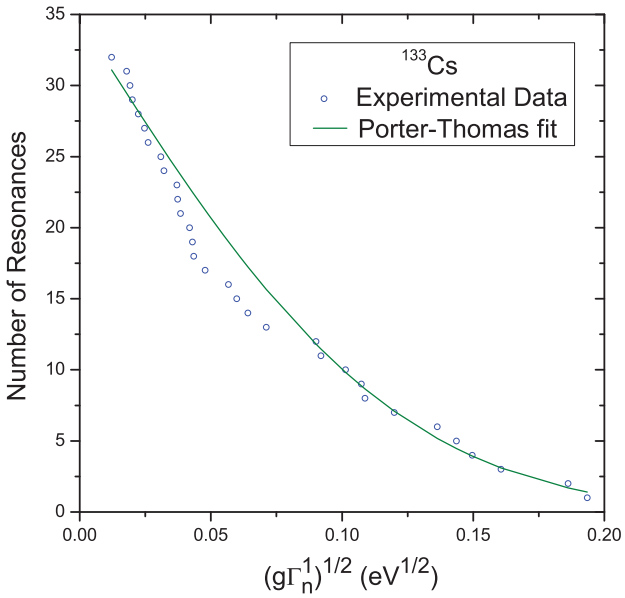

FIG. 3: Porter-Thomas distribution of reduced neutron widths, $g\Gamma_n^1$ for p-wave resonances of ^{133}Cs in the energy region below 387 eV where the p-wave resonances are detected.

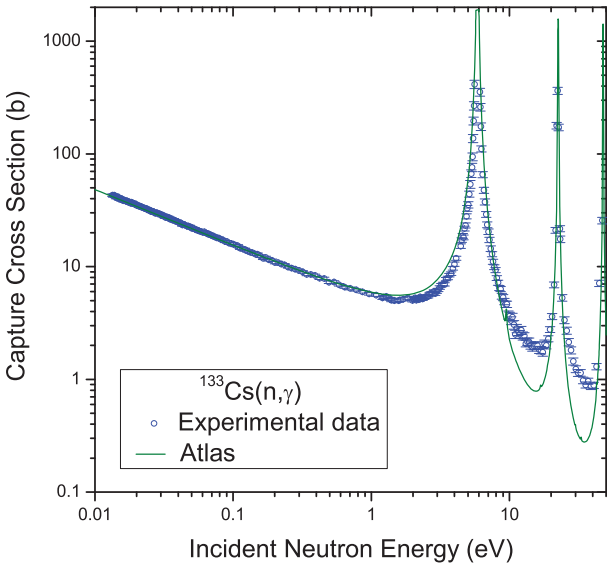

FIG. 4: Neutron capture cross section for ^{133}Cs in the thermal and resolved resonance energy region. The calculated cross section is Doppler-broadened to 300^o K; the experimental resolution is not included. Two bound levels were invoked in order to fit the thermal constants.

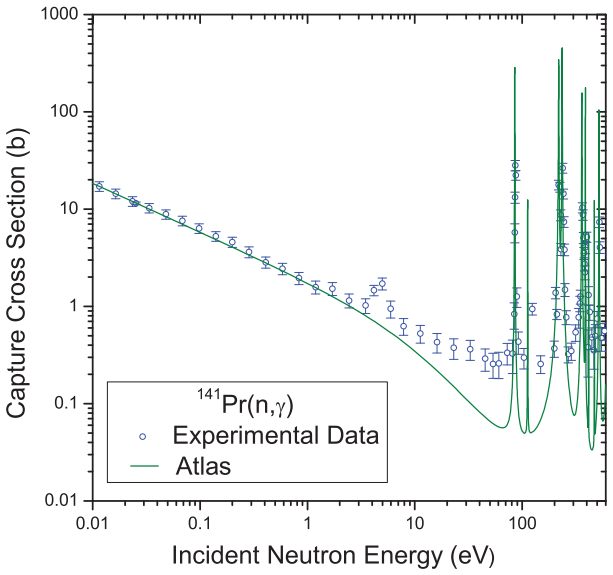

FIG. 5: Neutron capture cross section for ^{141}Pr in the thermal and resolved resonance energy region. The calculated cross section is Doppler-broadened to 300^o K; the experimental resolution is not included. Two bound levels were invoked in order to fit the thermal constants.

Instead of working with the Porter-Thomas distribution, it is much simpler to analyze the resonance parameters data with the cumulative Porter-Thomas distribution. The result is:

$$N(y) = N_r(1 - erf(y)) \tag{18}$$

where N_r is the corrected total number of resonances, $N(y)$ is the total number of resonances larger than a specified value of y determined by the experimental detectability level:

$$y = \frac{\Gamma_n^l}{2 < \Gamma_n^l >} \tag{19}$$

and Γ_n^l is the reduced neutron width for orbital angular momentum l and $< \Gamma_n^l >$ is its average value.

Since resonances with small neutron widths are usually missed in measurements, it is necessary to exclude resonances whose reduced widths are smaller than a certain magnitude. By setting a cutoff value, *i.e.* a minimum magnitude of reduced width, the effect of missed small resonances on the resulting average parameters is reduced significantly.

The two parameters N_r and $\langle g\Gamma_n^l \rangle$ are determined through the fitting procedure. The resulting neutron strength function S_l and average level spacing D_l in a determined energy interval ΔE are then calculated by:

$$S_l = \frac{\langle g\Gamma_n^l \rangle \cdot N_r}{(2l+1) \cdot \Delta E} \tag{20}$$

$$D_l = \frac{\Delta E}{N_r - 1} \tag{21}$$

The cross sections in the unresolved resonance region are generated by the in-house utility code INTER with input parameters from the Atlas [30].

The average radiative widths of neutron resonances are determined from measurements in the resolved energy region by calculating the weighted, as well as unweighted, values. For nuclei with unmeasured radiative widths, the systematics of s-, p- and d-wave radiative widths as a function of atomic mass number are used [30].

Figs. 6 and 7 show the evaluated capture cross sections in the unresolved energy resonance region, compared with the available experimental data, for ^{133}Cs and ^{141}Pr, respectively. The unresolved resonance region is extended up to the first excited level, which is 90 keV for ^{133}Cs and 141 keV for ^{141}Pr. At higher energies (fast neutrons), the evaluations were done by the code EMPIRE. We note an excellent match of cross sections in the boundary of the two energy regions.

4. Fast neutron region

All new ENDF/B-VII.0 evaluations in the fast neutron region were performed with one of the two reaction model

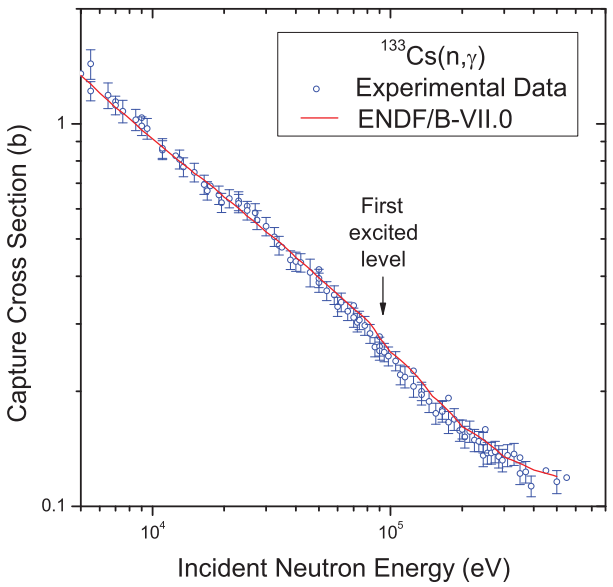

FIG. 6: Neutron capture cross section for ^{133}Cs in the unresolved resonance energy region extended up to the first excited level. Evaluation at higher energies was performed by EMPIRE.

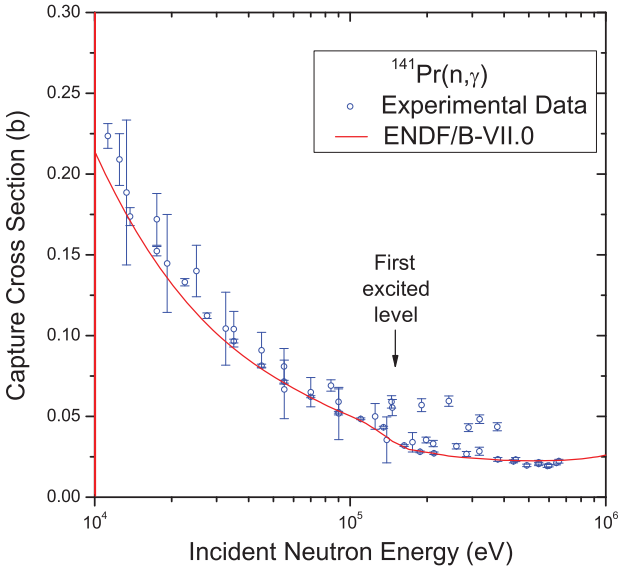

FIG. 7: Neutron capture cross section for ^{141}Pr in the unresolved resonance energy region extended up to the first excited level. Evaluation at higher energies was performed by EMPIRE.

codes: Los Alamos used an updated version of the well-tested GNASH code; while all evaluations involving BNL relied on the new EMPIRE code that has been used for the first time to provide a number of consistent, complete evaluations (72) to the national nuclear data library.

Although the two codes were developed independently and their coding styles reflect the times the codes were conceived, to a large extent they both use the same nuclear reaction models and cover similar sets of observables. In particular, GNASH and EMPIRE calculate cross sections for all relevant reaction channels, angular distributions (EMPIRE only), exclusive and inclusive particle- and γ-spectra, double-differential cross sections, and spectra of recoils. Both codes observe angular momentum coupling (at least in the statistical decay part) and are, therefore, capable of detailed modeling of the γ-cascade providing γ production spectra, intensities of discrete transitions, and isomeric cross sections. Nuclear reaction models included in the codes can be classified into three major classes: (i) optical model and direct reactions (coupled-channels [CC] and distorted-wave Born approximation [DWBA]), (ii) preequilibrium emission, and (iii) Hauser-Feshbach statistical decay. Inclusion of multiple preequilibrium processes allows us to cover incident energies ranging from the upper limit of resolved resonances up to about 150 MeV.

We refer readers interested in details to the original paper [22] as far as the GNASH code is concerned, and to the extensive description of the evaluation methodology employed at BNL [25]. In the following we only give a brief descriptive outline of the models and the way they were used in developing new evaluations for ENDF/B-VII.0.

a. Optical model and direct reactions: We used spherical optical models to calculate transmission coefficients for all ejectiles involved in a reaction[2].
In the case of spherical nuclei, the same calculations also determined reaction (absorption) cross sections. For deformed nuclei, the incident channel was treated in terms of coupled-channels rather than the spherical optical model. In the latter case, proper coupling also provided cross sections for inelastic scattering to collective levels and related angular distributions of scattered neutrons. In certain cases we also included direct scattering to the collective levels embedded in the continuum. Generally, we chose optical model potentials from a vast selection available in the RIPL-2 library [34] (co-authored by some of the same authors as the present paper) but in the course of ENDF/B-VII.0 development, the original RIPL-2 potentials were often adjusted to improve agreement with recent experimental data, and in some cases totally new potentials were constructed.

[2] In practice, in GNASH we often use CC transmission coefficients for the ejectiles, too.

b. Compound nucleus decay: Although many theoretical models were utilized in the ENDF/B-VII.0 evaluations, the statistical model provides the basic underpinning for the whole procedure. The decay of the compound nucleus is modeled by the Hauser-Feshbach equations, using transmission coefficients and level densities to represent the relative probabilities of decay in the various open channels. The transmission coefficients are obtained from an optical model calculation, commonly using the ECIS code [26]. As a rule, spherical optical potentials were used for the outgoing channels. Note that, mostly for historical and technological reasons in the case of the GNASH code, and deliberately in case of the EMPIRE code[3] , momentum (l) and spin (j) dependent transmission coefficients $T(l,j)$, are collapsed into $T(l)$ values. However, in most physical situations, the effect of this approximation is negligible.

Schematically, the cross section for a reaction (a,b) that proceeds through the compound nucleus mechanism can be written as

$$\sigma_{a,b} = \sigma_a \frac{\Gamma_b}{\sum_c \Gamma_c} \tag{22}$$

The summation over compound nucleus spin J and parity π, and integration over excitation energy E (in case of daughter CN) is implicit in Eq. 22. The decay width Γ_c is given by

$$\Gamma_c = \frac{1}{2\pi\rho_{CN}(E)} \times \sum_{c'} \int_0^{E-B_c} \rho_c(E')T_c(E-B_c-E')dE', \tag{23}$$

where B_c is the binding energy of particle c in the compound nucleus, ρ is the level density, and $T_c(\epsilon)$ stands for the transmission coefficient for particle c having channel energy $\epsilon = E - B_c - E'$ Again, for simplicity, we drop explicit reference to the spin and parity in Eq. 23 and the summation extends over all open channels c'. Since the ENDF/B-VII.0 evaluations extend at least up to 20 MeV, and in many cases reach as far as 150 MeV, sequential multi-particle particle emission had to be included in the Hauser-Feshbach calculations, which in practice implies an energy convolution of multiple integrals of the type of Eq. 22.

In order to account for the competition between γ-emission and emission of particles along the deexcitation chain, our calculations always involve a full modeling of the γ-cascade that conserves angular momentum. The formalism for γ-rays transitions is based on the Giant Multipole Resonance model known as the Brink-Axel hypothesis [45, 46] that allows the cross section for photoabsorption by an excited state to be equated with that of the ground state. The parameters of the Giant Multipole Resonances are taken from the experimental compilation and/or systematics contained in the RIPL-2 library. We note, that our calculations account for splitting of the Giant Dipole Resonance due to nuclear deformation. In GNASH, the γ-ray transmission coefficients are obtained from the γ-ray strength function formalism of Kopecky and Uhl [47] where absorption on an excited state is allowed to differ from the ground state. EMPIRE allows for a suite of γ-ray strength functions. Typically, we used Mughabghab and Dunford's prescription known as GFL [48] or Plujko's modified Lorentzian referred as MLO1 [49]. In both codes the γ-ray strength functions can be, and often are, normalized to experimental information on $2\pi\Gamma_\gamma/D_0$ or adjusted to reproduce capture cross sections.

Nuclear level densities along with optical model transmission coefficients are the two most important ingredients of the statistical model. Therefore, particular attention was dedicated to a proper selection of the model and its parameters. Several approaches are built into the GNASH and EMPIRE codes. With the exception of the standard Gilbert-Cameron model, the approaches used in both codes are not equivalent. However, by construction they agree at the neutron binding energy and all match the density of known discrete levels.

In GNASH, the description of the level densities in the continuum follows the Ignatyuk form of the Gilbert-Cameron formalism, including a washing-out of shell effects with increasing excitation energy. This modification is important for extending calculations to incident energies above 20 MeV where energy dependence of the level density parameter a cannot be ignored.

Apart from a few evaluations for which the standard Gilbert-Cameron approach was adopted, most of the evaluations performed with EMPIRE employed level densities that are specific to the EMPIRE code. The formalism uses the super-fluid model below a critical excitation energy and the Fermi gas model at energies above it. Collective enhancements due to nuclear vibration and rotation are taken into account in the nonadiabatic approximation, i.e., they are washed out when excitation energy increases. Differently from other formulations, EMPIRE-specific level densities account explicitly for the rotation-induced deformation of the nucleus and determine spin distributions by subtracting rotational energy from the energy available for intrinsic excitations. The deformation enters level density formulas through moments of inertia and through the level density parameter a that increases with increase in the surface of the nucleus. As in GNASH, the a-parameter is energy dependent due to the shell corrections that vanish with increasing excitation energy. Experimental results or systematics provide

[3] EMPIRE code has been originally developed to include the capability of calculating Heavy Ion induced reactions that typically involve large angular momenta and tens of decaying nuclides. To ensure flexibility of the code the transmission coefficients for all nuclei are stored in a single 4-dimensional array. The collapsed $T(l)$'s help to keep the size of this array within tractable limits and allow faster calculations.

values for the a-parameter, with measured values given priority over the systematics prediction. The average ratio of the experimental values to the results of systematics is used to normalize predictions for nuclei for which there are no experimental results. In this way a form of "local systematics" is constructed for the nuclei involved in the calculation run.

c. Width fluctuation correction: At low-incident energies, the statistical approximation that entrance and exit channels are independent (Bohr independence hypothesis) is not valid anymore due to interferences in the elastic channel. The Hauser-Feshbach equations have to be modified in order to include the so-called width fluctuation correction factors. Over the years, three models (Moldauer [50], HRTW [51] and exact Gaussian Orthogonal Ensemble (GOE) theory [52]) have been developed to estimate these correction factors. All three models are implemented directly in McGNASH which is a modernized, not yet released, version of the code GNASH. To do so, the usual Hauser-Feshbach loops have to be expanded to include the coupling between the incident and outgoing waves in the elastic channel. This difference in implementation is required only for the first compound nucleus decay.

The GNASH code does not calculate these correction factors but rather imports them as the result from an auxiliary code (usually COMNUC [53], which uses the Moldauer model). Although somewhat cumbersome, this approach proves to be sufficiently accurate in most cases. EMPIRE, by default, uses internal implementation of the HRTW approach that can be summarized with the following equation:

$$\sigma_{ab}^{HRTW} = V_a V_b \left(\sum_c V_c \right)^{-1} \left[1 + \delta_{ab} \left(W_a - 1 \right) \right]. \quad (24)$$

This formula is, essentially, equivalent to the Hauser-Feshbach expression but the elastic channel is enhanced by the factor W_a. This change must be compensated by appropriate modifications of other channels so that total flux remains conserved. In Eq. 24 the quantities V_c replace optical model transmission coefficients that appear in the original Hauser-Feshbach formula in order to take care of this reduction. In our calculations with EMPIRE we used Eq. 24 with an improved elastic enhancement factor W_a [54].

d. Semi-classical preequilibrium models: The probability that a system composed of an incident neutron and a target nucleus decays before the thermal equilibrium is attained becomes significant at incident energies above 10 MeV, while the actual process occurs even at lower energies. This mechanism, referred to as preequilibrium emission, must therefore be taken into account in any modern evaluation methodology. The preequilibrium boom in the 1970's and 80's produced a number of approaches that, according to their physical content, can be classified into two major groups: semi-classical and quantum-mechanical.

In any preequilibrium model, the excited nuclear system (composite nucleus) follows a series of ever more complicated configurations, where more and more particle-hole (p-h) states are excited. In each stage, a possible emission of a particle competes with the creation of an intrinsic particle-hole pair that brings the system towards the equilibrium stage. Particle emission from the early stages is characterized by a harder spectrum and forward peaked angular distributions. These two features exclude any possibility of simulating preequilibrium emission within the compound nucleus formalism and necessitate explicit use of adequate modeling.

The exciton model is a semi-classical formulation of the preequilibrium emission that is used in GNASH and EMPIRE. The core of the model is the so called master-equation that governs time dependence of occupation probabilities for various p-h stages

$$\hbar \frac{dP_n}{dt} = \sum_m \Lambda_{n,m} P_m - \Gamma_n P_n, \quad (25)$$

where the total decay width of the stage n is given in terms of the partial transition widths $\Lambda_{l,n}$ and partial width $\Gamma_{e,n}$ for the emission of particle e by

$$\Gamma_n = \sum_l \Lambda_{l,n} + \sum_e \Gamma_{e,n}. \quad (26)$$

Due to the two-body nature of the nuclear force, intrinsic transitions occur only between neighboring stages, and the transition matrix Λ is tri-diagonal; the off-diagonal terms accounting for backward and forward transitions. Eq. 25 applied without any restrictions would also include the equilibrium limit. We choose to avoid it, since the compound nucleus theory is more rigorous and accounts for angular momentum and parity coupling as well as for discrete levels that are not all included in the exciton model. Therefore, we allow for a fairly limited number of p-h stages (typically 3). In addition, in EMPIRE we set to zero backward transition rates, which implies that the system is evolving towards equilibrium without return (never-come-back approximation).

In GNASH, the preequilibrium phase is addressed through the semiclassical exciton model in combination with the Kalbach angular-distribution systematics [55]. These systematics provide a reasonably reliable representation of the experimental database. Some limited comparisons have been performed with the quantum mechanical approach of Feshbach-Kerman-Koonin (FKK) [56] and have shown a fairly good agreement between the two approaches. These results confirm that in most practical applications the exciton model can be used to model preequilibrium emission providing that the direct reaction contribution is accounted for by the CC or DWBA approach.

EMPIRE implements a suite of preequilibrium models including two versions of the exciton model (PCROSS and DEGAS [57]), and the Monte-Carlo approach DDHMS [58–60] in addition to the quantum-mechanical Multistep Direct and Multistep Compound models discussed below. PCROSS has no angular momentum and parity coupling, uses Kalbach angular-distribution systematics, and allows for preequilibrium emission of clusters and γ-rays. DEGAS is a particular implementation with full account of angular momentum but lacks angular distributions and cluster emission. We often use DEGAS for predicting primary γ-spectra produced by neutrons with incident energies above 10 MeV.

In their original formulations, both semi-classical and quantum-mechanical formulations take into account the pre-equilibrium emission of one particle only, under the assumption that the remaining excitation energy in the residual nucleus is too small to allow further particle emission. Although this assumption remains valid up to few tens of MeV, it is not valid anymore at higher-incident energies. In order to account for multiple pre-compound emission, both GNASH and EMPIRE use a simple procedure designed by Chadwick [61] that assumes that

- the first residue contains 2 excitons only,
- emission probability of the single excited particle can be approximated by the s-wave transmission coefficient.

A more rigorous method, also implemented in both codes, is a new Monte Carlo pre-equilibrium model, as formulated in Refs. [58–60]. This approach allows unlimited emission of pre-equilibrium neutrons and protons, and is therefore well suited for the study of high-energy reactions up to a few hundreds of MeV. The Monte Carlo simulation also presents some advantages over traditional approaches. In particular, center-of-mass to laboratory kinematic transformations can be performed exactly. Also, correlations in energy and angular distribution among preequilibrium ejectiles can be obtained straightforwardly.

e. Quantum-mechanical preequilibrium models: The model of choice in EMPIRE is the statistical Multi-step Direct (MSD) theory of preequilibrium scattering to the continuum originally proposed by Tamura, Udagawa and Lenske (TUL) [62]. The evolution of the projectile-target system from small to large energy losses in the open channel space is described in the MSD theory with a combination of direct reaction (DR), microscopic nuclear structure and statistical methods. As typical for the DR-approach, it is assumed that the closed channel space can be treated separately within the Multi-step Compound mechanism that has to follow MSD.

From the physics point of view, the MSD model describes multiple interaction of the incident particle with the target nucleus that results in the energy and angular momentum transfer to the target. These transfers are modulated by the response of the target to such interactions. This response is modeled in terms of the Random Phase Approximation accounting for the excitation of the vibrational states. Therefore, transfers compatible with vibrational excitations in the target are strongly favored leading to the distinct peaks in the high energy end of the spectrum. The current implementation of the MSD mechanism in EMPIRE is limited to inelastic scattering in which collective excitations are by far strongest. The charge exchange channels have to be treated within semi-classical models.

The modeling of Multi-step Compound (MSC) processes in EMPIRE follows the approach of Nishioka *et al.* (NVWY) [52]. Like most of the precompound models, the NVWY theory describes the equilibration of the composite nucleus as a series of transitions along the chain of classes of closed channels of increasing complexity. Formal structure of the NVWY formula resembles matrix representation of the master-equation typical for classical preequilibrium models. However, NVWY formalism is strictly derived from basic principles assuming well proven GOE statistics for single particle nuclear levels. Microscopic quantities that constitute ingredients of the NVWY formula were linked to the macroscopic, experimentally known, quantities in Ref. [63] which was an essential step allowing for practical application of the theory. We use three MSC classes, which are generally sufficient to cover the most important part of the MSC spectrum and to delegate the rest of the decay to the Hauser-Feshbach model.

f. Coupling between MSC and MSD in EMPIRE The NVWY theory includes a possibility of feeding higher MSC classes directly from the MSD chain, in addition to the normal transitions between bound states of increasing complexity. This effect, known also as gradual absorption, is included in the EMPIRE code by distributing the incoming flux over different MSD and MSC classes in proportion to the respective state densities and to the average value of the squared matrix elements coupling unbound to unbound ($< V_{uu}^2 >$) and unbound to bound states ($< V_{ub}^2 >$).

g. Preequilibrium emission of clusters: Preequilibrium emission of clusters (typically α-particles, deuterons, tritons and ^{3}He) is considered in both codes. GNASH uses phenomenological expressions by Kalbach [55, 64] while EMPIRE employs the Iwamoto-Harada model [65] parameterized and improved in Refs. [66–68]. The latter model contains two essential features that increase production of composite particles during the equilibration stage:

- inclusion of the pickup-type contribution that allows some nucleons which constitute the emitted composite particle to come from levels below the Fermi energy.
- information on the intrinsic wave function of the composite particle (cluster) is incorporated in the energy-dependent formation factor.

h. Fission: The relation used in the statistical model for the fission cross section is

$$\sigma_{a,f}(E) = \sum_{J\pi} \sigma_a(EJ\pi) P_f(EJ\pi), \qquad (27)$$

where $\sigma_a(EJ\pi)$ is the population of the fissioning nucleus in the state $EJ\pi$ and $P_f(EJ\pi)$ represents the fission probability.

In GNASH fission probabilities are calculated from the quantum-mechanical transmission coefficient through a simple double-humped fission barrier, using uncoupled oscillators for the representation of the barriers. The barrier penetrabilities are computed using the Hill-Wheeler formula for inverted parabolas. An additional parameter is used to account for level density enhancement due to asymmetry at saddle points.

Version 2.19 (Lodi) of the EMPIRE introduces an advanced fission formalism that is applicable to multi-chance fission induced by light particles and photons. It uses an optical model for fission to calculate transmission through coupled single-, double- and triple-humped fission barriers, starting from sub-barrier excitation energies. In the case of a double-humped barrier, the expression is generalized to account for multi-modal fission. For light actinides, a triple-humped fission barrier with a shallow tertiary well, which accommodates undamped vibrational states, is employed. This fission model can provide good description of experimental data (including gross vibrational resonant structure at sub-barrier energies), has reasonably good predictive power, and improves the accuracy of determination of fission barrier parameters.

i. Exclusive spectra: The standard ENDF-6 format requires exclusive particle spectra in the formatted files. For example, the neutron spectrum associated with the (n,2n) reaction must include both the first and the second neutron that were emitted to create the relevant (n,2n) residue. Consequently, the first emitted neutron, if followed by any other particle emission, must not be counted in the (n,n') spectrum. This requirement is a challenge for standard model codes that often do not carry over enough history to disentangle emission spectra into the exclusive ones.

Both GNASH and EMPIRE are capable of providing such exclusive spectra. In the case of GNASH, emission histories are stored in the file and analyzed by a dedicated code, RECOIL, once the GNASH calculations are completed.

EMPIRE performs this calculation internally using the concept of "population spectra". Fig. 8 sketches the procedure involved in the calculations. The separate "population spectra" are associated with each energy bin in the discretized continuum. They represent cumulative spectra for each type of ejectile that contributed to the population of a given energy bin in the residue. Each time a particle is emitted it removes a part of the "population spectra" in the bin from which it originates and deposits it on the population spectrum of the final bin. The particle itself contributes to the final bin population spectrum a spike at the energy with which particle was emitted.

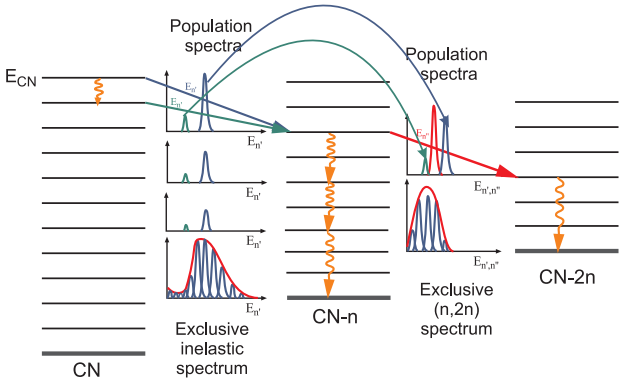

FIG. 8: Schematic representation of the algorithm for calculation of exclusive spectra (see text for details).

In this calculational scheme, γ-transitions play a particular role of transferring "population spectra" down to the excitations stable against particle emission. These contributions (undepleted) sum up on the residual nucleus ground state to form exclusive spectra associated with the residue.

j. Recoils: Spectra of recoils are particularly important for calculation of the radiation damage and heating caused by reaction products in various construction materials. GNASH and EMPIRE provide recoil spectra in the laboratory system accounting for the energy boost due to the center of mass motion. The LANL RECOIL code calculates, and then stores in the ENDF-6 format, the recoil spectra. At higher energies (>20 MeV) for LA150 evaluations, a model was developed to calculate the energy distributions of all recoil nuclei in the GNASH calculations by Chadwick in 1996. The recoil energy distributions are represented in the laboratory system in MF=6, MT=5, and are given as isotropic in the lab system. All other data in MF=6,MT=5 are given in the center-of-mass system. This method of representation utilizes the LCT=3 option approved at the November, 1996, CSEWG meeting.

In EMPIRE, spectra of recoils are calculated internally using an algorithm analogous to the one used for the exclusive spectra. Accordingly, energy correlations between subsequent emissions are taken into account. The resulting spectra are integrated over angles and summed over intermediate spins. However, the asymmetric angular distribution of the first ejectile is taken into account when parent nucleus and ejectile velocity vectors are added to produce the residual nucleus (recoil) velocity.

k. Prompt fission neutron spectra: The Los Alamos (Madland-Nix) model of the prompt fission neutron spectrum and average prompt neutron multiplicity is based upon classical nuclear evaporation theory and utilizes an

isospin-dependent optical potential for the inverse process of compound nucleus formation in neutron-rich fission fragments [69]. The model accounts for the physical effects of (a) the motion of the fission fragments emitting the neutrons, (b) the distribution of fission-fragment residual nuclear temperature that results from the initial distribution of fission-fragment excitation energy, (c) the energy dependence of the cross section for the inverse process of compound nucleus formation, and (d) the effects of and competition between first-, second-, third-, and fourth-chance fission, wherein the neutrons emitted prior to fission in multi-chance fission are included in the total prompt fission neutron spectrum.

The Los Alamos model, in its exact energy- dependent formulation, has been used to calculate the prompt fission neutron spectrum matrix for the n + ^{235}U, n + ^{238}U, and n + ^{239}Pu systems, and these appear in ENDF/B-VII with the tabulated distribution (LF=1) law.

The prompt fission neutron spectrum matrix for a given system is calculated in three steps. **First**, one starts by collecting together the published experimental measurements of the prompt spectra and average prompt neutron multiplicities for that system including the multiplicities for the fissioning nuclei occurring in multichance fission and the measurements of the fission probabilities for multichance fission, if they exist, for that same system. If the required fission probabilities have not been measured they must be calculated in a Hauser-Feshbach approach. Such approaches have the measured total fission cross section as the single constraint in the fission channel and therefore the sum of the multichance fission probabilities is well determined, but the individual multichance fission probabilities are less well determined. **Secondly**, least-squares adjustments are performed with respect to the nuclear level-density parameter in the Los Alamos model and each measured spectrum for the incident neutron energies below the threshold for 2nd-chance fission. The determination of the level-density parameter for a given measured spectrum at a given incident neutron energy requires that the tail of the spectrum have been measured out to at least 7 or 8 MeV. Measured spectra not meeting this requirement are excluded. The incident neutron energy dependence of the extracted nuclear level-density parameters must be smooth and within physical expectations. Measurements falling strongly outside these expectations are disallowed. **Thirdly**, the multichance fission components of the total spectrum are calculated using the normalized distributions of excitation energy for each fissioning compound nucleus occurring together with either measured or calculated fission probabilities for that compound nucleus and then the Los Alamos model spectrum for that compound nucleus, as described in detail in [69] for the original calculation of the n + ^{235}U prompt fission neutron spectrum matrix.

The calculation of the prompt fission neutron spectrum matrices for the n +^{235}U, n + ^{238}U, and n + ^{239}Pu systems for ENDF/B-VII.0 differ from the calculations for those same systems in ENDF/B-VI by the facts that the Los Alamos model was not used for the latter two systems in ENDF/B-VI and that although the Los Alamos model was used in ENDF/B-VI for the n + ^{235}U system the ENDF/B-VII.0 calculation for n + ^{235}U made extensive use of experimental data that were not available in 1982.

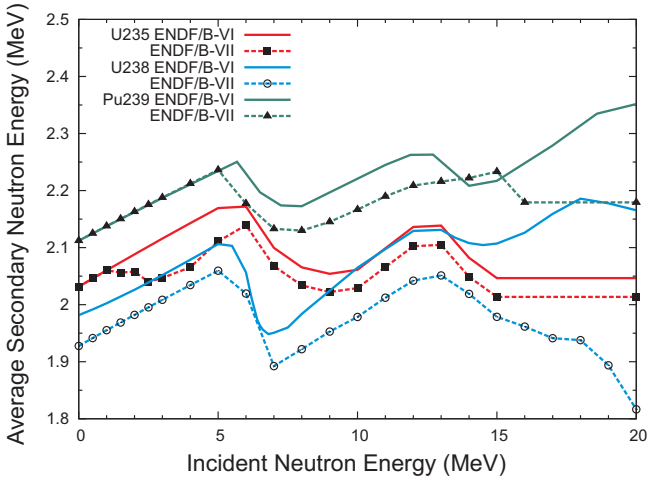

FIG. 9: First moments (average energies) of ^{235,238}U and ^{239}Pu prompt fission neutron spectra for ENDF/B-VII.0 calculated with the Los Alamos model [69] in comparison with those of ENDF/B-VI.

Fig. 9 shows the average prompt fission neutron emission energy, as a function of incident energy, for ^{235,238}U and ^{239}Pu, for both the new ENDF/B-VII.0 evaluations and the old ENDF/B-VI evaluations. These results are described in more detail below, in the subsections devoted to each of the major actinides. An example of the way the emission spectrum changes with incident energy is shown in Fig. 10, where the spectrum is divided by the thermal spectrum for clarity (hence the constant value of 1.0 on this 3D graph for an incident energy of zero). This figure illustrates the staircase-like effect at the peak regions of the spectra due to the onset of successive multiple-chance fissions and, correspondingly, the heating and subsequent cooling in the tail regions of the spectra as each successive multi-chance fission neutron emission prior to fission occurs.

B. Actinides

New evaluations were performed for ENDF/B-VII.0 of neutron reactions on the major actinides ^{235,238}U, and ^{239}Pu, as well as on ^{232}Th, ^{231,233}Pa, ^{232,233,234,236,237,239,240,241}U, and ^{241,242g,242m,243}Am.

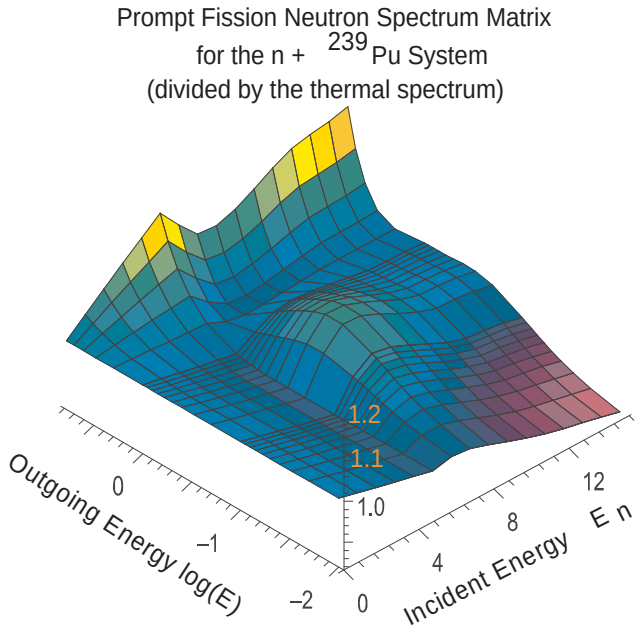

FIG. 10: Prompt fission neutron spectrum matrix for the n+^{239}Pu system, shown as a ratio to the thermal spectrum, and calculated with the Los Alamos model [69].

1. *Evaluation procedure*

The goals for the evaluations are to comply as closely as possible with experimental microscopic data from the CSISRS database (also known as EXFOR) [70] and at the same time to accurately match results from simple benchmark critical experiments. The sequence usually followed in the evaluations above the resonance region was to optimize agreement of modern nuclear model code calculations to the experimental database by careful model parameter selection.

For processes such as elastic and inelastic scattering and (n,xn) reactions, the calculations were generally utilized directly for the evaluated cross sections and energy/angle distributions. In cases where highly accurate experimental data were available, the experimental database was used directly in the evaluations. Examples are the ^{235,238}U and ^{239}Pu fission cross sections, which were taken exactly from the results of the ENDF/B-VII.0 neutron standards analysis. Other experimental data used in the evaluations were also adjusted to ENDF/B-VII.0 standards. In the case of ^{233}U and the major actinides ^{235}U and ^{239}Pu, the final step in the evaluations was to make minor adjustments in prompt $\bar{\nu}$ (generally within experimental data uncertainties) to enhance agreement with simple fast critical benchmark measurements.

2. ^{235}U

First, we describe the evaluation in the fast neutron region performed by LANL, then we proceed by describing the evaluation in the unresolved resonance region performed by ORNL. The remaining data were taken over from ENDF/B-VI.8.

a. Fast neutron region: The previous ^{235}U ENDF/B-VI.8 evaluation has performed reasonably well in integral validation tests based on simulations of critical assemblies, especially since the improvements developed by Lubitz [71] for ENDF/B-VI.3 and subsequent refinements by ORNL in ENDF/B-VI.5. The principle deficiency we wanted to remove was an underprediction of reactivity - for instance, the calculated $k_{\rm eff}$ for Godiva, a fast critical assembly based upon HEU in a spherical configuration, was 0.996, compared to experiment of 1. This reflected, in part, a previous evaluated fission cross section that was too low by about 1-1.5% in the fast range, coming from the 1990 ENDF/B-VI standards analysis of experimental data that unfortunately had a bug in the Bayesian analysis code.

The new ^{235}U evaluation builds upon the previous ENDF/B-VI.8 file, with the following improvements from Los Alamos:

1. The fission cross section is from the new IAEA/WPEC/CSEWG Standards group, which is about 0.5-1.5% higher than the ENDF/B-VI.8 evaluation in the fast region (1 - 5 MeV) and 1-5% different above 14 MeV where new measurements have become available (see Figs. 11 and 72).

2. Prompt $\bar{\nu}$ is based on a covariance analysis of experimental data, with consideration of consistency with fast critical benchmark experiments.

3. New (n,2n), (n,3n) cross sections are based on a GNASH analysis of new GEANIE (n,2nγ) data from a LLNL/LANL collaboration at the LANSCE facility.

4. New prompt fission spectra are taken from Madland's analysis (except at thermal, where the previous evaluations was maintained, as discussed below).

5. New delayed neutron data.

6. Improved inelastic scattering at 14 MeV and below, based on improved preequilibrium and direct reaction cross section modeling and integral pulsed-sphere experiments.

7. An improved unresolved resonance analysis from Oak Ridge in the 2.25 keV - 25.0 keV region. We note that the earlier Release 8 evaluation included some major advances from Oak Ridge for the resonance region. For the first time integral data were included with microscopic experimental data in the

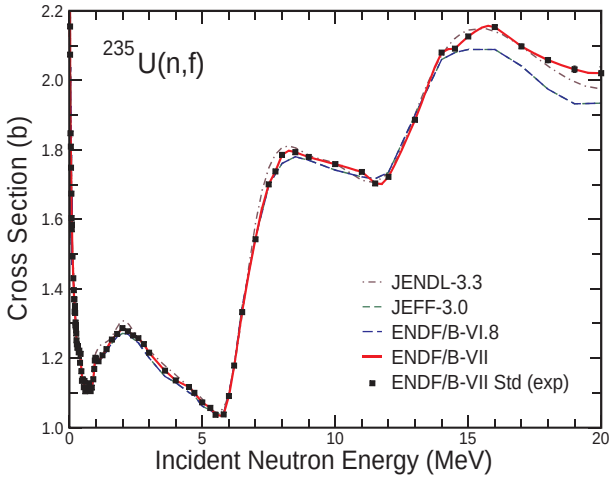

FIG. 11: Evaluated fission cross section compared with measured data, as represented by a covariance analysis of experimental data (referred to as ENDF/B-VII.0 Standard) - our new evaluation follows the Standard evaluation of the experimental data. The lower plot focuses on the lower-energy region. Other evaluations from JEFF and JENDL are also shown. See also Fig. 72.

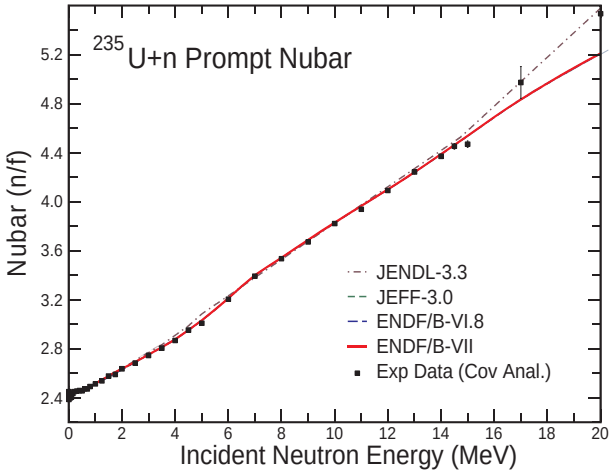

FIG. 12: Evaluated prompt fission multiplicity, $\bar{\nu}$, compared with measured data, as represented by a covariance analysis of experimental data. Other evaluations from JEFF and JENDL are also shown. (See also discussion in Section III.B.9.)

fitting procedure, and the multilevel R-matrix analysis with the SAMMY code [27] resulted in close fits to both the integral and microscopic data.

8. Delayed γ-ray data (LLNL) are incorporated for the first time.

The ^{235}U fission cross section is shown in Fig. 11, with comparison to the previous ENDF/B-VI.8 evaluation, and to the latest JEFF and JENDL evaluations (see also Fig. 72). This new result comes from the international standards project under the auspices of the IAEA, WPEC, and CSEWG, and the evaluation follows the statistical analysis of the pertinent measured data. This evaluation is 0.5-1.5% higher than the previous ENDF/B-VI Standard in the 1-5 MeV region, and significantly higher above 15 MeV (because of new fission measurement data now available at the higher energies). The impact of the higher fission cross section in the fast region (few MeV) is particularly important, having the effect of increasing the criticality of fast systems.

The new prompt fission multiplicity, $\bar{\nu}_p$, is shown in Fig. 12. The new evaluation follows our covariance analysis of the experimental data, generally within uncertainties, and includes renormalization of the measured values to the latest standard value for californium. The structure in the Version VI covariance analysis around E_n=0.1-0.4 MeV, which was smoothed in the ENDF/B-VI evaluation, was restored in the Version VII.0 evaluation. Also, the evaluation was adjusted slightly between 1.0 and 2.5 MeV to better represent the covariance analysis. It is evident that the new evaluation is rather close to the previous ENDF/B-VI.8 data.

D. Madland, LANL led a group of physicists from various countries under the auspices of the Nuclear Energy Agency/WPEC Subgroup 9 to study the fission prompt neutron spectrum for ^{235}U. This work considered new measured data and modeling methods, and led to a new set of prompt fission spectra as a function of incident neutron energy (the χ matrix). The final report [72] noted that significant uncertainties still exist in the prompt spectrum at thermal energies, due to inconsistencies in measured neutron spectrum data, and information from dosimetry activation studies. Because of this uncertainty, we have adopted Madland's new χ matrix for all energies except thermal, where we have preserved the previous ENDF/B-VI evaluation which is an earlier evaluation using the Los Alamos (Madland-Nix) model. New measurements at thermal are now underway, and this may lead to a future upgrade in the ^{235}U thermal prompt spectrum. Furthermore, the previous ENDF/B-VI.8 prompt neutron spectrum evaluation at thermal energy appeared to perform better in integral data testing of thermal systems, and was therefore turned over to ENDF/B-VII.0.

In Fig. 13 we show the prompt fission neutron emission spectrum, compared with measurements by Boykov *et al.* [73] for 2.9 MeV neutrons on ^{235}U. The present calculation (used in ENDF/B-VII.0) is compared with the data and with the older ENDF/B-VI evaluation. The present calculation with the Los Alamos involves a least-squares adjustment to best represent the data. Fig. 14 shows these same results, plotted in ratio to the σ_c = constant approximation to the Los Alamos model [69]. It is evident that the present ENDF/B-VII.0 agrees better with the Boykov data. A similar comparison at 14.7 MeV is shown in Fig. 15 for our new ENDF/B-VII.0 data, labeled Los Alamos model, compared with Boykov data. The (small) underestimate of the emission spectra data in the 6 - 9 MeV region is because of the lack of inclusion of preequilibrium processes in the current im-

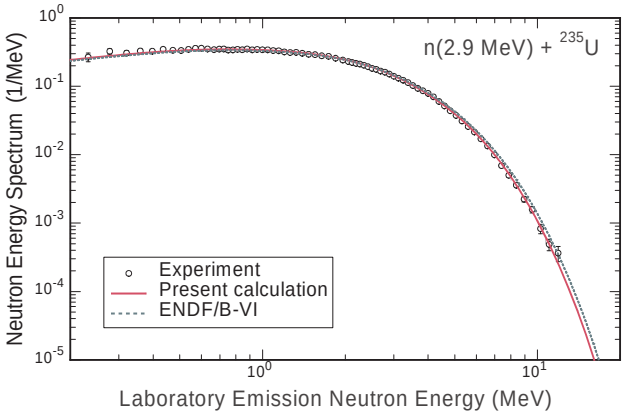

FIG. 13: Prompt fission spectrum for 2.9 MeV neutrons incident on ^{235}U, for ENDF/B-VII.0 and ENDF/B-VI (an earlier implementation of the Los Alamos model). The data are from Boykov [73].

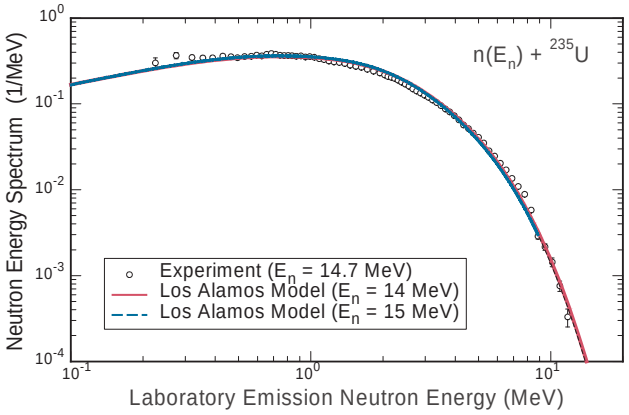

FIG. 15: Prompt fission neutron spectrum for 14.7 MeV neutrons incident on ^{235}U. The experimental data of Boykov [73] are shown together with predictions of the Los Alamos model.

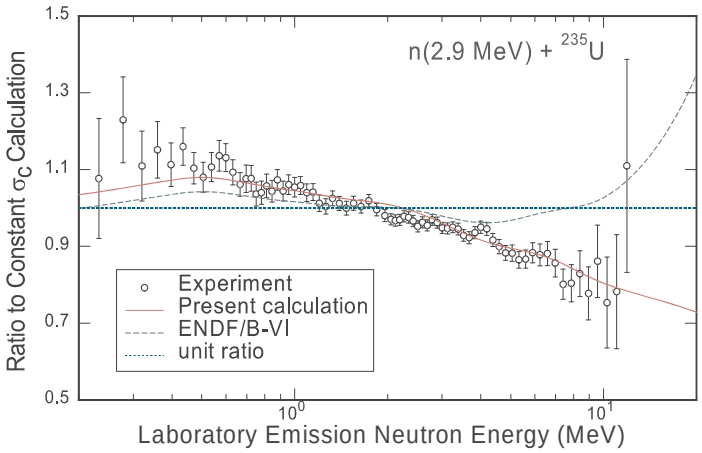

FIG. 14: Prompt fission spectrum for 2.9 MeV neutrons incident on ^{235}U shown in ratio to the σ_c = constant approximation to the Los Alamos model. The data are from Boykov [73].

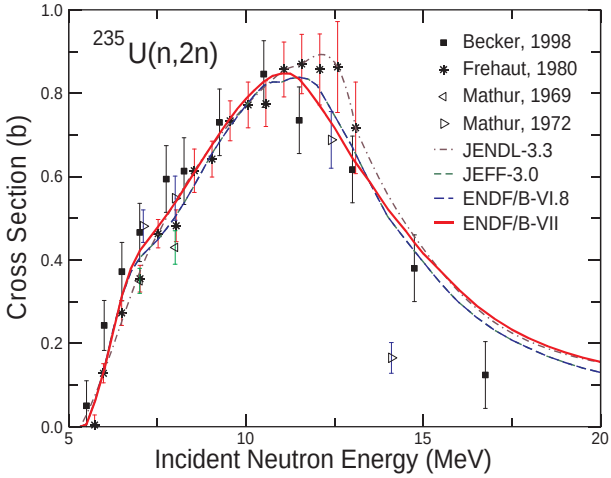

FIG. 16: Evaluated ^{235}U$(n, 2n)$ cross section compared with data, and with previous evaluations.

plementation of the Los Alamos model - a feature that we will include in future work.

The new ^{235}U$(n, 2n)$ cross section comes from a GNASH code theory prediction, baselined against the measured data. A comparison with experimental data, and with ENDF/B-VI.8, JEFF-3.0 and JENDL-3.3 is given in Fig. 16. The faster rise from threshold of the new cross section, as seen in this figure, was motivated by the recent GEANIE-project $(n, 2n\gamma)$ data obtained by Younes and Becker [74]. This measurement was supplemented by GNASH calculations to augment measured contributions with unmeasurable contributions.

The previous ^{235}U evaluation was known to poorly model Livermore pulsed sphere data that measure the downscattering of 14 MeV neutrons, in the region corresponding to inelastic scattering (the 2-4 MeV excitation energy region in ^{235}U). No reliable microscopic data exist for this process at 14 MeV for ^{235}U, so we postulated that the collective inelastic scattering processes measured for ^{238}U by Baba are likely to be similar for ^{235}U (see the description in the ^{238}U section). This allowed us, using DWBA methods, to generate inelastic scattering contributions high into the continuum with deformation parameters for each inelastic state. The angle-integrated spectrum obtained in this way, for 14 MeV, is shown in Fig. 17, and the oscillatory structure between 9 and 13 MeV emission energy is due to the new inelastic scattering to collective states. Our treatment provides inelastic data not just at 14 MeV, but at other incident energies based on predictions from the ECIS code using the same deformation parameters that we used at 14 MeV. This is the first time that preequilibrium and DWBA mechanisms for inelastic scattering have been included high into the continuum for evaluated actinide databases. In ENDF/B-VII.0 this approach was followed

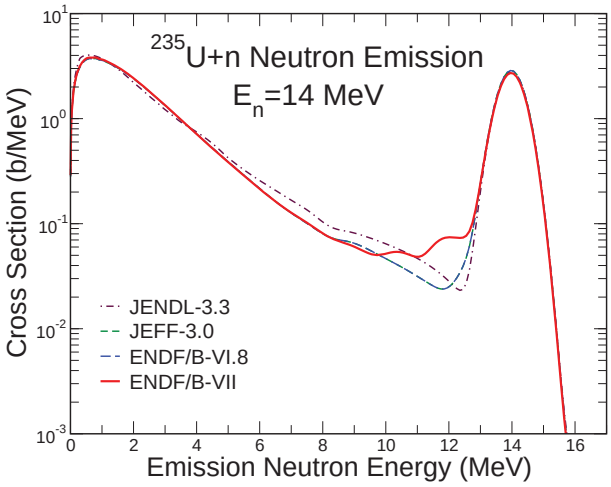

FIG. 17: Evaluated ^{235}U(n,xn) neutron production energy-spectrum compared with previous evaluations. No measured data exist, though our calculations were guided by measured data for ^{238}U.

for ^{233,235,236,238}U, ^{239}Pu, ^{232}Th, and ^{231,233}Pa. As discussed in the data testing section (Section X.F), our new evaluation now leads to good agreement with the Livermore pulsed sphere data.

Section X discusses integral data validation of this new evaluation against fast, intermediate, and thermal critical assemblies (with good performance).

There are some remaining possible deficiencies that we know about. Firstly, radiative capture in our new evaluation has been carried over from ENDF/B-VI.8, and we note that in the 30 keV - 1 MeV region this evaluation is lower than the JENDL evaluation by about 10% (they are based on different, inconsistent, measurements for the fission to capture ratio, see Fig. 18). Future studies, and new measurements, may point to changes needed in the capture cross section. Secondly, as discussed in Section X, critical assembly reaction rate simulations of the ^{238}U fission/^{235}U fission rate (a measure of the hardness of the spectrum as ^{238}U is a threshold fissioner) in HEU assemblies show a 4-5% underprediction of data. Since the fission cross sections used in the simulations are likely to be very accurate, this suggests that particle transport codes lead to a neutron spectrum in HEU that is too soft. This in turn may reflect deficiencies in the ^{235}U cross section data for processes that down-scatter neutrons, *i.e.*, inelastic scattering, or in the prompt fission spectrum.

b. Unresolved resonance region: The SAMMY code has been used to perform an unresolved resonance evaluation of the ^{235}U cross sections from 2.25 keV up to 25 keV [75]. The evaluation includes the first four angular momenta, that is, the s-, p-, d-, and f-waves. The energy dependence of the parameters is obtained using the Bethe theory for level density, the Hill-Wheeler fission barrier penetration for the fission widths and the giant dipole model for the capture widths. SAMMY generates average resonance parameters based on a statistical model analysis of the experimental average cross sections. These parameters are then converted into the ENDF-6 format for use in a Single-Level Breit-Wigner cross-section calculation. The primary use of the average resonance parameters is to reproduce the fluctuations in the cross sections for the purposes of energy self-shielding calculations.

TABLE VII: Parameters of the SAMMY fit of the ^{235}U experimental data in the energy region 2.25 to 25 keV.

Angular momentum	s-wave	p-wave
Neutron strength function $10^4 S_l$	0.905 ± 0.005	1.812 ± 0.021
Average capture width (meV)	36.06 ± 1.91	14.09 ± 2.11
Distant level parameter R^∞	-0.153 ± 0.002	0.104 ± 0.004
Effective scattering radius R' (fm)	9.680 ± 0.020	7.517 ± 0.211

Three sets of ORELA (Oak Ridge Electron Linear Accelerator) experimental data were used in the SAMMY evaluation of ^{235}U from 2.25 to 25 keV.

- Effective average total cross sections of Harvey *et al.* [76] obtained from the experimental transmission were analyzed; these data are from a time-of-flight transmission measurement performed at a 80.4-m flight path for two sample thicknesses of 0.0328 and 0.00236 atm/barn. The samples were cooled to liquid-nitrogen temperature to reduce the Doppler broadening of the resonances. Average cross sections were derived by Derrien *et al.* [77] and corrected for the self-shielding effect.

- Fission cross sections measured by Weston and Todd [78] at a 86.5 m flight path were analyzed.

- Capture data from the capture-to-fission ratio of Weston [79] were also used in the evaluation.

Parameter values obtained from the fit of the experimental data are shown in Table VII. The strength function listed in Table VII is 2.8 % larger than the value of $(0.88 \pm 0.09)10^{-4}$ calculated in the resolved resonance region (0 to 110 eV).

The ^{235}U unresolved resonance evaluation is consistent with the resolved resonance evaluation since both were done using the SAMMY code. Average resolved resonance parameters obtained in the resolved resonance evaluations were used as the starting parameters in the unresolved resonance evaluation. Higher-energy portions of the experimental data base used in the resolved resonance evaluation were also used in the unresolved evaluation, including total, fission, and capture data. A good representation of the average cross section was achieved with the new evaluation.

We remind the reader that the thermal $\bar{\nu}$ value for ^{235}U, which was taken over from ENDF/B-VI.8, is 2.4367. This value is slightly higher than that from the

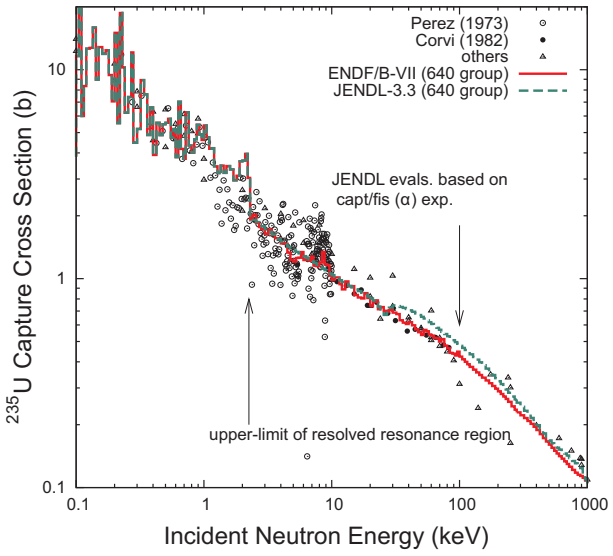

FIG. 18: Evaluated ^{235}U(n,γ) capture cross section compared with data, and with the JENDL-3.3 evaluation.

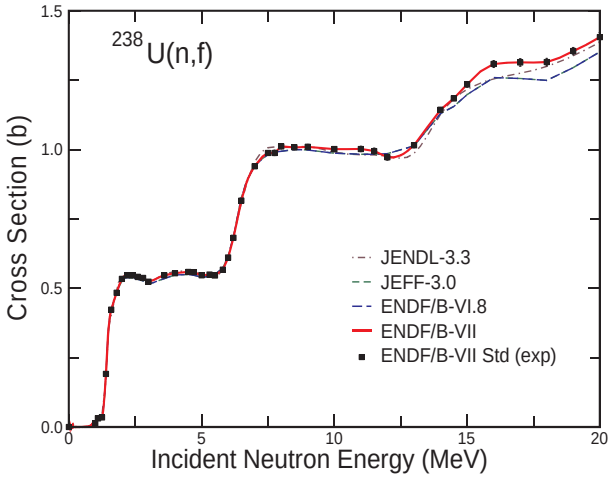

FIG. 19: Evaluated ^{238}U fission cross section, based on a covariance analysis of the experimental data from the Standards project (labeled Std).

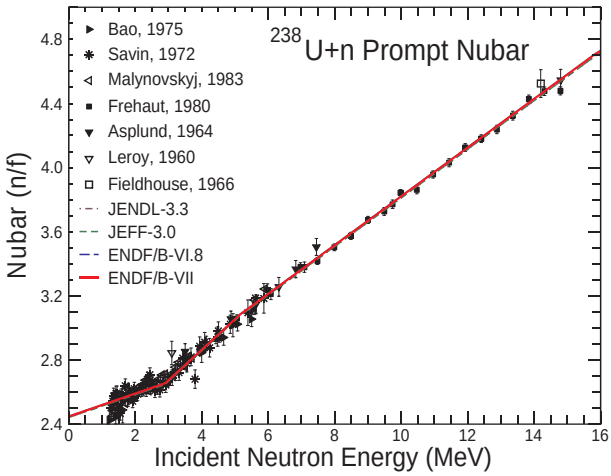

FIG. 20: Evaluated ^{238}U prompt fission multiplicity, based on a covariance analysis of the experimental data.(Also, see discussion in Section III.B.9.)

neutron standards 2.4355 but within experimental uncertainties, so as to optimize agreement with the critical assembly benchmarks.

3. ^{238}U

First, we describe the evaluation in the fast neutron region performed by LANL, then we proceed by describing the evaluation in the resonance region performed by ORNL.

a. Fast neutron region: Major modifications have been made to the ^{238}U evaluation, in both the resonance region (ORNL, CEA, and the WPEC subgroup), and in the fast and high energy region (Los Alamos). The new ENDF/B-VII.0 evaluation is based upon evaluations of experimental data and use of GNASH nuclear model calculations to predict cross sections and spectra. Prior to the present work, there were some longstanding deficiencies, as evident in critical assembly integral data testing. First, there was the reflector bias - the phenomenon whereby fast critical assemblies showed a reactivity swing in the calculated $k_{\rm eff}$ in going from a bare critical assembly (*e.g.*, Godiva (HEU) or Jezebel (^{239}Pu)) to a ^{238}U-reflected critical assembly (*e.g.*, Flattop-25, or Flattop-Pu), whereas measurements showed $k_{\rm eff} = 1$ for both assemblies (see the bias shown in the open symbols for ENDF/B-VI.8 in Fig. 86). Secondly, thermal critical assemblies involving ^{238}U have showed a calculated underreactivity for ENDF/B-VI.8, as described in detail in the next subsection. Thirdly, some intermediate energy critical assemblies involving large quantities of ^{238}U, such as Big-10, were modeled very poorly using ENDF/B-VI.8 data (see Fig. 86). As shown in Section X and Fig. 86, the nuclear data improvements made for ENDF/B-VII.0 largely remove these deficiencies.

The fission cross section was taken from the new recommendations of the IAEA/WPEC/CSEWG Standards group, based on a Bayesian analysis of measured data. As can be seen in Fig. 19 and Fig. 73 the fission cross section differs from the previous ENDF/B-VI.8 cross section in some important ways, being ≈1.5% larger in the 2-4 MeV region, and 1-5% in the 14-20 MeV region. Above 14 MeV the principle reason for the change is newer and more precise measurements from various laboratories, which were not available for ENDF/B-VI.

For the prompt fission multiplicity, the ENDF/B-VII.0 data is identical to ENDF/B-VI, except the energy range was extended from 20 to 30 MeV. The ENDF/B-VI data are based on an evaluation by Frehaut [80], see Fig. 20.

The prompt fission spectrum in ENDF/B-VII.0 for

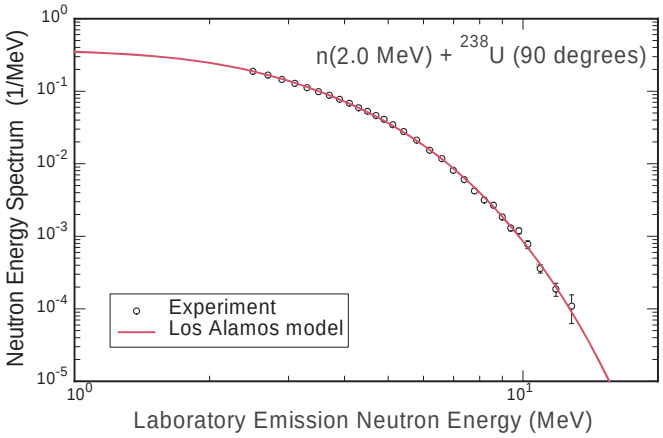

FIG. 21: Prompt fission neutron spectrum for 2.0 MeV neutrons incident on ^{238}U. The data of Baba [81] are shown together with the least-squares adjustment to the Los Alamos model.

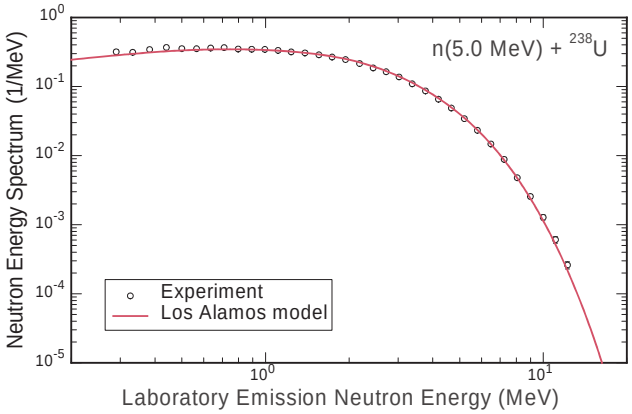

FIG. 22: Prompt fission neutron spectrum for 5.0 MeV neutrons incident on ^{238}U. The data of Lovchikova [82] are shown together with the least-squares adjustment to the Los Alamos model.

^{238}U came from a new analysis by Madland using the Los Alamos model. An example is shown in Fig. 21, where the model is compared with 2.0 MeV data by Baba *et al.* [81]. Similarly good agreements are seen at 5 MeV when the Los Alamos model is compared to the Lovchikova data [82], Fig. 22. New experimental data have been obtained using the Los Alamos LANSCE/FIGARO detector, for the prompt fission neutron spectrum as a function of incident energy. These data by Ethvignot *et al.* [83], together with average energies extracted from older measurements, are compared with Los Alamos model predictions in Fig. 23, and the agreement is seen to be good. The staircase-like change in the average emission energy as multichance fission opens up is evident. Note that the lower average energies in our new ENDF/B-VII.0 data, compared to ENDF/B-VI (see Fig. 23), appear to be supported by these measurements. However, it is worth noting that the uncertainties on the measured data can be large because experiments typically are not able to measure the whole emission energy range because of detector cut-offs, and the unmeasured regions must be supplied by theory predictions.

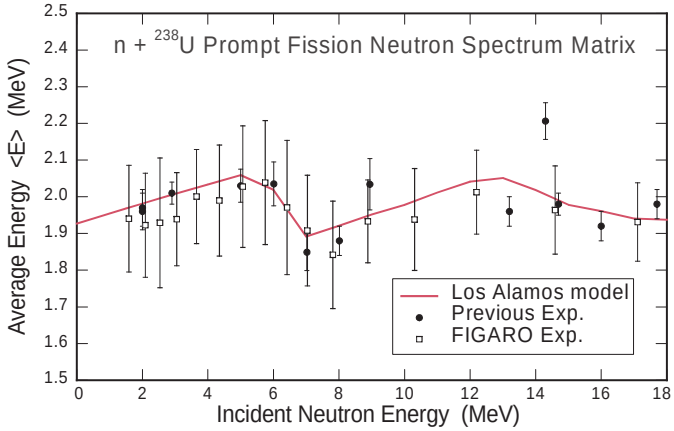

FIG. 23: First moment (average energies) of the n+^{238}U prompt fission neutron spectrum matrix calculated with the Los Alamos model shown together with those extracted from earlier experiments and the more recent CEA/Los Alamos FIGARO measurements [83].

Nuclear reaction modeling with the GNASH and ECIS codes played an important role for improving the treatment of inelastic scattering to discrete levels and to the continuum. This work impacts both the scattering in the fast region, as well as at 14 MeV and below. In the former case - inelastic scattering in the fast (few MeV) region - we will show later in the integral validation section (Section X) that our improved data for inelastic scattering results in significant improvements in the critical assembly validation tests, not just for fast critical assemblies, but also for more moderated and thermal assemblies (the LEU-COMP-THERM series). The total inelastic scattering we now obtain is shown in Fig. 24.

At 14 MeV, there are differential data from Baba et. al. that show a significant amount of inelastic scattering high into the continuum (1-4 MeV excitation energy). By assuming significant collective strength in the continuum for these reactions, we were able to model these measured spectra fairly accurately, both for the overall angle-integrated neutron spectra, as well as the spectra at various angles. An example is shown in Fig. 25. The accuracy of this new evaluation was also tested successfully in integral 14 MeV pulsed-sphere simulations, see Fig. 115 in Section X.E.

An example of the secondary neutron emission spectrum at 6.1 MeV incident energy on ^{238}U is shown in Fig. 26, for an emission angle of 45 degrees. It is evident that the new ENDF/B-VII.0 evaluation provides a much more accurate representation of the secondary spectrum, and its angular distribution, than the earlier ENDF/B-VI.8 evaluation. This is because of our more

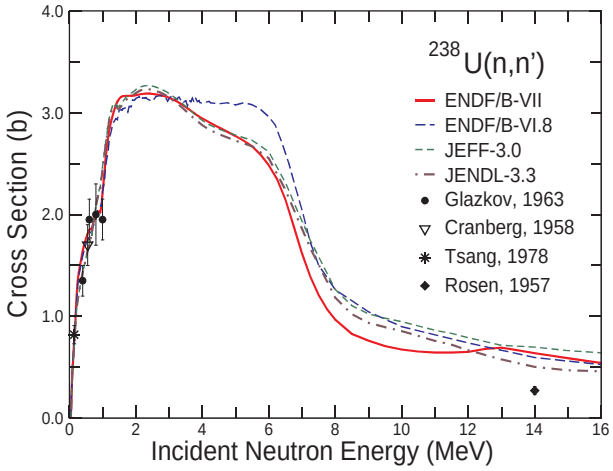

FIG. 24: Evaluated ^{238}U(n,n') inelastic cross section compared with data, and with previous evaluations.

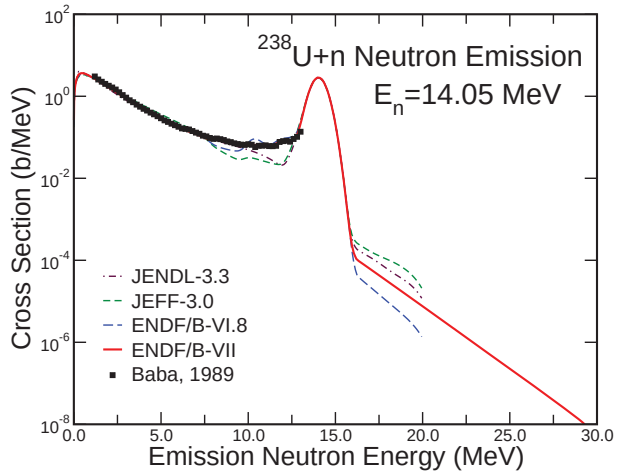

FIG. 25: Evaluated ^{238}U(n,xn) neutron production energy-spectrum, compared with data, and with different evaluations.

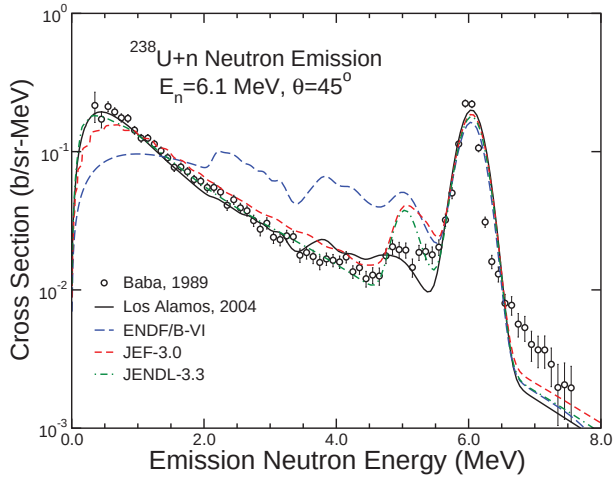

FIG. 26: Evaluated ^{238}U(n,xn) neutron production energy-spectrum, compared with data, and with different evaluations.

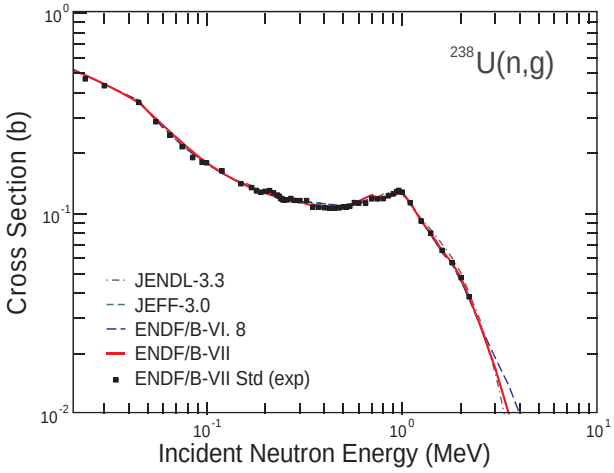

FIG. 27: Evaluated ^{238}U(n,γ) neutron capture cross section, compared with data (labeled Std), and with previous evaluations.

accurate modeling of inelastic and prompt fission reaction processes.

Our evaluated neutron capture cross section is shown in Fig. 27, and is compared with the result from the Standards project (which represents a Bayesian analysis of a large amount of experimental data). The small modifications compared to the Standards analysis were made to smooth the results from the Bayesian analysis of experimental data, and also to optimize the performance in some criticality benchmarks . This capture cross section is not formally considered a standard, but the capture cross section is included in the standard project analysis. It should be noted that in the MeV region, the evaluated cross section lies below the bulk of the measurements that one might find in the CSISRS (EXFOR) experimental database. This is intentional, and represents the conclusions of evaluators who have studied the various measurements made and concluded that the lower measurements are most accurate. See for instance, the Nuclear Energy Agency WPEC Subgroup-4 report [84].

The neutron capture cross section on ^{238}U can be tested in an integral way, by comparing production of ^{239}U in a critical assembly for various neutron spectra in different critical assemblies, ranging from soft spectra to hard spectra. To perform such validation tests, we use the MCNP code to simulate these different fast assemblies, using the model descriptions provided in the International Criticality Safety Benchmark Evaluation Project (ICSBEP) Handbook [85] and/or the CSEWG benchmark descriptions. (Of course, we must first ensure we model $k_{\rm eff}$ accurately, and this is the case - see Section X). Then, the calculated reaction rates for capture (in ratio to fission) are compared with the measured values. The results, shown in Fig. 107, show that the evaluation reproduces these integral capture rates well,

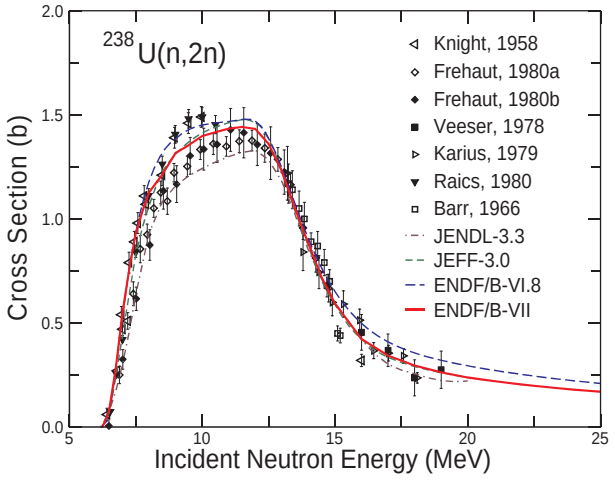

FIG. 28: Evaluated ^{238}U$(n,2n)$ cross section, compared with data and with previous evaluations.

though there is considerable spread in the measurements.

Like radiative capture, cross sections such as $(n,2n)$ and $(n,3n)$ are also important for production-depletion studies of uranium isotope inventories and transmutation. Our new evaluation of the $(n,2n)$ cross section is shown in Fig. 28 compared with ENDF/B-VI.8 and with measured data. It follows the LANL radiochemistry measurements of Knight in the rise from threshold, and the value from Barr at 14.1 MeV. This cross section can also be tested against integral critical assembly $(n,2n)$ reaction rate measurements, as shown in Fig. 106.

b. Resolved and unresolved resonance region, "ORNL5" evaluation: In the previous ENDF/B-VI.8 library, the resonance parameters of ^{238}U below 10 keV came from the evaluation work performed by M. Moxon *et al.* [86]. However, numerous criticality studies, involving low-enriched thermal benchmarks from the ICSBEP and CSEWG benchmarks books, demonstrated a systematic eigenvalue under-prediction of about -0.5% (-500 pcm) with ENDF/B-VI.8. Within the framework of WPEC, Subgroup-22 was formed to solve this problem. First, the ^{238}U capture cross sections were investigated using specific integral experiments sensitive to the capture resonance integral such as:

- correlation between $k_{\rm eff}$ and ^{238}U capture fraction.
- measurements of ^{238}U spectral indices and effective capture resonance integral (Hellstrand correlations).
- post-irradiation experiments (PIE) which measures the ^{239}Pu isotopic ratio as a function of burn-up.

As summarized in [87], these tests did not demonstrate a significant error in the ^{238}U capture resonance integral of ENDF/B-VI.8; integral experiments were generally predicted within the experimental uncertainty margins. However, a trend of decreasing $k_{\rm eff}$ versus ^{238}U capture fraction and a slight overestimation of ^{239}Pu build-up in PIE experiments were observed. These findings supported a slight reduction of the effective resonance integral between 0.5% and 1%.

To investigate this point, a new analysis of the ^{238}U cross section in the resolved-resonance range was undertaken at ORNL in collaboration with the CEA [88]. The resonance parameters were evaluated below 20 keV from a sequential SAMMY Reich-Moore fit of the most recent high-resolution transmission and capture measurements listed in Table VIII.

TABLE VIII: Overview of the main experiments used in the analysis of ^{238}U resonances.

Energy range	Reference	Measurement type
6 eV - 100 keV	de Saussure *et al.* (1973) [89]	Capture
0.5 eV - 4 keV	Olsen *et al.* (1977) [90]	Transmission
300 eV - 100 keV	Olsen *et al.* (1979) [91]	Transmission
250 eV - 130 keV	Macklin *et al.* (1988)[92]	Capture
1 keV - 100 keV	Harvey *et al.* (1988)[76]	Transmission

A paper to be published in *Nucl. Sci. Eng.* will provide an extensive description of the evaluation, which can be summarized as follows:

The ^{238}U(n,γ) thermal cross section, recently recommended by A. Trkov *et al.* [93], $\sigma_0 = 2.683 \pm 0.012$ *b*, was adopted in the present evaluation. The scattering cross-section at thermal energy was also revisited using the latest interferometric measurements of neutron coherent scattering length. The effective scattering radius $R_{\rm eff}$ as well as the parameters of the external levels have been carefully assessed. The new value, $R_{\rm eff} = 9.48 fm$, is close to the previous determination, $R_{\rm eff} = 9.42 fm$, adopted in ENDF/B-VI.8.

The SAMMY analysis of the lowest s-wave resonances below 102 eV led to resonance parameters slightly different from those of ENDF/B-VI.8 as shown in Table IX. Using the Crystal Lattice Model (CLM) of SAMMY, special attention was paid to the modeling of Doppler broadening for low-energy resonances.

With the new evaluation, thick-sample transmissions calculated from the resonance parameters and averaged over 1-keV energy intervals agree within about 1% with the reference experimental values of Harvey. Note that the fits of capture data could not be obtained without large normalization and background corrections.

The resolved-resonance range was extended to 20 keV, taking advantage of the transmission data of Harvey and capture data of Macklin. Above 10 keV, poorer experimental resolution makes resonance analysis difficult so

TABLE IX: Resonance parameters of the ^{238}U s-wave resonances in ENDF/B-VI.8 and ENDF/B-VII.0.

	ENDF/B-VII.0 R' = 9.48 fm		ENDF/B-VI.8 R' = 9.42 fm	
Energy eV	Γ_γ meV	Γ_n meV	Γ_γ meV	Γ_n meV
6.673	23.00	1.476	23.00	1.493
20.87	22.86	10.09	22.91	10.26
36.68	23.00	33.55	22.89	34.13
66.03	23.31	24.18	23.36	24.60
80.75	23.39	1.874	23.00	1.865
102.56	24.08	70.77	23.40	71.70

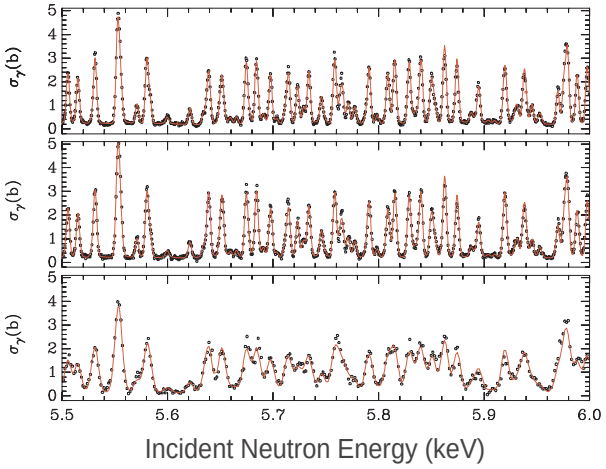

FIG. 29: Experimental capture data on ^{238}U (one sample measured by De Saussure and two samples by Macklin) compared to the results of the SAMMY fit in the range 5.5 - 6.0 keV.

that only large s-wave resonances could be reliably identified. To represent small s or p resonances, a "pseudo-resonance" approach was used; a set of resonances is proposed that fits the transmission and capture data but does not represent actual resonances.

Statistical tests using results from Gaussian Orthogonal Ensemble theory (GOE) were also carried out to check the evaluation. These tests include the analysis of spacings and widths distribution, Δ_3 statistics, correlation coefficient between adjacent spacings and other useful GOE statistics.

Fig. 29 shows an example of the SAMMY fit of capture measurements in the keV energy range. As suggested by integral experiments, this new evaluation proposes a slight decrease of the effective capture resonance integral (dilution around 50 b) by about 0.6%, compared to ENDF/B-VI.8. One expected consequence of this new evaluation is an increase of the calculated multiplication factor for low-enriched lattices from about 0.1 to 0.15% (100 to 150 pcm), depending on the moderation ratio. Note that the combination of the new LANL ^{238}U inelastic data in the fast neutron region, described in the previous section, with the ORNL resonance parameter set gave a satisfactory correction of the reactivity underprediction (see Section X.B.4).

The unresolved range starts at 20 keV and extends to 300 keV. It is represented by two ENDF files: File 2 contains average resonance parameters, essential for shielding factors calculations, from the evaluation of Fröhner [94]. File 3 provides pointwise cross sections at infinite dilution and was described in the previous section. An independent analysis of the unresolved range was carried out at ORNL. This work was based on simultaneous fit of carefully selected transmission and capture measurements with the statistical model implemented in SAMMY. This work led to cross-section values and average resonance parameters very close to the present ENDF/B-VII.0 evaluation up to 300 keV.

4. ^{239}Pu

First, we describe our evaluation in the fast neutron region performed by LANL, then we briefly describe our evaluation in the resonance region.

a. Fast neutron region: The following upgrades have been made to the ^{239}Pu evaluation:

1. New experimental data from a LANSCE GEANIE experiment are combined with older data and GNASH theoretical calculations to produce a new evaluation of the ^{239}Pu(n,2n) cross section;
2. A fission cross section as provided by the IAEA/WPEC/CSEWG Standards Group;
3. A new analysis of the prompt fission neutron spectrum matrix based on the Los Alamos Madland-Nix model;
4. New improved delayed neutron data;
5. $\bar{\nu}$ data - modifications were made to the ENDF/B-VI.8 evaluation to improve agreement with the results of a covariance analysis of experimental data and with integral experimental results;
6. Improved inelastic scattering at 14 MeV and below, allowing a good representation of Livermore pulsed-sphere data.
7. β-delayed γ-rays were added for the first time, from Livermore.

The earlier ^{239}Pu ENDF/B-VI.8 evaluation exhibited an under-reactivity, with the simulated Jezebel $k_{\rm eff}$ being $\approx$0.997. The new evaluation is more reactive, mainly because of the higher fission cross section in the fast region,

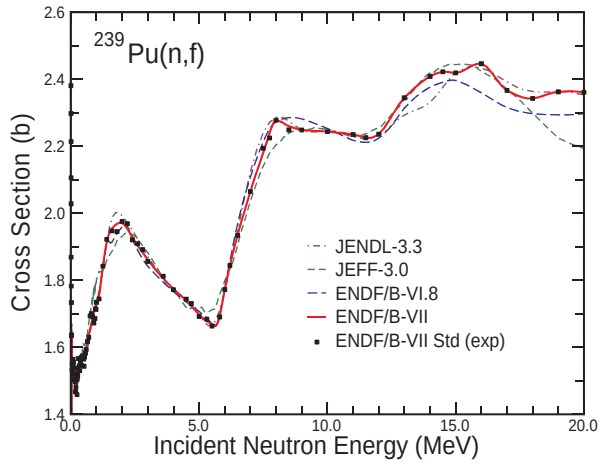

FIG. 30: Evaluated fission cross section compared with measured data, as represented by a covariance analysis of experimental data (referred to as ENDF/B-VII.0 Standard) - our new evaluation follows the Standard evaluation of the experimental data. Other evaluations from JEFF and JENDL are also shown.

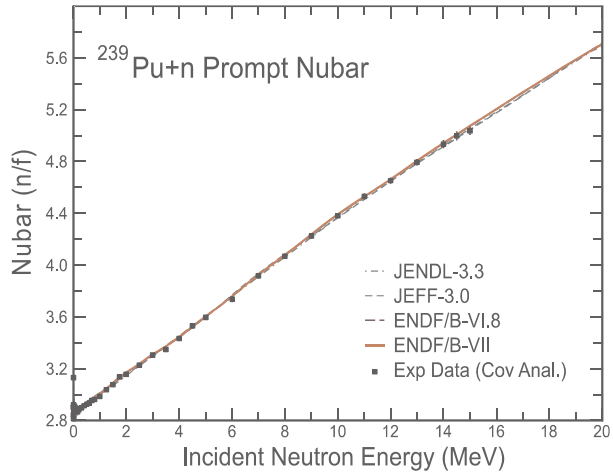

FIG. 31: Evaluated prompt fission multiplicity, $\bar{\nu}_p$ compared with measured data, as represented by a covariance analysis of experimental data. Other evaluations from JEFF and JENDL are also shown. (Also, see discussion in Section III.B.9.)

with $k_{\rm eff} \approx 1$ (see the discussion on integral data testing in Section X.B.2 and Fig. 88).

The new fission cross section is shown in Fig. 30 compared with the older ENDF/B-VI.8 evaluation. Because the earlier ^{235}U ENDF/B-VI.8 standard fission cross section was too low in the fast neutron energy region, and has now been increased in ENDF/B-VII.0, this leads to an increased ^{239}Pu fission cross section in this energy region too, since the plutonium fission cross section is strongly dependent on ^{239}Pu/^{235}U fission ratio measurements. This cross section was provided by the IAEA/WPEC/CSEWG Standards Group, see Section V.

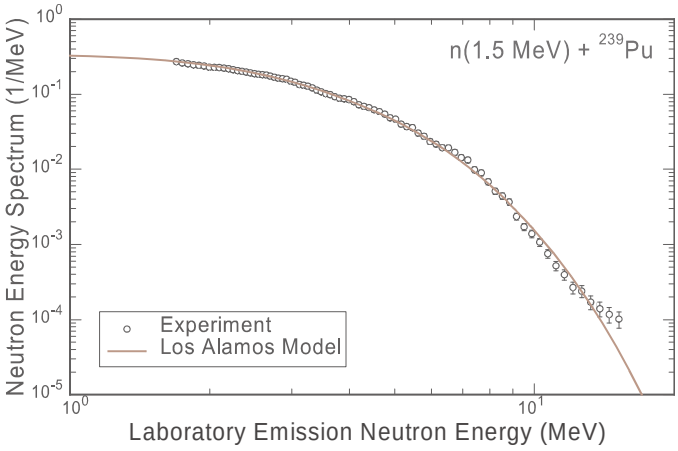

FIG. 32: Prompt fission neutron spectrum for 1.5 MeV neutrons incident on ^{239}Pu. The data of Staples [95] are shown together with the least-squares adjustment to the Los Alamos model.

The evaluated prompt fission nubar is shown in Fig. 31, compared with our statistical covariance analysis of all measured data (again renormalized to the latest californium standard). In the fast region, our evaluation follows the upper uncertainty bars of the statistical analysis of the experimental data, allowing us to optimize the integral performance in criticality benchmarks for the fast Jezebel ^{239}Pu spherical assembly.

The prompt fission neutron spectrum, as a function of incident energy, was reevaluated using the Madland-Nix approach. An example of the prompt fission spectrum is shown in Fig. 32, for 1.5 MeV neutrons incident on ^{239}Pu, compared with the Staples *et al.* [95] data. Likewise, new delayed neutron data were determined from Wilson and Moller's analysis, see Section III.C.1.

The new $(n, 2n)$ cross section was based upon a major Livermore – Los Alamos collaboration, involving GEANIE gamma-ray measurements of the decay gamma-rays in ^{238}Pu, together with GNASH code theory predictions of unmeasured contributions to the cross section. Prior to this work, precision activation measurements had been made near 14 MeV by Lougheed *et al.* [96]. Other measurements based on measuring the two secondary neutrons by Frehaut and by Mather were thought to be problematic - Mather's being unrealistically high near threshold, and Frehaut's being unrealistically low - and were therefore discounted in the evaluation. Such measurements were very difficult because of the large background of two neutron events in coincidence with fission. The evaluated data obtained by McNabb and Chadwick, see [97] and [98], are based on a covariance analysis of both the GEANIE-GNASH measurements that extend from threshold to 20 MeV, and the Lougheed data near 14 MeV, and are referred to as GEANIE-project data in Fig. 33, and adopted for ENDF/B-VII.0.

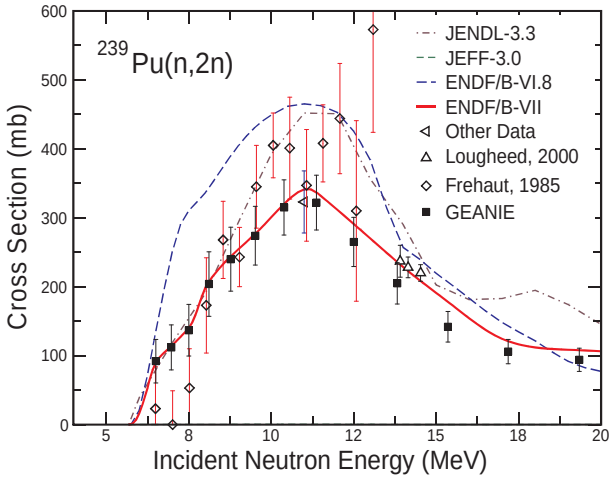

FIG. 33: Evaluated ^{239}Pu$(n,2n)$ cross section compared with data, and with previous evaluations.The evaluation was based upon the GEANIE-GNASH data and the Lougheed 14 MeV data [96]. The ENDF/B-VII.0 evaluation (red line) is also refered to as the "GEANIE-project" evaluation.

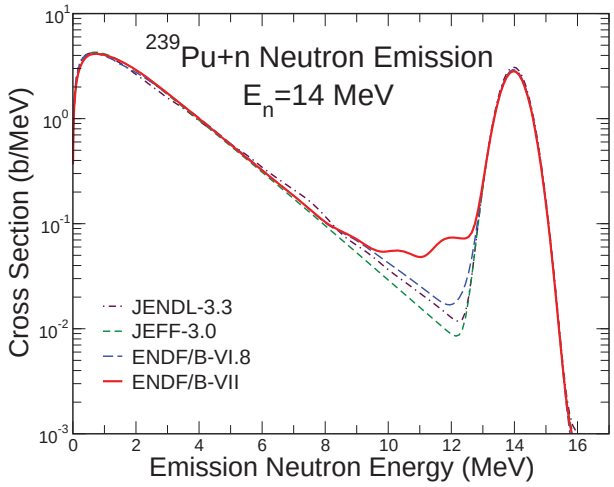

FIG. 34: Evaluated ^{239}Pu(n,xn) neutron production energy-spectrum, compared with previous evaluations. No fundamental experimental data exist for this reaction, although Livermore pulsed data for transmission do exist (see Fig. 116).

As was the case for ^{235}U, the previous ^{239}Pu evaluation did not include enough inelastic scattering into the continuum for 14 MeV neutron energy and below, leading to poor performance in simulations of Livermore pulsed spheres in the 2-4 MeV excitation energy region. As for ^{235}U, no direct measurements exist here, and so we inferred collective excitation strength from direct reaction analyses of ^{238}U data by Baba *et al*, and assumed similar strengths for ^{239}Pu. Fig. 34 shows the new angle-integrated neutron spectrum data compared to the ENDF/B-VI.8 evaluation (no measurements exist). This procedure led to a much improved MCNP modeling of the pulsed-sphere data, as shown in Fig. 116 in Section X.E.

b. Resonance region: The evaluation by Derrien and Nakagawa of the resonance region was taken over from the ENDF/B-VI.8 library without any change.

5. ^{233}U

First, we describe our evaluation in the fast neutron region performed by LANL, then we proceed by describing the evaluation in the resonance region performed by ORNL.

a. Fast neutron region: At the higher energies in the fast region, the new ^{233}U evaluation is based upon a new GNASH/ECIS calculational analysis, together with use of all available experimental data for fission, scattering, capture, etc. The fission cross section is taken from a covariance statistical analysis of all experimental data, including ^{233}U/^{235}U fission ratio measurements converted using the ENDF/B-VII.0 standard ^{235}U cross section, as shown in Fig. 35. The somewhat higher ^{233}U

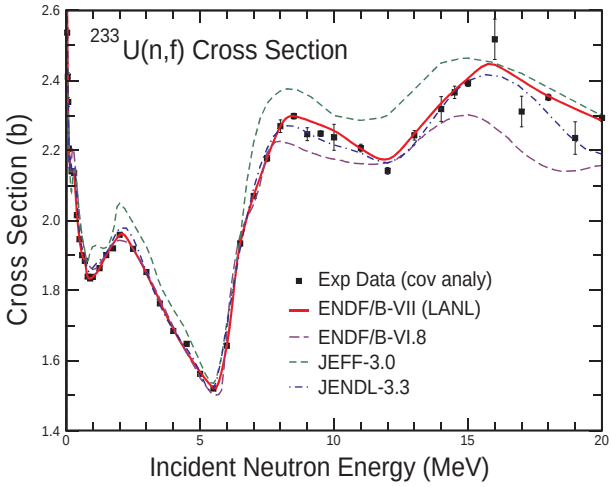

FIG. 35: Evaluated fission cross section that follows the measured data (shown as a covariance analysis of the experimental data). Other evaluations from JEFF and JENDL are also included.

fission cross section in the fission spectrum region produces better agreement with fast critical benchmark experiments. The evaluated prompt fission multiplicity is shown in Fig. 36, compared with our covariance analysis of measured data. Again, the experimental data are normalized using ENDF/B-VII.0 standards.

The evaluated data are mainly within uncertainties when compared with our covariance analysis of measured data. The capture cross section is shown in Fig. 37 and is based on our GNASH analysis, normalized using limited experimental data. The figures illustrate the significant change in the ^{233}U evaluated cross sections. In Section X we show how these improvements in the fundamental evaluated data lead to significant improvements

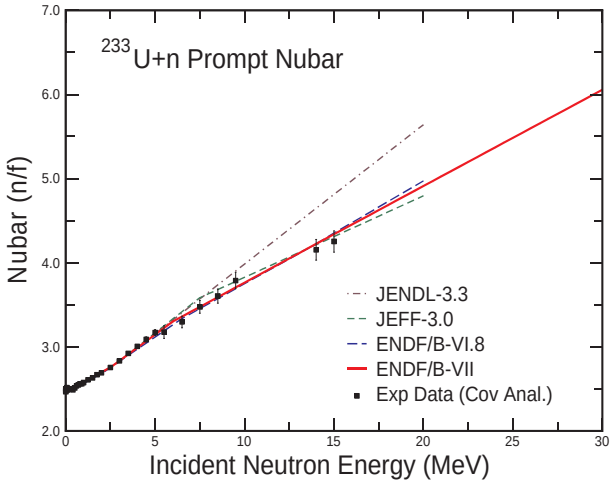

FIG. 36: Evaluated prompt fission multiplicity, $\bar{\nu}_p$, compared with measured data, as represented by a covariance analysis of experimental data. Other evaluations from JEFF and JENDL are also shown. (See also Section III.B.9.)

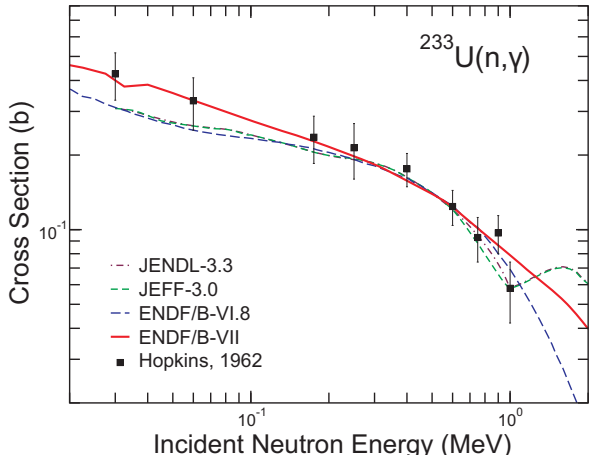

FIG. 37: Evaluated ^{233}U(n,γ) capture cross section compared with data, and with previous evaluations.

in our integral data testing results for critical assemblies involving ^{233}U, for both fast and more thermal assemblies. The improvement for Jezebel-23 (a sphere of ^{233}U) is particularly noteworthy, see Fig. 86.

b. Resolved and unresolved resonance region: To address criticality safety concerns for nuclear systems in which ^{233}U is present, resolved [99] and unresolved [100] resonance evaluations for this isotope were done with the SAMMY code.The resolved resonance analysis was carried out from thermal to 600 eV, resulting in a set of resonance parameters that gives a good description of the experimental data. Five high resolution transmission measurements performed at the Oak Ridge Linear Electron Accelerator (ORELA) [101], five fission measurements [102], and one simultaneous capture and fission measurement [103] were included in the analysis.

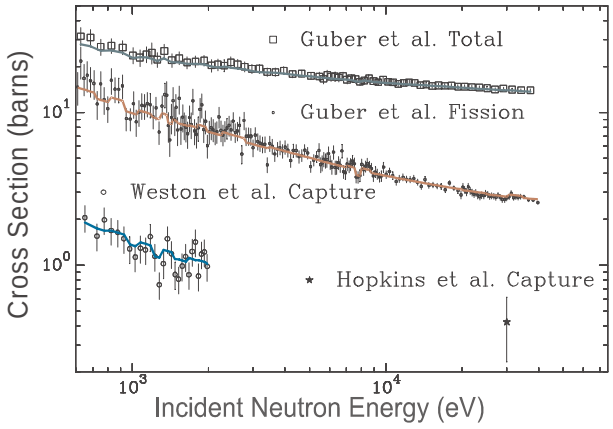

FIG. 38: Comparisons of average total, fission and capture cross sections calculated with SAMMY with the experimental data for ^{233}U.

Sequential fitting of the data using the Reich-Moore formalism were done with SAMMY to determine the set of resonance parameters that best describe the data. Statistical tests of the resonance parameters were performed, and average values of the observed resonance parameters were computed for use as starting values in the analysis in the unresolved resonance region. Parameter values were converted to those required by the ENDF-6 format, and reported to ENDF at 27 reference energies; these energies were chosen based on the observed fluctuations in the experimental data, which are due to unresolved multiplets of resonances. Results of the fit to experimental data are shown in Fig. 38. The solid line represents the SAMMY fit, showing good agreement with the experimental data. The unresolved multiplets of resonances are clearly seen in the figure. Benchmark calculations have demonstrated that the new evaluation substantially improves the prediction of effective multiplication factors, see Section X.B.6.

6. ^{232,234,236,237,239,240,241} U and ^{241} Pu

^{232,234,236,237,239,240,241}U. Depending upon the isotope, varying amounts of measured data are available. In some cases, the experimental database is extremely sparse. For example, for ^{237}U, there are no direct measurements of the fission cross section at monoenergetic incident neutron energies, and there are no capture measurements. However, for ^{237}U and ^{239}U, indirect information does exist on the fission cross section in the few-MeV region, using surrogate (t,p) direct reaction experiments from Los Alamos, which have recently been re-analyzed by Younes and Britt at Livermore [104] and from a more recent LLNL experiment by Bernstein at al [105]. These data allow an assessment of the equivalent neutron-induced fission cross section, and Younes and Britt have shown that such surrogate approaches can be accurate to better

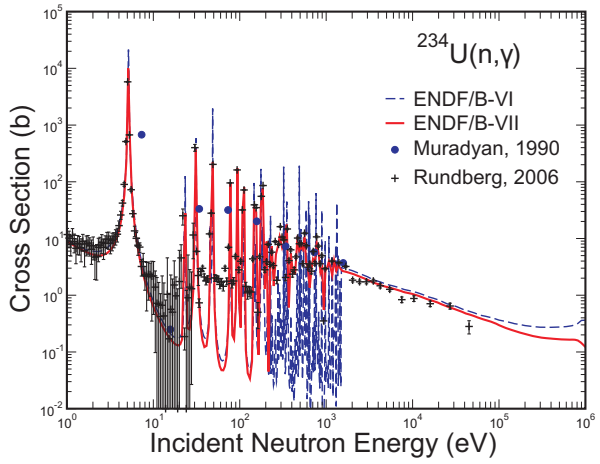

FIG. 39: Evaluated ^{234}U(n,γ) capture cross section compared with data, and with previous evaluations. The evaluation follows the 2006 DANCE data, which are significantly lower than the previous Russian data from Muradyan.

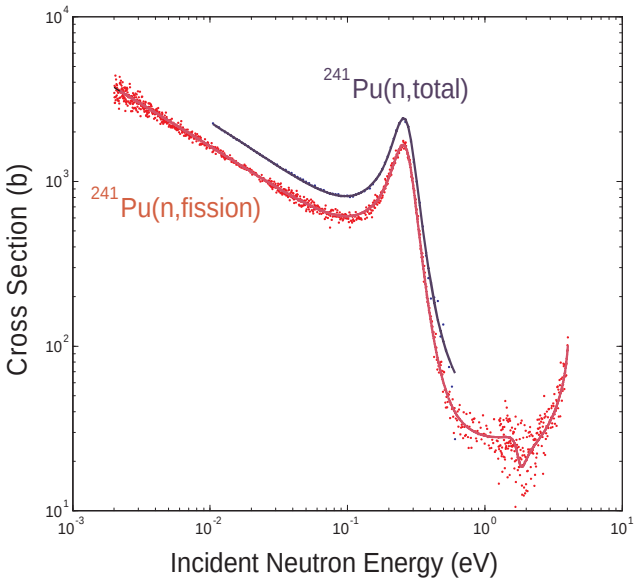

FIG. 40: ^{241}Pu total cross section of Young and Smith and fission cross section of Wagemans in the energy range below 10 eV are compared with the results of a SAMMY calculation (solid lines) using the new resonance parameters.

then 15 %. In the case of ^{237}U, a measurement has been made of the fission cross section in a fast fission spectrum within a Flattop (fast) critical assembly, at two locations - the centre region. and the tamper region (where the spectrum is softer). This kind of measurement also provides indirect information on the fission cross section.

Because of the general paucity of data, we have relied heavily on GNASH nuclear model calculations, where the calculations were done for the whole chain of uranium isotopes in a systematic manner. This is important because one can use fission barriers inferred from certain reactions, where data are available, to model neutron reactions where no fission cross section data are available. As an example, modeling first chance fission in n+^{238}U reactions, using experimental data to deduce the fission barriers for ^{239}U, provides input for second-chance fission in n+ ^{239}U reactions. In a similar way, we can take advantage of systematic trends in optical potentials and nuclear level densities, both for ground-state deformations and for fission transition states for strongly deformed configurations.

We have also been able to use some new capture data from the DANCE detector, at LANSCE, for unstable targets prepared by the Chemistry Division, for both ^{234}U and ^{236}U. Previous data exist for ^{236}U, but only one previous measurement existed for ^{234}U capture, from Muradyan. In the case of ^{236}U, the new Los Alamos DANCE capture data were consistent with the bulk of the previous measurements. However, for ^{234}U, the new Rundberg measurements were significantly lower than the previous data set, see Fig. 39. We have adopted this new lower cross section in our evaluation, as shown in the figure. This had non-trivial implications on the calculated criticality of uranium assemblies - for example, the HEU fast critical assembly, Godiva, has about 1 % ^{234}U in it, and the significantly lower capture cross section compared to our earlier evaluation results in an increase in calculated $k_{\rm eff}$ of $\approx$ 0.1 %.

^{241}Pu. In ENDF/B-VI.8, the ^{241}Pu resonance parameters were evaluated below 300 eV by H. Derrien and G. de Saussure [106]. After this work, a new measurement was performed in 1991 [107] to check the shape of the fission cross-section in the thermal range. This measurement showed that the shape follows the usual 1/v law, contrary to previous data. Consequently, ^{241}Pu resonance parameters were revised in 1993 [108] in the energy range from 0.002 to 3 eV. Nevertheless, integral tests of the data through Post-Irradiated Experiment (PIE) were still not satisfactory. The analysis of the measured isotopic ratios ^{241}Pu/^{238}U and ^{242}Pu/^{238}U in PIE suggested that the ^{241}Pu capture was still significantly underestimated [109]. In collaboration with CEA/Cadarache, a new SAMMY analysis of the ^{241}Pu resonance parameters was recently performed below 20 eV [110]. This revision features a much higher ^{241}Pu capture cross-section in the 0.26 eV resonance and is still compatible with the differential measurements. Integral tests demonstrated that the new set of resonance parameters improves prediction of ^{242}Pu build-up as well as ^{243}Am, ^{244}Cm and ^{245}Cm in PWRs.

Total and fission cross sections on ^{241}Pu below 10 eV obtained by SAMMY are compared with experimental data in Fig. 40.

7. $^{241,242g,242m,243}Am$

Data on americium isotopes are especially important for applications involving transmutation and advanced reactors with high minor actinide burnup. Large uncertainties and discrepancies in existing libraries need to be reduced and resolved for the development of such nuclear applications.

The suite of neutron-induced reactions on americium isotopes ^{241,242g,242m}Am, and ^{243}Am has been reevaluated for ENDF/B-VII.0 for incident neutron energies above the unresolved resonance region and up to 20 MeV. Modern theoretical models and computational techniques (GNASH and ECIS reaction modeling codes) were extensively used due to the rather limited experimental information. However, when available, experimental data were used to guide and benchmark the present evaluation work. We note that recent BNL calculations of n+Am cross sections with the code EMPIRE-2.19 [111] for a set of isotopes provided useful input for the present evaluation.

A detailed description of these evaluations is given by Talou *et al.* [112], and only a brief summary is reported here.

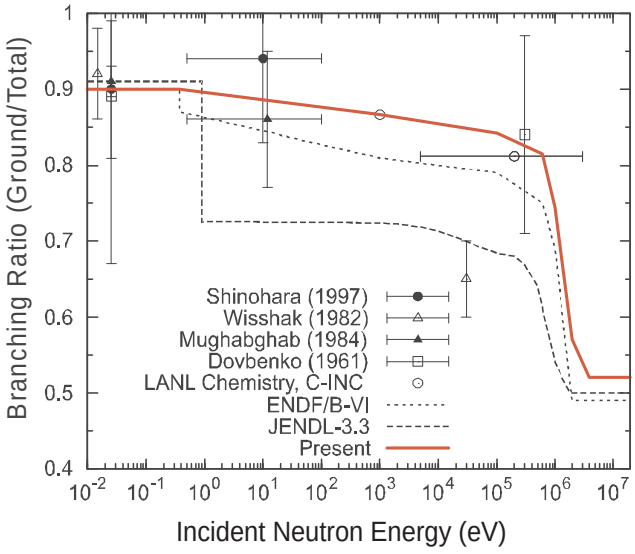

FIG. 41: Branching ratio for neutron capture to produce the ground-state of ^{241}Am, compared with experimental and evaluated data.

The ^{241}Am capture cross section was reevaluated based on experimental capture and capture/fission ratio data. The new result is about 15% larger than the ENDF/B-VI.8 data in the hundreds-keV energy region.

The isomer-to-ground-state capture ratio was increased significantly over earlier evaluations (JENDL-3.3 and ENDF/B-VI), based on new differential data and integral measurements (see Fig. 41). This new higher value for the isomeric ratio in the thermal energy region is supported by a recent post-irradiation experiment [113].

The $\overline{\nu}_p$ values were reevaluated, and the (n,2n) cross section was also modified in view of newer measurements available in the 14-MeV region, see Fig. 42. Specifically, a measurement near 14 MeV by Gancarz (Los Alamos), was made in the early 1980s and was found consistent with the Lougheed (Livermore) data. Our evaluation reflects these 2 measurements as opposed to the lower Filatenkov data. Below 14 MeV, we rely on an (n,2n) excitation function shape from our GNASH calculations. Recent data reported by Perdikakis [114] appear contradictory, and were not used in the evaluation. Furthermore, preliminary measurements by a TUNL-LANL-LLNL at the TUNL facility appear to be in good agreement with our evaluation. These TUNL data (not shown) should be finalized soon.

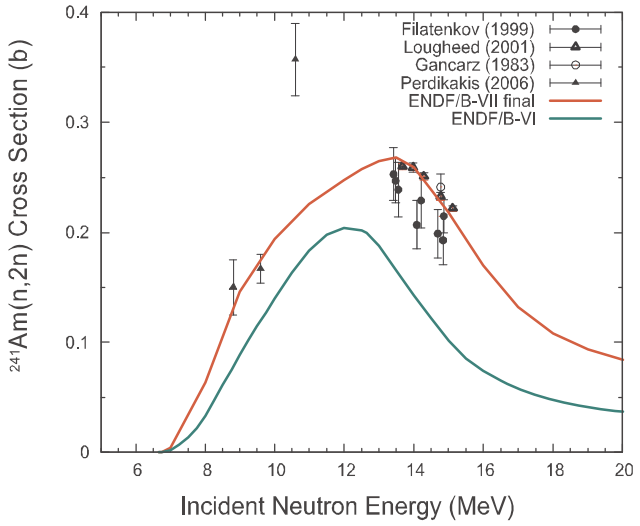

FIG. 42: Evaluated ^{241}Am(n,2n) cross sections compared with data.

Entirely new evaluations were performed for n+^{242g}Am and n+^{242m}Am. The evaluated fission cross section for ^{242m}Am, represented in Fig. 43, is the result of a generalized least-squares analysis of experimental data. The evaluation of ^{242g}Am, for which no data exist (half-life of only 16h), was done almost entirely from model calculations, but whose input parameters were derived from the study of ^{242m}Am. Indirect (surrogate) data from Younes *et al.* [115] are in good agreement with our evaluated result.

Finally, ^{243}Am was largely carried over from the previous ENDF/B-VI.8 evaluation.

8. ^{232}Th *and* $^{231,233}Pa$

Recent development of innovative fuel cycle concepts and accelerator-driven systems for the transmutation of nuclear waste have created a new interest in high quality nuclear data for light actinide nuclei. Knowledge of accurate neutron induced cross sections (particularly fis-

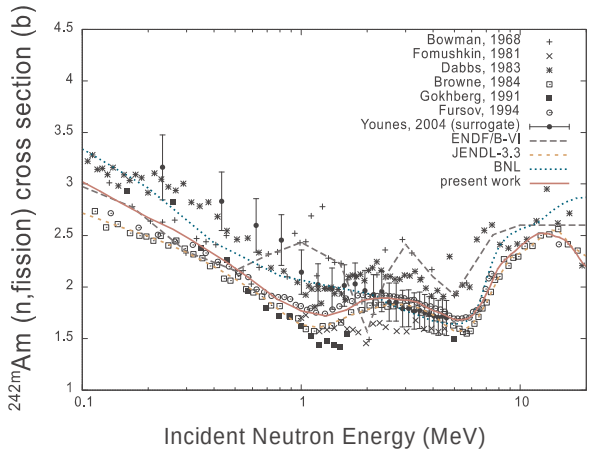

FIG. 43: Neutron-induced fission cross section of ^{242m}Am obtained with a generalized-least-square technique. It is compared to available experimental data, to the ENDF/B-VI.8 and JENDL-3.3 evaluations, and to the recent theoretical result of BNL by D. Rochman *et al.* [111]. The determination of this cross section by Younes et al. [115] from a surrogate reaction is also shown.

sion) is also crucially important for design of various reactor systems. There is an additional scientific interest in the fission of light actinides due to the effect known as the "thorium anomaly" [116]. It was demonstrated that in the thorium region second-order shell effects split the outer fission barrier giving the so-called triple-humped structure.

In recent years, several studies of neutron induced reactions on thorium and protactinium were carried out in the framework of a IAEA Coordinated Research Program [117, 118] involving a considerable US contribution. The ^{232}Th and ^{231,233}Pa evaluations in the ENDF/B-VII.0 result from this collaboration.

The resonance parameters for ^{232}Th were obtained by Leal and Derrien, ORNL [119] from a sequential Bayes analysis with the SAMMY computer code of the experimental data base including Olsen neutron transmission data at ORELA [120], and not yet published capture data by Schillebeeckx (GELINA), and Gunsing (n-TOF) in the energy range 1 eV to 4 keV. The resolved single-level Breit-Wigner (SLBW) resonance parameters of ^{231}Pa were evaluated by Mughabghab. The resolved resonance parameters of ^{233}Pa were adopted from an earlier evaluation by Morogovskij and Bakhanovich [121]. A minor revision of the adopted resonance evaluations for Pa isotopes was carried out by Leal. Unresolved resonance parameters for ^{232}Th (4-100 keV), ^{231}Pa nuclei (115 eV-78 keV) and ^{233}Pa nuclei (16.5 eV-70 keV) were derived by Sirakov *et al* [122], and Maslov *et al* [123, 124] respectively.

Evaluations in the fast energy region [125] were fully based on nuclear model calculations using the EMPIRE-2.19 nuclear reaction code [126, 127]. Starting values for nuclear model parameters were taken from RIPL-2. A crucial point in a successful evaluation of actinide nuclei is the selection of the proper coupled-channel optical model potential. In this work, the direct interaction cross sections and transmission coefficients for the incident channel on ^{232}Th and ^{231,233}Pa were obtained from the dispersive coupled-channel potential of Soukhovitskii *et al* (RIPL 608) [128] using five coupled levels for all nuclei. Total cross sections, average resonance parameters and angular distributions of neutron and proton scattering on the studied nuclei were shown to be in excellent agreement with the available experimental data. The same optical model potential was used to calculate direct excitation of the collective levels in the continuum by the DWBA method (similar to what was done for U isotopes described earlier). The preequilibrium emission was accounted for within the one-component exciton model model (PCROSS), which includes nucleon, γ and cluster emission. Hauser-Feshbach [129] and Hofmann-Richert-Tepel-Weidenmüller [51] versions of the statistical model were used for the compound nucleus cross section calculations. Both approaches include fission decay probabilities deduced in the optical model for fission [130] and account for the multiple-particle emission, and the full gamma-cascade. A modified Lorenzian (MLO) radiative-strength function was taken as recommended by Plujko [49] and allowed for an excellent description of the experimental neutron capture cross sections [131].

It should be noted that a new model to describe fission on light actinides, which takes into account transmission through a triple humped fission barrier with absorption, was developed [130] and applied for the first time to fission cross section evaluations. This formalism is capable of interpreting complex structure in the light actinide fission cross section in a wide energy range - it was applied at sub- and above-barrier energies. The agreement with experimental fission cross sections is very good as can be seen in Figs. 44 and 45. The complex resonance structure in the first-chance neutron induced fission cross section of ^{232}Th and ^{231}Pa nuclei has been very well reproduced by the proposed model, as shown in detail in the corresponding inset. Prompt fission neutron spectra and $\bar{\nu}$ values were calculated using a new PFNS module of the EMPIRE code system. The calculated $\bar{\nu}$ values for thorium were normalized to BROND-3 values [132], which are based on extensive experimental database and contain covariance information.

The ENDF-formatted data from EMPIRE calculations were merged with the resonance data, including resonance covariance file and the delayed neutron data from the BROND-3 file [132]. Since the evaluation extends up to 60 MeV exclusive spectra are only given for the first 3 emissions, such as (n,3n) and (n,2np), while all the remaining channels are lumped into MT=5. This approach provides uniform treatment of each individual MT number over the entire energy range without artificial change of the representation at 20 MeV.

Validation of the thorium file on a selected set of bench-

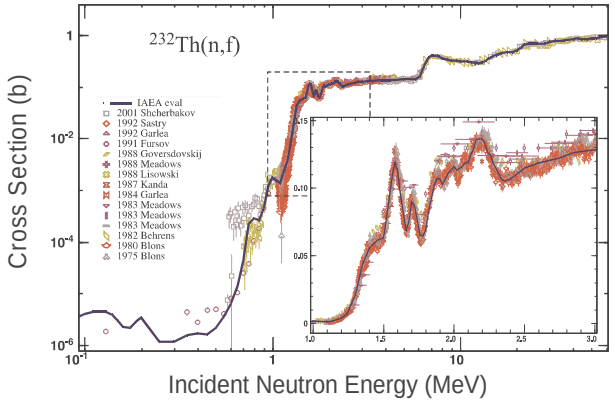

FIG. 44: Neutron induced fission cross section on ^{232}Th compared with experimental data from the CSISRS/EXFOR database.

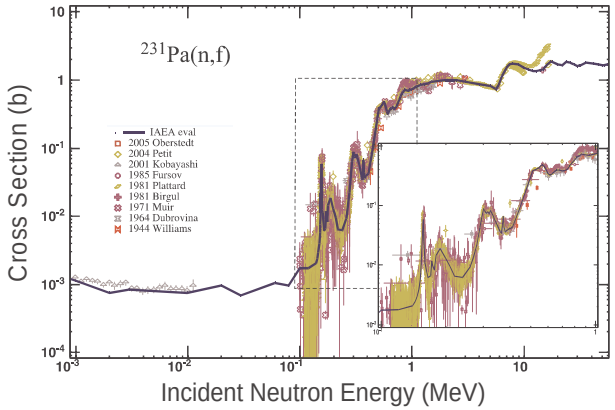

FIG. 45: Neutron induced fission cross section on ^{231}Pa compared with experimental data from the CSISRS/EXFOR database.

marks was carried out by A. Trkov, IAEA and IJS Ljubljana, showing improvement over previous evaluations. This is discussed in more detail in Section X.B.6.

9. *Analysis of $\bar{\nu}$ values*

Our analyses of the average number of neutrons per fission ($\bar{\nu}$, nubar) for actinides in ENDF/B-VII.0 evaluations, primarily ^{233}U, ^{235}U, ^{238}U and ^{239}Pu, are based on the experimental database with the added constraint that the evaluations closely predict results from simple critical benchmark experiments.

The experimental database for nubar was adapted from the database developed for the ENDF/B-VI evaluation effort by making a small adjustment for different ENDF/B-VII.0 standards, particularly, ^{252}Cf nubar from spontaneous fission. Covariance analyses were available for ^{235}U and ^{239}Pu from the ENDF/B-VI effort, and a more recent one was available for ^{233}U. During this work it was discovered that that nubar measurements relative to ^{252}Cf in the old ENDF/B-VI data base had been incorrectly normalized to the ENDF/B-VI standard value for total nubar rather than for prompt nubar (see values given in the Table XXII caption). This resulted in most of the earlier ENDF/B-VI database being 0.23% too high. In ENDF/B-VII we corrected this earlier ENDF/B-VI mistake.

TABLE X: Components of fission energy release for thermal incident neutron energy.

Fission Energy Release Term	Definition
E_{FR}	Kinetic energy of the fission products
E_{NP}	Kinetic energy of the prompt neutrons
E_{ND}	Kinetic energy of the delayed neutrons
E_{GP}	Total energy of the prompt photons
E_{GD}	Total energy of the delayed photons
E_B	Total energy released by delayed betas
$E_{neutrino}$	Energy carried away by anti-neutrinos
E_T	Sum of the partial energies given above (which corresponds to the total energy release per fission, or the Q-value).
E_R	Total energy less the neutrino energy, E_T - $E_{neutrino}$; also equal to the pseudo-Q value given in MF=3 for MT=18.

Corrected results from the covariance analysis of ^{235}U experimental data are compared to the ENDF/B-VII.0 evaluations in Fig. 12. The evaluation agrees closely with the corrected experimental data base. Similar comparisons are made to ^{239}Pu covariance results in Fig. 31. Again, the ENDF/B-VII.0 evaluation agrees well with the corrected experimental values at most energies. The most serious departure from the covariance data occurs below 1.5 MeV, where the evaluation lies about two standard deviations above the experimental data. This difference, however, was influenced strongly by the need to match the integral data results for the JEZEBEL fast critical experiment. Finally, corrected nubar experimental data for ^{238}U are compared to the ENDF/B-VII.0 evaluation in Fig. 20. Again, the evaluated results are quite consistent with the experimental database.

10. *Fission energy release*

The ENDF/B-VII.0 library includes new information for the energy released in fission for the major actinides, ^{235,238}U and ^{239}Pu. We use the ENDF-6 format and describe how the NJOY processing code obtains results for various quantities such as the energy released in fission, energy deposition, the energy dependent prompt fission Q-value, and KERMA (precise definitions for these quantities are given below). We also describe how previous (small) bugs in NJOY have been fixed and how we utilize some of the new results from Madland's work [133]. We emphasize that a full implementation of Madland's work has not been completed because it would require a revision of the ENDF-6 format.

File 1, section 458 (MF=1, MT=458) contains information on the components of energy release following fission, see Table X. These components and an estimate of their uncertainty appear in an 18-element LIST record that has no provision for incorporating dependence on the incident neutron energy, e_n. However, energy dependencies are given in the ENDF-6 format manual. In particular, $E_i(e_n) = E_i(0) - \delta E_i(e_n)$, where i refers to one of the nine energy release terms in Table X, energy $E_i(0)$ is constant and $\delta E_i(e_n)$ is expresed by energy dependent equation given for the ith term. Among these equations, we note the unphysical assertion that $\delta E_{FR}(e_n) = \delta E_{GP}(e_n) = 0$. Other energy dependencies include:

$$\delta E_{NP}(e_n) = -1.307 e_n - 8.07 \times 10^6 [\bar{\nu}(e_n) - \bar{\nu}(0)] \quad (28)$$

$$\delta E_{GD}(e_n) = \delta E_B(e_n) = 0.075 e_n \quad (29)$$

$$\delta E_{\rm neutrino}(e_n) = 0.100 e_n \quad (30)$$

$$\delta E_R(e_n) = -1.057 e_n - 8.07 \times 10^6 [\bar{\nu}(e_n) - \bar{\nu}(0)] \quad (31)$$

The reader should note that the δE$_{\rm neutrino}$ given above corrects a typographical error appearing on the August 2004 update to the ENDF-6 manual, where the e_n coefficient is erroneously given as 1.000. Previous editions of the manual have the correct coefficient for this term.

A recent study by Madland [133] finds an alternate representation for the prompt fission product, prompt neutron, and prompt photon energy functions. Their sum, the average total prompt fission energy deposition, is given by

$$< E_d(e_n) >= E_{FR}(e_n) + E_{NP}(e_n) + E_{GP}(e_n) \quad (32)$$

The study is based upon published experimental measurements and application of the Los Alamos model [69] and it shows that, to first order, these quantities can be represented by linear or quadratic polynomials in the incident neutron energy

$$E_i(e_n) = c_0 + c_1 e_n + c_2 e_n^2 \quad (33)$$

where E_i is one of E_{FR}, E_{NP} or E_{GP}. The recommended coefficients for ^{235,238}U and ^{239}Pu are provided in Table XI. The average total prompt energy deposition obtained using these coefficients is shown in Fig. 46. It is important to note that the excitation energy of the compound fissioning nucleus appears in the e_n dependence of E_{FR}, E_{NP} and E_{GP}. Based upon past practice, the c_0 coefficients from these polynomials would appear in File 1, MT=458.

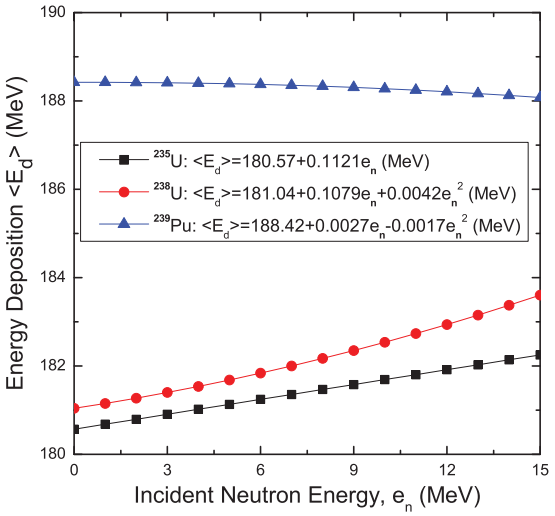

FIG. 46: Average total prompt fission energy deposition as a function of the incident neutron energy.

TABLE XI: Madland's recommended energy release polynomial coefficients, in MeV.

Nuclide	Parameter	c_0	c_1	c_2
^{235}U	E_{FR}	169.13	-0.2660	0.0
	E_{NP}	4.838	+0.3004	0.0
	E_{GP}	6.600	+0.0777	0.0
^{238}U	E_{FR}	169.8	-0.3230	0.004206
	E_{NP}	4.558	+0.3070	0.0
	E_{GP}	6.6800	+0.1239	0.0
^{239}Pu	E_{FR}	175.55	-0.4566	0.0
	E_{NP}	6.128	0.3428	0.0
	E_{GP}	6.741	+0.1165	-0.0017

Madland's recommended c_0 values for E_{FR} have been adopted in the new ENDF/B-VII.0 files for ^{235,238}U and ^{239}Pu. We note, however, that the c_0 coefficients for the E_{NP} and E_{GP} terms represent redundant data since they can also be calculated using yield and energy spectrum data found elsewhere in the evaluated file. In particular, for E_{NP}, the average prompt neutron energy can be calculated from the prompt fission spectrum given in File 5, MT=18, multiplied by the number of prompt neutrons, $\bar{\nu}_p(e_n)$ given in File 1, MT=456. That is,

$$E_{NP}(e_n) = \bar{\nu}_p(e_n) < E(e_n) > \quad (34)$$

where $< E(e_n) >$ is the first moment (average energy) of the prompt fission neutron spectrum. We note that the energy dependence of E_{NP} in Eq.(34), which is a fit to experimental data, indicates that the (older) parameterization in Eq.(28) is not very realistic. For E_{GP}, the average prompt photon energy can be calculated from the spectrum given in File 15, MT=18, while the number of

emitted photons is given in File 12, MT=18.

We have calculated, at zero energy, the average prompt neutron energy with NJOY for ^{235,238}U and ^{239}Pu. When coupled with $\bar{\nu}_p(e_n \approx 0.0eV)$ we obtain E_{NP} values of 4.916 MeV, 4.719 MeV and 6.070 MeV, respectively. These values are close to the c_0 coefficients for E_{NP} recommended by Madland. Recognizing that these spectral and yield data have received extensive data testing, and in order to maintain the internal consistency of these files, the E_{NP} data noted in this paragraph are what appear in ENDF/B-VII.0.

Photon energies and yields appearing in the preliminary ENDF/B-VII evaluations were unchanged from ENDF/B-VI.8, implying E_{GP} values of 6.718 MeV, 7.254 MeV and 7.011 MeV for ^{235,238}U and ^{239}Pu, respectively. In contrast to the prompt neutron data, these prompt photon data are relatively old and differ from Madland's recommended c_0 coefficients by up to 8%. The recommended Madland data are judged to be most accurate, therefore, we have modified the prompt photon yields appearing in File 12, MT=18 as necessary so that the combined File 12, MT=18 and File 15, MT=18 produce the Madland's recommended c_0 values for E_{GP} as shown in Table XI.

In summary, for ^{235,238}U and ^{239}Pu, new File 1, MT=458 include Madland's recommended c_0 polynomial coefficients for E_{FR} and E_{GP}. The E_{NP} data are self-consistent with the spectral and yield data given elsewhere in the file and are in close, but not exact, agreement with Madland's recommendations. Delayed and neutrino energy components are unchanged from ENDF/B-VI. Summation terms, E_R and E_T, have been recalculated. The revised E_R datum, also known as the fission pseudo-Q value, has also been propagated into File 3, MT=18, 19, 20, 21 and 38. Energy release data exist for a number of other fissioning nuclides in ENDF/B-VI; these data have been carried forward into ENDF/B-VII.0 without modification.

Nuclear heating is an important quantity in any nuclear system, and a complete presentation of this complex topic is beyond the scope of the present discussion. Nevertheless, we briefly explore this topic, its relationship to the energy release data presented above and its use by the NJOY processing code.

In general, heating as a function of energy, $H(e_n)$, may be given in terms of KERMA (Kinetic Energy Released in Materials) factors, $k(e_n)$, as

$$H(e_n) = \sum_i \sum_j \rho_i k_{ij}(e_n)\Phi(e_n) \qquad (35)$$

where ρ_i is the number density of the ith material, $k_{ij}(e_n)$ is the KERMA coefficient[4] for the ith material and jth reaction at energy e_n and $\Phi(e_n)$ is the scalar flux. A rigorous calculation of the KERMA coefficient for each reaction requires knowledge of the total kinetic energy carried away by all secondary particles following that reaction; data that frequently are not available in evaluated files. An alternative technique, known as the energy balance method [135], is used by NJOY. KERMA coefficient calculations by this method require knowledge of the incident particle energy, the reaction Q-value and other terms.

The prompt fission reaction Q-value required for prompt fission KERMA including the energy dependent prompt fission Q-value can be calculated by NJOY99.136 and later versions as

$$\begin{aligned} Q(e_n) &= E_R - 8.07 \times 10^6[\bar{\nu}(e_n) - \bar{\nu}(0)] + \\ &\quad 0.307e_n - E_B - E_{GD} \end{aligned} \qquad (36)$$

This equation begins with the pseudo-Q value from File 3, MT=18 (which is replicated as ER in File 1, MT=458, and therefore shown as E_R in Eq.(36). Energy dependency similar to that specified in the ENDF-6 manual and noted above are included, and, finally, in order to reflect prompt data only, the delayed beta and delayed photon kinetic energy release terms are subtracted.

We make several observations about Eq.(36). First, the delayed neutron term, $E_{ND}(e_n)$ should also be subtracted here. However, since its value is typically several orders of magnitude smaller than the terms that are included, its omission has no practical impact upon the calculated Q-value. Secondly, previous versions of NJOY (prior to NJOY99.136) used a -0.043 coefficient on the e_n term in Eq.(36). We now believe that this coefficient to be in error. The impact of these changes is noted below in Tables XII and XIII. Finally, the $\bar{\nu}$ energy dependence used by NJOY in Eq.(36) is total $\bar{\nu}$. Whether total or prompt $\bar{\nu}$ is more appropriate is a matter for debate, but as a practical matter the difference between the two calculations is insignificant.

Given the relationship among E_T, E_R and the various energy release terms in Table X, including their energy dependencies, other combinations of these data can be used to calculate the prompt fission Q-value. In particular, a simple sum of the prompt components, E_{FR}, E_{NP} and E_{GP} minus the incident neutron energy, e_n yields this quantity. Since these are just the terms defined in Madland's recent work, it is particularly useful to calculate this sum. We tabulate this value for the major actinides for both ENDF/B-VI.8 and the new ENDF/B-VII.0 evaluations in Table XII.

Calculations are presented using the simple sum of prompt terms with either the standard ENDF energy dependencies (*i.e.*, no energy dependency for E_{FR} or E_{GP}, and Eq.(28) for E_{NP}) and based upon NJOY calculations with its original and newly modified prompt fission Q formula. The Madland column is obtained using Eq.(33) together with the polynomial coefficients in Table XI for the sum of $E_{FR} + E_{NP} + E_{GP}$ appearing in

[4] ICRU-63 [134] recommends using the name "KERMA coefficient" instead of "KERMA factor".

TABLE XII: Prompt fission Q-values in MeV obtained with ENDF/B-VI.8 data[a].

Nuclide	Incident energy e_n	ENDF	Madland[b]	NJOY (old [c])	NJOY (Eq. 36)
^{235}U	0.0253 eV	180.88	180.57	180.89	180.89
	1.0 MeV	180.42	179.68	180.08	180.43
	14.0 MeV	169.31	168.14	164.49	169.39
^{238}U	0.0253 eV	181.31	181.04	181.33	181.33
	1.0 MeV	181.04	180.15	180.71	181.06
	14.0 MeV	169.62	169.37	164.88	169.78
^{239}Pu	0.0253 eV	189.45	188.42	189.44	189.44
	1.0 MeV	188.65	187.42	188.30	188.65
	14.0 MeV	177.07	174.12	172.19	177.09

[a] Given for the sum of prompt fission products, prompt neutrons, and prompt gammas. To obtain energy deposition, the incident neutron energy should be added to these Q-value numbers.
[b] Madland values are based upon Table XI and Eq.(33). See preceding text for further explanation.
[c] Uses Eq.(36), but the e_n coefficient was -0.043 prior to NJOY99.136.

TABLE XIII: Prompt fission Q-values in MeV obtained with ENDF/B-VII.0 data[a].

Nuclide	Incident energy e_n	ENDF	Madland[b]	NJOY (old [c])	NJOY (Eq. 36)
^{235}U	0.0253 eV	180.65	180.57	180.65	180.65
	1.0 MeV	180.19	179.68	179.84	180.19
	14.0 MeV	169.07	168.14	164.24	169.14
^{238}U	0.0253 eV	181.28	181.04	181.30	181.30
	1.0 MeV	181.02	180.15	180.68	181.03
	14.0 MeV	169.59	169.37	164.86	169.76
^{239}Pu	0.0253 eV	188.38	188.42	189.37	188.37
	1.0 MeV	187.58	187.42	187.24	187.59
	14.0 MeV	175.98	174.12	171.10	176.00

[a] See corresponding note in Table XII.
[b] Madland values are based upon Table XI and Eq.(33). See text preceding Table XII for further explanation.
[c] Uses Eq.(36), but the e_n coefficient was -0.043 prior to NJOY99.136.

Eq.(32). Then, e_n is subtracted from this sum, consistent with the ENDF column.

The old ENDF/B-VI.8 results follow in Table XII. At thermal and 1 MeV, energies of great interest to the traditional reactor design community, the NJOY and ENDF results are seen to be very similar. At thermal energies, the only difference between ENDF and either NJOY calculation is due to NJOY omission of the E_{ND} energy release term. At higher energies, the deficiency in NJOY original formula becomes more obvious while the corrected formula yields values more in line with the ENDF calculation. Again, the difference is due to NJOY omission of the E_{ND} energy release term as well as use of ν_T when calculating prompt fission Q-value whereas ν_p is used in Eq.(28) when calculating the E_{NP} contribution to the ENDF column. Differences from Ref. [133] highlight changes resulting from the newer data.

Results based upon our new ENDF/B-VII.0 are presented in Table XIII. We note that the prompt fission Q-value calculated with the traditional ENDF formulas are now in much better agreement with Madland's calculations. At thermal energies this is because Madland's c_0 coefficients for E_{FR} and E_{GP} have been adopted in the ENDF file, while the difference in the adopted $E_{NP}(0)$ values versus those recommended by Madland are small. In fact the agreement would be exact except that Madland's c_0 term for E_{NP} results from a fit to all prompt neutron spectral data whereas the c_0 term appearing in the data files is that calculated from the thermal spectrum only. At higher energies, the ENDF and corrected NJOY results remain in good agreement with Madland. This, despite the lack of energy dependency in ENDF for the E_{FP} and E_{GP} terms, suggests that the ENDF recommended energy dependency for E_{NP} is a fortuitously good match to the combined $(E_{FR}+E_{NP}+E_{GP})$ energy dependency recommended by Madland. Similar observations have recently been made by Rowlands [136] in a study of Madland's work.

The experimental facts are that the energy dependencies of E_{FR} and E_{GP} are finite, not zero as the ENDF-6 format manual recommends. Therefore, a conclusion of the present work is that CSEWG should address the incident neutron energy dependence equations for the components of energy release in fission. We show in Table XIV how the individual prompt fission energy release terms, E_{FR}, E_{NP} and E_{GP}, differ at selected incident neutron energies when calculated using the historical ENDF equations versus Madland's fits to experimental data.

Since the corrected NJOY results in Table XIII for prompt fission Q-vaulues are in good agreement with those obtained by Madland, we do not expect to make further changes in the NJOY prompt fission Q algorithm until CSEWG addresses the deficiencies in the current energy dependencies of the components of the fission energy release.

C. Delayed neutrons and photons

1. *Delayed neutrons*

Delayed neutrons, also referred to as temporal fission-product delayed neutrons, are stored in MF=1, MT=455. Related experiments typically report data only in terms of a single series of exponential terms. An experiment includes measurements characteristically made for a set of irradiation, cooling, and counting periods. Integral detected delayed neutrons, adjusted for efficiencies and assigned uncertainties, are then fit for maximum likelyhood with an exponential series best representing the

TABLE XIV: Energy release values for prompt fission products (E_{FR}), prompt neutrons (E_{NP}), prompt photons (E_{GP}) and energy deposition (E_d, per eq. 32), for ENDF/B-VII.0, determined using traditional ENDF or new Madland formulas.

Nuclide	Incident Energy e_n	$E_{FR}(e_n)$		$E_{NP}(e_n)$		$E_{GP}(e_n)$		$< E_d >$	
		ENDF	Madland	ENDF	Madland	ENDF	Madland	ENDF	Madland
^{235}U	0.0253 eV	169.130	169.130	4.916	4.838	6.600	6.600	180.65	180.57
	1.0 MeV	169.130	168.864	5.455	5.138	6.600	6.678	181.19	180.68
	14.0 MeV	169.130	165.406	7.343	9.044	6.600	7.688	183.07	182.14
^{238}U	0.0253 eV	169.800	169.800	4.804	4.558	6.680	6.680	181.28	181.04
	1.0 MeV	169.800	169.481	5.536	4.865	6.680	6.804	182.75	181.15
	14.0 MeV	169.800	166.102	7.113	8.856	6.680	8.415	183.59	183.37
^{239}Pu	0.0253 eV	175.550	175.550	6.070	6.128	6.741	6.741	188.36	188.42
	1.0 MeV	175.550	175.093	6.293	6.471	6.741	6.856	188.58	188.42
	14.0 MeV	175.550	169.158	7.684	10.927	6.741	8.039	189.98	188.12

experiment.

The most common function used has been a series of six exponential terms emulating the sum of contributions of six uncoupled delayed-neutron precursors or precursor groups of differing time constants – hence the use of "six-group fits" in common parlance. This series is generally given in terms of $\bar{\nu}_d$ – the total number of delayed neutrons per fission – times the normalized sum of six exponential terms giving the temporal production at time t following a fission event.

ENDF/B-V and earlier versions used, for each fission system, one 6-group temporal function from a selected experiment to describe delayed neutron production. This approach is also true of a recent NEA WPEC Subgroup-6 survey [137].

In preparation for ENDF/B-VI a new approach was embraced. Radionuclide inventory CINDER-10 summation calculations of fission pulses, using basic nuclear data subject to evaluation, were done for the temporal delayed neutron spectrum for each system; these results — then available for unlimited temporal combinations — would be fit with the exponential series for inclusion in ENDF/B-VI. Nuclear data needed for each pertinent radionuclide included half-lives, decay branching fractions, probabilities of neutron emission (P_n values), delayed neutron emission spectra, and fission-product yields (FPY). This effort, completed in 1989, used pre-ENDF/B-VI data. The decay data describing some major precursors were available from experiments, but the bulk of half-lives, delayed branching fractions and P_n data came from the systematics of Kratz and Herrmann [138]. FPY data came from a 1989 evaluation of yield data for 50 fission systems.

Measured delayed neutron spectra were also available for only a few major delayed neutron precursors and were typically incomplete in some energy ranges and/or relative only. Most precursor spectra were modeled using either the BETA code of Mann, Dunn and Schenter [139] or an evaporation spectrum. Detailed fine-binned spectra were accumulated for the six temporal groups by assigning contributions of each precursor to neighboring temporal groups while enforcing maximum likelihood to total spectra. The comprehensive spectral work is the subject of Brady's thesis report [140], which also summarizes other delayed neutron data, excluding FPY, for the set of 271 delayed neutron precursors.

Benchmarking of the CINDER-10 calculations contributing to ENDF/B-VI showed good agreement with measured $\bar{\nu}_d$ data [139]. However, application of the ENDF/B-VI temporal fits showed that the mean delayed neutron emission time following a fission event was lower by a factor of 2 to 3 than that predicted by functions fit to measurements. Subsequent summation calculations were made with the newer CINDER'90 code, retaining the same P_n values but using ENDF/B-VI half lives and other delayed branching fractions values with the 1993 evaluated FPY data of England and Rider [141]. Results of these calculations and benchmarking with the temporal fits to them showed outstanding improvements in agreement with fits to measured data.

CINDER'90 calculations of a single fission pulse were replaced with a series of calculations for a variety of irradiation periods followed by decay times to 800 s, defining a surface of delayed neutron production in terms of irradiation and cooling times improving fits at very short and very long cooling times. Details of this effort are summarized in [142].

Subsequent improvements in P_n and half-life data were obtained using evaluated measured data of Pfeiffer [143] and NUBASE2003 [144]. Use of the earlier systematics of Kratz and Herrmann was then replaced by results obtained with our own model.

In our theoretical model of β decay [145], we calculate the wave function of the initial state in the parent nucleus and the wave functions of all possible final states in the daughter nucleus. These wave functions are determined from a deformed single-particle model with the addition of pairing forces and a residual Gamow-Teller interaction. The next step is that we calculate the transition rates to the various states in the daughter nucleus. By summing up all possible transitions we calculate the half-life, $T_{1/2}$, of the decay. By summing up all the transition rates to states above the neutron separation energy, S_n, we can calculate the fraction of the decays that lead

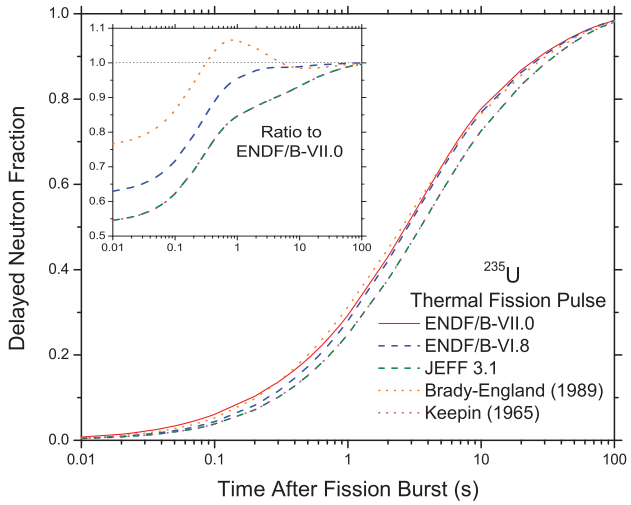

FIG. 47: Delayed neutron fraction as function of time following a ^{235}U thermal fission pulse for ENDF/B-VII.0, ENDF/B-VI.8, JEFF 3.1, Brady-England [148] and Keepin [149]. The inset shows the ratio of the delayed neutron fractions for the other evaluations to the ENDF/B-VII.0.

to delayed-neutron emission. Contributions from first-forbidden decays are treated in the gross theory statistical model. The nuclear ground-state deformations and masses of the parent and daughter nuclei are obtained from the FRDM (1992) mass model [146], except that when experimental masses for the parent and daughter nuclei are known, then these are used to calculate the Q-value of the decay. Full details of the calculations are given in [145, 147].

A new CINDER'90 data library, including all delayed neutron data developed, now includes 534 delayed neutron precursors, with 477 precursors in the fission-product range $65 < A < 173$. Use of the FPY data [141] results in the production of 281 to 440 of these precursors yielded in the 60 fission systems. These data have been used to produce new temporal delayed neutron fits for all 60 fission systems. Fits for some systems are included in this release of ENDF/B-VII.0; spectra, where present, are taken from the ENDF/B-VI.8 files using the new group abundances.

For illustration, in Fig. 47 we show delayed neutron fraction emitted as function of the time following a ^{235}U thermal fission pulse. As shown in the inset, differences between ENDF/B-VII.0 and the other evaluations are smaller than 20% for times larger than 1 second.

2. ^{235}U thermal $\bar{\nu}_d$

When G. R. Keepin [149] measured delayed nubar ($\bar{\nu}_d$) for ^{235}U, he found a difference between thermal and fast values: 0.0158±0.0005 and 0.0165±0.0005, respectively. Since second-chance fission was above the energy of his measurements, he assumed it was experimental error, and recommended the cleaner fast data for kinetics applications, including thermal. This posed a problem for thermal reactor designers: use the more accurate fast value, or the more relevant thermal data. Mostly, they opted for the latter.

S. A. Cox, ANL provided the delayed neutron data for ENDF/B-IV, specifying a constant value over 0 - 4 MeV, but raising Keepin's fast value to 0.0167. That value is in ENDF/B-V and VI, and was in the preliminary versions of ENDF/B-VII.0.

Experiments continued to send mixed signals. References [150] and [151] supported a difference between fast and thermal, and thermal reactor kinetics calculations failed to show a problem with the lower value. Fast measurements, and summation calculations tended to raise the 0.0167 even higher.

Two recent developments provided a plausible resolution of this problem:

1. Fission theory allowed an energy-variation of delayed nubar in the resonance region [152], [153]. Basically, a nucleus can fission through more than one deformed shape, or mode, and the branching ratios to these modes vary across resonances. Each mode has its own fission-product yields, so that different numbers of DN precursors are produced as the energy varies.

   The change in ^{235}U delayed nubar is a series of small dips, one at each resonance, but for engineering purposes, only the average value over the thermal region is important. As the energy increases, the fluctuations decrease and the value approaches the higher fast value.

2. Analyses of beta-effective measurements supported the view that thermal delayed nubar is about 5% lower than the fast value [154], [155], [156].

Other considerations supported lowering thermal delayed nubar:

- WPEC Subgroup 6 (delayed neutrons) recommended a lower thermal value than fast, 0.0162 rising to 0.0167 at 4 MeV [137]. Those values were adopted for JEFF-3.1.
- JENDL-3.3 adopted a lower thermal value than fast, 0.01585 rising to 0.0170 at 4 MeV.
- The commercial thermal reactor industry uses the lower value, and it is consistent with their beta-effective database [157].
- It is probable that the American National Standard Delayed Neutron Working Group, ANS-19.9, will recommend a lower thermal value [158].

The ENDF/B-VII.0 ^{235}U delayed nubar file is not a re-evaluation of the data, but a minimum adjustment to ENDF/B-VI which reflects current usage and recognizes the thermal-fast difference. An appropriate time to revisit this issue will be when the ANS-19.9 Standard is finalized.

The delayed value at thermal (0.01585) was taken from JENDL-3.3. It then ramps linearly to 0.0167 at 50 keV. JENDL ramps to 0.0162, but 0.0167 minimizes the change to ENDF/B-VI. Above 50 keV, the ENDF/B-VI data are unchanged.

To avoid disturbing thermal criticality benchmark results, which depend on total nubar, the thermal prompt value was changed to keep total nubar the same: 2.42000 to 2.42085.

3. Delayed photons

Delayed photons, also referred to as post-fission β-delayed photon production data, are stored in MF=1, MT=460 (time distribution) and in MF=12, MT=460 (photon yields). Our evaluations of delayed data following fission are based upon both extensive measured data, as well as nuclear structure and decay predictions using a β-decay model.

Increased interest in developing active interrogation systems to detect special nuclear materials (SNM) in seagoing cargo containers [159] has stimulated the Monte Carlo neutron-photon transport community to improve the representation of photon- and neutron-induced fission processes. Since out-of-beam counting reduces backgrounds significantly, there has been increased interest in using β-delayed neutron and photon production from fission as a characteristic signal for the presence of special nuclear materials.

In response to this need, we have for the first time in ENDF included data for the β-delayed photon signal from neutron-induced fission. The data for ^{239}Pu including 3129 γ lines were taken from [160], where it was generated by directly sampling prompt fission product yield distributions and then following the decay of each individual fission fragment in time and tabulating the resulting photon production spectrum. Details regarding how the data have been tabulated in ENDF/B-VII.0 can be found in [161] and [162].

In a similar way, β-delayed photon data for ^{235}U were also prepared for ENDF/B-VII.0.

D. Fission product evaluations

The ENDF/B-VI.8 library contained 196 materials that fall into the range of fission products, defined as materials with Z = 31 - 68. We follow this definition, with the understanding that it covers also several other important materials such as structural materials Mo and Zr, and absorbers Cd and Gd.

Many of the ENDF/B fission product evaluations had not been revised for very long period of time. As a consequence, an analysis performed by Wright and MacFarlane in 2000 revealed the following major deficiencies in the ENDF/B-VI library [163]:

- 65% of the evaluations were performed more than 30 years ago using outdated evaluation methods and old experimental data,
- 55% of the evaluations used unrealistic, isotropic angular distribution for neutron elastic scattering,
- 30% of the evaluations used the outdated pointwise representation in the neutron resonance region, and
- 30% of the evaluations used the outdated single-level Breit-Wigner representation for neutron resonances.

In this situation, fission product evaluations in ENDF/B-VI.8 were completely abandoned and ENDF/B-VII.0 adopted new or recently developed evaluations. For a set of 74 materials, including 19 materials considered to be of priority, entirely new evaluations were performed for ENDF/B-VII.0. These new evaluations were produced by the following laboratories:

- 24 materials were evaluated by BNL,
- 38 materials were evaluated by BNL in collaboration with KAERI, S. Korea (33 materials) and with JAERI renamed JAEA, Japan (5 materials),
- 8 materials were evaluated by BNL, including covariances produced by BNL-ORNL-LANL collaboration, and
- 4 materials of specific interest evaluated by LLNL (^{74,75}As), LANL-BNL (^{89}Y) and BNL (^{90}Zr).

For the remaining bulk of fission products consisting of 147 materials, evaluations from the recently developed International Fission Product Library of Neutron Cross Section Evaluations (IFPL) were adopted. This was made possible by the international project under the NEA Working Party on Evaluation Cooperation (WPEC Subgroup 23) that completed the IFPL library in December 2005 [164].

1. Atlas-EMPIRE evaluation procedure

All new evaluations used the Atlas-EMPIRE evaluation procedure developed by the National Nuclear Data Center, BNL. This procedure covers both the neutron resonance region and the fast neutron region. The methodology is described in detail in another paper [25] and was summarized in the beginning of this Section. Therefore, we restrict ourselves to a couple of comments only.

In the thermal, resolved resonance and unresolved resonance regions the evaluations are based on Mughabghab's new Atlas of Neutron Resonances [30]. We note that Mughabghab uses the multi-level Breit-Wigner representation for neutron resonances. Resonance parameters, both for observed resonances and those placed below the neutron binding energy (negative), are adjusted to reproduce measured thermal cross sections.

Evaluations at fast neutron energies are based on the nuclear reaction model code system EMPIRE-2.19 developed by M. Herman *et al.*. EMPIRE couples together a set of nuclear reaction models and databases, as well as an extensive set of utility codes that facilitate the evaluation process.

All new evaluations are complete: they include all reaction channels of importance for neutronics calculations; the unresolved resonance region extends up to the first excited level of the target nucleus; and photon production is always provided.

2. Priority fission products

New evaluations were performed for materials considered to be priority fission products. The list includes 10 materials discussed here (^{95}Mo, ^{99}Tc, ^{101}Ru, ^{103}Rh, ^{105}Pd, ^{109}Ag, ^{131}Xe, ^{133}Cs, ^{141}Pr,^{153}Eu), and 9 materials (^{143,145}Nd, ^{147,149,150,151,152}Sm, ^{155,157}Gd) extended to cover complete isotopic chains, which we discuss later.

This selection was based on the analysis by DeHart, ORNL in 1995 [165]. It was motivated by the need to improve existing evaluations for materials of importance for a number of applications, including criticality safety, burn-up credit for spent fuel transportation, disposal criticality analysis and design of advanced fuels. Improved neutron capture cross sections in the keV range are important in reactor design. Many fission products in a reactor core have large neutron capture cross sections in thermal, resonance and keV energy ranges. Consequently, neutrons absorbed by fission products represent a significant portion in the total loss of neutrons.

Evaluations for priority fission products were performed under the BNL-KAERI collaboration. Low energy evaluations (MF=2, neutron resonance parameters) were completed and included in the ENDF/B-VI.8 library in 2001 [29]. An initial set of evaluations in the fast neutron region followed [166] and full files were created by merging with MF=2 files [167]. Later, in 2005-2006, these evaluations were thoroughly reviewed and reexamined, both in the low energy and fast energy regions. This last step meant a complete re-evaluation of all priority materials based on a more refined evaluation methodology, use of the latest data including elemental measurements, and improved modeling and consistent parameterization. Details are listed below:

^{95}Mo. This is an important fission product and neutron absorber. A new evaluation was performed by Kim *et al.* [168]. In the low energy region it updates an earlier evaluation by Oh and Mughabghab [29] included in ENDF/B-VI.8. In the fast neutron region it represents a completely new evaluation. In Fig. 48 we compare neutron total cross sections on ^{95}Mo with experimental data and ENDF/B-VI.8. This plot illustrates clear improvement achieved by our new evaluation. Fig. 49 shows neutron total inelastic cross sections and illustrates the typical unphysical shape of older ENDF/B-VI.8 evaluations at higher energies.

^{99}Tc. The long-lived radioactive ^{99}Tc, with its half-life of 2.1x10^5 years, is of top importance for nuclear waste management and waste transmutation applications. A new evaluation was performed by Rochman *et al.* [169]. Importantly, the thermal capture cross section was fixed to reproduce the latest value of 22.8 b [30], see Fig. 50. In Fig. 51 we further illustrate this evaluation by showing neutron capture cross sections in the unresolved resonance region.

^{101}Ru. The new evaluation was performed by Kim *et al.* [168]. In the low energy region it updates an earlier evaluation by Oh and Mughabghab [29] included in ENDF/B-VI.8. In the fast neutron region it represents a completely new evaluation.

^{103}Rh. This is an important fission product and neutron absorber. The new evaluation was performed by Kim *et al.* [168] and it replaced the 1974 evaluation by Schenter, HEDL. Fig. 52 shows neutron inelastic cross sections on ^{103}Rh demonstrating excellent agreement with (n,n') to the isomeric state, thereby giving confidence in our evaluated total (n,n').

^{105}Pd. The new evaluation was performed by Kim *et al.* [168]. In the low energy region it updates an earlier evaluation by Oh and Mughabghab [29] included in ENDF/B-VI.8. In the fast neutron region it represents a completely new evaluation.

^{109}Ag. The new evaluation was performed by Kim *et al.* [168]. In the low energy region it updates an earlier evaluation by Oh and Mughabghab [29] included in ENDF/B-VI.8. In the fast neutron region it represents a completely new evaluation.

^{131}Xe. The new evaluation was performed by Kim *et al.* [168]. In the low energy region it updates an earlier evaluation by Oh and Mughabghab [29] included in ENDF/B-VI.8. In the fast neutron region it represents a completely new evaluation.

^{133}Cs. The new evaluation was performed by Kim *et al.* [168]. In the low energy region it updates an earlier evaluation by Oh and Mughabghab [29] included in ENDF/B-VI.8. In the fast neutron region it represents a completely new evaluation.

^{141}Pr. The new evaluation was performed by Kim *et al.* [168]. In the low energy region it updates an earlier evaluation by Oh and Mughabghab [29] included in

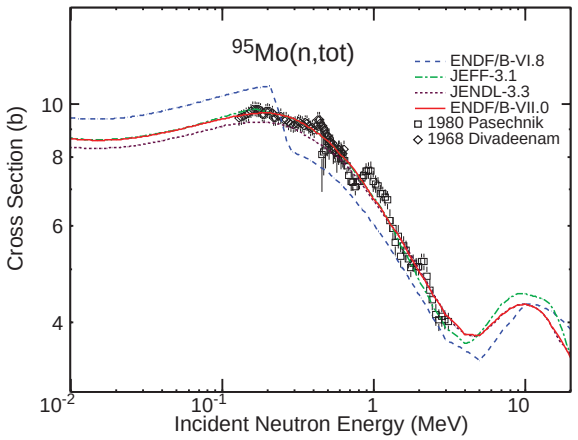

FIG. 48: Total neutron cross sections on ^{95}Mo compared with other evaluations and with experimental data. The ENDF/B-VI.8 curve suffers from poor matching between resonance and fast neutron regions.

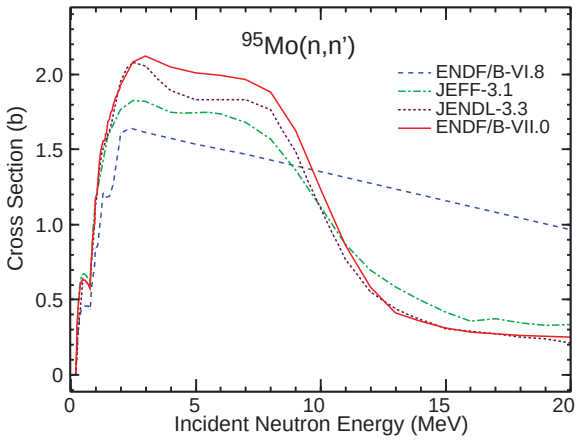

FIG. 49: Inelastic cross sections on ^{95}Mo compared with other evaluations. The ENDF/B-VI.8 curve shows typical unphysical shape of older evaluations.

ENDF/B-VI.8. In the fast neutron region it represents a completely new evaluation.

^{153}Eu. The new evaluation was performed by Obložinský *et al.* in 2006. In the low energy region this evaluation is completely new. In the fast neutron region this is also a new evaluation that was facilitated by an excellent coupled-channel optical model potential developed earlier by P. Young, LANL.

3. Isotopic chains: Ge, Nd, Sm, Gd, Dy

A new feature of our evaluation work is a simultaneous evaluation of complete isotopic chain for a given element. This is possible due to tremendous progress in the development of evaluation tools in recent years. As described

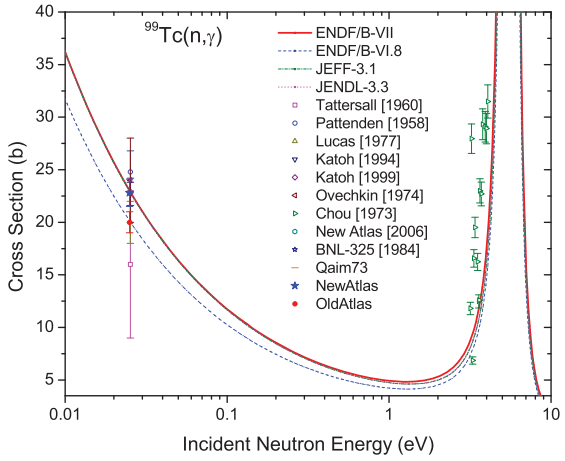

FIG. 50: Neutron capture cross sections for ^{99}Tc in the thermal region compared with other evaluations and experimental data.

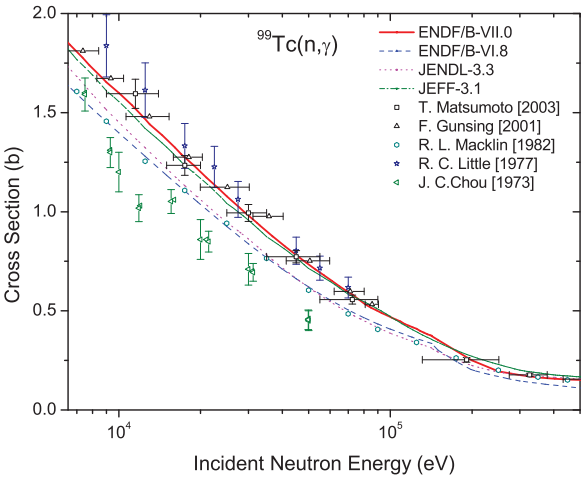

FIG. 51: Neutron capture for ^{99}Tc in the unresolved resonance region compared with other evaluations and experimental data.

above, the combined capabilities of the Atlas of Neutron Resonances, the nuclear reaction model code EMPIRE, input parameter libraries such as RIPL-2, experimental cross section library CSISRS/EXFOR, and numerous ENDF formatting and checking utilities has facilitated such a complex evaluation work. A considerable advantage of this approach is a full and consistent utilization of data that are often measured on natural elements rather than isotopes, a consistent application of model parameters, and comparisons with data by summing up isotopic evaluations into a single elemental representation.

Altogether, complete isotopic chains for Ge, Nd, Sm,

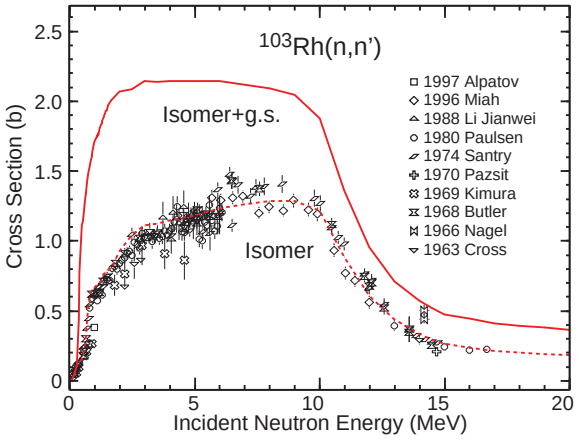

FIG. 52: Neutron inelastic cross sections on ^{103}Rh. Partial (n,n') cross sections (dashed curve) show good agreement with experimental data, giving confidence in total (n,n') values evaluated by EMPIRE (full curve).

Gd and Dy, totaling 37 materials, were evaluated as summarized in Table XV.

Ge isotopes. A complete isotopic chain for germanium include 4 stable isotopes and long-lived radioactive ^{76}Ge. This evaluation was performed by Iwamoto *et al.* [170]. Germanium is of special interest for simulation calculations by the MCNP community that repeatedly requested photon production data for detector development.

Nd isotopes. A set of neodymium evaluations include two priority fission products, ^{143,145}Nd, another 5 stable isotopes, and the radioactive ^{147}Nd. Neodymium is one of the most reactive rare-earth metals. It is important in nuclear reactor engineering as a fission product which absorbs neutrons in a reactor core. A new evaluation was performed by Kim *et al.* [168]. In Fig. 53 we show total neutron cross sections on all Nd isotopes in comparison with available data measured on isotopic samples (including Wisshak 1997) as well as on elemental samples.

Of special interest to radiochemical applications is the radioactive ^{147}Nd for which no data exist. A good fit to available data on other stable isotopes gives confidence that our predictions for ^{147}Nd cross sections are sound. This is illustrated in Figs. 54 and 55 where we show (n,2n) and neutron capture cross sections respectively for all Nd isotopes.

Sm isotopes. A complete set of samarium isotopes includes 5 priority fission products, ^{147,149,150,151,152}Sm, another 2 naturally occurring isotopes, and the radioactive ^{151,153}Sm isotopes. With its high absorption cross sections for thermal neutrons, samarium is an important material for nuclear reactor control rods and for neutron shielding. New evaluations were performed by Kim *et al.* [168]. In Fig. 56 we show (n,2n) cross sections on all isotopes of Sm, compared to available experimental data. A good fit to these data provides an additional support of predictive capabilities for (n,2n) cross sections on isotopes where no data exist.

Gd isotopes. A complete isotopic chain for gadolinium includes two priority fission products, ^{155,157}Gd, another 5 stable isotopes, and the long-lived radioactive ^{153}Gd. Gadolinium has an extremely high capture cross section for thermal neutrons. It is of significant interest for nuclear criticality safety applications. New evaluations were performed, including the resolved resonance region, unresolved resonance and fast neutron region. Covariance data in MF=32 and MF=33 were also included as described in Section III.H.3.

Detailed description of these evaluations can be found in the forthcoming papers by Rochman *et al.* [171] and [172]. In Fig. 57 we compare neutron capture cross sections for all 8 isotopes, at energies above 10 keV, with recent experimental data. We note very good agreement with data that include recent careful measurements by Wisshak and Käppeller at FZ Karlsruhe.

Dy isotopes. The dysprosium isotopic chain includes 7 isotopes. With its high thermal neutron absorption cross sections and high melting point, dysprosium is of interest for use in nuclear reactor control rods. A new evaluation was performed by Kim *et al.* [168]. In Fig. 58 we show evaluated neutron spectra at several neutron incident energies. The prominent structure below the elastic peak results from our advanced modeling of direct reactions in terms of Coupled-Channels and Multistep-Direct approaches.

TABLE XV: Summary of 37 new evaluations of 5 complete isotopic chains in the fission product range for the ENDF/B-VII.0 library.

Z	Element	A	Total
32	Ge	70,72,73,74,76	5
60	Nd	142,143,144,145,146,147,148,150	8
62	Sm	144,147,148,149,150,151,152,153,154	9
64	Gd	152,153,154,155,156,157,158,160	8
66	Dy	156,158,160,161,162,163,164	7

4. ^{89}Y and ^{90}Zr

^{89}Y. The new evaluation was performed jointly by T-16 (LANL) and the NNDC (BNL). The dosimetry cross sections for (n,n') and (n,2n) reactions were evaluated by LANL. For the (n,2n) cahnnel, we also give evaluations for the separate component to the ground state and two short-lived isomers, using LANSCE/GEANIE data and GNASH calculations. The remaining data were supplied by BNL, including the thermal region, the resolved neutron resonance region, and all missing reaction channels

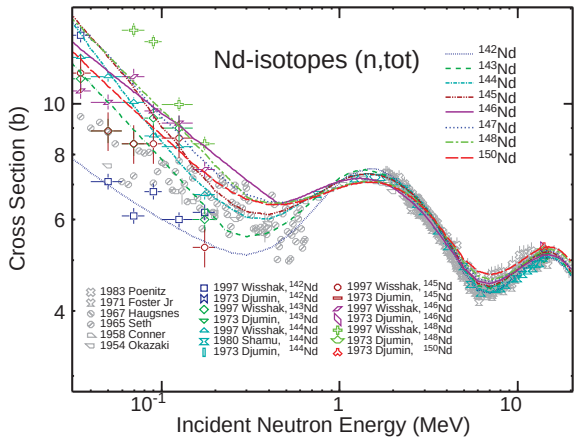

FIG. 53: Total cross sections for Nd isotopes. Symbols in gray represent measurements on the natural Nd. Note the consistency among different isotopes resulting from the simultaneous evaluation of the full chain of neodymium isotopes.

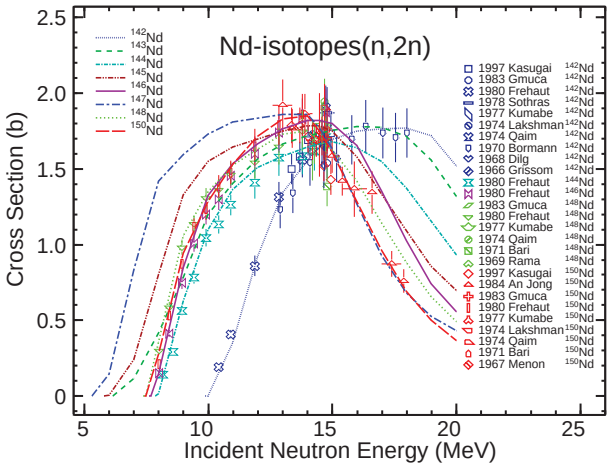

FIG. 54: (n,2n) cross sections for Nd isotopes. Good fit to the available data justifies our prediction of cross sections for the radioactive ^{147}Nd.

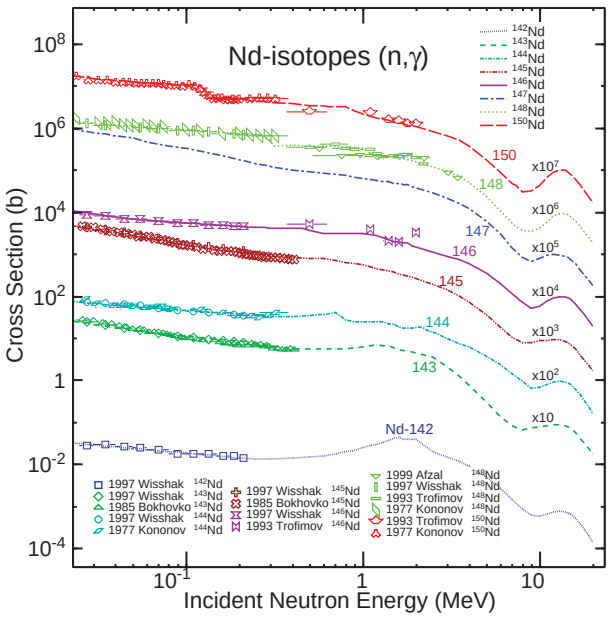

FIG. 55: Neutron capture cross sections for Nd isotopes. Good fit to the available data endorses our prediction of cross sections for the radioactive ^{147}Nd.

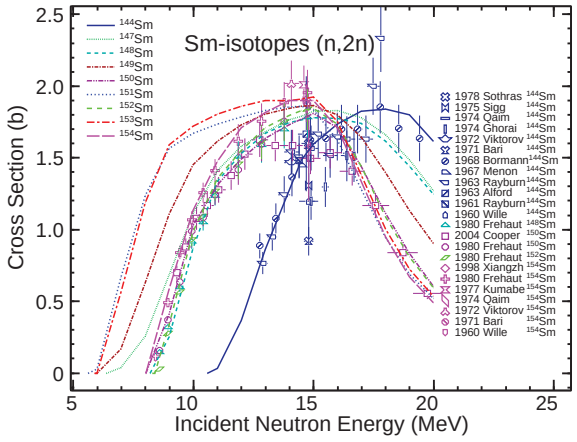

FIG. 56: (n,2n) cross sections for Sm isotopes showing odd-even effect and isospin dependence of the thresholds.

in the fast neutron region. In addition, cross section covariances (MF=33) were evaluated from the thermal energy up to 20 MeV, using the Atlas-KALMAN method at low energies and the EMPIRE-KALMAN method at higher energies, see Section III.H.3.

^{90}Zr. Zirconium is an important material for nuclear reactors since, owing to its corrosion-resistance and low absorption cross-section for thermal neutrons, it is used in fuel rods cladding. Preliminary versions of the ENDF/B-VII library contained full set of zirconium isotopes provided by the project carried out under aspices of the NEA WPEC (see the next section for details). However, benchmark testing performed at Bettis and KAPL showed an undesirable drop in the reactivity when the new library was used in place of ENDF/B-VI.8. Sensitivity studies indicated that this shortage could be counteracted by the increase of the elastic cross section in ^{90}Zr.

Taking into account the importance of zirconium in reactor calculations, NNDC (BNL) undertook an entirely new evaluation of the fast neutron region in ^{90}Zr using EMPIRE code. It was confirmed, indeed, that all suitable optical potentials in the RIPL-2 library provide elastic cross sections that are significantly higher than the preliminary evaluation. On the other hand, these potentials failed to match the quality of the description of the total cross section provided by the preliminary evaluation. This ambiguity was solved by the dispersive optical model potential [173–175], which provided a very

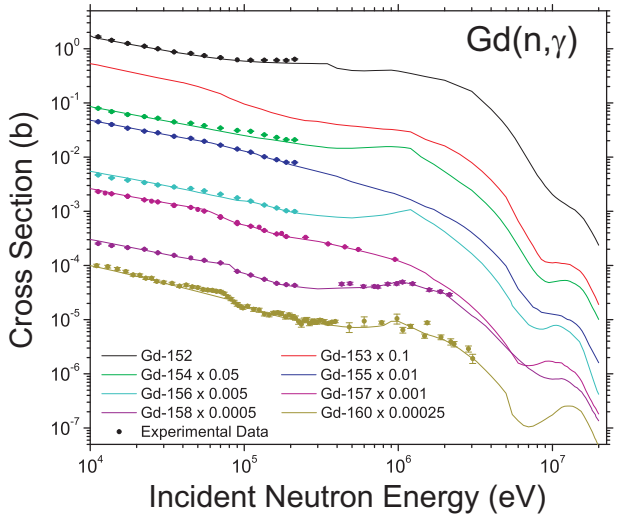

FIG. 57: Capture cross sections for Gd isotopes compared to experimental data in the fast neutron region. The neighbouring curves and data are offset by factors indicated in the legend.

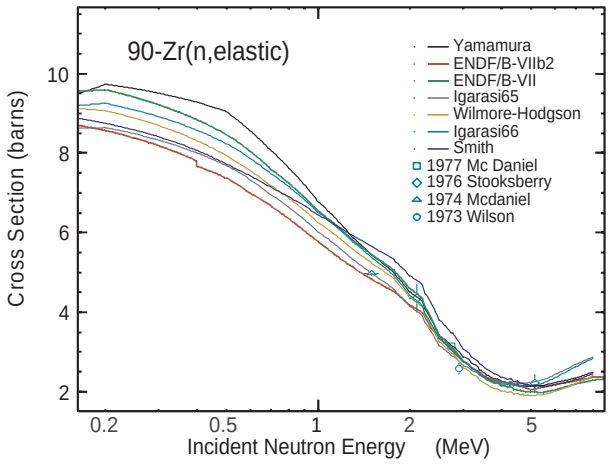

FIG. 59: Comparison of elastic cross sections on ^{90}Zr calculated with various optical model potentials. The preliminary ENDF/B-VII evaluation (denoted ENDF/B-VIIb2) yields the lowest cross sections. The final ENDF/B-VII evaluation is considerably higher, as suggested by the integral experiments.

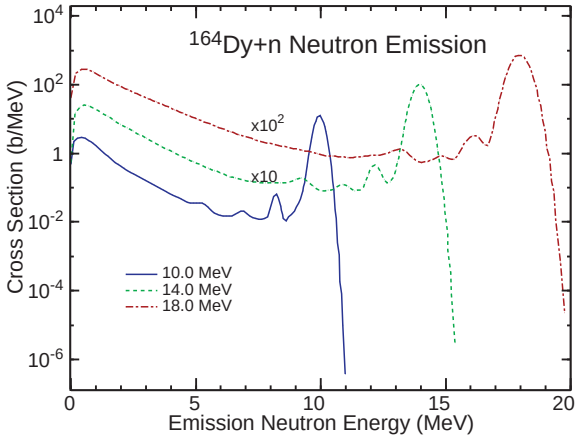

FIG. 58: Spectra of neutrons emitted from ^{164}Dy for three incident neutron energies. The structure in the high energy part of the spectra results from inelastic scattering to collective levels as predicted by Coupled-Channels (discrete levels) and Multi-step Direct (continuum).

good description of the total cross section on ^{90}Zr and confirmed the higher elastic scattering cross section, see Fig. 59. The new file met expectations when validated against integral measurements at KAPL.

5. *Bulk of fission products*

Recognizing a need to modernize the fission product evaluations, an international project was conducted to extract the best from the available evaluated nuclear data libraries. The project, sponsored by the NEA Working Party on International Nuclear Data Evaluation Cooperation (WPEC) and led by P. Obložinský, BNL, proceeded in two steps. First, in 2001 – 2004, review and assessment of neutron cross sections for fission products was performed, looking into all available evaluations [176]. Second, in 2004 – 2006, the library of 219 materials was created and partly validated [164]. Evaluated nuclear data libraries of five major efforts were considered, namely the United States (ENDF/B-VI.8 and Preliminary ENDF/B-VII), Japan (JENDL-3.3, released in 2002), Europe (JEFF-3.0, released in 2000), Russia (BROND-2.2, released in 1992) and China (CENDL-3.0, made available for the present project in 2001). Intercomparison plots of evaluated data in these five libraries were prepared for the most important reaction channels along with a comparison from the experimental reaction database CSISRS/EXFOR, totaling almost 1900 plots.

The WPEC activity included 10 active reviewers from Brookhaven, JAERI, IPPE Obninsk, KAERI and CNDC Beijing. This made it possible to review each material individually within a relatively short period of two years. The low-energy region (thermal point, resonances), and the fast neutron region, for each material, was reviewed separately. A review report for each material was written that described the review procedure, an analysis of the evaluation methodology, comparisons with recent data, and summarized findings and recommendations of the best evaluation for the low-energy and the fast neutron regions. A detailed account of this work can be found in Ref. [177].

These reviews were discussed at the workshop held at BNL in April 2004, and final recommendations were made for the best evaluations for each material. The most frequently recommended library was JENDL-3.3 (27 full files, 7 resonance files and 63 fast region files). It was followed by CENDL-3.0 (11 full files, 26 fast re-

gion files), and by the preliminary ENDF/B-VII evaluations as available in April 2004. The Atlas of Neutron Resonances was recommended for 109 materials, while default EMPIRE calculations were recommended, as a quick remedy in the fast neutron range for 25 materials of relatively limited importance.

These recommendations were revised during 2005 by taking into account a considerably increased number of new evaluations for ENDF/B-VII. New evaluations were mostly due to new BNL resonance data from the Atlas of Neutron Resonances combined with new BNL evaluations in the fast neutron region. In addition, many new resonance evaluations from the Atlas were combined with non-US evaluations in the fast neutron region.

A follow-up WPEC activity was set up for the period of 2004-2006 with the goal to produce the actual fission product library. Based on the above recommendations, the library was assembled. Initial testing was done leading to a number of adjustments particularly at the boundary between the resonance region and the fast neutron region. Then, the library underwent Phase 1 testing (data verification), which involved standard checking codes, and basic runs with the NJOY-99 processing code, followed by test runs with the MCNP4 Monte Carlo transport code. This ensured that the library can be processed and used in transport calculations.

As the final step, limited data validation was undertaken for some materials (Zr, Gd) using a few available benchmarks. As a result, the International Fission Product Library of Neutron Cross Section Evaluations (IFPL) was created for 219 materials. Afterwards, IFPL was adopted in full by the ENDF/B-VII.0 library, see Table XVI for a summary.

TABLE XVI: Summary of 219 fission product evaluations included in the ENDF/B-VII.0 library. Data from the Atlas of Neutron Resonances were adopted for 148 materials, either as a part of new US evaluations (74 materials) or merged with older US (13 materials) and newer non-US evaluations (71 materials) in the fast neutron region.

Library (Data Source)	**Full File**	**Resonance Region**	**Fast Region**
ENDF/B-VI.8, released in 2001	1	3	13
New evals for ENDF/B-VII.0	74	74	-
JEFF-3.1, released in 2005	1	-	-
JENDL-3.3, released in 2002	47	7	56
CENDL-3.0, released in 2001	11	-	15
BROND-2.2, released in 1992	1	-	-
Total number of materials	135	84	84

In summary, ENDF/B-VII.0 adopted an entirely new set of fission product evaluations, representing a major update. This is the most significant change in fission product evaluations in the ENDF/B library over the last 30 years. It will be important to undertake additional validation data testing of this fission product data for reactor applications.

E. High energy extensions to 150 MeV

The version of the ENDF/B-VI.6 library released in 1996, included extensions up to 150 MeV maximum energy for about 40 neutron and 40 proton reactions on certain target isotopes, supporting applications that included the design of accelerator-driven systems (ADS) for energy production, waste transmutation, tritium production, for spallation neutron source (SNS) design, and for external beam neutron and proton cancer therapy. The isotopes included in this "LA150" library were those important for spallation targets, blanket materials, collimation and structural materials, and isotopes in human tissue. These cross sections are important for radiation transport code simulations of neutron production, neutron fluences, energy deposition and dose, shielding, and activation.

The higher energy cross section data, which were based upon measurements, and on GNASH nuclear model code predictions, were documented in detail in Ref. [178]. Similar research has been undertaken in Europe, Japan, and Russia, in support of ADS technologies.

Unfortunately, a bug was later found in the GNASH code that was used to predict secondary emitted particle production. The legacy GNASH code at Los Alamos was being modernized and rewritten as McGNASH in modern FORTRAN-90 by Chadwick, and in the course of validation and verification tests, the bug was located. The impact of this bug was to over-calculate the amounts of secondary particle (neutron, proton, *etc.*) production at the higher incident energies, when the code was used in an "inclusive cross section" mode - the mode used to generate the MT=5 LA150 high energy cross sections, where it becomes impractical to represent each exclusive cross section separately because of their large number. Fortunately, the impact of this bug was only modest for light isotopes, and for heavy isotopes used in spallation targets, but for medium-mass isotopes the impact was significant above 50 MeV. The bug had no impact on other previous ENDF cross sections created with GNASH over the years, since those evaluations used the exclusive cross section calculation mode.

For ENDF/B-VII.0 we have recalculated the high energy LA150 data, and updated the earlier LA150 evaluations with these new corrected results. A full detailing of the new results, for each isotope (over 40 for neutrons, and 40 for protons) is given in comparison figures on our Los Alamos web site, http://t2.lanl.gov/.

F. Light element evaluations

Several light-element evaluations were contributed to ENDF/B-VII.0, based on R-matrix analyses done at Los Alamos using the EDA code. Among the neutron-induced evaluations were those for ^{1}H, ^{3}H, ^{6}Li, ^{9}Be, and ^{10}B. For the light-element standards, R-matrix results for $^{6}\mathrm{Li}(n,\alpha)$ and $^{10}\mathrm{B}(n,\alpha)$ were contributed to the stan-

dards process, which combined the results of two different R-matrix analyses with ratio data using generalized least-squares, as described in a following section (Section V). Differences persisted between the two R-matrix analyses even with the same data sets that are not completely understood, but probably are related to different treatments of systematic errors in the experimental data.

Below we summarize upgrades that have been made for ENDF/B-VII.0. Where no changes have been made compared to ENDF/B-VI.8 (*e.g.*, for n + D) we do not discuss reactions on these isotopes.

^{1}H. The hydrogen evaluation came from an analysis of the $N-N$ system that includes data for $p+p$ and $n+p$ scattering, as well as data for the reaction ^{1}H$(n,\gamma)^{2}$H in the forward (capture) and reverse (photodisintegration) directions. The R-matrix parametrization, which is completely relativistic, uses charge independent constraints to relate the data in the $p+p$ system to those in the $n+p$ system. It also uses a new treatment of photon channels in R-matrix theory that is more consistent with identifying the vector potential with a photon "wavefunction". In the last stages of the analysis, the thermal capture cross section was forced to a value of 332.0 mb (as in ENDF/B-VI.8), rather than the "best" experimental value of 332.6 ±0.7 mb [179], since criticality data testing of aqueous thermal systems showed a slight preference for the lower value. Also, the latest measurement [180] of the coherent $n-p$ scattering length was used, resulting in close agreement with that value, and with an earlier measurement of the thermal scattering cross section [181], but not with a later, more precise value [182]. This analysis also improved a problem with the $n+p$ angular distribution in ENDF/B-VI.8 near 14 MeV, by including new measurements [183, 184] and making corrections to some of the earlier data that had strongly influenced the previous evaluation. We refer the reader to Sec. V for further details.

^{3}H. The n+^{3}H evaluation resulted from a charge-symmetric reflection of the parameters from a p+^{3}He analysis that was done some time ago. This prediction [185] resulted in good agreement with $n+t$ scattering lengths and total cross sections that were newly measured at the time, and which gave a substantially higher total cross section at low energies than did the ENDF/B-VI evaluation (which was carried over from a much earlier version). At higher energies, the differences were not so large, and the angular distributions also remained similar to those of the earlier evaluation.

^{9}Be. The n+^{9}Be evaluation was based on a preliminary analysis of the ^{10}Be system that did a single-channel fit only to the total cross section data at energies up to about 14 MeV. A more complete analysis is underway that takes into account the multichannel partitioning of the total cross section, especially into the (n,2n) channels. An adequate representation of these multibody final states will probably require changes in the EDA code. For ENDF/B-VII.0 the elastic (and total) cross section was modified to utilize the new EDA analysis which accurately parameterizes the measured total elastic data, while the previous ENDF/B-VI.8 angular distributions were carried over. Data testing of the file (including only the changes in the total cross sections) appeared to give better results for beryllium reflecting assemblies (see Section X.B.2 and Figs. 90 and 91), and so it was decided to include this preliminary version in the ENDF/B-VII.0 release.

G. Other materials

Previous sections indicate that our main evaluation effort was concentrated on the major actinides and the fission products (Z = 31 - 68) that together cover more than half of the ENDF/B-VII.0 neutron sublibrary. Outside of these two groups, there were a few materials that were fully or partially evaluated. These materials are briefly described below. The remaining isotopes were either migrated from the ENDF/B-VI.8 or taken over from other national libraries if the materials were missing in ENDF/B-VI.8, or if evaluations in other libraries were clearly superior.

1. New evaluations (O, V, Ir, Pb)

^{16}O. The evaluated cross-section of the ^{16}O(n,α_0) reaction in the laboratory neutron energy region between 2.4 and 8.9 MeV was reduced by 32% at LANL. The ^{16}O(n,α) cross section was changed accordingly and the elastic cross sections were adjusted to conserve unitarity. This reduction was based upon more recent measurements. We note that this led to a small increase in the calculated criticality of LCT assemblies, see Section X.B.4.

^{nat}V. Cross sections for the (n,np) reaction were revised at BNL [186] by adjusting the EMPIRE-2.19 calculations to reproduce two indirect measurements by Grimes [187] and Kokoo [188] at 14.1 and 14.7 MeV respectively. This resulted in the substantial reduction (about 350 mb at the maximum) of the (n,np) cross section. Similarly, the (n,t) reaction was revised to reproduce experimental results of Woelfle *et al.* [189] The inelastic scattering to the continuum was adjusted accordingly to preserve the original total cross section.

^{191,193}Ir. These are two entirely new evaluations performed jointly by T-16 (LANL) and the NNDC (BNL) in view of recent GEANIE data on γ-rays following neutron irradiation. The resolved and unresolved resonance parameters are based on the analyses presented in Ref. [30]. New GNASH model calculations were performed for the γ-rays measured by the GEANIE detector, and related (n,xn) reactions cross sections were deduced [190]. We

also include an evaluation of the ^{193}Ir(n,n') reaction to the isomer. The remaining cross sections and energy-angle correlated spectra were calculated with the EMPIRE code. The results were validated against integral reaction rates, see Section X.D and Fig. 109. In addition, the covariance data in the fast neutron region were determined using EMPIRE-generated sensitivity matrices, experimental data and the KALMAN filtering code, see Section III.H.3.

^{208}Pb. A new T-16 (LANL) analysis with the GNASH code was performed over the incident neutron energy range from 1.0 to 30.0 MeV. The Koning-Delaroche optical model potential [191] from the RIPL-2 data base was used to calculate neutron and proton transmission coefficients for calculations of the cross sections. Minor adjustments were made to several inelastic cross sections to improve agreement with experimental data. Additionally, continuum cross sections and energy-angle correlated spectra were obtained from the GNASH calculations for (n,n'), (n,p), (n,d), (n,t), and (n,α) reactions.

Elastic scattering angular distributions were also calculated with the Koning-Delaroche potential and incorporated in the evaluation at neutron energies below 30 MeV.

As discussed in Section X.B.2 and Fig. 89, this new ^{208}Pb evaluation led to a significant improvement in the lead-reflected critical assembly data. This is especially true for fast assemblies, but some problems remained for thermal assemblies. The improvements in the secondary neutron spectrum are evident from the transmission data shown in Fig. 110.

2. Evaluations from other libraries

JENDL-3.3. This is a Japanese library that provided most of the evaluations taken from other sources. In particular, an extended set of minor actinides was reviewed and slightly improved by R.Q. Wright (ORNL). This set includes the following 23 actinides: ^{223,224,225,226}Ra, ^{225,226,227}Ac, ^{227,228,229,233,234}Th, ^{235}Np, ^{246}Pu, ^{244,244m}Am, ^{249,250}Cm, ^{250}Bk, ^{254}Cf, ^{254,255}Es, and ^{255}Fm. Two relatively old ENDF/B-VI.8 evaluations for ^{nat}S and ^{32}S were replaced by a consistent set of ^{32,33,34,36}S files evaluated by Nakamura. Similarly, the files for the ^{39,40,41}K isotopes by the same author replaced very old evaluations in ENDF/B-VI.8. The JENDL-3.3 results were also adopted for the full chain of Ti isotopes.

JEFF-3.1. This is European library that was selected as a source of evaluations for ^{40,42,43,44,46,48}Ca and ^{204,206,207}Pb. These are totally new evaluations in the fast neutron region, created with the nuclear model code TALYS [192], and originating from Koning's collection called NRG-2003. We also adopted JEFF-3.1 evaluations for ^{22}Na and for the ^{58,58m}Co isotopes which were missing in the ENDF/B-VI.8 library. A very fragmentary evaluation for ^{59}Ni, available in ENDF/B-VI.8, was replaced by its much more complete counterpart from JEFF-3.1.

BROND-2.2. This is Russian library that is the only library containing data for Zn. It filled the gap in ENDF/B-VII.0 by providing evaluation for ^{nat}Zn. Zinc has been a much neglected element. For reasons unknown to us, the US, European and Japanese nuclear data communities have ignored Zn in past, no evaluations have been performed, and we have continued that tradition.

H. Covariances

A covariance matrix specifies uncertainties and correlations for a collection of physical quantities such as cross sections or neutron multiplicities ($\bar{\nu}$, nubar). Covariances are required to correctly assess uncertainties of integral quantities such as design and operational parameters in nuclear technology applications. The error estimation of calculated quantities relies on the uncertainty information obtained from the analysis of experimental data and is stored as variance and covariance data in the basic nuclear data libraries such as ENDF/B-VII.0.

General properties of covariance matrices and early procedures for generating nuclear data covariances were widely discussed in the 1970's and 1980's (*e.g.*, see [193]). Accordingly, many of the presently existing covariance data were developed about 30 years ago for the ENDF/B-V library [194, 195]. This earlier activity languished during the 1990's due to limited interest by users, as well as constrained resources available to nuclear data evaluators to do the work.

More recently, intensive interest in the design of a new generation of nuclear power reactors, as well as in criticality safety and national security applications has stimulated a revival in the demand for covariances. This stems from the steadily growing need for nuclear data uncertainty information to be used in reactor core calculations (*e.g.*, estimation of uncertainty in $k_{\rm eff}$, criticality safety studies, in the adjustment of nuclear data libraries [196, 197]), in radiation shielding designs), and for various other applications, in order to assess safety, reliability, and cost effectiveness issues.

The recent revival resulted in a significant improvement in the methodology for the generation of covariance data, mostly as a consequence of the utilization of advanced nuclear modeling, and information merging techniques. The determination of reliable covariances is difficult and normally requires considerably more effort than the evaluation of the cross sections themselves. Furthermore, the generation of covariances cannot be decoupled from the core evaluation process itself. New covariance data have been produced for only a few elements because the resources needed to obtain this information have tended to lag behind the demand. However, our

TABLE XVII: List of covariance files (identified by MF and MT numbers) in the ENDF/B-VII.0 neutron sublibrary. Of 48 materials with covariances in ENDF/B-VI.8 only 13 were partly migrated to ENDF/B-VII.0, and 13 new materials were added. See Appendix A for MF and MT definitions [4], and Table XIX for explation of MF numbers.

Neutron sublibrary								
No	Material	Lab.	MF=31	MF=32	MF=33	MF=40	1^{st} author	Comment
1	^{6}Li	LANL			105		Hale	
2	^{7}Li	LANL			1, 2, 4, 25, 102, 104, 851		Young	MT=851 lumps MT=16,24,51-82
3	^{10}B	LANL			107, 800, 801		Hale	
4	^{19}F	CNDC+			4, 16, 22, 28		Zhao	
5	^{23}Na	ORNL		151			Larson	
6	^{48}Ti	KUR			1, 4, 16, 28, 102, 103,107		Kobayashi	
7	^{nat}V	ANL+			1		Smith	
8	^{59}Co	ANL+			1, 16, 103, 107		Smith	
9	^{58}Ni	LANL+			16		Chiba	
10	^{89}Y	BNL+			1, 2, 4, 16, 102, 103, 107		Rochman	New
11	^{93}Nb	LANL+			1	4	Chadwick	
12	^{99}Tc	BNL+			1, 2, 4, 16, 102, 103		Rochman	New
13	^{152}Gd	BNL+		151	1, 2, 4, 16, 102, 103, 107		Rochman	New
14	^{153}Gd	BNL+		151	1, 2, 4, 16, 102, 103, 107		Rochman	New
15	^{154}Gd	BNL+		151	1, 2, 4, 16, 102, 103, 107		Rochman	New
16	^{155}Gd	BNL+		151	1, 2, 4, 16, 102, 103, 107		Rochman	New
17	^{156}Gd	BNL+		151	1, 2, 4, 16, 102, 103, 107		Rochman	New
18	^{157}Gd	BNL+		151	1, 2, 4, 16, 102, 103, 107		Rochman	New
19	^{158}Gd	BNL+		151	1, 2, 4, 16, 102, 103, 107		Rochman	New
20	^{160}Gd	BNL+		151	1, 2, 4, 16, 102, 103, 107		Rochman	New
21	^{191}Ir	BNL+			1, 2, 4, 16, 102, 103		Rochman	New
22	^{193}Ir	BNL+			1, 2, 4, 16, 102, 103		Rochman	New
23	^{197}Au	LANL			1		Young	
24	^{209}Bi	LANL+			1		Chadwick	
25	^{232}Th	IAEA	452	151	1, 2, 5, 17, 18, 51, 102, 851-855		CRP	New, up to 60 MeV
26	^{235}U	LANL	452, 456				Young	
Total no. of MT files			3	10	124	1		

intention for ENDF/B-VII.0 was to provide covariance data for some test cases as a demonstration of the new methodologies we are developing, as a first step towards a future expanded covariance database.

Covariance data in ENDF/B-VII.0 can be found in three sublibraries. In the neutron reaction sublibrary, covariances are available for 26 materials listed in Table XVII. Table XVIII shows the neutron standards sublibrary with covariance files for 6 materials. Finally, in the decay data sublibrary, there is one material with the covariance data for emitted neutrons from the radioactive ^{252}Cf.

The covariance information included in the ENDF/B-VII.0 neutron sublibrary consists of selected files migrated from ENDF/B-VI.8 plus accepted new covariances that had been prepared after the release of ENDF/B-VI.8. These two categories are discussed below separately.

TABLE XVIII: List of covariance files (identified by MF and MT numbers) in the ENDF/B-VII.0 standards sublibrary.

Standards sublibrary					
No	Material	Lab.	MF=31	MF=33	1^{st} author
1	^{6}Li	IAEA		105	CRP
2	^{10}B	IAEA		107, 800, 801	CRP
3	^{nat}C	LANL+		2	Chadwick
4	^{197}Au	IAEA		102	CRP
5	^{235}U	IAEA	452, 456	18	CRP
6	^{238}U	IAEA		18	CRP
Total no. of MT files			2	8	

1. *Covariances from ENDF/B-VI.8*

Covariances for 48 materials with 755 covariance MT files can be found in the ENDF/B-VI.8 neutron sublibrary [198]. They are categorized by identifiers MF = 31, 32, 33, 34, 35 and 40, corresponding to the physi-

cal quantities as described in Table XIX. The numbers of files available in ENDF/B-VI.8 for each of these six categories are also shown in Table XIX.

TABLE XIX: Comparison of covariance MT files in the ENDF/B-VI.8 and ENDF/B-VII.0 neutron sublibraries.

Neutron sublibrary			
MF	Description of covariances	ENDF/B-VI.8 All (migrated)	ENDF/B-VII.0 All (new)
31	Nubar, $\bar{\nu}$	9 (2)	3 (1)
32	Resonance parameters	4 (1)	10 (9)
33	Cross sections	739 (31)	124 (93)
34	Angular distributions	-	-
35	Emitted particles*	-	-
40	Radioactive nuclei	2 (1)	1 (0)
Total no. of MT files		754 (35)	138 (103)

*) Covariance data for emitted neutrons from ^{252}Cf can be found in the decay data sublibrary.

The covariance files included in the ENDF/B-VII.0 consist of selected files migrated from ENDF/B-VI.8 and new evaluations prepared for ENDF/B-VII.0. Table XIX indicates the number of files from ENDF/B-VI.8 that were considered to be viable candidates for inclusion in ENDF/B-VII.0 following an initial review, along with the number of new files that were also treated as candidates. The ultimate decisions concerning which files to include in ENDF/B-VII.0 have been based on an assessment of the quality of this information. Our review of covariance information that led to the results given in Table XIX considered the following factors related to quality:

- methods used to generate the covariances,
- adequacy of uncertainty detail provided,
- availability and extent of correlation information provided, and
- appropriate and efficient use of allowed covariance formats [199].

Each of the files considered was examined explicitly, and information provided by the evaluators was assessed in arriving at decisions for inclusion or exclusion of specific files in the first-pass candidate list. It is evident that this screening process led to a dramatic reduction in the number of files that might qualify for inclusion in ENDF/B-VII.0 relative to the content of ENDF/B-VI.8. This would appear to be a step backwards, but the price of demanding improved quality of the covariances was a reduction in content.

Many of the covariance files in ENDF/B-VI.8 were based on rough, *ad hoc* estimates of uncertainty, often with no correlation information provided. Covariances ought to emerge as a consequence of objective evaluations based on statistical analysis of errors in experimental data, propagation of uncertainties in nuclear model parameters, and rigorous methods for combining the two. Most of the more recent evaluations follow this modern approach but many of the older ones did not.

A detailed list of the candidate files that survived the screening procedure is given in Table XVII, together with the new covariance data files. It was decided that even though many earlier covariance files would not be migrated to ENDF/B-VII.0, they could still be obtained, if desired, by referring to ENDF/B-VI.8 and thus would not be lost.

Following the screening process described above, the candidate covariance files that passed the first test were subjected to two further tests:

- to determine whether they could be processed as required for use in nuclear application codes, and
- to a visual inspection.

Both the ERRORJ code [14, 200] and the PUFF code [15] were available for this excercise. All the files listed in Table XVII from ENDF/B-VI.8 were adequately processed by PUFF, while several files failed with ERRORJ due to incomplete covariance information. Plots of uncertainty and correlation profiles were generated, inspected, and 35 MT files for 13 materials were ultimately accepted for inclusion in ENDF/B-VII.0, while the reamining were rejected.

2. New evaluation methodology

New covariance data in the ENDF/B-VII.0 neutron sublibrary were produced for 13 materials using the new evaluation techniques summarized in Table XX. Below we describe the three most frequently used methods, the remaining methods will only be outlined together with the respective evaluations.

TABLE XX: Summary of the new methods used for the ENDF/B-VII.0 covariance evaluations.

Energy region	Evaluation method	Material
Resolved resonances	Direct SAMMY*	^{232}Th
	Retroactive SAMMY	$^{152-158,160}$Gd
	Atlas-KALMAN	^{89}Y,^{99}Tc,^{191,193}Ir
Unresolved resonances	Experimental	^{232}Th
	Atlas-KALMAN	^{99}Tc, ^{193}Ir
	EMPIRE-KALMAN	$^{152-158,160}$Gd,^{89}Y,^{191}Ir
Fast neutrons	EMPIRE-KALMAN	$^{152-158,160}$Gd and ^{89}Y,^{99}Tc,^{191,193}Ir
	EMPIRE-GANDR	^{232}Th

*) See Section III.A.2 for description of this method.

Resonance region: Retroactive SAMMY. Covariance data in the resonance region produced via the computer code SAMMY [27] are based on the fitting of

data using the generalized least square formalism. During the evaluation process, uncertainties in the experimental data are incorporated into the evaluation process in order to properly determine the resonance-parameter covariance matrix (RPCM). Among these uncertainties are normalization, background, and uncertainty in the time-of-flight, uncertainty in the sample thickness, temperature uncertainty, and others.

For existing resonance parameter evaluations where no RPCM data are available, an alternative approach is to use retroactive resonance-parameter covariance generation. Even when performing a new evaluation, it is sometimes convenient to concentrate first on finding a set of resonance parameters that fit the data, and later focus on determining an appropriate associated RPCM. In practice, we have found that covariance matrices determined retroactively are quite similar to covariance matrices produced directly in the course of the evaluation. The retroactive scheme is described in the subsequent discussion.

First, artificial "experimental data" are generated using R-matrix theory with the already-determined values for the resonance parameters. Transmission, capture, fission, and other data types (corresponding to those used in the actual evaluation) are calculated, assuming realistic experimental conditions (Doppler temperature and resolution function).

Second, realistic statistical uncertainties are assigned to each data point, and realistic values are assumed for data-reduction parameters such as normalization and background. Let D represent the experimental data and $V$the covariance matrix for those data. Values for V (both on- and off-diagonal elements) are derived from the statistical uncertainties on the individual data points and from the uncertainties on the data-reduction parameters, in the usual fashion:

$$V_{ij} = \nu_i \delta_{ij} + \sum_k g_{ik} \Delta^2 r_k g_{jk} \qquad (37)$$

In this equation, $\Delta^2 r_k$ represents the uncertainty on the k^{th} data-reduction parameter r_k, and g_{ik} is the partial derivative of the cross section at energy E_i with respect to r_k. The data covariance matrix V_{ij} then describes all the known experimental uncertainties.

Third, the generalized least-squares equations are used to determine the set of resonance parameters P' and associated RPCM M' that fit these data. If P is the original set of resonance parameters (for which we wish to determine the covariance matrix), and T is the theoretical curve generated from those parameters, then, in matrix notation, the least-squares equations are

$$P' = P + M + G^t V^{-1}(D - T) \quad \text{and} \quad M' = (G^t V^{-1} G)^{-1} \qquad (38)$$

Here, G is the set of partial derivatives of the theoretical values T with respect to the resonance parameters P; G is sometimes called the sensitivity matrix.

The solutions of Eq.(38) provide the new parameter values P' and the associated resonance parameter covariance matrix M', fitting all of the artificial data simultaneously and using the full off-diagonal data covariance matrix for each data set.

If we were analyzing measured data, P' would be different from P. However, because we are analyzing artificially created data, P' is very nearly identical to P; this follows directly from Eq.(38) when $D = T$. The matrix M', which was derived as the covariance matrix associated with the updated parameters P', is therefore an appropriate representation for the resonance parameter covariance matrix associated with the original set of resonance parameters P.

Resonance region: Atlas-KALMAN. This new method was developed by the collaboration between BNL and LANL. The method combines the wealth of data given in the Atlas of Neutron Resonances of BNL with the filtering code KALMAN [200, 201] of LANL. The Atlas provides values and uncertainties for neutron resonance parameters and integral quantities (such as thermal capture cross section and capture resonance integral). The procedure is as follows:

- One starts with the resonance parameters as given in MF=2 file. In general, for new evaluations these are identical or very close to the parameters in the Atlas.
- Cross sections are calculated, in a suitable multigroup representation, for the thermal region and the resolved resonance region.
- Uncertainties of resonance parameters are propagated to cross sections with the code KALMAN, which provides cross section correlations and uncertainties. To reproduce uncertainties on thermal capture (or fission) cross section, resonance parameter uncertainties are appropriately adjusted.
- File MF=33 with cross section covariances is produced.

When fitting the thermal capture uncertainty, it is usually sufficient to adjust parameter uncertainties for the first resonance. In the case of a bound level (negative-energy resonance), as no parameter uncertainties are given in Ref. [30], the uncertainties are assigned to the resonance energy (E_0), neutron width (Γ_n), capture width (Γ_γ) and, if applicable, to the fission width (Γ_f). If there is no bound level, there are two possibilities: (i) keep the parameter uncertainties given in Ref. [30] and accept that calculated uncertainties on integral values might be different from the integral uncertainties given in Ref. [30], or (ii) adjust parameter uncertainties for the first resonance so that the calculated uncertainties for the integral values agree with those quoted in Ref. [30].

The resulting cross section uncertainties are based on a solid ground of experimental uncertainties on resonance

parameters as evaluated in the Atlas of Neutron Resonances.

Fast neutron region: EMPIRE-KALMAN. This methodology for generating cross section covariances in the fast neutron range was developed recently by the National Nuclear Data Center (BNL) in collaboration with the T-16 group (LANL). It employs a sensitivity matrix produced with the code EMPIRE (thus compatible with the actual evaluation), and uses it in the KALMAN code for determining covariances while taking into account relevant experimental data.

Use of the Kalman filtering approach to determine nuclear data covariances was originally developed for the JENDL-3.3 library by Kawano [200, 201]. The KALMAN code is an implementation of the Kalman filter for nuclear reaction calculations. It can be used for cross sections evaluations, assessment of model parameters, and also to determine cross section uncertainties and their correlations.

To obtain the sensitivity matrix with the EMPIRE code, about 10-15 of the most relevant model parameters (optical model, level density and preequilibrium strength) were varied independently, typically by $\pm$ 5 % around the optimal value, to determine their effect on total, elastic, inelastic, capture, (n,2n), (n,p) and (n,α) cross sections in the full energy range of the evaluation. Sensitivity matrix elements were calculated as a change of a given reaction cross sections in response to the change of a particular model parameter. A series of scripts was employed to transfer such sensitivity matrix information along with the experimental data to the KALMAN code, and to prepare adequate input.

Although the KALMAN code performs complete calculation involving all considered reaction channels simultaneously (and provides cross correlations among various reactions) we choose to treat each reaction separately. In order to do so, KALMAN was given experimental data for only a single reaction at a time and the self-correlation matrix and uncertainties for this reaction were further processed. Therefore, we deliberately disregard covariances among different reactions resulting from the constraint of model parameters imposed by the experimental data. Including such correlations will be done on future.

To preserve internal consistency, covariances for the elastic channel was coded as a difference between the total and the sum of all reaction channels. Final uncertainties were adjusted to reproduce error bars on the best measurements by preventing errors on model parameters (initially set at 10 %) from falling below reasonable limits (3 %). This procedure was necessary since the Kalman filter tends to reduce uncertainties on model parameters if many consistent experimental data are well reproduced by the model calculations. In doing so, the Kalman filter ignores approximations inherent in the nuclear reaction models and parameter adjustments introduced during the evaluation.

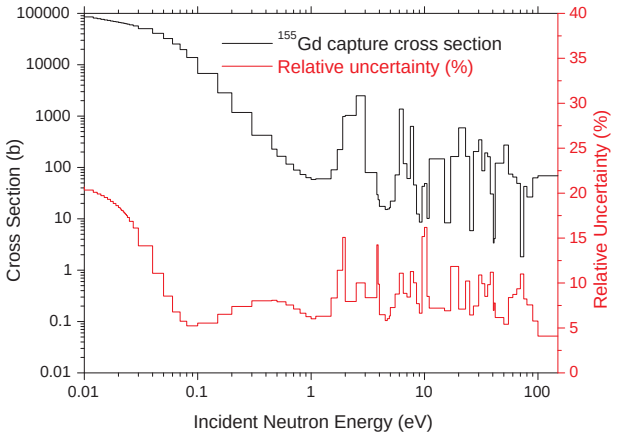

FIG. 60: Uncertainties of capture cross sections on ^{155}Gd obtained by the retroactive SAMMY method in ENDF/B-VII.0 compared with the ^{155}Gd(n,γ) cross section. The left scale is for the cross section (black curve) and the right scale is for the relative uncertainty (red curve).

3. New evaluations

Gd isotopes. There are 7 stable Gadolinium isotopes: ^{152}Gd, ^{154}Gd, ^{155}Gd, ^{156}Gd, ^{157}Gd, ^{158}Gd, and ^{160}Gd, with percentage natural abundances of 0.2, 2.18, 14.8, 20.47, 15.65, 24.84, and 21.86, respectively. In addition, there is the radioactive ^{153}Gd with a half-life of 240 days. All covariances were evaluated using the SAMMY retroactive method in the resolved resonance region, and the EMPIRE-KALMAN method for higher energies.

To generate resonance covariance data in the resolved resonance region, the multi-level Breit-Wigner (MLBW) resonance parameters produced at BNL for the basic ENDF/B-VII.0 library were used. Then, the retroactive methodology described above was used for generating the resonance parameter covariance matrix (RPCM), which was subsequently converted into the ENDF-6 format. During this process, the original multi-level Breit-Wigner representation for MF=2 was replaced by a Reich-Moore representation. In Fig. 60 uncertainties obtained with with the retroactive SAMMY method are presented for the capture cross section on ^{157}Gd.

The covariances for the unresolved resonance and fast neutron regions were produced with the EMPIRE-KALMAN method. The complete file with covariance data was processed with the ERRORJ code [200], developed to process ENDF uncertainty files into a multigroup structure usable in transport calculations.

In Fig. 61 we show relative uncertainties for ^{157}Gd(n,tot), ^{157}Gd(n,el) and ^{157}Gd(n,γ) cross sections for incident neutron energies above 1 keV resulting from the processing of the ENDF-6 formatted file with the ERRORJ code using 71 energy groups.

Fig. 62 shows the correlation matrix for the ^{157}Gd(n,γ) cross section. This correlation matrix reveals complicated structures with strong correlations aligned within a relatively narrow band along the diagonal. This comes from the inclusion of experimental data in the correlation calculation. Without experimental data, an essentially flat and a highly correlated shape is obtained in the model-based calculations. The positive long-range correlations, typical for model predictions, are annihilated or turned into anticorrelations, leaving only short- and medium-range positive correlations when the experimental data are factored in.

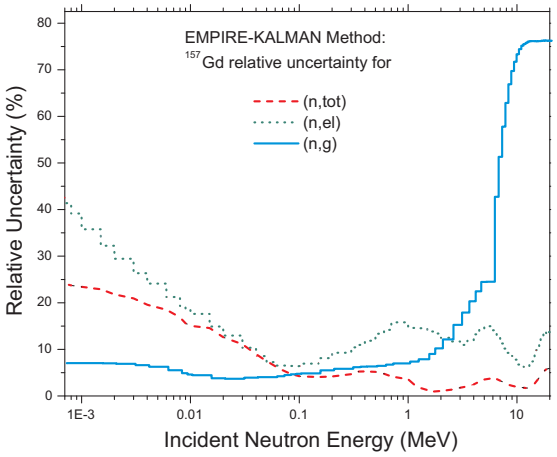

FIG. 61: Relative uncertainties for the total, elastic and capture cross sections on ^{157}Gd obtained with the EMPIRE-KALMAN method.

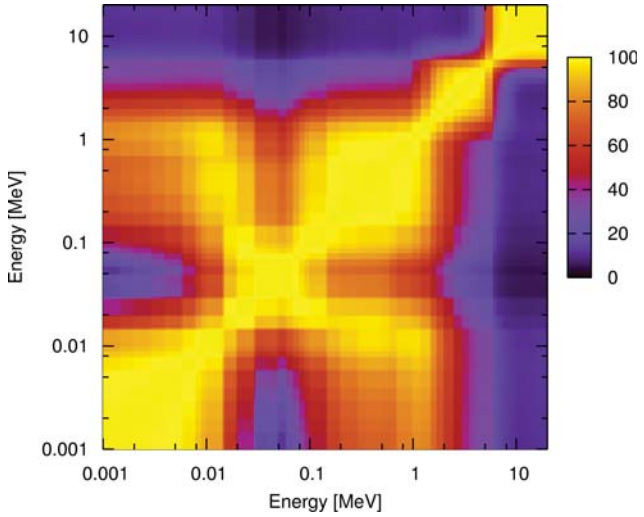

FIG. 62: Correlation matrix for the ^{157}Gd neutron capture cross sections in the fast neutron region obtained with the EMPIRE-KALMAN method.

^{232}Th. The covariance evaluation for ^{232}Th includes the resolved resonance, unresolved resonance, and the fast neutron regions as well as $\bar{\nu}$.

In the resolved resonance region, a Reich-Moore evaluation was performed [202] in the energy range from 0 to 4 keV using the code SAMMY. Because the fission cross section is negligible below 4 keV, each resonance of ^{232}Th in the Reich-Moore formalism is described by only three parameters: the resonance energy E_0, the gamma width Γ_γ, and the neutron width Γ_n. The original ENDF format available for representing the resolved parameter covariance matrix (RPCM) in the resolved resonance region is the LCOMP=1 format, in which the entire covariance matrix is listed. In a newer LCOMP=2 format, the RPCM is represented in a compact form, permitting reduction in the size of the covariance matrix at the expense of accuracy. For the case of ^{232}Th, the LCOMP = 1 format was used; the resulting MF=32 file contains more than 10,000 lines.

In the unresolved resonance region the exeprimental method was used [122]. The covariances were deduced from the covariance matrix of experimental data and the sensitivity matrix or the partial derivatives with respect to the adjusted parameters. The covariance matrix of the experimental data was constructed by supposing specific uncertainties on total total cross section (correlated 1.0%; uncorrelated resonance part 1.5% and non-resonance part 0.5%) and capture cross section (correlated 1.5%, uncorrelated 1.5%). The sensitivity matrix was deduced with the code RECENT around the final average resonance parameters used to construct MF=2. The resulting covariance matrix was created for MF=32. To this end, a very small relative uncertainty on the level distance was introduced, and it was supposed that the relative covariance elements for the reduced neutron widths can be approximated by the relative covariance elements of the neutron strength funstions.

Cross section covariance data in the fast neutron region were generated by the Monte Carlo technique [203] using the EMPIRE code. In the Monte Carlo approach a large collection of nuclear parameter sets (normally more than 1000) is generated by randomly varying these parameters with respect to chosen central values. These parameter sets are then used to calculate a corresponding large collection of nuclear model derived values for selected physical quantities, such as cross sections and angular distributions. These results are subjected to a statistical analysis to generate covariance information. The GANDR code system [204] updates these nuclear model covariance results by merging them with the uncertainty information for available experimental data using the generalized least-squares technique.

Most of the ^{232}Th fission cross section measurements were given as ratios to the ^{235}U values, and therefore the covariances were effectively determined for the ratios. To obtain the covariance matrix of the fission cross section, reference was made to the covariance matrix of the most recent evaluation of the cross section standards.

Covariances for $\bar{\nu}$ were obtained from the unpublished evaluation for the Russian library BROND-3 (this library

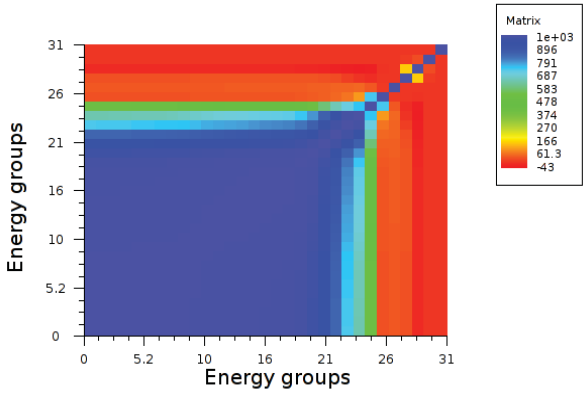

FIG. 63: Correlation matrix for ^{232}Th neutron capture cross sections in the thermal and resolved resonance region (up to 4 keV). Correlations are shown for 31 energy groups and are scaled by factor 10^3.

has not been released yet) performed by A. Ignatyuk, Obninsk. This evaluation was based on the analysis of experimental data.

The final ^{232}Th evaluation was processed using the SCALE code [8] into 44-group structure. The results of the processing codes ERRORJ and PUFF-IV [15] were cross-checked in the resolved-resonance region with results obtained from a similar calculation with SAMMY and no major differences were found. Thirty-one of the energy groups in the 44-group structure are in the energy range below 4 keV. The correlation matrix for the capture cross section is shown in Fig. 63.

^{89}Y, ^{99}Tc and ^{191,193}Ir. Covariance evaluations for these 4 isotopes were performed in the entire energy range using the BNL-LANL method.

In the thermal and the resolved resonance regions, the Atlas-KALMAN method was applied using the number of resonances given in Table XXI. As no resonance parameter uncertainties for the bound levels are given in the Atlas of Neutron Resonances for these 4 isotopes, these uncertainties were introduced to reproduce the uncertainty of the thermal capture cross sections. As for the regular resonance parameters, three parameters (E_0, Γ_n, Γ_γ) plus the scattering radius R' were allowed to vary for each of the resonances. In Fig. 64 uncertainties obtained with the Atlas-KALMAN method are shown for the capture cross section on ^{99}Tc.

In the unresolved resonance region, two approaches were adopted. For materials with the MF=2 unresolved resonance data available (^{99}Tc, ^{193}Ir), the Atlas-KALMAN method was used. To this end, three free parameters were considered: (i) scattering radius R', (ii) the average radiative width, and (iii) the s-wave average level spacing. For materials with no MF=2 unresolved resonance data available (^{89}Y, ^{191}Ir), the

TABLE XXI: Summary of resolved resonances for 4 isotopes used to calculate low-energy covariances with the Atlas-KALMAN method. Bound resonance levels were available for 4 and unresolved resonances for 2 isotopes.

Isotope	Number of resonances	Upper resonance energy	Bound level	Unresolved region in ENDF/B-VII.0
^{99}Tc	538	6.366 keV	Yes	Yes
^{89}Y	401	408.9 keV	Yes	No
^{191}Ir	46	151.8 eV	Yes	No
^{193}Ir	40	309.0 eV	Yes	Yes

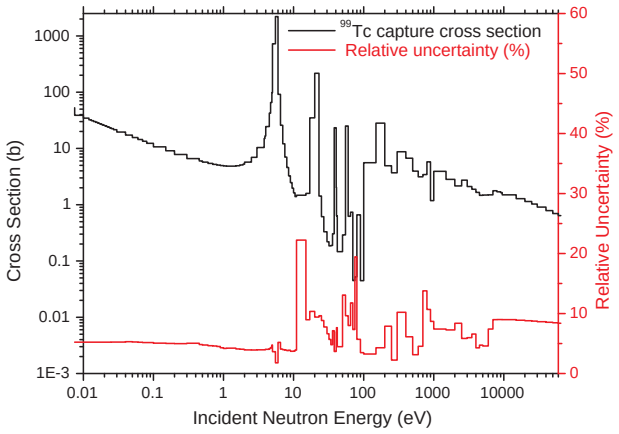

FIG. 64: Uncertainties of capture cross sections on ^{99}Tc obtained by the Atlas-KALMAN method in ENDF/B-VII.0 compared with the ^{99}Tc(n,γ) cross section. The left scale is for the cross section (black curve) and the right scale is for the relative uncertainty (red curve).

EMPIRE-KALMAN method, extended down to the unresolved resonance region, was employed.

In the fast neutron region, the EMPIRE-KALMAN methodology was used. First, a complete evaluation of all main reaction channels was performed with the EMPIRE code. Then, the sensitivity matrices were produced by varying model parameters around optimal values used in the evaluation. A total of 20 parameters were considered including real and imaginary surface depth of the optical potential for the compound nuclei, particle- and γ-emission widths, level densities, and mean free path in the exciton model. Finally, selected experimental data along with the sensitivity matrices were used as input for the KALMAN code. Fig. 65 shows our results for the uncertainties of total, (n,2n) and capture cross sections on ^{193}Ir. While the uncertainties on (n,2n) fall below 10% near 14 MeV (where many measurements exist), the uncertainties become much larger at lower energies near the (n,2n) threshold. Likewise, the (n,γ) cross section uncer-

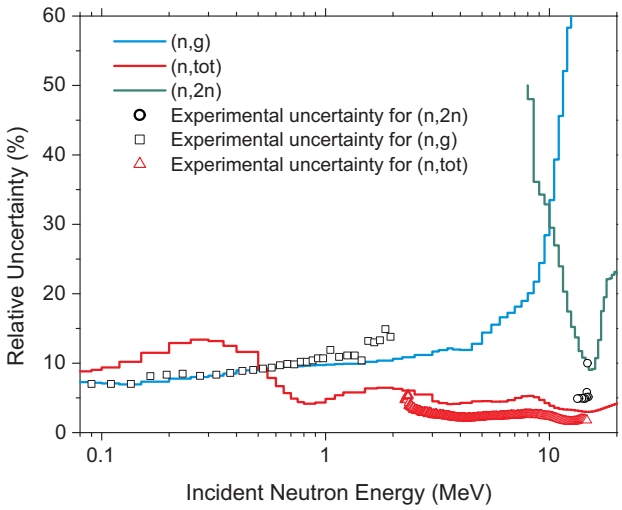

FIG. 65: Relative uncertainties on ^{193}Ir for the neutron total, (n,2n) and capture cross sections obtained with the EMPIRE-KALMAN method. The experimental uncertainties considered in the analysis are also included.

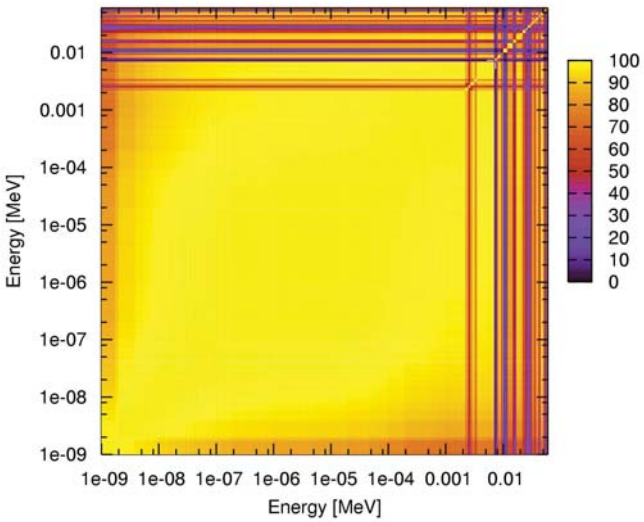

FIG. 66: Correlation matrix for the total neutron cross sections on ^{89}Y in the thermal and resolved resonance region (below 400 keV).

tainty becomes large above a few MeV where data are sparse, and where the cross section is very small.

Fig. 66 shows the calculated correlation matrix for the total cross section on ^{89}Y. In this case the long range correlations are mostly due to the scattering radius R' (yellow color in Fig. 66). The first positive resonance is at 2.6 keV, which means that up to this energy the cross section is fully correlated with the bound level. Then, the contribution from other resonances becomes noticeable. In the case of capture, this pattern is retained but the scattering radius R' has no effect.

^{233,235,238}U and ^{239}Pu. There was insufficient time to complete new covariance evaluation for these important actinides prior to the release of the ENDF/B-VII.0 library. The covariance evaluation work is underway, and will be available in future ENDF/B-VII releases. Furthermore, preliminary partial evaluations will be available in the recently reestablished ENDF/A library.

IV. THERMAL NEUTRON SCATTERING SUBLIBRARY

This sublibrary contains 20 evaluations out of which 7 were reevaluated or updated due to the combined efforts of MacFarlane, Los Alamos, and by Mattes and Keinert, IKE Stuttgart [6]. The remaining evaluations were taken over from ENDF/B-VI.8. Below, we briefly describe only seven new/revised evaluations.

A. Methodology

New thermal neutron scattering evaluations were generated at the Los Alamos National Laboratory using the LEAPR module of the NJOY code [205]. The physical model has been improved over the one used at General Atomics in 1969 to produce the original ENDF/B-III evaluations [206]. The alpha and beta grids have been extended to allow for larger incident energies and to properly represent the features of $S(\alpha,\beta)$ for the various integrations required. The physical constants have been updated for ENDF/B-VII.0 to match the current hydrogen and oxygen evaluations. The LANL changes include some additional alpha and beta points, interpolating the rotational energy distributions and translational masses onto the new temperature grid, and slightly reducing the rotational energies to improve the energy region between 0.01 and 0.1 eV.

B. Evaluations

1. *H_2O and D_2O*

H_2O. This evaluation was generated by Mattes and Keinert in 2004 using the LEAPR module of the NJOY Nuclear Data Processing System and modified at LANL in 2006 to use a temperature grid more like the other ENDF evaluations and to fit the experimental data slightly better.

Water is represented by freely moving H_2O molecule clusters with some temperature dependence to the clustering effect. Each molecule can undergo torsional harmonic oscillations (hindered rotations) with a broad spectrum of distributed modes. The excitation spectra were improved over the older ENDF model, and they are given

with a temperature variation. In addition, there are two internal modes of vibration at 205 and 436 meV. The stretching mode was reduced from the older ENDF value of 480 meV to account for the liquid state. Scattering by the oxygen atoms is not included in the tabulated scattering law data. It should be taken into account by adding the scattering for free oxygen of mass 16.

Note that the new H_2O thermal scattering kernel in ENDF/B-VII.0 led to a slight increase in calculated criticality of LEU-COMP-THERM critical assemblies, as discussed in Section X.B.4.

D_2O. This was based on the IKE-IAEA-JEFF-3.1 evaluation done by Mattes and Keinert in 2004. Changes made for ENDF/B-VII include using a more ENDF-like temperature grid and an extension of the α and β grids to improve results for higher incident energies.

2. O in UO_2 and U in UO_2

Uranium dioxide has a structure similar to flourite, CaF_2. A lattice dynamical model was developed by Dolling, Cowley, and Woods to fit dispersion curve measurements. In additional to short-range core-core forces, the model includes shell-core, shell-shell, and long-range Coulomb interactions. Weighted frequency distributions were calculated from a dynamical matrix based on this model. The O in UO_2 part is kept separate from the U in O_2 part, and one-fourth of the coherent elastic cross section from the original General Atomics evaluation is included here. The various constants were updated to agree with the ENDF/B-VII.0 evaluation of oxygen.

3. H in ZrH

The lattice dynamics of ZrH were computed from a central force model. The slightly tetragonal lattice of ZrH_2 was approximated by a face-centered-cubic lattice. Four force constants (μ, γ, ν, and δ) were introduced describing respectively the interaction of a zirconium atom with its nearest neighbors (8 H atoms) and its next nearest neighbors (12 Zr atoms), and the interaction of a hydrogen atom with its next nearest neighbors (6 H atoms) and its third nearest atoms (12 H atoms). Eigenvalues and eigenvectors of the dynamical matrix were calculated, and a phonon frequency spectrum was obtained by means of a root sampling technique. Weighted frequency spectra for hydrogen in ZrH were then obtained by appropriate use of the dynamical matrix eigenvectors.

The final values of the four force constants were obtained by fitting both specific heat and neutron data. The position of an optical peak observed by neutron scattering techniques to be centered roughly around 0.14 eV determines the constant μ, while the overall width and shape of this peak determine ν and δ, respectively. Existing neutron data are not sufficiently precise to confirm the structure predicted in the optical peak by the central force model. Specific heat data were used to determine the force constant γ, which primarily determines the upper limit on the phonon energies associated with acoustic modes.

4. Other modified materials

Liquid methane at 100^{o}K used the model of Agrawal and Yip as implemented by Picton, modified to include a diffusive component.

Solid methane at 22^{o}K used the model of Picton based on the spectrum of Harker and Brugger.

Liquid para and ortho hydrogen at 20^{o}K were computed with LEAPR. The scattering law is based on the model of Keinert and Sax [207], which includes spin correlations from the Young and Koppel [208] model, diffusion and local hindered motions from an effective translational scattering law based on a frequency distribution, and intermolecular coherence after Vineyard [209].

Data for aluminum are provided for temperatures of 20, 80, 293.6, 400, 600 and 800^{o}K using frequency distribution of Stedman, Almqvist, and Nilsson [210].

^{56}Fe is modeled using iron frequency distribution of Brockhouse, Abou-Helal, and Hallman [211]. The full bound coherent cross section for ^{56}Fe is used without any allowance for isotopic incoherence. The data are given at 20, 80, 293.6, 400, 600 and 800^{o}K.

V. NEUTRON CROSS SECTION STANDARDS SUBLIBRARY

Below, we briefly describe this important new sublibrary. A complete description of new standards evaluations can be found in the IAEA technical report [7].

A. Overview

The standards are the basis for the neutron reaction cross section libraries since neutron evaluations are based on measurements made relative to the standard values that are known more precisely than other cross sections. Significant improvements have been made in the standard cross section database since the last complete evaluation of the neutron cross section standards, almost 20 years ago. Modifications (new releases) are not allowed for the standards so the original standards for ENDF/B-VI have not been changed during that entire time.

The standards were evaluated for ENDF/B-VII.0 using new experimental data in addition to the previous experimental database that was used for the ENDF/B-VI standards valuation, and using improved evaluation techniques. In addition to a CSEWG Task Force, the NEA WPEC formed a Subgroup and the IAEA formed a Co-

ordinated Research Project (CRP), all of which worked cooperatively to improve the evaluation process.

The IAEA CRP provided the largest contribution to the evaluation. The main objectives of the evaluation were: To improve the covariance matrices used in the evaluations; study the reasons for uncertainty reduction in R-matrix and model independent fits; and establish a method for combining the R-matrix and model independent evaluations used to obtain the final evaluations of the neutron cross section standards. To realize these objectives, the following tasks were undertaken: Improvements to the experimental data in the standards database and methods for handling discrepant data; an R-matrix evaluation of the hydrogen scattering cross section and conversion of measurements relative to the hydrogen cross section to the new standard; studies of Peelle's Pertinent Puzzle (PPP) and its effect on the standards; evaluation work on microscopic calculations leading to independent determinations of R-matrix scattering poles; studies of the small uncertainties that result from some evaluations; investigation of smoothing procedures; and finally the end result, the ENDF/B-VII.0 standards.

The ^{238}U(n,f) cross section, which is a NEA-NDC/INDC standard, was accepted as a new standard for ENDF/B-VII.0. However 2 MeV was recommended as the lower bound for use of this cross section as a standard. The use of this cross section from threshold to 2 MeV as a standard is discouraged due to the very rapid change of this cross section in that energy range and the very small cross section in the threshold energy region. Table XXII shows the list of standards and energy their ranges. Extended energy ranges compared with the ENDF/B-VI results were obtained for the cross sections for H(n,n), ^{10}B(n,α), ^{10}B(n,$\alpha_1\gamma$), ^{235}U(n,f) and ^{238}U(n,f).

TABLE XXII: List of neutron cross section standards.

Reaction	Energy Range
H(n,n)	1 keV to 200 MeV
^{3}He(n,p)	0.0253 eV to 50 keV
^{6}Li(n,t)	0.0253 eV to 1 MeV
^{10}B(n,α)	0.0253 eV to 1 MeV
^{10}B(n,$\alpha_1\gamma$)	0.0253 eV to 1 MeV
C(n,n)	0.0253 eV to 1.8 MeV
Au(n,γ)	0.0253 eV, 0.2 MeV to 2.5 MeV
^{235}U(n,f)	0.0253 eV, 0.15 to 200 MeV
^{238}U(n,f)	2 MeV to 200 MeV

B. Database studies

A large database of measurements, a significant portion of which were assembled by Poenitz [212] for the ENDF/B-VI standards evaluation, was used for the present evaluation. In addition, the data sets introduced after the ENDF/B-VI evaluation and before the initiation of this evaluation were included in the database. More than 30 data sets were added to the standards database since the initiation of the present evaluation effort. Many of the experiments were done in response to suggestions from those working on this evaluation.

The status of the standards database [213] has been discussed recently. Recent improvements were obtained for the thermal constants used in the evaluation. This was largely due to an improved analysis of the Gwin [214] nubar ($\bar{\nu}$) uncertainties and the very accurate coherent scattering measurements for ^{235}U obtained by Arif [215] that were used to provide a more accurate scattering cross section.

The database also included data involving the ^{238}U(n,γ) and ^{239}Pu(n,f) cross sections that improved the database as a result of ratio measurements of those cross sections to the traditional standards. Also scattering and total cross section data were included for ^{6}Li and ^{10}B since they provide information on the standard cross sections.

Discrepancies in experimental data sets were handled by adding a medium energy range correlation component. This component was added if the difference from the evaluation was more than two sigma for a single point or more than one sigma for two or more consecutive energy points. This results in a much better chi square per degree of freedom and larger uncertainty in the evaluated results. The change in the cross section resulting from this procedure is small.

It is useful to summarize the thermal constants in the standards reaction sublibrary and compare them with the values for the same reactions given in the neutron reaction sublibrary. This is done in Table XXIII. One can see that there are differences between the two sublibraries, though these are generally very small and within ≈ 0.5 standard deviation.

C. Evaluation details

1. *Hydrogen scattering*

Many of the data in the standards database were measurements relative to the hydrogen scattering cross section. To obtain improved cross sections from these data, the hydrogen scattering cross section was evaluated using the R-matrix code EDA [28]. Calculations of the angular distribution using these R-matrix parameters are in much better agreement with recent measurements [216] than the old ENDF/B-VI evaluation, see Section III.F.

All the data in the database relative to hydrogen cross sections were converted so they are relative to the new standard. The database contained measurements relative to several different versions of total cross sections. Also a number of experiments were in the database that used different laboratory angles, and different versions

TABLE XXIII: Thermal (0.0253 eV) constants obtained from the standards evaluation, g_f and g_{abs} being the Westcott factors. The only item shown in this table that is considered a standard is the thermal ^{235}U(n,f) cross section. Given in brackets are values taken from the neutron sublibrary. The ENDF/B-VII.0 standards nubar for ^{252}Cf is $\bar{\nu}_{tot}$ = 3.76921075 ± 0.12469%, comprised of $\bar{\nu}_p$=3.7606 and $\bar{\nu}_d$=0.0086. In ENDF/B-VI.8, $\bar{\nu}_{tot}$ was 3.7676, comprised of $\bar{\nu}_p$=3.759 and $\bar{\nu}_d$=0.0086.

Quantity	^{233}U	^{235}U	^{239}Pu	^{241}Pu
σ_{nf}(b)	531.22± 0.25% (531.22)	584.33± 0.17% (585.09)	750.00± 0.24% (747.40)	1013.96± 0.65% (1011.85)
$\sigma_{n\gamma}$(b)	45.56± 1.50% (45.24)	99.40± 0.72% (98.69)	271.50± 0.79% (270.33)	361.79± 1.37% (363.05)
σ_{nn}(b)	12.11± 5.48% (12.15)	14.087± 1.56% (15.08)	7.800±12.30% (7.975)	12.13± 21.50% (11.24)
g_f	0.9956±0.14% (0.9966)	0.9773± 0.08% (0.9764)	1.0554±0.20% (1.0542)	1.0454± 0.53% (1.046)
g_{abs}	0.9996±0.11% (0.9994)	0.9788± 0.08% (0.9785)	1.0780±0.22% (1.0782)	1.0440± 0.19% (1.042)
$\bar{\nu}$	2.497 ±0.14% (2.504)	2.4355± 0.09% (2.4367)	2.8836±0.16% (2.8789)	2.9479± 0.18% (2.9453)

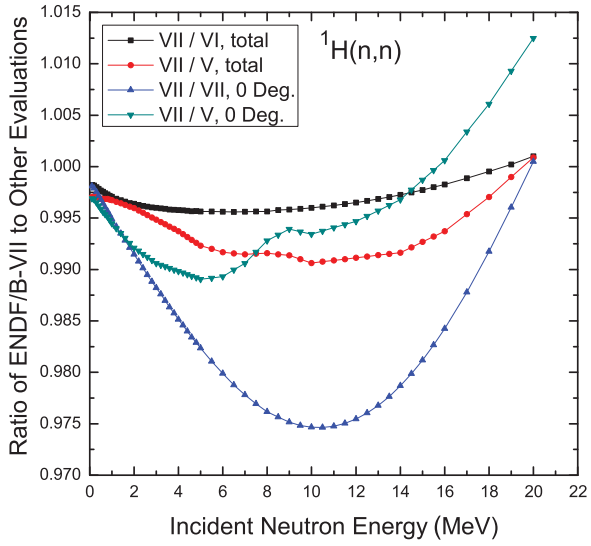

FIG. 67: The ENDF/B-VII.0 H(n,n) evaluation compared with the ENDF/B-VI and ENDF/B-V evaluations. The zero degree results are ratios of the center-of-mass-system cross sections at 180 degrees (which corresponds to zero degree protons in the laboratory system).

of the differential cross section. Careful clarification of this point was important since mismatch in laboratory and centre-of-mass values had a non-negligible impact on evaluations. The effect of the change in the hydrogen standard cross section caused, for example, a change as large as 0.5% for the evaluated ^{235}U(n,f) cross section.

2. *Peelle's pertinent puzzle (PPP)*

Problems associated with PPP were observed early in the evaluation process [217]. A test run using a model-independent least squares code fitting the logarithm of the cross section produced higher cross sections than a run fitting the cross section. There were discrepant data in the test run. The problem appears to be the result of using discrepant data (denoted as the mini-PPP effect) but its influence is strongly magnified by the existence of data correlations. This is the so-called maxi-PPP effect vs mini-PPP effect.

The GMA code, which was used as the model independent least squares code for the ENDF/B-VI standards evaluation, was modified by adding the Chiba-Smith [218] option to handle PPP problems. This option, called GMAP [219] renormalizes the experimental absolute errors on the assumption that it is the fractional error that actually reflects the accuracy the experimenter has provided. This approach appears to reduce the effect of PPP significantly. Comparisons using the Chiba-Smith and logarithmic transformation methods for handling PPP are in good agreement for a number of test cases. The experience obtained from the standards evaluation indicates that to improve the quality of nuclear data evaluations in general, special care should be exercised to minimize the PPP effect.

3. *Verification of evaluated results*

Concerns had been expressed about the small uncertainties obtained for the standards in the ENDF/B-VI evaluation [220]. Work has been done on the small uncertainty problem and comparisons of cross section results through comparisons of several tests of model-independent and R-matrix codes using common databases. The R-matrix codes used in the present study were EDA [28], SAMMY [27], and RAC [221]. The

generalized least squares codes used were GLUCS [222], GMAP, and SOK [223]. A code based on an analytical approximation model, PADE2 [224] was also used.

For the verification tests, it was assumed that no correlations existed between the data sets. The only correlations within the data sets were assumed to be short energy range (statistical) and long energy range (normalization). The generalized least squares codes were easily shown to be in good agreement. Work with these codes led to the discovery of an error in the GMA code used for the ENDF/B-VI standards evaluation that caused a small effect on those standard cross sections results. Comparisons of the R-matrix codes proved to be more difficult since the input conditions were difficult to standardize. Additional work with these codes led to acceptable agreement between the codes especially if the differences in approach and numerical precision differences were considered. Important conclusions from the present work were that proper consideration of correlations within and between data sets is required to obtain more realistic uncertainties and that it is essential to consider the covariances, not just the variances, in applications of cross sections to practical systems.

D. Evaluation procedure

A combination procedure somewhat similar to that used for the ENDF/B-VI standards evaluation was used to obtain the standards. In the case of ENDF/B-VII.0 the code GMAP [219] was used for the combining process described below rather than a specialized merging code as was the case for ENDF/B-VI. All the standards except the H(n,n), ^{3}He(n,p) and C(n,n) cross sections were evaluated using the GMAP code with input from the RAC and EDA R-matrix analyses and a thermal constants evaluation.

For the thermal constants evaluation, the Axton evaluation [225] with the associated variance-covariance data for ^{233}U, ^{235}U, ^{239}Pu and ^{241}Pu was used as input to the GMAP code since it includes accurate cross sections which have been measured relative to the neutron cross section standards. Thus this evaluation had an impact on the determination of the standards.

The R-matrix analyses used charged-particle data and the entire lithium and boron neutron databases, including total and scattering cross section data for these nuclides. The only lithium and boron data used in the GMAP code were the ratio measurements to standards. Thus the R-matrix and GMAP data sets were independent (no common or correlated data sets). For both the ^{6}Li(n,t) and boron work, the cross sections obtained from the RAC and EDA R-matrix analyses were not identical. For the ^{6}Li(n,t) cross section the two analyses agreed within 2% at all energies. The agreement was not as good for the ^{10}B(n,$\alpha_1\gamma$) and ^{10}B(n,α) cross sections where there were differences as large as several percent in some energy regions. In each case the RAC and EDA analyses were averaged (unweighted) and the result was used as the R-matrix input to GMAP.

The covariance matrix used with these central values was that from the RAC code since its results appeared more physically reasonable. The R-matrix input and thermal constants data were treated like the additions of other data sets to the GMAP code. At each energy point, half the difference between the RAC and GMAP results was treated as a model uncertainty that was added quadratically to the RAC covariance of uncertainties. This then takes into account the small differences between the RAC and EDA analyses.

The results obtained from the combination procedure were not smooth in some cases. For the ^{6}Li(n,t), ^{10}B(n,$\alpha_1\gamma$), and ^{10}B(n,α) cross section smoothing was not required due to the large weight given to the cross sections from the R- matrix analyses. For the heavy element standards, it was determined that a simple smoothing algorithm was satisfactory, which was used sparingly. A patch using the shape of the Maslov [226] evaluated curve was applied in the 50-60 MeV region for the ^{235}U(n,f) cross section where a rather large fluctuation, assumed to be statistical, occurred.

E. Results of the evaluation

Representative results from the evaluations for the H(n,n), ^{6}Li(n,t), ^{10}B(n,$\alpha_1\gamma$), ^{10}B(n,α), Au(n,γ), ^{235}U(n,f), and ^{238}U(n,f) standard cross sections are shown in Figs. 67-73. All uncertainties shown are one standard deviation values. These uncertainties are generally somewhat larger than those obtained in the ENDF/B-VI standards evaluation. The C(n,n) standard cross section was carried over from the ENDF/B-VI evaluation since very little new data have been obtained subsequent to that evaluation; what were obtained were in good agreement. The ^{3}He(n,p) standard was not re-evaluated. It was also carried over from ENDF/B-VI. Cross sections for the ^{238}U(n,γ) and ^{239}Pu(n,f) reactions were also obtained from this evaluation, see Figs. 27 and 30.

Some benchmark data testing has been done using these data. K1, the Gwin thermal reactivity parameter[3] calculated from the evaluation is 721.6 b. This should be compared with the "preferred" value of 722.7 ± 3.9 b determined by Hardy [227]. The agreement is quite good when one considers that the uncertainty in the Hardy value is 3.9 b. Criticality calculations using these data are generally in better agreement than those obtained with the ENDF/B-VI standards, as discussed in Section X.

[3] The Gwin thermal reactivity parameter is defined as K1 = $\bar{\nu}$ g_f σ_f - g_{abs} σ_{abs}, where fission and absorption cross sections are given at the thermal energy, and g_f and g_{abs} are Westcott factors for fission and absorption, respectively.

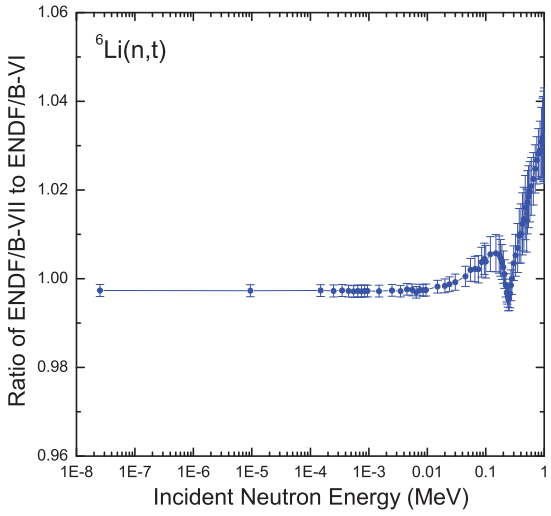

FIG. 68: The ENDF/B-VII.0 ^{6}Li(n,t) evaluation compared with the ENDF/B-VI evaluation. The curve connects the central values of VII.0 to VI.8 ratios.

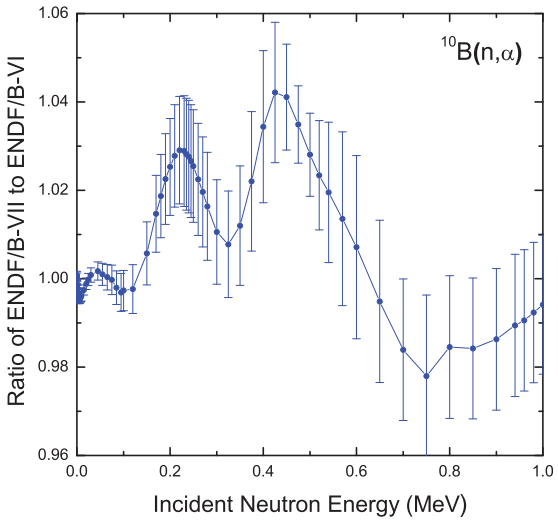

FIG. 70: The ENDF/B-VII.0 ^{10}B(n,α) evaluation compared with the ENDF/B-VI evaluation. The curve connects the central values of VII.0 to VI.8 ratios.

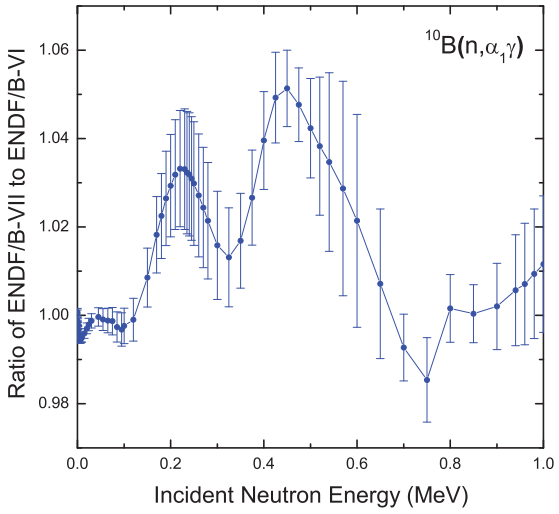

FIG. 69: The ENDF/B-VII.0 ^{10}B(n,$\alpha_1\gamma$) evaluation compared with the ENDF/B-VI evaluation. The curve connects the central values of VII.0 to VI.8 ratios.

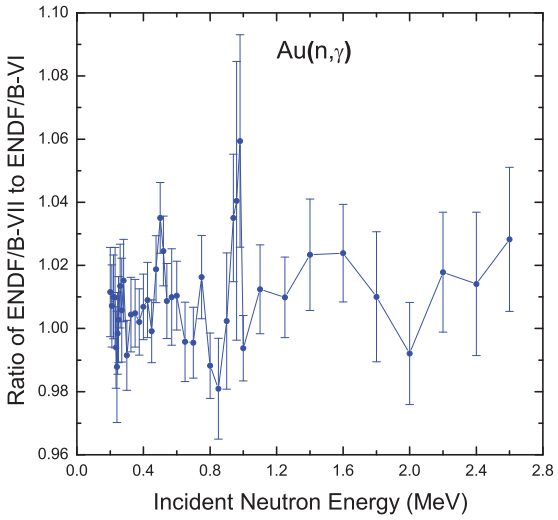

FIG. 71: The ENDF/B-VII.0 Au(n,γ) evaluation compared with the ENDF/B-VI evaluation. The curve connects the central values of VII.0 to VI.8 ratios.

Table XXIII shows the thermal constants obtained from this evaluation - but note that the only item considered a standard there is ^{235}U(n,f) - see also Table XXII. The small differences shown in this table between the standards work and the values used in the neutron transport files (neutron sublibrary) are because ENDF evaluators have been given the freedom to make small changes, typically within the experimental uncertainty.

VI. PHOTONUCLEAR REACTION SUBLIBRARY

The photonuclear evaluated data files described here represent the first time that such data are available in the official evaluated ENDF/B library, including representations of the secondary energy and angle spectra, suitable for use in radiation transport calculations. Prior to

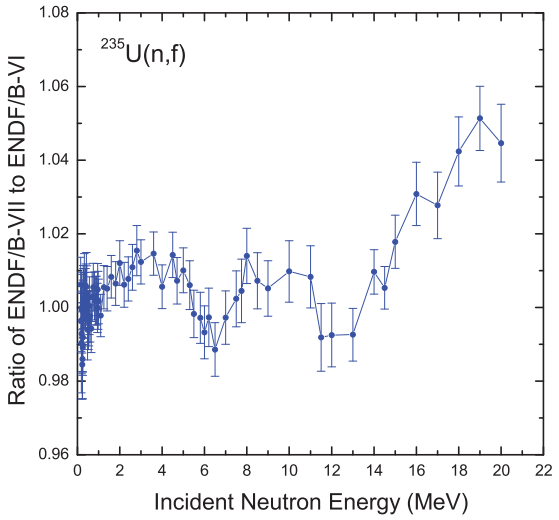

FIG. 72: The ENDF/B-VII.0 ^{235}U(n,f) evaluation compared with the ENDF/B-VI evaluation for the common energy region. The present evaluation extends to 200 MeV, however comparisons cannot be made to the ENDF/B-VI evaluation since that evaluation only extends to 20 MeV. The curve connects the central values of VII.0 to VI.8 ratios.

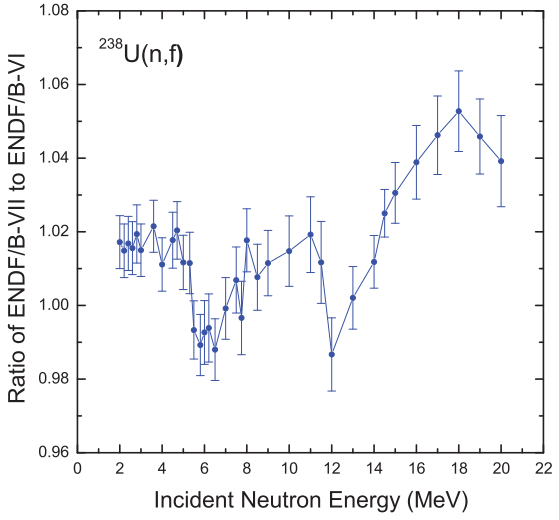

FIG. 73: The ENDF/B-VII.0 ^{238}U(n,f) evaluation compared with the ENDF/B-VI evaluation for the common energy region. The present evaluation extends to 200 MeV, however comparisons cannot be made to the ENDF/B-VI evaluations since that evaluation only extends to 20 MeV. The curve connects the central values of VII.0 to VI.8 ratios.

this, many of these data have been made available informally from LANL and the IAEA following a collaborative IAEA Coordinated Research Project [5].

A. Evaluations

The cross sections and spectra have been evaluated through use of both measured data, and nuclear model calculations. The use of nuclear reaction theory, in particular, facilitates the evaluation of the energy-spectra of the ejectiles (since there are only a limited number of measurements for monoenergetic incident photons). This distinguishes the present work from some previous photonuclear data evaluations and compilations [228–230], which focused on cross sections but not ejectile spectra. The evaluation procedure also had to assess the most probable value of a cross section where discrepant measurements exist. While such considerations play a role in all nuclear data evaluation activities, the situation is particularly difficult for photonuclear data, since some of the most extensive experimental programs (for instance at Livermore and Saclay) have systematical differences in the magnitudes of reported cross sections [231, 232]. This is, in part, due to the different experimental methods used to produce photon radiation, which include positron annihilation, bremsstrahlung tagged-photons, bremsstrahlung, and electron-induced reactions.

Photonuclear data evaluations have been completed for 163 isotopes. The materials studied are those that are important for applications. For example, simulations of dose in external beam photon and electron cancer therapy requires photonuclear cross sections for accelerator and beam collimator structures (*e.g.*, Al, Fe, Co, Cr, Ni, Cu, Pb), for bremsstrahlung conversion targets (*e.g.*, Ta, W, Be), and for human tissue materials (*e.g.*, C, N, O, P, Ca). Similarly, simulations supporting nonproliferation technologies that aim to detect special nuclear materials (SNM) require photonuclear (including photofission) cross sections on actinide isotopes.

Detection of chemical explosives can be accomplished through resonant absorption of photons on nitrogen. To this end, the ^{14}N evaluation was extended by BNL and LANL to include the resonance region around 9.172 MeV [233]. For this particular case, photonuclear resonance parameters were deduced from Ajzenberg-Selove [234].

Most of our photonuclear evaluations extend up to 140-150 MeV energy, the pion threshold, although a few extend just to 20-30 MeV. This upper energy is sufficiently high for calculations of photonuclear reactions in most medical electron accelerators that typically operate with maximum energies in the 10-25 MeV region. The data are complete in terms of their coverage of incident and outgoing energies and angles, and include information not only on the photoneutron cross sections, but also information describing all possible light and heavy ejectiles including nuclear recoils. This allows their use in studies of radiation transport, energy deposition (absorbed

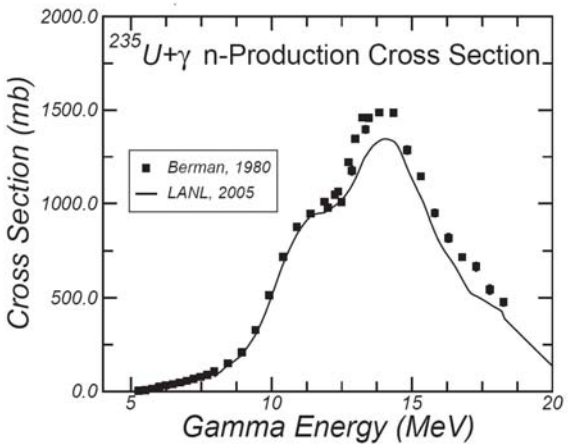

FIG. 74: Neutron production cross sections for photons incident on ^{235}U. The LANL evaluation, adopted for ENDF/B-VII.0, is compared with the experimental data. The reason that the evaluation is discrepant with the Berman data above 12 MeV, is that the evaluated photoabsorption cross section was taken from the Varlamov evaluation.

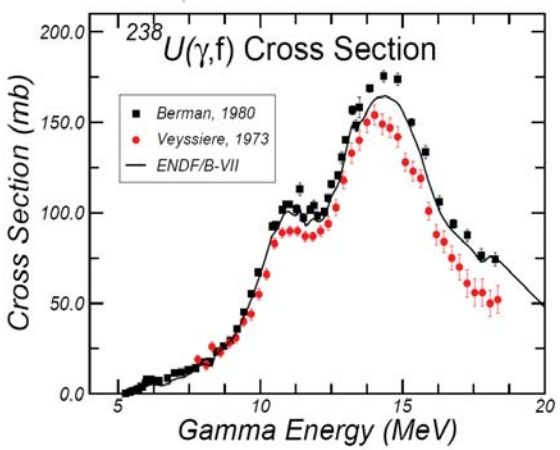

FIG. 75: Fission cross sections for photons incident on ^{238}U. The ENDF/B-VII.0 evaluation is compared with the available experimental data.

dose), relative biological effectiveness (RBE), activation, and shielding.

The data included in ENDF/B-VII.0 are based upon those produced recently by an IAEA Coordinated Research Project (CRP), led by Chadwick and Obložinský from the US CSEWG project. The ENDF data evaluations were developed at the laboratories participating in this project (Los Alamos, Brookhaven, Sao Paulo, Obninsk, Moscow, JAERI, KAERI, Beijing, Vienna) and are also available from the IAEA. A technical report that describes these data in detail, including figures for all 164 isotopes (ENDF/B-VII.0 contains 163 materials) comparing the evaluated data with measurements, is available [5]. Journal articles detailing the photonuclear evaluations from Los Alamos have also been published [235–237].

Because these photonuclear evaluations have been documented in detail (with extensive comparisons against the measured data) [5, 235–237], we do not repeat these comparison figures here. However, we do describe a recent development for the actinide photonuclear data, motivated by needs in the nonproliferation community.

In the IAEA Coordinated Research Project, the original actinide cross section evaluations came from Obninsk, Russia. Because these evaluations did not include delayed neutron information from photofission, delayed neutron data were added to the Obninsk evaluations by Los Alamos. This is particularly important, since certain active interrogation schemes for detecting SNM involve pulsing a cargo container, for instance, with bremsstrahlung photons and measuring delayed neutron emission signals that point to fission, and therefore the presence of actinides.

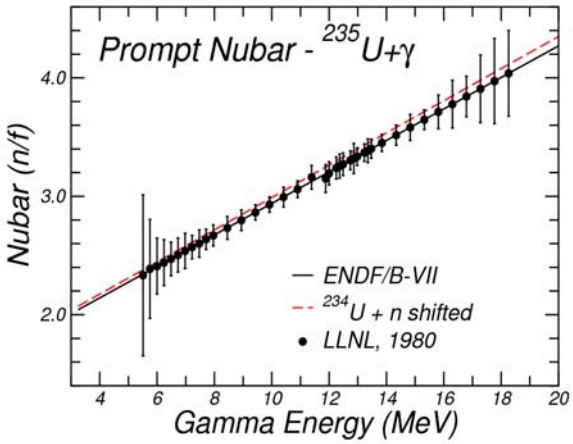

FIG. 76: Prompt nubar for photons incident on ^{235}U. Our evaluation uses the Caldwell data, LLNL.

Recently, at Los Alamos, in collaboration with CEA Saclay [236], we have evaluated the actinide photonuclear cross sections for ^{235,238}U, ^{239,240}Pu, ^{241}Am and ^{237}Np, having extended our GNASH modeling code to model the photofission processes. We were able to make extensive use of GNASH nuclear reaction modeling parameters already developed for our work on neutron reactions (*e.g.*, fission barriers, level densities, *etc*). This enabled us to use our more advanced computational tools for predicting exclusive cross sections, spectra, and angular distributions for the emitted neutrons. For illustration, evaluated neutron production cross sections for ^{235}U+γ are shown in Fig. 74 and evaluated ^{238}U(γ,f) cross sections in Fig. 75.

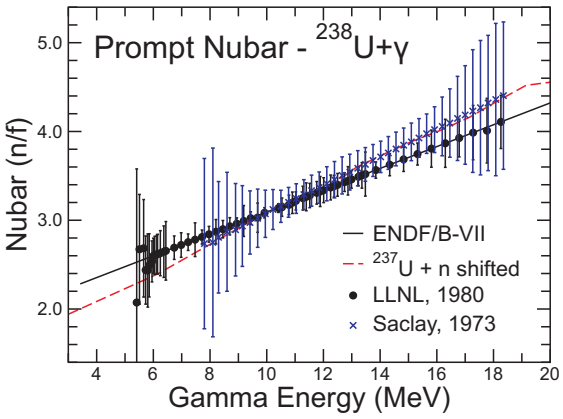

FIG. 77: Prompt nubar for photons incident on ^{238}U.

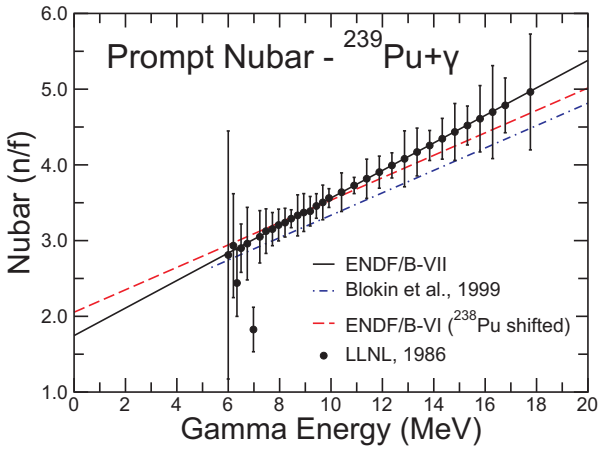

FIG. 78: Prompt nubar for photons incident on ^{239}Pu.

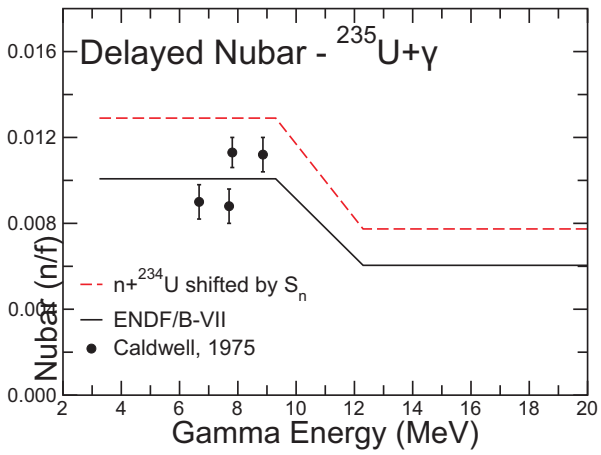

FIG. 79: Delayed nubar for photons incident on ^{235}U. Experimental data are for bremsstrahlung photons, data points refer to the average incident energy.

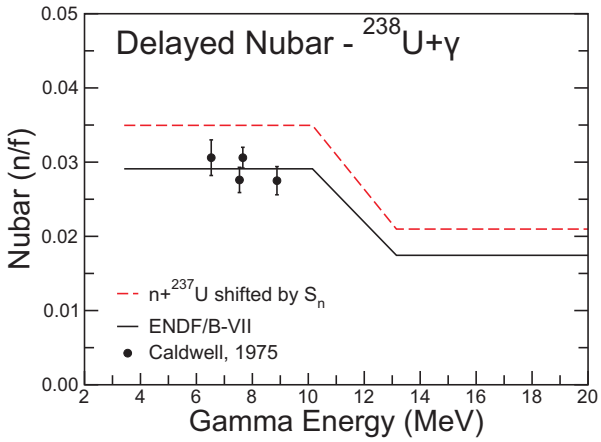

FIG. 80: Delayed nubar for photons incident on ^{238}U. Experimental data are for bremsstrahlung photons, data points refer to the average incident energy.

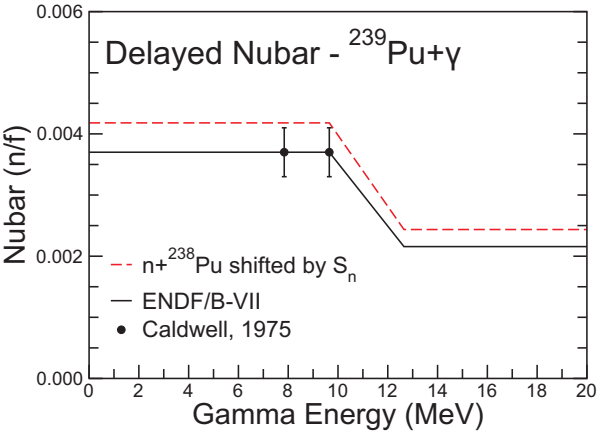

FIG. 81: Delayed nubar for photons incident on ^{239}Pu. Experimental data are for bremsstrahlung photons, data points refer to the average incident energy.

Our evaluations for the prompt fission neutron multiplicity, $\bar{\nu}_p$, were based on using the measured data from Livermore [238]. These data are shown in Figs. 76, 77 and 78 for ^{235,238}U and ^{239}Pu respectively. In Fig. 78 we show, for comparison, the results from the Russian (Obninsk) evaluation, labeled as Blokhin *et al.* (1999). We also show the results that would be obtained if one took the ENDF neutron evaluation for the A-1 system shifted by the neutron separation energy (*i.e.,* comparing γ + ^{239}Pu with n+^{238}Pu, shifted by the neutron separation energy), since one would expect these results to be similar (except for small effects due to the different angular momentum in the two channels). It is reassuring that indeed the two approaches lead to similar results.

For the photofission delayed neutron multiplicities, our approach has been to utilize the equivalent neutron induced evaluations for the A-1 system (shifted by the neutron separation energy), but then to renormalize these values so as to better match the measured data from

bremsstrahlung source measurements by Caldwell (this time when he was at Los Alamos), see Figs. 79, 80 and 81 for ^{235,238}U and ^{239}Pu, respectively. This approach has the merit that the equivalent neutron-induced A-1 data are available for monoenergetic incident energies, whilst we still make use of the bremsstrahlung-induced data to renormalize these results (their average incident energy is plotted in Figs. 79, 80 and 81). We note that a measurement program has been initiated at CEA Saclay to obtain new data for the delayed neutron multiplicities, initially for ^{238}U, with future measurements planned for ^{235}U. Such data will be valuable for testing and improving our evaluations. A full description of the new actinide evaluations is in preparation [239]. Documentation of our preliminary work was given in Ref. [236], though we note that some of our final ENDF/B-VII.0 evaluation differ slightly from those documented there.

B. Integral validation

The photonuclear evaluations can be tested and validated in an integral way by comparing simulated and measured prompt neutron production. Experimental data were obtained by Barber and George [240] using a well-characterized electron source and neutron detector to make absolute measurements of neutrons produced per electron incident on several thicknesses of various materials. A validation comparison, using these measurements, the MCNP 4C transport code, and substantially the same data as found on the current library, was recently presented by White *et al.* [237] and an example calculation from that study is shown here in Fig. 82. A similar study using the uranium data produced for the current library has also been done and one comparison for uranium is shown in Fig. 83.

The comparison to the uranium data is most typical of the results of the broader study. In general, we find that the simulation matches the data within a few percent at lower energy and generally become more discrepant with differences growing to 20-30 % at higher energies. The comparison to tantalum provides the only exception where the data remain within a few percent at higher energies. The simulations show a systematic under-prediction of the experimental data that needs to be better understood. Based on favorable comparisons of, in some cases, multiple independent measurements of cross-section data to the evaluated data, it is hard to argue that the discrepancy stems from the evaluations. It is recommended that additional experimental measurements be made to help resolve these discrepancies. In addition to repeating integral measurements of neutrons produced per electron as shown here, such measurements might include revisiting fundamental measurements of the cross sections, direct measurement of emission distributions, and measurements of bremsstrahlung spectra to validate the electron to photon conversion.

The actinide delayed neutron data have also been

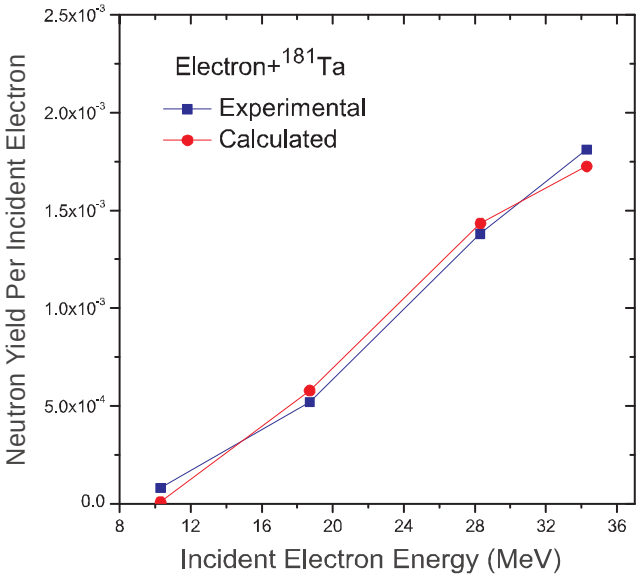

FIG. 82: Neutron yield per incident electron on a Ta target.

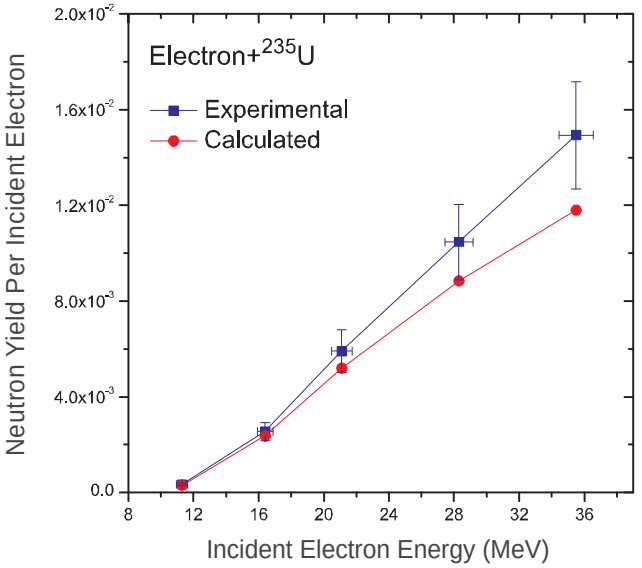

FIG. 83: Neutron yield per incident electron on a ^{235}U target.

tested via simulations of experiments recently performed at Los Alamos for nonproliferation applications. Here, a pulsed 10 MeV electron accelerator created a bremsstrahlung photon source that was incident on two configurations of highly-enriched uranium (HEU). The first had a mass of 4.8 kg and the second had a mass of 21.5 kg. Neutrons were detected between pulses. These neutrons are dominated by delayed neutrons from photofission and prompt neutrons from fission events induced by the delayed photofission neutrons.

Approximately 100 counts per second were observed with the small-mass HEU configuration, and approximately 1000 counts per second were observed with the

large-mass HEU configuration. The experiments were simulated with a version of MCNP modified to utilize photofission delayed neutron data. While absolute comparisons with experiment were not practical, the relative agreement was encouraging. The experimental count rate ratio (large object / small object) was 10.0 and the simulated value was 8.7 [241]

VII. CHARGED PARTICLE REACTION SUBLIBRARIES

The evaluation methods used for the charged-particle evaluations are similar to those used for the neutron sublibrary. One has to distinguish between very light targets, essentially few-body systems, and heavier nuclei that can be considered suitable for applying statistical methods. The reaction models used in the both cases are very different. There is no clear separation between the two regions although A=10 could be set as a tentative boundary. Actually, below this boundary there is an evaluation for protons on ^{9}Be performed with statistical models and above the boundary there is a p+^{13}C evaluation performed with the few-body (R-matrix) methodology. Otherwise, all evaluations for nuclei with A$\leqslant$10 were evaluated using the R-matrix formalism and all heavier ones using statistical GNASH reaction code methods. All non-proton charged-particle evaluations were performed for light nuclei and use a few-body methodology.

There are several new evaluations for charged-particle-induced reactions on light elements, including p+^{7}Li, d+^{6}Li, d+^{7}Li, t+^{6}Li, ^{3}He+^{6}Li, and p+^{10}B. These resulted from R-matrix analyses of reactions in the A =8, 9, and 11 systems, and include spectra for some of the reactions coming from breakup into three-body final states, calculated with the 3-body resonance-model code SPECT [242]. Having been developed primarily for thermonuclear and astrophysical applications, these evaluations do not always cover the energy range up to 20 MeV. However, they are complete transport evaluations (including all angular distributions and spectra) over their specified incident energy ranges.

A. Proton reaction sublibrary

The proton sublibrary contains 48 LANL evaluations, including 8 evaluations on light nuclei produced by the R-matrix approach, and 40 evaluations produced by statistical and direct reaction models extended up to 150 MeV.

1. Proton reactions for A $\leqslant$ 10

Reaction p+^{1}H. p-H elastic cross sections were calculated for E$_p$ between 0 and 150 MeV from an R-matrix analysis of p-p cross-section and polarization data in this energy range. The maximum nuclear partial wave allowed in the fit was $l = 6$, and the resulting χ^2 per degree of freedom was 1.8.

Reaction p+^{2}H. The evaluation of the ^{2}H(p,n2p) cross section is based on experimental data for both the p + ^{2}H and n + ^{2}H reaction (nonelastic) cross sections, since these appear to be indistinguishable at energies above about 20 MeV. Additionally, we utilized the Faddeev calculations for the evaluated cross section at lower energies. We were utilizing the results of G. Hale's R-matrix analysis of p + ^{2}H data at proton energies up to 4 MeV and experimental data up to an energy of 65 MeV for the evaluation of elastic scattering.

Reaction p+^{3}H. The p+^{3}H evaluation contains integrated cross sections and angular distributions for the reactions initiated by protons on tritons at proton energies up to 12 MeV. All the information has been calculated from the parameters of an extensive multi- channel R-matrix analysis of reactions in the ^{4}He system at proton energies up to 12 MeV.

Reaction p+^{3}He. The p+^{3}He evaluation includes p + ^{3}He elastic and p + ^{3}He $\rightarrow$ 2p + d reaction. The cross sections and the elastic scattering distributions were obtained from an R-matrix calculation with the EDA code. The energy-angle distributions for the reaction p + ^{3}He $\rightarrow$ 2p + d are assumed to follow a 3-body phase-space law.

Reaction p+^{6}Li. For the system p+^{6}Li the reactions ^{6}Li(p,p)^{6}Li and ^{6}Li(p,^{3}He)^{4}He were calculated from R-matrix analysis of reactions in the A=7 system, which included data for the ^{6}Li(p,p) and ^{6}Li(p,^{3}He) reactions at energies up to about 2.5 MeV.

Reaction p+^{7}Li. In the case of the p+^{7}Li, the reactions ^{7}Li(p,p), ^{7}Li(p,n), ^{7}Li(p,d) and ^{7}Li(p,α) were calculated from R-matrix analysis of reactions in the ^{8}Be system. The energy range of the evaluation is up to 10 MeV. The ^{7}Li(p,d) evaluation was obtained without fitting any experimental data on that reaction, although the reaction is constrained by the time inverse reaction, for which substantial data were entered.

Reaction p+^{10}B. The p+^{10}B evaluation consists of ^{10}B(p,p$_0$)^{10}B and ^{10}B(p,α_0)^{7}Be reactions calculated from an R-matrix analysis of reactions in the ^{11}C nuclear system in the range from 10 keV up to 3 MeV. The normalization of the low-energy ^{10}B(p,α_0)^{7}Be data is strongly constrained by the ^{10}B(p,p$_0$)^{10}B data starting at 0.5 MeV. The same is true for the other ^{10}B(p,α_0)^{7}Be data. The exact normalization of this data above 1.5 MeV has changed considerably at various stages of the analysis.

Reaction p+^{13}C. The p+^{13}C evaluation contains ^{13}C(p,γ_0)^{14}N reaction calculated from an R-matrix analysis of reactions in the ^{14}N nuclear system in the energy

range from 10 keV up to 2 MeV. The main aim of the analysis was twofold:

- accurate parametrization of the very narrow $J^\pi = 2^+$ resonance at $E_x = 9.1724$ MeV ($E_p = 1.7476$ MeV) which dominates the cross-section, and
- parametrization of the background resonance structure.

2. *LA150 proton reactions for A > 10*

These LA150 (Los Alamos 150 MeV library) evaluations were performed using statistical and direct reaction models. They provide a complete representation of the nuclear data needed for transport, damage, heating, radioactivity, and shielding applications over the incident proton energy range from 1 to 150 MeV. The evaluations utilize MF=6, MT=5 to represent all reaction data. Production cross sections and emission spectra are given for neutrons, protons, deuterons, tritons, α-particles, γ-rays, and all residual nuclides produced (A> 5) in the reaction chains. To summarize, the ENDF sections with non-zero data above are the following:

MF=3, MT=2: Integral of nuclear plus interference components of the elastic scattering cross section.

MF=3, MT=5: Sum of binary (p,n') and (p,x) reactions.

MF=6, MT=2: Elastic (p,p) angular distributions given as ratios of the differential nuclear-plus- interference to the integrated value.

MF=6, MT=5: Production cross sections and energy-angle distributions for emission of neutrons, protons, deuterons, and alphas; and angle-integrated spectra for gamma rays and residual nuclei that are stable against particle emission.

The evaluations are based on nuclear model calculations that have been benchmarked to experimental data. As for the neutron sublibrary, we used the GNASH code system, which utilizes Hauser-Feshbach statistical, preequilibrium and direct-reaction theories. Spherical optical model calculations were used to obtain particle transmission coefficients for the Hauser-Feshbach calculations, as well as for the elastic neutron angular distributions. In most cases, we used optical potential of Lohr and Haberli [243] for deuterons, the McFadden-Satchler potential [244] for α-particles, and for tritons the Beccheti-Greenlees [245] potential. For protons, we used the Becchetti-Greenlees potential below 20 MeV and the relativistic medium-energy global potential of Madland [246] above 20 MeV.

In certain cases, direct reaction cross sections to discrete states were calculated with the ECIS96 code [26] using deformation parameters compiled in Nuclear Data Sheets. The optical potential parameters were obtained using a combination of a grid search code and the interactive optical model viewer ECISVIEW [247], both built around the coupled channels code ECIS96. The energy dependence of the optical model parameters is as described in Ref. [191]. This optical potential was used for the calculation of neutron transmission coefficients and direct cross sections.

Discrete level data from Nuclear Data Sheets were matched to continuum level densities using the formulation of Ignatyuk *et al.* [248] and pairing and shell parameters from the Cook [249] analysis. Neutron and charged-particle transmission coefficients were obtained from the optical potentials. Gamma-ray transmission coefficients were calculated using the Kopecky-Uhl model [47].

Preequilibrium corrections were performed in the course of the GNASH calculations using the exciton model of Kalbach [250, 251], validated by comparison with calculations using Feshbach-Kerman-Koonin (FKK) theory. The energy-angle-correlations for all outgoing particles are based on Kalbach systematics [55].

As we discussed in Section III.E, for incident neutrons the LA150 evaluations were recreated by Trellue and Chadwick using a corrected version of the nuclear reaction model code GNASH. In this way we removed a bug that led to a previous overestimate of particle production in the earlier version (ENDF/B-VI.8) of the proton sublibrary [252].

Altogether, 40 evaluations (including ^{9}Be) falling into this category are contained in the proton sublibrary. They cover materials mostly relevant to the Accelerator Driven Systems and medical applications such as cancer radiation-therapy. Cross sections and spectra for producing individual residual nuclei are included for reactions that exceed a cross section of approximately 1 nb at any energy. Generally, the evaluated proton emission spectra are in reasonable agreement with the experimental data. For deuteron and α ejectiles, the quality of agreement is poorer. However, modeling cluster emission in these nuclei is difficult, and the cross sections are small, so the practical impact is low.

B. Deuteron reaction sublibrary

The deuteron sublibrary contains five LANL evaluations.

1. *Reactions d+d and d+t*

Reaction d+d. The d+d evaluation is based on the ^{4}He system R-matrix analysis by G. Hale, LANL. It contains integrated cross sections and angular distributions for the reactions initiated by deuterons on ^{2}H at deuteron energies up to 10 MeV. All the information has been calculated from the parameters of an extensive multi- chan-

nel R-matrix analysis of reactions in the ^{4}He system at deuteron energies up to 10 MeV.

Cross sections are given for D(d,n) (MT=50) and D(d,p) (MT=600) at energies between 100 eV and 10 MeV. Legendre coefficients are given for differential elastic cross sections (MT=2) using (LAW=5) the exact nuclear amplitude (LTP=1) expansion. The identity of the deuterons is automatically taken into account in this representation. Angular distributions are also given for the D(d,n) (MT=50) and D(d,p) (MT=600) reactions. These should be used with caution at energies above 5 MeV, because no data of this type were included in the analysis at energies between 5 and 10 MeV.

Reaction d+t. The evaluation is based on ^{5}He system R-matrix analysis by G. Hale, LANL and T(d,n) Legendre coefficients evaluated by M. Drosg, TU Vienna. It contains integrated cross sections and angular distributions for the reactions initiated by deuterons on tritons at deuteron energies up to 10 MeV. The energy range for the T(d,n)^{4}He reaction has been extended to 30 MeV by matching to Legendre coefficients obtained by Drosg. The information below 10 MeV comes primarily from the solution parameters of an extensive multi-channel R-matrix analysis of reactions in the ^{5}He system (including n-α elastic scattering) at deuteron energies up to 10 MeV (neutron energies up to 29 MeV), for which the χ^2 per degree of freedom is about 1.6.

The R-matrix data set for T(d,n)^{4}He reaction contained 1169 data points, including the recent measurements of the low-energy integrated cross section by Jarmie and Brown [253], recent measurements of the differential cross section in the MeV range by Drosg, and 13 different types of polarization measurements. The matching energy for joining the R-matrix results with Drosg's Legendre coefficients to be 7 MeV. The data set for the T(d,n)^{4}He* reaction (final product in the first excited state) contained 11 data points, including the measurement of the zero-degree excitation function, and an angular distribution at one energy, by Poppe [254].

In case of the d+t elastic scattering the angular distributions were calculated from the R-matrix fit using the exact (LAW=5) nuclear amplitude representation (LTP=1). Nuclear partial waves up through H-waves were allowed in the analysis, giving Legendre orders L=0 to 10 in the nuclear cross section and L=0 to 5 in the complex nuclear amplitude that interferes with the Coulomb amplitude.

For the T(d,n)^{4}He reaction the coefficients to L=10 are given for calculated neutron angular distributions at energies up to 7 MeV. Above that energy, the evaluated coefficients of Drosg [255] are used. Data included the most recent differential cross section measurements in the MeV range. α-particle distributions are obtained by recoil (LAW=4). Two-body (LAW=2) Legendre coefficients up to L=2 at 10 MeV are given for T(d,n)^{4}He*. The decay of the residual ^{4}He* into p and t is approximated by a phase-space (LAW=6) representation.

2. Other reactions

Reaction d+^{3}He. The ^{3}He(d,p)^{4}He reaction was calculated from a two-channel R-matrix analysis of reactions in the ^{5}Li system. This analysis includes new TUNL measurements of cross sections and analyzing powers for the reaction, which imply a lower energy (413 keV) for the 430- keV resonance. Measurements of the integrated reaction cross section were also included at energies up to 1.4 MeV.

Legendre moments for the d+^{3}He elastic scattering were calculated from the ^{5}Li R-matrix analysis that included the d+^{3}He elastic scattering data, at deuteron energies up to 1 MeV. Legendre moments for the ^{3}He(d,p)^{4}He reaction were also calculated from the R-matrix analysis that included differential cross sections measured at energies up to 1 MeV.

Reaction d+^{6}Li. The reactions ^{6}Li(d,d) (MT=2), ^{6}Li(d,n) (MT=50), ^{6}Li(d,p) (MT=600) and ^{6}Li(d,α) (MT=800) were calculated from the R-matrix analysis. We stress, however, that deuteron energy range of the evaluation is up to 5 MeV. Since no data for ^{6}Li(d,d) were entered below E_d of 3 MeV this particular reaction may not be reliable below 3 MeV. Because the isospin components of ^{6}Li(d,n) and ^{6}Li(d,p) reactions the two are related by isospin symmetry and ^{6}Li(d,n) reaction is constrained by ^{6}Li(d,p).

Care was taken to make all data consistent with the convention that the integrated cross section should be divided by a factor of two for identity of the outgoing alpha-particles.

Legendre moments were calculated from the R-matrix analysis. Data that determines moments have, for the most part, been entered for MT=2, 50, 600 and 800 up to E_d of 5 MeV. However, such data have not been entered for MT=2 for E_d below 3 MeV, and for MT=50 above 3.7 MeV.

Reaction d+^{7}Li. The reactions ^{7}Li(d,d)^{7}Li (MT=2) and ^{7}Li(d,t)^{6}Li (MT=700) were calculated from R-matrix analysis of reactions in the ^{9}Be system. In the case of the ^{7}Li(d,n α)^{4}He reaction (MT=22) spectra and integrated cross sections were computed using the resonance code. In the neutron spectra for this reaction, the narrow peak corresponding to the ground state of ^{8}Be has been artificially broadened (preserving area) in order to show up with the number of digits allowed for the outgoing energy by the ENDF format. Although calculated data are given for energies up to 20 MeV, they should be used with caution above 5 MeV, since that was the upper limit of data included in the analysis.

C. Triton reaction sublibrary

The triton sublibrary contains three LANL evaluations.

Reaction t+^{3}H. Integrated cross sections for ^{3}H(t,t)^{3}H (MT=2) and ^{3}H(t,2n)α (MT=16) were calculated from a charge-symmetric R-matrix analysis of the T=1 part of the A=6 system, that fit t+t and ^{3}He(^{3}He,p) data at energies up to 2.2 MeV.

Legendre coefficients for the elastic scattering of tritons (MT=2) were calculated from the charge-symmetric, A=6, T=1 R-matrix analysis that included the t+t elastic scattering data of Holm and Argo [256]. Neutron and α-particle spectra for the ^{3}H(t,2n)α (MT=16) reaction were calculated using a three-body resonance model, including the n+^{5}He(g.s.) and ^{4}He+n+n resonances, taking into account exchange contributions that arise from symmetrizing in the identical neutrons. The shape of an experimental measurement of the neutron spectrum at E_t= 50 keV by Wong [257] was used to determine the relative amplitudes of the resonant contributions.

Although calculated data are given for some reactions at energies up to 20 MeV, they should be used with caution at energies above 2.2 MeV, since that was the upper limit of data included in the analysis.

Reaction t+^{3}He. The cross sections for ^{3}He(t,t)^{3}He (MT=2), ^{3}He(t,np)^{4}He (MT=28) and ^{3}He(t,d)^{4}He (MT=650) reactions were calculated from R-matrix analysis of the ^{6}Li system that also includes d+^{4}He scattering data. Cross-section data for the t+^{3}He reaction were included at energies up to E_t=3 MeV. Extensions to 20 MeV for MT=28 and MT=650 are "best guesses" based on higher energy measurements of the t+^{3}He reaction cross section and the integrated cross section for the ^{4}He(d,t)^{3}He inverse reaction.

The angle and energy distributions for the elastic scattering ^{3}He(t,t)^{3}He at energies below 3 MeV were calculated from the R-matrix analysis since no measurements exist in this energy region. Neutron, proton and α spectra for the ^{3}He(t,np)^{4}He reaction were calculated using a three-body resonance model, including the n+^{5}Li(g.s.), p+^{5}He(g.s.), and ^{4}He+n-p resonances. The relative amplitudes of the resonant contributions were determined by fitting the shapes of the experimental proton and α spectra measured by Smith, Jarmie, and Lockett [258] at E_t = 1.9 MeV. These amplitudes were used all the way up to 20 MeV. Legendre moments for the ^{3}He(t,d)^{4}He reaction were calculated from the R-matrix parameters at energies up to 3 MeV. Strong asymmetries in the angular distribution about 90 degrees (violations of the Barshay-Temmer theorem [259]) were reproduced with an isospin-conserving R matrix.

Although calculated data are given for some reactions at energies up to 20 MeV, they should be used with caution at energies above 3.2 MeV, since that was the upper limit of data included in the R-matrix analysis.

Reaction t+^{6}Li. The ^{6}Li(t,t)^{6}Li (MT=2) and ^{6}Li(t,d)^{7}Li (MT=650) reactions were calculated from R-matrix analysis of reactions in the ^{9}Be system. The spectra and integrated cross sections for the ^{6}Li(t,n α)^{4}He reaction were computed using the resonance code based on LANL data. In the neutron spectra for this reaction, the narrow peak corresponding to the ground state of ^{8}Be has been artificially broadened (preserving area) in order to show up with the limited number of digits allowed for the outgoing energy by the ENDF-6 format. Although calculated data are given for energies up to 20 MeV, they should be used with caution above 5 MeV, since that was the upper limit of data included in the analysis.

D. ^{3}He reaction sublibrary

The ^{3}He sublibrary contains two LANL evaluations.

Reaction ^{3}He+^{3}He. Integrated cross sections for ^{3}He(^{3}He,^{3}He)^{3}He (MT=2) and ^{3}He(^{3}He,2p)α (MT=111) were calculated from charge-symmetric R-matrix analysis of the T=1 part of the A=6 system, that fit t+t and ^{3}He(^{3}He,p) data at energies up to 2.2 MeV.

Angle and energy distributions for ^{3}He(^{3}He,^{3}He)^{3}He (MT=2) were calculated from the charge-symmetric, A=6, T=1 R-matrix analysis that included the t+t elastic scattering data of Holm and Argo [256]. Proton and α spectra for the ^{3}He(^{3}He,2p)α reaction were calculated using a three-body resonance model, including the p+^{5}Li(g.s.) and ^{4}He+p-p resonances, taking into account exchange contributions that arise from symmetrizing in the identical protons. The relative amplitudes of the resonant contributions were taken to be the same as those for the t+t reaction, which were determined by a measurement of the neutron spectrum by Wong *et al.* [257] at E_t = 50 keV.

Although calculated data are given for some reactions at energies up to 20 MeV, they should be used with caution at energies above 2.2 MeV, since that was the upper limit of data included in the analysis.

Reaction ^{3}He+^{6}Li. The ^{6}Li(^{3}He,^{3}He)^{6}Li (MT=2) and ^{6}Li(^{3}He,d)^{7}Be (MT=650) were calculated from R-matrix analysis of reactions in the ^{9}B system. The ^{6}Li(^{3}He,p α)^{4}He reaction spectra were calculated with resonance code. Integrated cross sections were obtained from the R-matrix analysis of ^{9}B. In the proton spectra for this reaction, the narrow peak corresponding to the ground state of ^{8}Be has been artificially broadened (preserving area) in order to show up with the limited number of digits allowed for the outgoing energy by the ENDF-6 format. Although calculated data are given for energies up to 20 MeV, they should be used with caution at energies above 5 MeV, since that was the upper limit of data included in the analysis.

VIII. DECAY DATA SUBLIBRARY

A. Evaluation methodology

The decay data part of the ENDF/B-VII.0 library was produced by A. A. Sonzogni of the NNDC, BNL.

This sublibrary contains 3830 materials and is mostly derived from the Evaluated Nuclear Structure Data File (ENSDF) [260] and the 2006 edition of the Nuclear Wallet Card [261]. Each material corresponds to the ground state or an isomeric level of a given nucleus. The library provides information for stable and unstable nuclei, from the neutron to ^{283}Rg (Z=111).

The earlier version of the library contained 979 materials, focusing primarily on nuclei that are of relevance in nuclear fission applications, and as a consequence most radionuclides included were β- emitters. The current library covers all known nuclei. Because of the expansion in coverage and the limitations of the original scheme to obtain material numbers, the material numbers used in this section are ordered sequentially by Z and A. This should not be a problem as each material can be identified by the Z, A and isomer count (LISO).

For sections of the library corresponding to unstable levels, the half-life, decay modes and energy released during the decay is presented. For stable levels, the only information given is the spin and parity of the level.

The energy released can be given with varying degrees of detail. The most basic information is:

- mean electromagnetic energy (EEM), which includes mean gamma and X-ray energies,
- mean light particle energy (ELP), which includes mean energies from electrons and positrons emitted in β- and electron capture and β+ decay as well as conversion and Auger electrons,
- mean heavy particle energy (EHP), which includes the energy from protons, neutrons, alpha particles and fission fragments.

Moreover, it is possible to give the mean energy for each component as well as the energy and intensity for the individual transitions.

For materials whose decay scheme is well known, *i.e.* satisfying that the sum of the average energies for each radiation type is very close to the effective Q-value, the ENSDF database was used and discreet radiation information was also provided. In contrast, for materials with unknown or poorly known decay schemes, the Nuclear Wallet Cards database was used. In this case, a simple rule was used to obtain the mean energies. If for instance the level in question undergoes beta decay, it was assumed that EEM and ELP corresponds each to a third of decay Q-value, while the neutrinos took the remaining third. For β-delayed particle emission, it was assumed that the neutrinos carried away a quarter of the available energy and that leptons, baryons and photons took a quarter each.

The measurement of the decay characteristics of fission products becomes increasingly difficult as the fission products are further from the valley of stability. Typically, as the β- decay Q-value increases, more weak gamma rays are produced which are difficult to place or simply escape detection. To address this issue, a series of measurements using a ^{252}Cf source and a Total Absorption Gamma Spectrometer (TAGS) were performed at INL, Idaho [262]. Using this data, EEM and ELP values were obtained for 48 materials, which has improved the decay heat predicting power of the library [263]. To obtain the EEM and ELP values from TAGS experiments we have followed the prescription developed by Hagura *et al.* [263], where it is assumed that the decay from excited levels proceeds only by gamma emission, i.e., conversion electrons are neglected. As a result the EEM values is really an upper limit and the ELP a lower one. The effect of electron conversion is expected to be small, expected to be less than 10% of EEM.

Additionally, the following features are included:

- Internal conversion coefficients were calculated for all gamma rays of known multipolarity using the code BRICC [264].
- For ^{36}Cl, ^{59}Fe, ^{99}Tc, ^{129}I and ^{137}Cs average β- energies for second forbidden non-unique transitions were calculated using the code SPEBETA [265]. The LOGFT code used in ENSDF assumes an allowed shape for these transitions resulting in quite different values of average energies.
- Theoretical β- decay half-lives from Moller *et al.* [147] are used for some neutron rich nuclei where a) the experimental value is an upper or lower limit, and b) the nucleus is produced in the fission of ^{235}U and ^{239}Pu.

B. Decay heat calculations

A plot of the decay heat following a fission event of ^{235}U can be seen in Fig. 84. The total decay heat is separated in two components, electromagnetic and light particles. The former includes gamma and X-rays, while the latter includes electrons from β- decay as well conversion and Auger electrons. A heavy particle component, including neutrons and alphas is negligible. The data comes from the 1989 compilation of Tobias [266]. The effect of the TAGS data is clearly visible. Without including it, we would be using incomplete decay schemes with many missing weak gamma rays, resulting in artificially high values of electron and neutrino mean energies as well as artificially low values of mean gamma energies.

The JEFF 3.1 decay data library was released in 2005 and shares a similar spirit and scope with the ENDF/B-VII.0 decay data library. The main difference is that JEFF 3.1 did not include TAGS data. One possible way of comparing both libraries would be to plot decay heats for ^{235}U *with ENDF/B-VII.0 without TAGS data*. This is shown in Fig. 85 and as expected both libraries give very similar results under this condition.

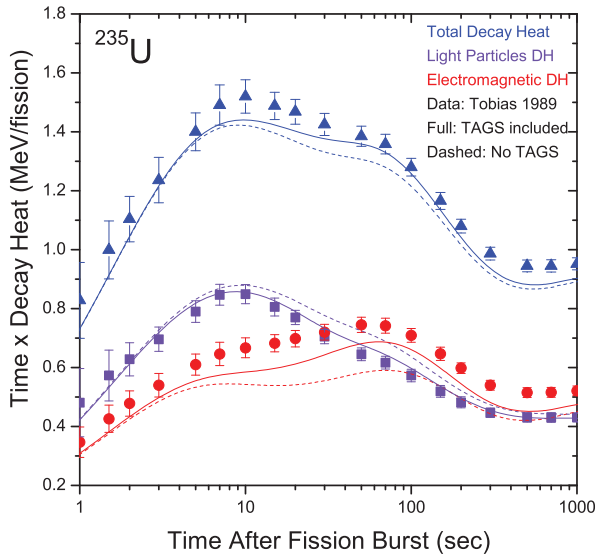

FIG. 84: Decay heat per fission for a ^{235}U sample as a function of time.

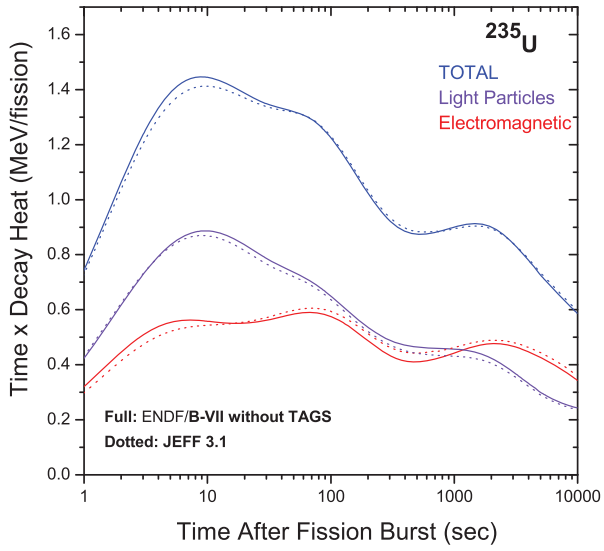

FIG. 85: Decay heat per fission for a ^{235}U sample as a function of time using the JEFF 3.1 and the ENDF/B-VII.0 (without TAGS data) decay data libraries.

IX. OTHER SUBLIBRARIES

We briefly describe 5 sublibraries that have been taken over from ENDF/B-VI.8 without any change. These are two fission yields sublibraries and three atomic data sublibraries.

A. Fission yields

The fission yields from the 1989 LANL evaluation of T.R. England and B.F. Rider [267] are used in ENDF/B-VII.0. Fission yield measurements reported in the literature and calculated charge distributions have been used to produce a recommended set of yields for the fission products. Independent yields are taken from a calculated charge distribution model. A Gaussian charge distribution was calculated by using the most probable charge and Gaussian width. The weighted average experimental independent yields, the weighted average experimental cumulative yields and the calculated cumulative yields (where no data were available) were combined statistically to form a recommended value.

1. *Neutron-induced fission yields sublibrary*

The sublibrary includes 31 materials, from ^{227}Th to ^{255}Fm at 3 neutron energies (thermal, 500 keV and 14 MeV). While for some materials, such as ^{235}U, yields are given for all 3 energies, for many other materials, yields are given for 1 or 2 neutron energies.

2. *Spontaneous fission yields sublibrary*

The sublibrary contains yields for 9 materials: ^{238}U, ^{244,246,248}Cm, ^{250,252}Cf, ^{253}Es and ^{254,256}Fm.

B. Atomic data

The ENDF/B-VII.0 library contains three atomic interaction data sublibraries that have been taken over from the ENDF/B-VI.8 library. These are photo-atomic, atomic relaxation and electro-atomic sublibraries, developed in the 1990s by LLNL [268–270].

The three atomic interaction data sublibraries are designed to be used in combination to perform detailed coupled electron-photon radiation transport calculations. An example would be transport calculation by the Monte Carlo code TART for radiation shielding application as discussed by Cullen, LLNL [271]. The sublibraries are completely consistent with one another in terms of all using the same atomic parameters (e.g., subshell binding energies). These sublibraries include details that were previously not available, or not considered, when performing calculations using what can be called traditional photon interaction data.

1. *Photo-atomic sublibrary*

The evaluated photo-atomic data sublibrary describes the interaction of photons with matter as well the direct

production of secondary photons and electrons. The sublibrary contains elemental data for 100 materials (Z = 1 - 100) over the energy 10 eV to 100 GeV [268].

2. Atomic relaxation sublibrary

The atomic-relaxation data sublibrary describes the relaxation of atoms back to neutrality following an ionizing event. It describes the spectra of fluorescence photons from radiative transitions as an ionized atom returns to neutrality. The sublibrary contains elemental data for 100 materials (Z = 1 - 100) over the energy 10 eV to 100 GeV [269].

3. Electro-atomic sublibrary

The evaluated electro-atomic data sublibrary describes the interaction of electrons with matter as well as the direct production of secondary electrons and photons. The sublibrary contains elemental data for 100 materials (Z = 1 - 100) over the energy 10 eV to 100 GeV [270].

X. VALIDATION

A. Introduction

Integral data testing of the ENDF/B-VII.0 cross sections plays an important role for validation purposes. This testing involves using radiation transport codes to simulate certain well-characterized experiments. The importance is twofold: Firstly, since many of the integral experiments are very well understood (especially the critical assembly experiments), they provide a strong test of the accuracy of the underlying nuclear data used to model the assemblies, and can point to deficiencies that need to be resolved. Secondly, such integral data testing can be viewed as a form of "acceptance testing" prior to these data being used in various applications. Many applications, ranging from reactor technologies to defense applications, have a high standard required of a nuclear database before it is adopted for use. Critical assemblies, whilst involving many different nuclear reaction processes, can still be thought of as "single-effect" phenomena that probe the neutronics and nuclear data (but not other phenomena), and therefore an important acceptance test is that a sophisticated radiation transport simulation of the assembly should reproduce the measured $k_{\rm eff}$ to a high degree.

In recent years the value of critical assembly data testing has increased. An international collaborative project sponsored by the OECD Nuclear Energy Agency (NEA) - the International Criticality Safety Benchmark Evaluation Project (ICSBEP) [85] - has been a tremendously successful project that has led to careful evaluation of criticality experiments (recent ones, and older measurements), with the configurations of over 400 experiments carefully detailed (geometry, compositions, *etc.*) together with input decks from many commonly used transport codes. The measured $k_{\rm eff}$ is also given, as are uncertainty assessments. This project has been led by Blair Briggs, INL, with participation from many laboratories around the world.

Additionally, the accuracy of radiation transport codes has increased so much - especially codes such as the continuous energy Monte Carlo MCNP(X) code - that it is now felt that the numerical errors associated with the transport methods are almost negligible, allowing comparisons between the simulated and measured $k_{\rm eff}$ to assess principally the accuracy of the nuclear cross sections and decay properties.

The different critical assembly simulations that we describe below probe different nuclear cross sections and different energy regions. For example, the metal assemblies are sensitive to cross sections in the keV up to MeV range; various thermal assemblies test low energy nuclear data; and intermediate assemblies probe energy regions between these extremes. The Flattop type assemblies involve a fissile core material surrounded by some reflector material to make the assembly critical. Such assemblies provide useful insights into the scattering cross sections of the reflector materials.

We want to emphasize that in order to build confidence in the validation process, multiple independent simulation pathways were adopted. In particular:

- Processing by the code NJOY, followed by extensive Monte Carlo calculations with the code MCNP were done independently at LANL and at NRG Petten, the Netherlands.

- Extensive Monte Carlo calculations were done by the code MCNP developed at LANL and by the code TRIPOLI developed by CEA Cadarache, France [272]. These two codes produced results that were in excellent agreement, the bias between them being negligible. Agreement with predictions from the U.S. Naval Reactor Labs code RACER [273, 274] and RCP01 [275] was also very good.

The present Section is organized as follows. First, we discuss criticality data testing. We subdivide our analyses into discussions of fast, intermediate and thermal assemblies. Then, we discuss reaction rate testing, followed by beta-effective and shielding (transmission) testing. We also cover other data testing, and give our conclusions.

B. Criticality testing

1. Introduction

C/E values for $k_{\rm eff}$ (see footnote[5]) have been calculated for hundreds of critical benchmarks using continuous energy Monte Carlo programs including MCNP (versions 4c3 or 5), RCP01, RACER and VIM [276]. These calculations generally use benchmark models derived from the Handbook of the International Criticality Safety Benchmark Evaluation Project (ICSBEP) [85]. Benchmark evaluations in this Handbook are revised and extended on an annual basis. Unless otherwise noted, benchmark models derived from the 2004 or 2005 editions of the Handbook were used in the calculations reported below

Since the C/E values for $k_{\rm eff}$ reported below have all been obtained using continuous energy Monte Carlo calculations there is a stochastic uncertainty associated with each C/E value for $k_{\rm eff}$. However, since the C/E value for $k_{\rm eff}$ estimates are generally derived from tracking many millions of neutron histories, the magnitude of this uncertainty is very small, typically less than 25 pcm (0.025%, see footnote[6]). This is often as small as, or smaller than, the plot symbol used to display the calculated $k_{\rm eff}$ and so the Monte Carlo uncertainty is not shown in the figures that follow.

A paper by S.C. van der Marck [277] presents independent European data testing of ENDF/B-VII.0, using MCNP4c3 with data processed by NJOY, and also shows extensive neutron transmission benchmark comparisons. Later in this section we summarize some of the main findings from this companion paper.

2. Fast U and Pu benchmarks

Bare, and ^{238}U reflected, assemblies. A large number of well-known LANL fast benchmark experiments have been incorporated into the ICSBEP Handbook and are routinely calculated to test new cross section data. Unmoderated enriched ^{235}U benchmarks include Godiva (HEU-MET-FAST-001 or HMF1)[7],

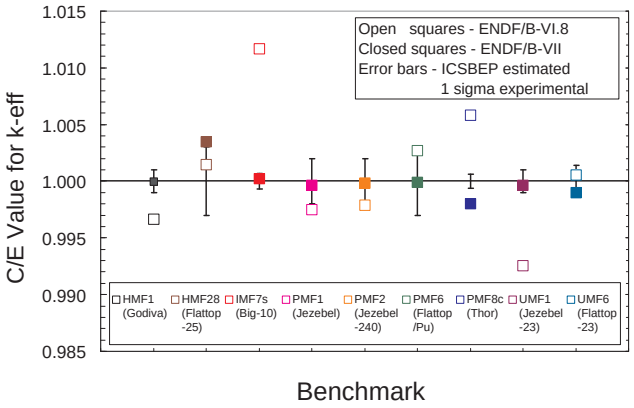

FIG. 86: LANL HEU, Pu and ^{233}U unmoderated benchmark C/E values for $k_{\rm eff}$ calculated with ENDF/B-VI.8 and ENDF/B-VII.0 cross section data.

Flattop-25 (HMF28), and Big-10 (IEU-MET-FAST-007, or IMF7) which has a neutron spectrum that is softer than the Godiva and the Flattop assemblies. Unmoderated plutonium benchmarks include Jezebel (PU-MET-FAST-001, or PMF1), Jezebel-240 (PMF2), Flattop-Pu (PMF6) and Thor (PMF8). Unmoderated enriched ^{233}U benchmarks include Jezebel-23 (U233-MET-FAST-001, or UMF1) and Flattop-23 (UMF6). Results of MCNP5 $k_{\rm eff}$ calculations with ENDF/B-VI.8 and ENDF/B-VII.0 cross sections for this suite of benchmarks are displayed in Fig. 86. The improved accuracy in calculated $k_{\rm eff}$ for these systems with the new ENDF/B-VII.0 cross sections is readily apparent. All calculated $k_{\rm eff}$ except for Flattop-25 have moved closer to unity and seven of the nine C/E values for $k_{\rm eff}$ are now within the estimated 1σ experimental uncertainty. The Flattop-25 assembly's increased reactivity is due to the more reactive highly enriched uranium (HEU) core (note that the bare HEU Godiva assembly has an extremely accurate calculated $k_{\rm eff}$, with C/E = 1.000).

We note that the changes we have made in ENDF/B-VII.0 to the ^{238}U elastic scattering distributions have significantly improved the reflector bias for the Flattop assemblies. This can be seen in the relative change in C/E in going from the bare assemblies to the ^{238}U-reflected Flattop assemblies, i.e. Godiva versus Flattop-25, Jezebel v. Flattop/Pu, and Jezebel-23 v. Flattop-23

[5] For the sake of clarity and a broader acceptability we use the term "C/E value for $k_{\rm eff}$" rather than the term "normalized eigenvalue" throughout this discussion. Here, C/E stands for the ratio of calculated to experimental values, and $k_{\rm eff}$ means the effective multiplication factor defined as the ratio of the average number of neutrons produced to the average number of neutrons absorbed per unit time.

[6] pcm is derived from Italian "per cento mille", meaning per hundred thousands. It is a unit of reactivity, where 1 pcm = 0.00001 Δk/k *i.e.*, 100 pcm is a 0.1% discrepancy.

[7] The character string "HEU-MET-FAST-001" is the identifier assigned in the ICSBEP Handbook for this assembly. It is comprised of 4 parts which, respectively, classify the assembly by fissile materials (such as PU, HEU, LEU, *etc.*), fuel form (such as METal, SOLution, COMPound, *etc.*), and energy spectrum (FAST, INTERmediate, THERMal or MIXED), and benchmark number (-NNN). It is also common, as will be done herein, to use a shorthand form for this identifier, such as HMF1 for HEU-MET-FAST-001. A more complete description of this identifier is given in the Format Guide in the Forward of each volume of the ICSBEP Handbook [85].

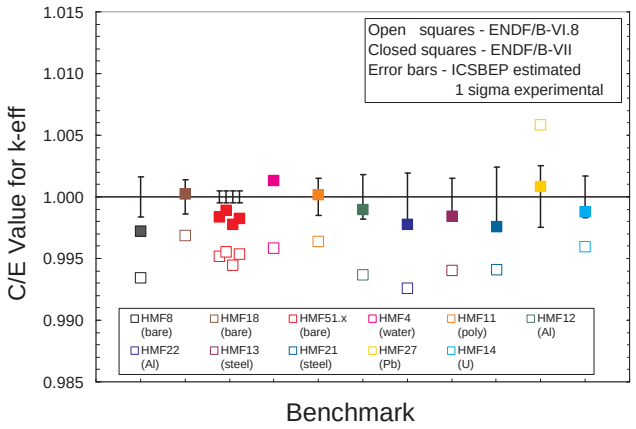

FIG. 87: HEU-MET-FAST benchmark C/E values for $k_{\rm eff}$ calculated with ENDF/B-VI.8 and ENDF/B-VII.0 cross section data.

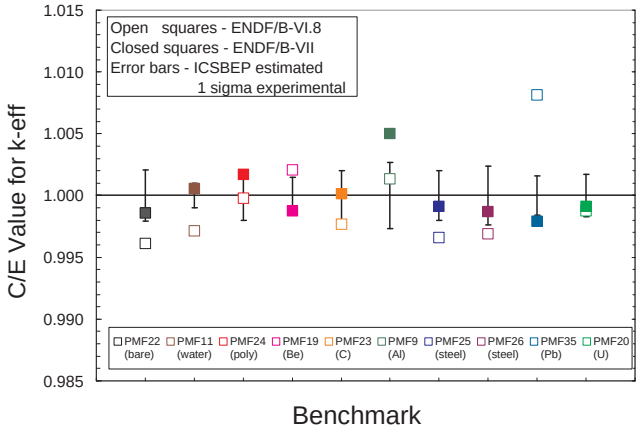

FIG. 88: PU-MET-FAST benchmark C/E values for $k_{\rm eff}$ calculated with ENDF/B-VI.8 and ENDF/B-VII.0 cross section data.

in Fig. 86. The change in criticality bias is largely reduced compared to that calculated with ENDF/B-VI.8 evaluations.

It is also evident in Fig. 86 that our modeling of the Big-10 assembly has dramatically improved compared to predictions based on ENDF/B-VI.8, which yielded calculated $k_{\rm eff}$ that were more than 1% too high. This probably reflects the improvements we have made to the ^{238}U inelastic and elastic scattering distributions.

Assemblies with various reflectors. A number of additional highly-enriched uranium benchmarks, either bare or with one of a variety of reflector materials including water, polyethylene, aluminum, steel, lead and uranium have also been calculated with MCNP5 and both ENDF/B-VI.8 and ENDF/B-VII.0 cross sections. The calculated values for $k_{\rm eff}$ are illustrated in Fig. 87. Once again, significant improvement in the calculated $k_{\rm eff}$ is observed with the ENDF/B-VII.0 cross section data set. In all fourteen cases the ENDF/B-VII.0 calculated $k_{\rm eff}$ is closer to unity, and in eight of these cases it is within the experimental uncertainty. Of the six cases that fall outside the estimated 1σ experimental uncertainty, that uncertainty is either very (to the point of being unrealistically) small or not given.

$k_{\rm eff}$ calculations have also been performed for a series of unmoderated plutonium cores. As with the HEU cores discussed above, these Pu systems were either bare or reflected by one of water, polyethylene, beryllium, graphite, aluminum, steel, lead or uranium. The C/E values for $k_{\rm eff}$ obtained with MCNP5 and either ENDF/B-VI.8 or ENDF/B-VII.0 cross sections are shown in Fig. 88. Once again significant improvement in ENDF/B-VII.0 based C/E $k_{\rm eff}$ is seen, with eight of ten C/E values for $k_{\rm eff}$ being closer to unity. Furthermore, in eight of the ten cases the ENDF/B-VII.0 based C/E $k_{\rm eff}$ is within the estimated 1σ experimental uncertainty.

Pb reflected assemblies. Two reflector elements of particular historical interest, for which there are extensive ICSBEP benchmark data, are lead and beryllium. One of the strengths of the ICSBEP Handbook is that there often are multiple evaluations that contain similar materials, in particular the same core with differing reflectors, thereby facilitating testing of cross section data for individual reflector materials. Such is the situation for lead, with calculated $k_{\rm eff}$for a variety of benchmarks displayed in Fig. 89. Of particular interest are the comparison of calculated $k_{\rm eff}$ between the HMF18 and HMF27 benchmarks, the PMF22 and PMF35 benchmarks and the LEU-COMP-THERM-002 (LCT2) and LCT10 benchmarks. HMF18 is a bare sphere consisting of ten pairs of hemispherical HEU shells; HMF27 is a reflected sphere, comprised of the nine smallest pairs of HEU shells from the HMF18 experiment plus a lead reflector. There is clearly a lead reflector bias in the ENDF/B VI.8 based calculations, with the calculated HMF18 C/E for $k_{\rm eff}$ being $\sim$300 pcm (0.3%) below unity while the calculated HMF27 $k_{\rm eff}$ is $\sim$600 pcm too high. With ENDF/B-VII.0 cross sections this bias is eliminated. Both calculated $k_{\rm eff}$ are within the experimental uncertainty and the difference in the bare versus lead reflected C/E for $k_{\rm eff}$ is less than 70 pcm (less than 0.07%). Similar observations can be drawn when comparing the C/E vaslue for $k_{\rm eff}$ for the PMF22 and PMF35 benchmarks where the common core material is plutonium. With ENDF/B-VI.8 cross sections there is a 1% bias between the bare and reflected system C/E $k_{\rm eff}$ whereas this bias is reduced to less than 70 pcm, again, with ENDF/B-VII.0 cross sections. The significant improvements in these lead-reflected calculated $k_{\rm eff}$ reflects improvements made in our new ENDF/B-VII.0 ^{208}Pb evaluation, which was based on modern calculational methods (the GNASH and ECIS codes) together with careful attention to accu-

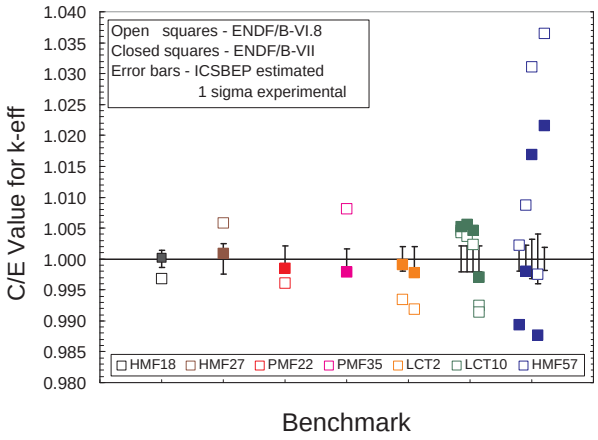

FIG. 89: Bare and lead reflected C/E values for $k_{\rm eff}$ calculated with ENDF/B-VI.8 and ENDF/B-VII.0 cross section data for several HMF, PMF and LCT benchmarks.

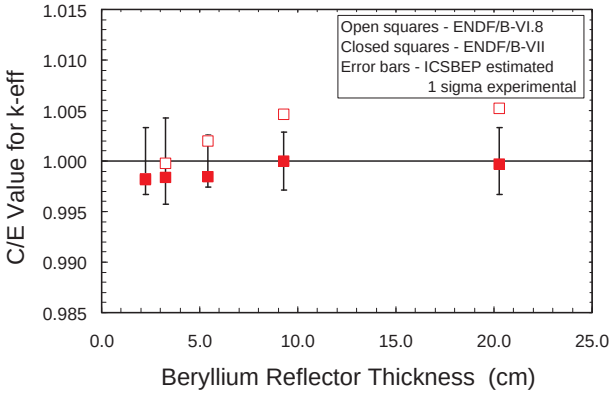

FIG. 90: HEU-MET-FAST-058 benchmark C/E values for $k_{\rm eff}$ with ENDF/B-VI.8 and ENDF/B-VII.0 cross section data as a function of the beryllium reflector thickness.

rately predicting cross section measurements.

The situation is not so clear cut for thermally moderated systems. Cases 4 and 5 from the LCT2 benchmark consist of three clusters of either 15 x 8 or 13 x 8 fuel rods, respectively, aligned so that the 15 or 13 rod rows are in line. The fuel rods are completely immersed in water, with cluster separation used to establish a critical configuration. Cases 1 through 4 of the LCT10 benchmark consist of the same three 13 x 8 fuel clusters, but now include two lead reflecting walls along the outermost row of 3 clusters x 13 rods. The walls are initially located so that they are parallel and adjacent to the unit cell boundary (LCT10, case 1). Cases 2, 3 and 4 describe lead wall locations that are progressively farther removed from the cluster unit cell boundary (0.66 cm, 1.321 cm and 5.405 cm, respectively). Therefore, the difference between calculated LCT2 and LCT10 C/E for $k_{\rm eff}$ in Fig. 89 will test the accuracy of lead cross section data. The LCT10 open square symbols display the calculated ENDF/B-VI.8 C/E for $k_{\rm eff}$. Results for Cases 1 and 4 are shown for both MCNP5 (at LANL) and RCP01 (at Bettis) calculations while cases 2 and 3 are RCP01 only C/E for $k_{\rm eff}$. Case 1, 2 and 3 the C/E values for $k_{\rm eff}$ are clearly biased high compared to the LCT2 (water only reflector) base case. Only LCT10 case 4, where the reflecting wall is ∼2 inches removed from the fuel lattice, agrees well with LCT2, an agreement that largely indicates the lead wall is sufficiently removed from the fuel lattice so as to be virtually invisible to neutrons leaving the lattice. With ENDF/B VI.8, the lead reflector C/E for $k_{\rm eff}$ bias is approximately 1%, a bias similar to that seen in the fast benchmarks. However, in contrast to the fast benchmarks, use of ENDF/B-VII.0 cross sections only reduces this bias by about 50% in thermal benchmarks. The LCT2 ENDF/B-VII.0 C/E for $k_{\rm eff}$ are significantly closer to unity (the general improvement in LCT benchmark C/E for $k_{\rm eff}$ with ENDF/B-VII.0 cross sections is discussed in more detail below), but the LCT10, case 1, 2 and 3 benchmark C/E for $k_{\rm eff}$ remain high by ∼0.5%. Once again, case 4 with its invisible lead wall agrees well with the water only reflected LCT2 base case.

$k_{\rm eff}$ calculations for the HMF57 benchmark are also shown in Fig. 89. This benchmark consists of either a spherical or cylindrical HEU core with a lead reflector. For spherical cores, the reflector is also spherical and surrounds the core and for cylindrical cores the reflector is a cylindrical annulus of the same height, or a cylindrical reflector including top and bottom caps. In any event, the C/E values for $k_{\rm eff}$ are significantly different from unity in most cases regardless of cross section data set. The HMF57 evaluator notes that the calculated $k_{\rm eff}$ are somewhat correlated with core/reflector interface surface area, but it is not clear why there are HMF57 ENDF/B-VII.0 calculated $k_{\rm eff}$ that are more than 1% low when other fast benchmarks are calculated so accurately.

Be reflected assemblies. C/E values for $k_{\rm eff}$ of beryllium reflected benchmarks are shown in Figs. 90 and 91. These comparisons are useful to assess the changes made in the ^{9}Be cross sections for ENDF/B-VII.0. The total elastic scattering cross section was modified in ENDF/B VII.0 based on an EDA code R-matrix analysis of measured total elastic scattering data, with a goal to improve the integral Be reflector bias discussed below. Once again, the results are not consistent across benchmarks. Fig. 90 displays results for HMF58, a benchmark consisting of a small (∼1 cm diameter) central sphere of beryllium surrounded by spherical HEU shells from ∼4.6 cm to ∼7.0 cm thick further surrounded by varying thicknesses of beryllium. With ENDF/B-VI.8 cross sections, there is a clear increasing C/E $k_{\rm eff}$ bias with increasing beryllium reflector thickness for the five cases in this benchmark. Using ENDF/B-VII.0 cross sections yields significant improvement in the C/E value

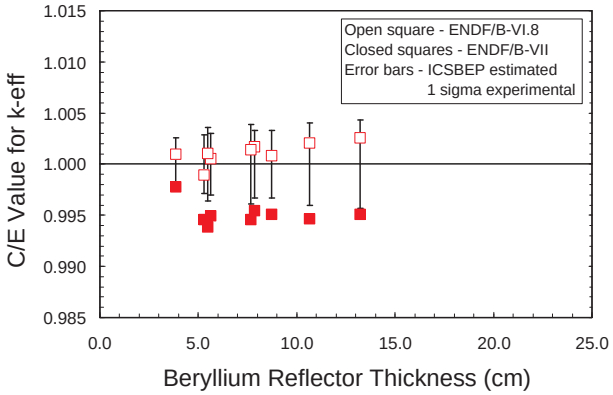

FIG. 91: HEU-MET-FAST-066 benchmark C/E values for k_{eff} for ENDF/B-VI.8 and ENDF/B-VII.0 cross section data as a function of the beryllium reflector thickness. The poorer agreement using ENDF/B-VII.0 appears to be in contradiction to our results shown in Fig. 90.

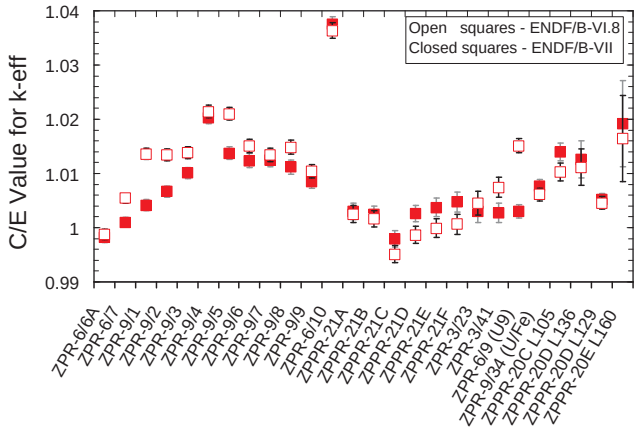

FIG. 92: C/E values for k_{eff} for 26 ZPR (zero power reactor) and ZPPR (zero power physics reactor) benchmarks from Argonne.

for k_{eff}, as the thinnest reflector configurations remain within the experimental uncertainty while the thickest reflector configurations no longer exhibit C/E k_{eff} bias. Similar improvements are observed in other beryllium reflector benchmarks such as HMF41 and MIX-MET-FAST-007 (MMF7). However, other beryllium reflected benchmarks, such as HMF66 which is shown in Fig. 91, were calculated very well with ENDF/B-VI.8 cross sections, but now exhibit a -500 pcm bias with ENDF/B-VII.0 cross sections. These results are particularly puzzling because the HFM66 core consists of the many of the same HEU hemispherical shells as were used in HMF58 benchmarks. The primary difference between HMF58 and HMF66 being that HMF66 contains a larger internal beryllium sphere, varying in diameter from ∼6.3 cm to ∼13.1 cm. The larger internal beryllium is not the source of this discrepancy as the recently approved HMF77 evaluation is also accurately calculated with ENDF/B VI.8 cross sections but also exhibit a -500 pcm bias with ENDF/B-VII.0 cross sections. This benchmark, which will appear in the 2006 edition of the ICSBEP Handbook, is identical to the HMF66 benchmark except the central beryllium region has been eliminated and replaced with air.

ZPR assemblies. The k_{eff} calculations by the code VIM for a suite of 26 Argonne ZPR or ZPPR benchmarks are presented in Fig. 92. These benchmarks come from various areas of the ICSBEP Handbook, including HEU-MET-FAST, HEU-MET-INTER, HEU-MET-MIXED, IEU-MET-FAST, IEU-COMP-FAST, PU-MET-FAST, PU-MET-INTER and MIX-MET-FAST. These benchmarks exhibit large variation in calculated k_{eff}, with the smallest k_{eff} being biased several tenth of a per cent below unity while the maximum positive C/E k_{eff} bias is in excess of 3%. Calculated k_{eff} with ENDF/B-VII.0 cross sections are generally an improvement over those obtained with ENDF/B-VI.8, but significant deviations from unity remain.

Several conclusions may be drawn from this set of benchmarks. The ENDF/B-VII.0 results for ZPR-6/6A and ZPR-6/7 (the traditional ^{235}U- and ^{239}Pu-fueled LMFBR benchmarks) show a small bias which is not observed in the very fast clean Godiva and Jezebel assemblies. The results for ZPR-9 assemblies 1-4 show a distinct degradation of performance with the replacement of ^{238}U with tungsten in these assemblies. Assembly 1 of this series of cores contains ^{235}U and but no tungsten. In assemblies 2, 3 and 4 the ^{238}U is progressively replaced with tungsten. With ENDF/B-VI, reactivity was rather uniformly overpredicted in these assemblies. The improved data for ^{238}U in ENDF/B-VII.0 improves the calculated reference assembly 1, which has no tungsten. This good performance degrades progressively by 2000 pcm as the tungsten replaces ^{238}U in these cores indicating a need to review the tungsten evaluation (which was not changed in ENDF/B-VII). Improved results are noted for the ZPR-6 assembly 9 (the ANL ZPR 9% enriched U analog to the LANL Big-10) resulting primarily from the improved ^{238}U data as noted above.

The very discrepant result (overprediction of reactivity by over 3500 pcm) for ZPR-6 assembly 10, the Pu/carbon/stainless steel benchmark assembly, is particularly noteworthy. It not only represents the most discrepant k_{eff} prediction (as confirmed by all data testing participants), but it also highlights some very strong sensitivities to some of the constituent materials. Furthermore, this assembly has an intermediate (soft) spectrum. It was noted that this assembly was very well predicted (C/E ≈ 1.001) with ENDF/B-V nuclear data and mis-predicted by over 3500 pcm with ENDF/B-VI. Systematic replacement of individual isotope evaluations (ENDF/BVII.0 replaced by ENDF/B-V) indicates

small positive and negative effects except for 3 materials, ^{239}Pu, chromium and manganese, which increase the calculated value by 1100 pcm, 1700 pcm and 600 pcm, respectively. The apparent overprediction of $k_{\rm eff}$ by over 1000 pcm by the ENDF/B-VII.0 ^{239}Pu in this soft spectrum assembly is consistent with the misprediction of ENDF/B-VII.0 data discussed below for the thermal Pu solution assemblies. Review of the data in the resonance regions for ^{239}Pu and chromium is a priority for future work on Version VII; review of the data for manganese in this energy range is in progress.

3. Thermal, high- and low-enriched ^{235}U solution benchmarkss

Thermal, highly enriched ^{235}U homogeneous solution benchmarks have been used to test the accuracy of low energy ENDF/B cross section data sets for many years. In the past, the benchmark configurations were obtained from various Oak Ridge National Laboratory and Rocky Flats progress reports, but in recent years these benchmarks have been incorporated into the ICSBEP Handbook, which forms the basis for the benchmark model results presented here. In addition, the ICSBEP Handbook has allowed data testers to expand their benchmark test suites to include low-enriched thermal solution experiments. We shall show how the new ENDF/B-VII.0 library, like the old ENDF/B-VI.8 library, performs well for these assemblies.

C/E values for $k_{\rm eff}$ have been calculated for a suite of 62 critical assemblies from 14 HEU-SOL-THERM (HST) or LEU-SOL-THERM (LST) benchmark evaluations. The HST benchmarks represent experimental work performed at Oak Ridge National Laboratory, or at Rocky Flats, while the LST benchmarks represent experiments performed at the Japanese STACY facility. These benchmarks have most commonly been correlated versus Above-Thermal Leakage Fraction (ATLF), e.g., $k_{\rm calc}$(ATLF) = b_0 + b_1*ATLF. ATLF is the net leakage out of the solution of neutrons whose energies exceed 0.625 eV. For large assemblies with minimal leakage such as HST42, near unity C/E $k_{\rm eff}$ provide an indication that thermal region data, such as thermal ^{235}U nu-bar, thermal ^{235}U fission and capture cross sections and the thermal hydrogen capture cross section are accurately defined. Smaller systems with large ATLF test the higher energy cross sections, the ^{235}U fission spectrum, elastic scattering angular distributions and, for reflected systems, the slowing down and reflection of above-thermal neutrons back into the fissile solution. Early ENDF/B cross sections, up to and including ENDF/B-VI.2, generally exhibited a significant increasing C/E $k_{\rm eff}$ trend in calculated HST C/E $k_{\rm eff}$ when correlated versus ATLF. Following Lubitz's work to revise the ^{235}U evaluation for ENDF/B-VI.3, these deficiencies were largely eliminated and have remained so through successive revisions. Regression coefficients based upon 42 calculated HST C/E values for $k_{\rm eff}$ from MCNP5 and the ENDF/B-VI.8 cross section data set are shown in Table XXIV.

TABLE XXIV: Linear regression coefficients for the above-thermal leakage fraction (ATLF) correlation of HST benchmark C/E values for $k_{\rm eff}$.

Cross section data set	Regression intercept, b_0 and its 95% confidence interval	Regression slope b_1 and its 95% confidence interval
ENDF/B-VI.8	1.0009 ± 0.0031	-0.0020 ± 0.0083
ENDF/B-VII.0	1.0008 ± 0.0032	-0.0011 ± 0.0085

Fig. 93 displays the calculated $k_{\rm eff}$ and the regression determined from these data. As seen in the Table, the ATLF ENDF/B-VI.8 regression intercept is 1.0009 ± 0.0031 while the slope is -0.0020 ± 0.0083. The uncertainties on these coefficients represent 95% confidence intervals. This intercept is statistically equivalent to unity, indicating no bias in C/E for $k_{\rm eff}$ for this class of critical benchmark. The slope is also statistically equivalent to zero, indicating the absence of an C/E $k_{\rm eff}$ trend versus ATLF for this class of benchmark. Similar results have been observed at Bettis and KAPL using their continuous energy Monte Carlo codes (RCP01 and RACER, respectively).

An important goal in developing the new ENDF/B-VII.0 library is to improve the data files while at the same time retaining the aforementioned good performance seen with ENDF/B-VI.8 (in the homogeneous solution benchmark category). This goal has been attained. Fig. 94 shows the same suite of HST benchmarks as displayed in Fig. 93, now calculated by MCNP5 with ENDF/B-VII.0 cross sections. The resulting regression coefficients are also presented in Table XXIV. The new intercept term is 1.0008 ± 0.0032, a result that remains statistically equivalent to unity while the new slope is -0.0011 ± 0.0085, a result that remains statistically equivalent to zero. These results have been confirmed with continuous energy Monte Carlo calculations at Bettis with the RCP01 code. For a similar suite of HST benchmarks, their regression coefficients are 1.0000 ± 0.0014 for the intercept and -0.0027 ± 0.0050 for the regression slope. Although not shown on these figures nor included in developing the regression coefficients, calculations have also been performed for a suite of 20 LST benchmarks (LST4, -7, -20 and -21). These configurations have ATLF values that range from ∼0.09 to ∼0.20 and ENDF/B-VII.0 calculated $k_{\rm eff}$ that range from 0.99780 ± 0.00009 to 1.00212 ± 0.00008; values that are within the predicted population 95% confidence interval for this regression. The consistency of the ENDF/B-VI.8 and ENDF/B-VII.0 cross section libraries for thermal solution benchmarks is also exhibited by noting that the average ENDF/B-VI.8 calculated $k_{\rm eff}$ for the suite of 62 (42 HST plus 20 LST) solution benchmarks is 1.0001 with a population standard deviation of 0.0039 while the corresponding ENDF/B-VII.0 average value is 1.0003 with a population standard deviation of 0.0040.

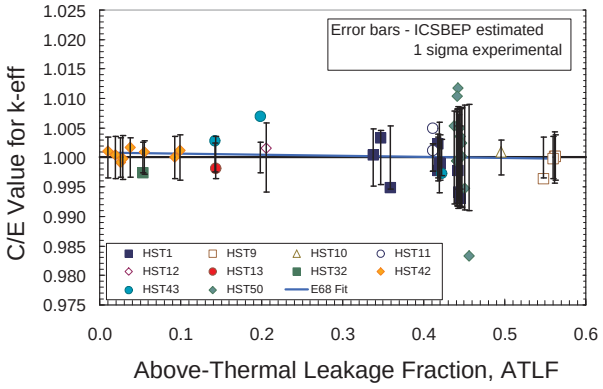

FIG. 93: HEU-SOL-THERM benchmark C/E values for $k_{\rm eff}$ with ENDF/B-VI.8 cross sections.

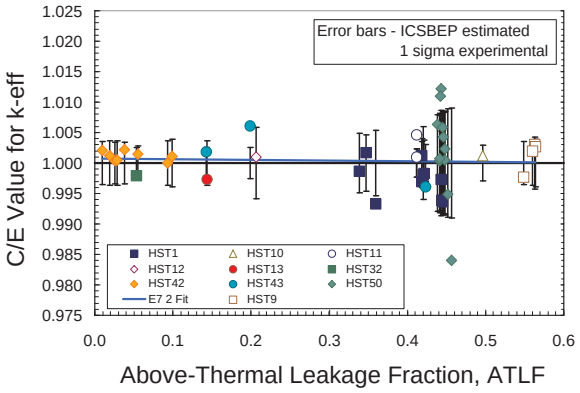

FIG. 94: HEU-SOL-THEM benchmark C/E values for $k_{\rm eff}$ with ENDF/B-VII.0 cross sections.

Therefore we can summarize that our ENDF/B-VII.0 library continues to perform very well for thermal ^{235}U high enriched and low enriched solution benchmarks. This result is nontrivial, since we have made changes in the ENDF/B-VII.0 library for ^{16}O (the n,α cross section was significantly reduced) and for Hydrogen (a new standard cross section, as well as an updated scattering kernel). Indeed, when one plots the results against ATLF, the ^{16}O and H changes separately did have a small impact upon the slope, but the two effects compensate one another to give the excellent final result illustrated in Fig. 94.

4. Thermal, low-enriched U fuel rod benchmarks

Our improvements to the ^{238}U cross section data in ENDF/B-VII.0 have led to major improvements in our ability to accurately calculate thermal low-enriched uranium benchmark C/E values for $k_{\rm eff}$, as discussed below.

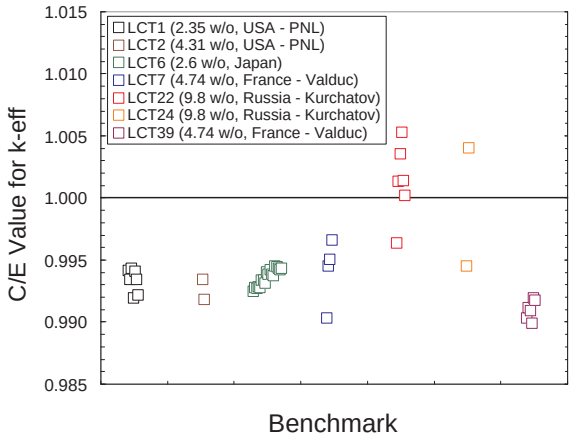

FIG. 95: LEU-COMP-THEM benchmark C/E values for $k_{\rm eff}$ with the old ENDF/B-VI.8 cross sections.

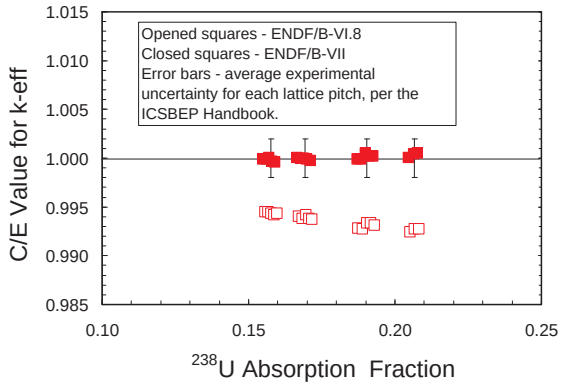

FIG. 96: LEU-COMP-THERM-006 benchmark C/E values for $k_{\rm eff}$ for the ENDF/B-VI.8 and ENDF/B-VII.0 cross sections.

Calculated C/E for $k_{\rm eff}$ for arrays of low-enriched UO_2 fuel rods have historically been biased low with previous data libraries including ENDF/B-VI.8, frequently falling 500 to 1000 pcm below unity. These C/E values for $k_{\rm eff}$ have also varied systematically when correlated against parameters such as rod pitch, average fission energy, unit cell H/U ratio or ^{238}U absorption fraction. Some of these characteristics are illustrated in Figs. 95, 96 and 97, which illustrate calculated $k_{\rm eff}$ obtained with MCNP5 and either ENDB/B-VI.8 and/or ENDF/B-VII.0 cross sections. Fig. 95 is a summary of 45 critical arrays from seven LCT evaluations that illustrates the generally poor C/E $k_{\rm eff}$ performance of ENDF/B-VI.8. These evaluations represent experiments from the United States (LCT1, LCT2), Japan (LCT6), France (LCT7, LCT39)

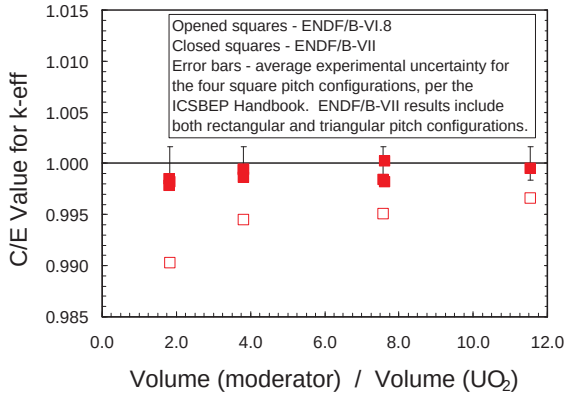

FIG. 97: LEU-COMP-THERM-007 benchmark C/E values for $k_{\rm eff}$ for the ENDF/B-VI.8 and ENDF/B-VII.0 cross sections.

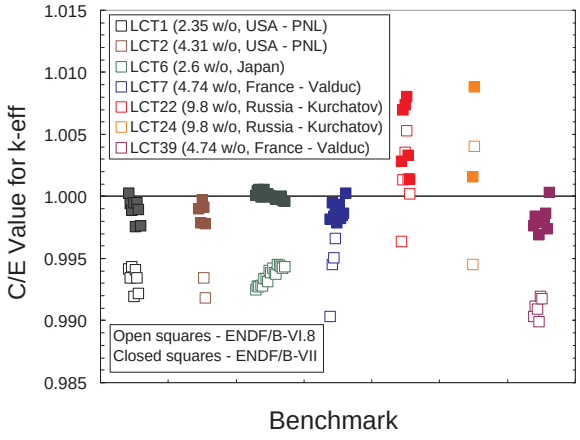

FIG. 98: LEU-COMP-THERM benchmark C/E values for $k_{\rm eff}$ for the ENDF/B-VI.8 and ENDF/B-VII.0 cross sections.

and Russia (LCT22, LCT24), with enrichments ranging from a low 2.3 w/o (weight %) ^{235}U to a maximum 10.0 w/o ^{235}U. Five of these seven benchmarks follow the historical trend of low C/E for $k_{\rm eff}$; only the two most highly enriched (LCT22 and LCT24) experiments yield calculated C/E values for $k_{\rm eff}$ that are greater than unity.

Fig. 96 illustrates how ENDF/B-VI.8 calculated $k_{\rm eff}$ vary as a function of ^{238}U absorption for the LCT6 benchmark series. This benchmark consists of 18 configurations, ranging in size from 15 x 15 rods to 21 x 21 rods. Multiple configurations exist at each of four basic rod pitch values, with water height used to control reactivity. The ENDF/B-VI.8 calculated $k_{\rm eff}$ are clearly low by at least 500 pcm, with a clear decreasing calculated $k_{\rm eff}$ trend with increasing ^{238}U absorption.

Fig. 97 illustrates how ENDF/B-VI.8 calculated $k_{\rm eff}$ vary as a function of rod pitch for the LCT7 benchmark series. This benchmark consists of 10 configurations, four set on a rectangular pitch that ranges from 1.26 cm to 2.52 cm. The remaining six configurations are set on a hexagonal pitch with rods arranged to yield a hexagonal or pseudo-cylindric shape when viewed from above. The hexagonal pitch varies from 1.35 cm to 2.26 cm; values that lead to similar sized unit cells in either rectangular or hexagonal space. In order to display these two geometry types on the same plot the abscissa presents the geometry data in terms of the unit cell moderator-to-fuel volume ratio. ENDF/B-VI.8 C/E values for $k_{\rm eff}$ have only been calculated for the four rectangular configurations, but exhibit a clear trend with unit cell moderator volume, exhibiting a bias of nearly -1000 pcm for the smallest pitch, decreasing to approximately -350 pcm for the largest pitch.

The average ENDF/B-VI.8 calculated $k_{\rm eff}$ for the 45 critical configurations from these seven benchmark evaluations is 0.9945 with a population standard deviation of 0.0035.

Results using the new ENDF/B-VII.0 cross sections are significantly more accurate, as shown in Figs. 96, 97 and 98. Fig. 96, described previously, illustrates calculated $k_{\rm eff}$ for the LCT6 benchmark with both ENDF/B-VI.8 and ENDF/B-VII.0 cross sections. The ENDF/B-VI.8 C/E values for $k_{\rm eff}$ trend and bias have both been eliminated with the ENDF/B-VII.0 cross section data set. Similarly, Fig. 97, also described previously, illustrates calculated $k_{\rm eff}$ for the LCT7 benchmark with both ENDF/B-VI.8 and ENDF/B-VII.0 cross sections. Once again the ENDF/B VI.8 C/E for $k_{\rm eff}$ trend and bias have both been eliminated with the ENDF/B-VII.0 cross section data set. Fig. 98 is similar to Fig. 95 and provides a summary of all water moderator and reflected LCT calculated $k_{\rm eff}$ calculated with MCNP5 at LANL. Previously identified deficiencies have been largely eliminated, although the LCT22 and LCT24 benchmark C/E values for $k_{\rm eff}$ remain too high. A total of 58 LEU-COMP-THERM benchmarks have been calculated with the ENDF/B-VII.0 cross section data set. The average calculated $k_{\rm eff}$ is 1.0000 with a population standard deviation of 0.0025. This standard deviation represents a significant decrease over that obtained with ENDF/B-VI.8 cross sections and is further evidence for the reduction or elimination in C/E $k_{\rm eff}$ trends, such as versus ^{238}U absorption fraction (Fig. 96) or versus H/U ratio (Fig. 97), with the ENDF/B-VII.0 cross section data set.

The ENDF/B-VII.0 cross section changes that are responsible for the improved C/E $k_{\rm eff}$ are due primarily (i) ORNL and CEA ^{238}U revisions in the resonance range for ^{238}U embodied in the "ORNL5" evaluation, and (ii) the new Los Alamos analysis of ^{238}U inelastic scattering in the fast region. The contribution to the increased calculated criticality of these two revisions are of about the same magnitude. Two additional cross section changes also contributed to increase the calculated $k_{\rm eff}$ of these assemblies: the reduced ^{16}O(n,α) cross section, and a revised scattering kernel for hydrogen bound in water.

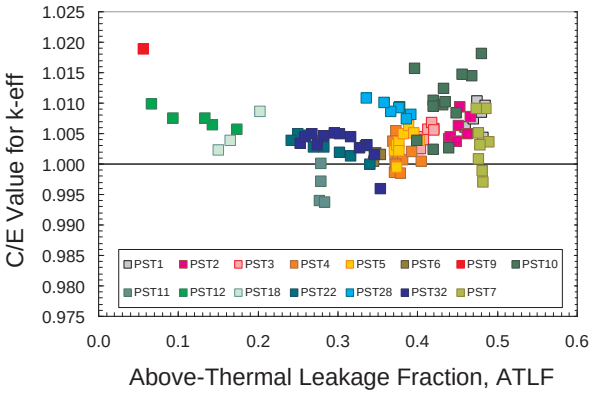

FIG. 99: PU-SOL-THERM benchmark C/E values for $k_{\rm eff}$ with ENDF/B-VII.0 cross sections as a function of the above-thermal leakage fraction.

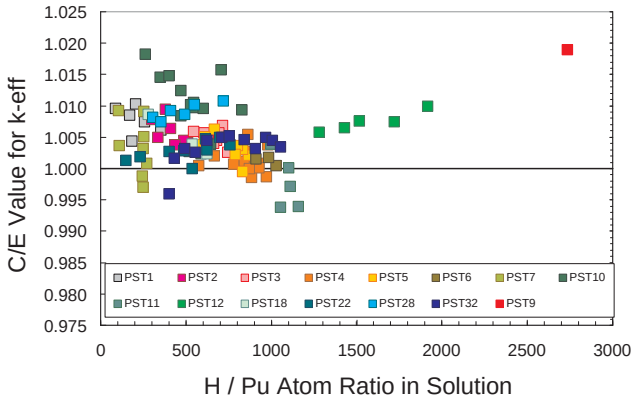

FIG. 100: PU-SOL-THERM benchmark C/E values for $k_{\rm eff}$ with ENDF/B-VII.0 cross sections as a function of the H/Pu ratio.

5. *Thermal Pu solution and MOX benchmarks*

While excellent calculated $k_{\rm eff}$ results continue to be obtained for thermal uranium solution critical assemblies, the same cannot be said for plutonium solution (PU-SOL-THERM, or PST) assemblies. Indeed, although ENDF/B-VII.0 includes Los Alamos improvements to the ^{239}Pu cross sections in the fast region, there has been no recent work on ^{239}Pu at lower energies. For this benchmark category, 109 critical assemblies from 14 ICSBEP evaluations have been calculated (PST1, -2, -3, -4, -5, -6, -7, -9, -10, -12, -18, -22, -28 and -32; note that PST18 has only recently been approved by the ICSBEP and will appear in the 2006 edition of the Handbook). The benchmarks represent experimental programs from the United States (Pacific Northwest Laboratory) and France (Valduc). The average MCNP5 C/E value for $k_{\rm eff}$, with ENDF/B-VI.8 cross sections, is 1.0039 with a population standard deviation of 0.0043. The range of calculated $k_{\rm eff}$ spans approximately 1.5%, with a low of 0.9941 and a maximum of 1.0194. When switching to ENDF/B-VII.0 cross sections there is little change. The average MCNP5 C/E value for $k_{\rm eff}$ increases by about 100 pcm to 1.0048 with a population standard deviation of 0.0045. The range of calculated $k_{\rm eff}$ is little changed; a low of 0.9938 and a high of 1.0189.

MCNP5 C/E values for $k_{\rm eff}$, calculated with ENDF/B-VII.0 cross sections are plotted versus ATLF, versus H/Pu ratio and versus ^{239}Pu atom percent of Pu in solution in Figs. 99, 100 and 101 respectively. There are obvious variations in these C/E values for $k_{\rm eff}$ when plotted versus ATLF or H/Pu ratio, but it is not obvious what changes in the plutonium cross section evaluation that could also be supported by the underlying microscopic experimental cross section data would mitigate these trends. It is unlikely that revisions are needed in the other important nuclides, namely hydrogen and

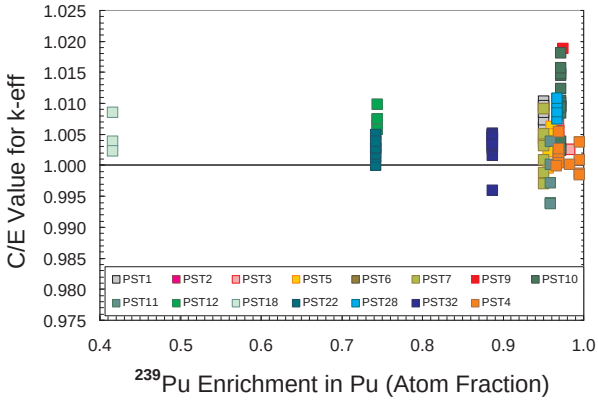

FIG. 101: PU-SOL-THERM benchmark C/E values for $k_{\rm eff}$ with ENDF/B-VII.0 cross sections as a function of the ^{239}Pu enrichment.

oxygen, given the excellent C/E $k_{\rm eff}$ results obtained for uranium solution systems. The plot versus ^{239}Pu/Pu is the cleanest, showing little variation as a function of ^{239}Pu fraction. This suggests that the deficiencies are not principally due to another Pu isotope such as ^{240}Pu. Note that in this plot the C/E for $k_{\rm eff}$ obtained for the PU-SOL-THERM-018 benchmark models (cases 4, 8 and 9), which represent the lowest ^{239}Pu atom per cent, are preliminary. This evaluation has only recently been approved for publication in the 2006 edition of the ICSBEP Handbook and the calculations shown here are based upon a draft, pre-publication, version of this evaluation. As noted previously, all other models are derived from benchmark specifications published in the 2005 edition of the Handbook.

The results for a MOX benchmark, six critical configurations from MIX-COMP-THERM-002, show less varia-

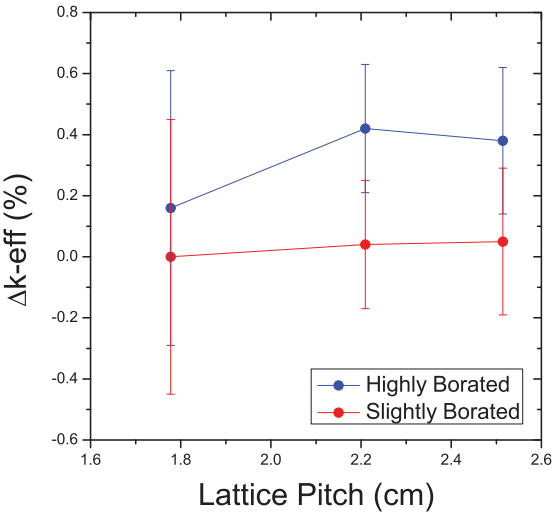

FIG. 102: Reactivity biases for slightly and heavily borated MOX benchmarks.

tion than the solutions, possibly because there are fewer of them. The fuel pins contain 2 wt.% MOX, and the plutonium contains 8% ^{240}Pu. The benchmarks include a highly (several hundred ppm) borated case and a slightly (a few ppm) borated case for each of three lattice pitches. The highly borated cases contain many more fuel pins than the slightly borated cases. As Fig. 102 shows, the slightly borated cases all fall within the reported benchmark uncertainty. The highly borated cases exhibit a small positive bias, but all three fall within a band of about a quarter of a percent in reactivity.

6. ^{233}U and ^{232}Th data testing

Data testing for ^{233}U in the fast range was shown in Fig. 86, see Jezebel 23 and Flattop 23. The fast region ^{233}U cross section improvement coming from our recent Los Alamos GNASH/ECIS calculations have led to the dramatic improvement over ENDF/B-VI.8 seen in the figure. Improvements for lower energy assemblies have come from the recent Oak Ridge ^{233}U resonance analysis, as is discussed below.

The U233-COMP-THERM-001 (UCT1) benchmark has been calculated to test the new ^{233}U and ^{232}Th evaluations. This benchmark consists of a series of either $^{235}UO_2$ seed rods surrounded by a blanket of $^{232}ThO_2$ rods (cases 1 and 6) or a blanket of $^{233}UO_2$–$^{232}ThO_2$ blanket rods (case 5), or $^{233}UO_2$ seed rods in water (case 3), surrounded by $^{233}UO_2$–$^{232}ThO_2$ blanket rods (cases 4 and 8) or surrounded by $^{232}ThO_2$ blanket rods (cases 2 and 7). MCNP calculations for these benchmarks have been performed by several analysts, using ENDF/B-VII.0 cross sections, or a close variation thereof and are presented in Table XXV. In particular, it is known that the preliminary ENDF/B-VII (beta2) ^{233}U nu-bar data does not match the recommended Standards value. This mis-match will be rectified prior to the final release of ENDF/B-VII.0 and C/E $k_{\rm eff}$ calculations with and without these latest data are presented in the Table XXV.

Comparisons among these calculations are generally good. The LANL/IAEA difference in Case 3 is surprisingly large, but since this benchmark is for seed rods in water only, and the water kernels used by the IAEA are slightly different than those in ENDF/B-VII.0, it is difficult to conclude that one model may need adjustment. The LANL/Petten difference in Case 8 is more severe, particularly since the similar Case 4 comparison is satisfactory. Investigations of this difference are continuing. In any event, the average C/E value for $k_{\rm eff}$ obtained for these benchmark cases are generally closer to unity than those obtained with calculations using the older, ENDF/B-VI.8, cross section data library.

7. ^{237}Np data testing

The new ^{237}Np cross sections have been tested in the fast region through comparisons with criticality predictions for the LANL composite spherical ^{237}Np-HEU assembly (SPEC-MET-FAST-008). This critical assembly consists of an ∼6kg ^{237}Np core surrounded by ∼60 kg of HEU. We calculate C/E=0.9954 for this assembly, a significant improvement over calculations that use ENDF/B-VI.8 data (C/E=0.9889). This improvement is due to both increases in the ^{237}Np fission cross section below ∼ 1 MeV (based on recent LANSCE fission cross section measurements), and in the ^{235}U data (which is more reactive compared to the earlier ENDF/B-VI.8 ^{235}U evaluation, as demonstrated above with the improved Godiva C/E $k_{\rm eff}$ calculation). We believe the remaining underprediction in the C/E values for this composite assembly may be due to the calculated surrounding ^{235}U driver neutron spectrum being too soft, thus leading to too few fissions in the ^{237}Np core. This supposition is supported, as is discussed below, by noting that calculated spectral indices for $^{238}U_f$/ $^{235}U_f$, and $^{237}Np_f$ /$^{235}U_f$ in Godiva are underpredicted by several percent. This suggests that the calculated neutron spectrum in HEU is too soft, possibly reflecting deficiencies in the ^{235}U inelastic cross sections or in the ^{235}U prompt fission neutron spectrum energy dependence.

8. D_2O data testing

During post-release testing of ENDF/B-VI.8 at LANL, it was discovered that the MCNP5 values for $k_{\rm eff}$ calculated for two series of HEU solution thermal critical experiments (HEU-SOL-THERM-004, or HST-004, and HST020 in the ICSBEP handbook) involving D_2O had decreased by about 1000 pcm relative to calculations per-

TABLE XXV: MCNP C/E values for $k_{\rm eff}$ for the U233-COMP-THERM-001 benchmark. No uncertainties are provided for the IAEA values. The large differences seen in case 8 between LANL and Petten and in case 3 between LANL and IAEA remain under investigation.

Benchmark Name and Configuration	LANL with ENDF/B-VII.0	Petten with ENDF/B-VII.0	LANL with ENDF/B-VII.0 plus ^{233}U Standards nubar	IAEA with ENDF/B-VII.0 plus ^{233}U Standards nubar but JEFF-3.1 H-H_2O kernel
UCT1, case 1 (SB-1)	0.99902(19)	0.99853(100)	0.99902(19)	0.99947
UCT1, case 2 (SB-2)	1.00372(21)	1.00341(103)	1.00138(21)	1.00123
UCT1, case 3 (SB-2.5)	1.00450(20)	1.00511(110)	1.00244(21)	1.00023
UCT1, case 4 (SB-3)	1.00301(17)	1.00198(92)	1.00058(17)	1.00040
UCT1, case 5 (SB-4)	0.99993(16)	0.99921(74)	0.99908(16)	0.99935
UCT1, case 6 (SB-5)	0.99783(18)	0.99944(95)	0.99783(18)	0.99907
UCT1, case 7 (SB-6)	1.00529(20)	1.00552(91)	1.00261(21)	1.00400
UCT1, case 8 (SB-7)	1.00297(18)	0.99934(84)	1.00027(18)	1.00092

formed with data for deuterium from ENDF/B-VI.4 and earlier releases. This decrease is caused by revisions to the energy-angle probability distributions for (n,d) elastic scattering at energies < 3.2 MeV, based on a coupled channels R-matrix analysis. Calculations performed using JENDL-3.3 deuterium data, for which the scattering distributions are obtained using a Faddeev three-body scattering formalism, produce eigeinvalues closer to those obtained using the older ENDF/B-VI data.

The HST assessments were supplemented by analyses of modern critical experiments performed in the ZED-2 reactor at the Chalk River Laboratories. These experiments involved various heterogeneous, low-leakage configurations of natural uranium (NU) fuel rods immersed in D_2O moderator. The results showed low reactivity sensitivity (< 100 pcm) to the deuterium nuclear data libraries, due to the much greater influence of ^{238}U in NU systems, but a small systematic shift of about 60 pcm in the difference between the calculation bias for configurations with fuel channels filled with D_2O or air as coolant, which lent support to the ENDF/B-VI.8 deuterium data.

Nevertheless, both the HST and ZED-2 results exhibit systematic trends as a function of calculated leakage, suggesting that further revision to the ENDF/B-VI.8 deuterium energy-angle elastic scattering data (which has been retained in ENDF/B-VII.0) may be beneficial. Moreover, the available (n,d) scattering experimental data were reviewed and found to be old, sparse and inconsistent. Additionally, few-nucleon theoretical models have advanced considerably, along with computational resources, such that very precise numerical calculations can now be performed for processes and systems involving three or fewer nucleons. Thus, new calculations based on solving the Alt-Grassberger-Sandhas (AGS) equation (an alternative, but equivalent, formulation to that of Faddeev) are in progress for (n,d) scattering and consideration is being given to undertake modern confirmatory measurements. It is anticipated that an improved energy-angle (n,d) scattering distribution for deuterium will be issued in a future release of ENDF/B-VII.

Notably, ENDF/B-VII.0 also includes revised thermal scattering law, S(α,β), data for deuterium bound in D_2O, based on the work of Mattes and Keinert [6]. Preliminary testing indicates relatively low reactivity impact (typically < 100 pcm), but an increasing trend with D/^{235}U atom ratio that reaches up to about +250 pcm in the high-leakage HST-020 critical experiments involving unreflected cylinders.

9. Replicate calculations for verification

A number of the ICSBEP benchmarks have been calculated by two or more analysts. In particular, S. van der Marck (Petten) has determined ENDF/B-VII.0 C/E values for $k_{\rm eff}$ for a test suite of 723 critical benchmarks. A separate report describing this work appears elsewhere in the Nuclear Data Sheets [277]. Of the several hundred ICSBEP benchmarks calculated at LANL, 218 are in common with the Petten work. Extensive intercomparison of our work is ongoing, but excellent agreement is observed among these common calculations, with approximately 2/3 of the Petten/LANL C/E $k_{\rm eff}$ ratios falling between 0.999 and 1.001. Approximately 10% of the ratios are either below 0.9985 or exceed 1.0015. The minimum Petten/LANL C/E value for $k_{\rm eff}$ ratio is 0.9964 and the maximum is 1.0024. These maximum deviations from unity are large enough to suggest fundamental differences in our respective benchmark models and are under review.

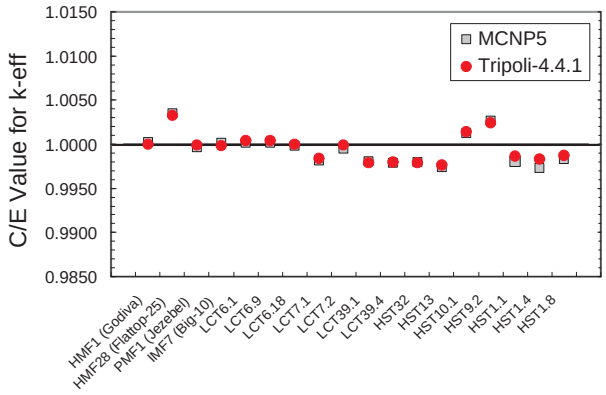

FIG. 103: MCNP5 and Tripoli-4.4.1 benchmark C/E values for $k_{\rm eff}$ with ENDF/B-VII.0. Excellent agreement is seen between these two independent calculations.

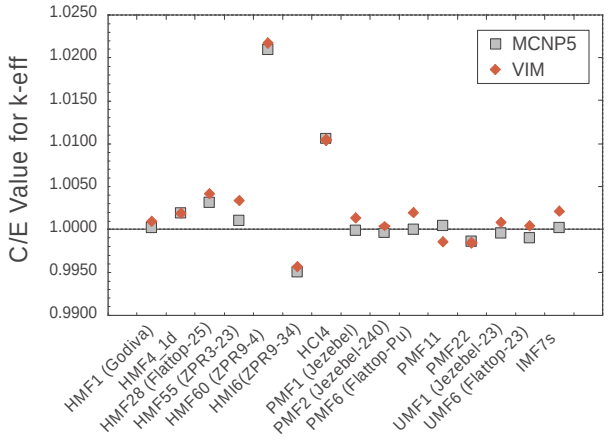

FIG. 104: C/E values for $k_{\rm eff}$ obtained with MCNP5 and VIM using ENDF/B-VII.0. Excellent agreement is seen between these two independent calculations.

In addition, calculations by J. C. Sublet (CEA-Cadarache) with the Tripoli code have been performed for 42 benchmarks that have also been calculated at LANL. The agreement in these 42 common C/E values for $k_{\rm eff}$ is excellent, with the minimum CEA/LANL C/E $k_{\rm eff}$ ratio being 0.9996 and the maximum being 1.0010. Fig. 103 illustrates the Tripoli and MCNP5 C/E $k_{\rm eff}$ agreement for a sample of these 42 common benchmarks, including unmoderated HEU and Pu systems as well as water moderated low-enriched fuel rod array and highly-enriched uranium solution systems. The excellent agreement in C/E $k_{\rm eff}$ using the US/ Los Alamos MCNP5 transport code and the French/CEA TRIPOLI-4.4.1 code, evident in Fig. 103, provides an important verification of our respective Monte Carlo tools. These codes have been developed independently, although there have been important common collaborative transport methods efforts in recent years to resolve cases where discrepancies had existed between the two codes.

Because all of the above comparisons rely on Monte Carlo libraries processed by NJOY, they provide verification only of the physics modeling in these calculations. Independent verification of the data libraries and the physics models for all of these results is provided by the agreement of the MCNP results with results obtained by the Naval Reactors RCP01 (Bettis) and RACER (KAPL) Monte Carlo codes and the VIM (ANL) Monte Carlo code. VIM results were obtained for 52 of the ICSBEP benchmarks using ENDF/B-VII.0. Similar good agreement was also observed between MCNP and VIM, as displayed in Fig. 104. Of the 44 benchmarks calculated by both codes, 54% of the C/E values agreed within $\pm 1\sigma$, 91% within $\pm 2\sigma$, and 98% within $\pm 3\sigma$.

10. Summary of criticality testing by van der Marck

In a companion paper, Steven van der Marck, NRG Pettenprovides extensive independent validation criticality data testing for ENDF/B-VII.0. It is useful to summarize his results, and to show the overview summary tables he gives in Section III.C of Ref. [277].

Table XXVI provides a summary of 723 benchmark criticality experiments that were simulated and compared with measurements. We follow the notation defined in Ref. [277] and in the ICSBEP Handbook.

Table XXVII summarizes the average value of C/E-1 (the average deviation of Calculation/Experiment from unity) for these benchmarks, as calculated by van der Marck. The values given are for the preliminary ENDF/B-VII (beta2) library. These files are substantially equivalent to the final evaluated files released as ENDF/B-VII.0 so that conclusions and observations made here are applicable to ENDF/B-VII.0. We show for comparison in *italics* the values for the previous ENDF/B-VI.8. While it is important to study the individual benchmark results for a more thorough understanding, it is still very useful to observe the overall averaged behavior shown in Table XXVII. One can make the following observations:

- The low-enriched U compound benchmarks are modeled much more accurately now (owing to our work on ^{238}U, as well as ^{16}O and ^{1}H).
- The intermediate-enriched U benchmarks are modeled more accurately.
- The Pu and high-enriched U fast benchmarks are modeled more accurately.
- The ^{233}U thermal benchmarks are modeled more accurately. Although the ^{233}U fast benchmarks simulations appear to have become worse, this is

TABLE XXVI: The number of benchmarks per main ICSBEP category for compound, metal and solution systems with thermal, intermediate, fast and mixed neutron spectrum.

	COMP				MET				SOL	Total
	ther	inter	fast	mix	ther	inter	fast	mix	ther	
LEU	257				1				49	307
IEU	6	4					16			26
HEU		6			42	5	66	5	87	211
MIX	34		1				4		3	42
PU		1				1	7	6	105	120
^{233}U	8						4		5	17
Total	305	11	1	0	43	6	97	11	249	723

TABLE XXVII: The average value of $C/E - 1$ in pcm (100 pcm = 0.1%) for ENDF/B-VII.0 per main ICSBEP benchmark category. Shown in *italics* are the values for the ENDF/B-VI.8 library.

	COMP				MET				SOL
	ther	inter	fast	mix	ther	inter	fast	mix	ther
LEU	20				-99				137
	452				*-279*				*107*
IEU	55	254					167		
	-372	*-283*					*596*		
HEU		1791			55	69	-15	785	122
		1442			*-316*	*-42*	*11*	*462*	*287*
MIX	448		73				194		178
	347						*69*		*168*
PU		1095				4707	244	927	618
		967				*4654*	*426*	*745*	*531*
^{233}U	156						-348		311
	-380						*-338*		*-292*

perhaps more due to deficiencies in our modeling of beryllium for two of the assemblies studied - for bare ^{233}U (Jezebel-23) our new ENDF/B-VII.0 are clearly much better.

- Lower energy Pu benchmarks were modeled poorly in ENDF/B-VI.8 and continue to be modeled poorly in our new library.

11. Conclusions from criticality testing

Hundreds of criticality benchmarks from the ICSBEP Handbook have been calculated to test the accuracy of the ENDF/B-VII.0 cross section library. Significant improvement in C/E values for $k_{\rm eff}$ has been observed in many cases, including bare and reflected fast uranium and plutonium systems and in particular for arrays of low-enriched fuel rod lattices. The C/E values for $k_{\rm eff}$ for bare HEU and Pu assemblies are larger compared to those obtained with ENDF/B-VI.8 data, and now agree very well with the measurements. The reflector bias for the ^{238}U reflected Flattop assemblies has been largely eliminated.

Furthermore, major improvements have been obtained in our calculations for intermediate energy assemblies such as Big-10 and, to a lesser extent, the Argonne ZPR assemblies. Homogeneous uranium solution systems have been calculated accurately with the last several versions of ENDF/B-VI cross sections, and these accurate results are retained with the ENDF/B-VII.0 cross section library. Many fast reflected systems are more accurately calculated with the ENDF/B-VII.0 cross section library, but disturbing discrepancies remain, particularly in lead and beryllium reflected systems (although certain reflector-bias improvements were obtained using our new data for these isotopes).

A significant accomplishment has been our excellent C/E for $k_{\rm eff}$ for the LCT assemblies, where the historical underprediction of criticality has been removed. This advance has come from our improved ^{238}U evaluation (both in the resonance region and in the fast region), together with revisions to the ^{16}O(n,α) cross section and the hydrogen bound in water scattering kernel. Plutonium solution systems are not calculated as well as uranium solutions, with C/E values for $k_{\rm eff}$ typically being several tenths of a per cent greater than unity. There is a 1.5% spread in these C/E values for $k_{\rm eff}$, but there does not appear to be a trend as a function of ^{239}Pu abundance. Although advances have been made at Los Alamos to the ^{239}Pu cross sections in the fast region, there has been no recent work on ^{239}Pu at lower energies clearly - such efforts are needed in the future.

Finally, we note that the performance of our new ENDF/B-VII.0 evaluations for ^{233}U and ^{232}Th is much improved in both fast and thermal critical assemblies, and that an analysis of the Np-U composite fast benchmark suggests important improvements have been made in our ^{237}Np fission cross section evaluation.

C. Delayed neutron testing, $\beta_{\rm eff}$

Delayed neutron data can be tested against measurements of the effective delayed neutron fraction $\beta_{\rm eff}$ in critical configurations. Unlike the situation for $k_{\rm eff}$, only a handful of measurements of $\beta_{\rm eff}$ have been reported in open literature with sufficiently detailed information. In Ref. [277] more than twenty measurements are listed, including several measurements of α, which is closely related to $\beta_{\rm eff}$ through the prompt neutron generation life time. Here we restrict ourselves to measurements of $\beta_{\rm eff}$ only, and then only the ones that are deemed most suitable for nuclear data testing. We avoid the term 'benchmark' for these cases, because a good benchmark description, comparable to those given in the ICSBEP Handbook, is not available.

We have chosen two thermal spectrum cores, and five fast spectrum ones, as listed below.

TCA: A light water moderated low-enriched UO_2 core

in the Tank-type Critical Assembly [154]. This core is closely related to benchmark LCT6 [85], but the loading pattern is different, as are the pitch and the water height.

IPEN/MB-01: A core consisting of 28 × 26 UO_2 (4.3% enriched) fuel rods inside a light water filled tank [278]. An MCNP model was kindly provided by the authors of Ref. [278].

Masurca: Measurements of $\beta_{\rm eff}$ by several international groups in two unmoderated cores in Masurca, viz. R2 and ZONA2. Core R2 had ∼30% enriched uranium as fuel, whereas ZONA2 had both plutonium and depleted uranium. Both cores were surrounded by a 50-50% UO_2-Na mixture blanket, and by steel shielding. R-Z model descriptions are given in Ref. [279].

FCA: Measurements of $\beta_{\rm eff}$ by several international groups in three unmoderated cores in the Fast Critical Assembly, namely, core XIX-1, XIX-2, and XIX-3. On core had highly enriched uranium, one had plutonium and natural uranium, and the third had plutonium as fuel. The cores were surrounded by two blanket regions, one with depleted uranium oxide and sodium, the other with only depleted uranium metal. R-Z model descriptions are given in Ref. [279].

Note that for a thermal spectrum, only the ^{235}U delayed neutron data are tested by these calculations, whereas for a fast spectrum both ^{235}U and ^{239}Pu data are tested.

The calculation of $\beta_{\rm eff}$ for these systems was done using a version of MCNP-4C3 with an extra option added to it as described in Ref. [280]. This method was used earlier to test delayed neutron data from JEFF-3.1 and JENDL-3.3 [281]. The results based on ENDF/B-VII.0 are given in Table XXVIII, as well as the results based on those other libraries.

D. Reaction rates in critical assemblies

The fast critical assemblies at the Los Alamos Critical Experiment Facility (LACEF), at TA-18, represent a unique capability within the DOE/NNSA complex for studying nuclear criticality. Measurements over the last 50 years at LACEF have provided integral data that provide important tests of fundamental nuclear cross sections. It is widely known that measurements of the criticality ("$k_{\rm eff}$") of a system can be used to test certain aspects of the fundamental nuclear data, as we discussed in the last subsection. In this subsection we discuss a less well-known use of critical assemblies, where they have been used to measure reaction rates of certain important nuclear processes within the neutron spectrum provided by the assembly, to provide important integral tests of the underlying nuclear cross section databases that we develop.

Many different critical assemblies have been developed over the years: Godiva is a bare sphere of highly-enriched uranium (HEU); Jezebel is a bare sphere of plutonium; Jezebel 23 is a bare sphere of ^{233}U. The Flattop experiments involved spherical cores of HEU or plutonium surrounded by ^{238}U reflector material to make the composite systems critical. These different systems all produce neutron spectra within them that are "fast", i.e. the neutrons are predominantly of energies in the 100 keV - few MeV region, but the exact spectra vary from system to system. Holes were drilled into the critical assemblies to allow foils of different materials to be placed, such that they are exposed to different neutron spectra depending upon their location. An assembly with a softer neutron spectrum is Big-10, which was made of large amounts of ^{238}U and ^{235}U.

The neutron spectrum gets softer as one moves out from the center of the assembly, thereby giving additional information about the quality of the cross section data in different energy regimes. An example of these data for ^{238}U(n,f) and (n,2n) as taken in the Flattop-25 and Topsy assemblies is shown in Fig. 105. (Topsy was an early mockup of a ^{235}U core reflected by natural uranium made by stacking cubes of material—its geometry is not as clean as the later Flattop experiment.) The calculations were done using multigroup methods based on MATXS cross sections from NJOY formatted with TRANSX for PARTISN. A very fine group structure with 1/16-lethargy intervals in the fast region was used for high accuracy. The multigroup results were checked by tallying in several 1-cm shells using MCNP5, and good agreement was obtained. Fig. 106 for ^{238}U(n,2n) shows a different presentation of these data in a form often used by radiochemists. The abscissa is a measure of the hardness of the spectrum, and this kind of plot often allows data from different assemblies to be compared on a common basis. This is demonstrated here using data from Flattop-25 and Topsy. Note how the calculated central ratio for Big-10 also fits into this kind of plot.

These comparisons of prediction with experiment provide some confidence in the quality of the ^{238}U(n,2n) cross section - both its magnitude and its energy-dependence. The overprediction (Fig. 106) of the measurements at lower spectral index values (though not for Big-10) suggests that our ^{238}U(n,2n) cross section close to its threshold may be too high, see Fig. 28. But other considerations in experiment (a desire to follow LANL radiochemistry measurement by Knight for the (n,2n) rise from threshold, and the LANL value by Barr at 14.1 MeV) led us to the evaluated data shown in Fig. 28.

In Fig. 107 we show a calculation compared with experimental values for ^{238}U neutron capture. Good agreement is found for most of the critical assembly measurements, though for harder-spectrum systems (large values of 238-fission/235-fission) there is an indication of an under prediction of the data by 5-10%. This is valuable information as it tells us that a new study of ^{238}U neutron capture in the ≈ 1 MeV region is needed. However, we

TABLE XXVIII: C/E values for $\beta_{\rm eff}$ of several critical systems, using ENDF/B-VII.0 and other nuclear data libraries. The uncertainties in the C/E values are statistical uncertainties from the calculations only.

System	Experiment	C/E			
		ENDF/B-VII.0	ENDF/B-VI.8	JEFF-3.1	JENDL-3.3
TCA	771 ± 17	1.042 ± 0.002	1.053 ± 0.011	1.029 ± 0.002	0.987 ± 0.012
IPEN/MB-01	742 ± 7	1.057 ± 0.005	1.054 ± 0.005	1.040 ± 0.005	1.019 ± 0.005
Masurca R2	721 ± 11	1.010 ± 0.009	1.035 ± 0.009	1.011 ± 0.009	1.018 ± 0.010
Masurca ZONA2	349 ± 6	0.948 ± 0.014	0.983 ± 0.015	1.021 ± 0.013	0.994 ± 0.014
FCA XIX-1	742 ± 24	0.996 ± 0.010	1.005 ± 0.011	1.010 ± 0.010	0.985 ± 0.011
FCA XIX-2	364 ± 9	1.007 ± 0.013	1.003 ± 0.014	1.054 ± 0.013	1.022 ± 0.013
FCA XIX-3	251 ± 4	0.988 ± 0.017	1.016 ± 0.016	0.997 ± 0.016	0.996 ± 0.016

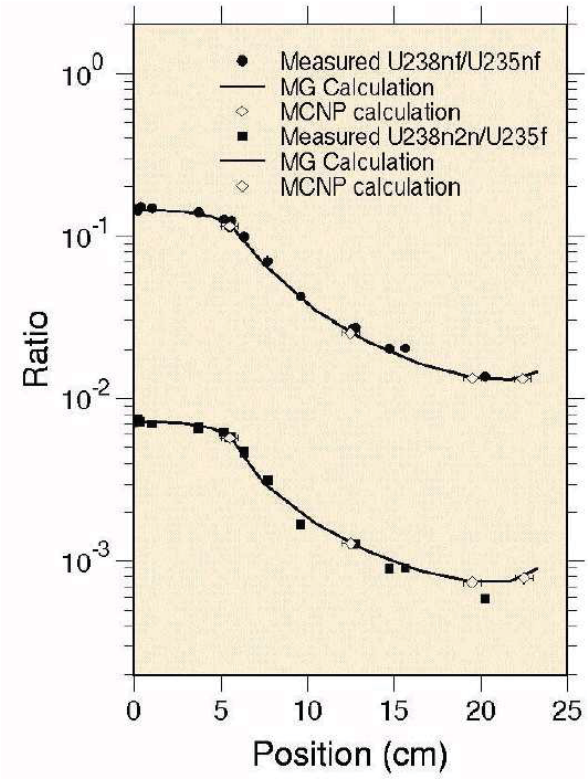

FIG. 105: Comparison of experimental radiochemical data from Flattop-25 and Topsy with calculated values for a radial traverse in the Flattop-25 assembly. The ratio of the ^{238}U(n,f) reaction rate to the ^{235}U(n,f) reaction rate (upper curve) and the ratio of the ^{238}U(n,2n) reaction rate to the ^{235}U(n,f) reaction rate (lower curve) are plotted versus radius.

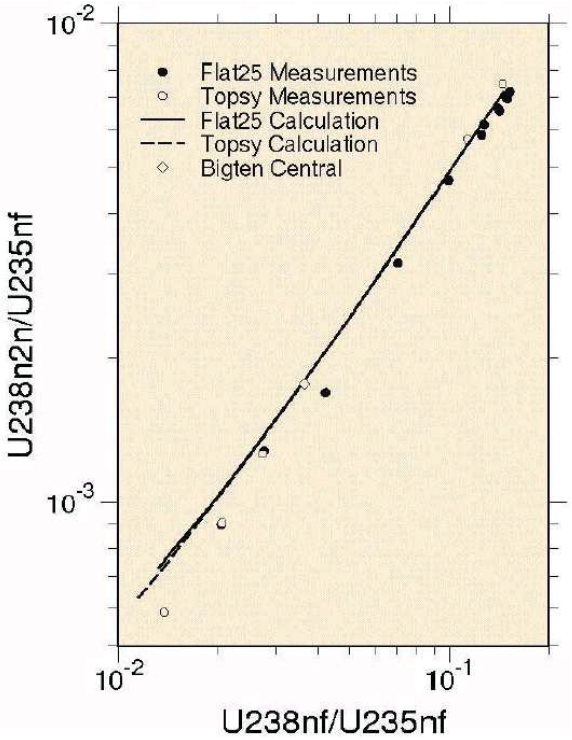

FIG. 106: Comparison of experimental radiochemical and calculated values for radial traverses in the Flattop-25 and Topsy assemblies. The ratio of the ^{238}U(n,2n) reaction rate to the ^{235}U fission rate is plotted against the ratio of the ^{238}U fission rate to the ^{235}U fission rate for different positions (with central positions to the right and positions in the reflector to the left). The abscissa is a measure of the hardness of the spectrum at that position. The Big-10 result is computed at the center of the assembly.

note that the fundamental ^{238}U(n,γ) data from the standards project are believed to be accurate better than 3% over the range $E_n = 10^{-4}$ to 2.2 MeV, see Section III.B.3.

Neutron capture on ^{241}Am is shown in Fig. 108, for different critical assembly spectra. In this reaction, the capture can lead to both an isomeric and ground state in ^{242}Am. It is the ground state that beta decays relatively quickly to make ^{242}Cm, which is then measured by radiochemists. Again, we see good agreement between the calculations and the measurements, except that for the hardest-spectrum system (Jezebel) the measurement appears to be underpredicted by up to 15%. This tells us that the ^{241}Am capture cross section to the ground state may be too low in our current evaluation in the ≈ 0.5 - 1 MeV region - something that we are currently studying using theory and experiment in new LANL project on americium.

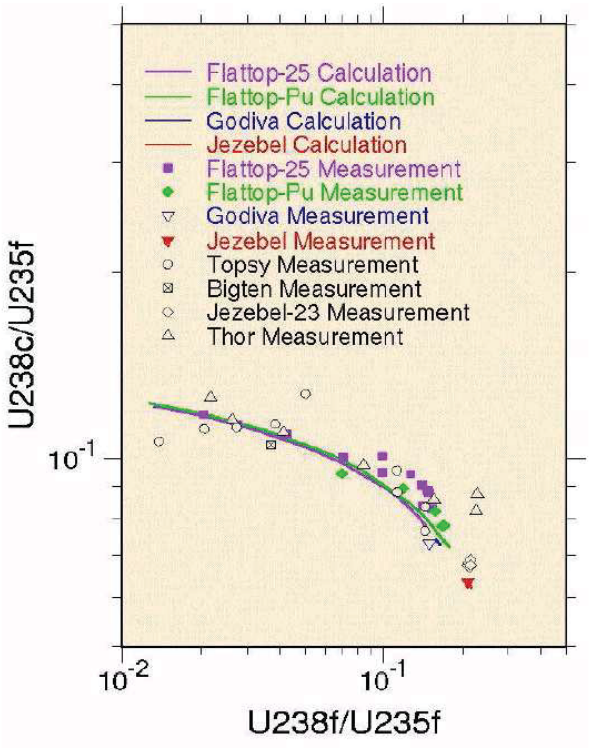

FIG. 107: The integral ^{238}U neutron capture rate (divided by the ^{235}U fission rate) as a function of spectral index for different critical assembly locations.

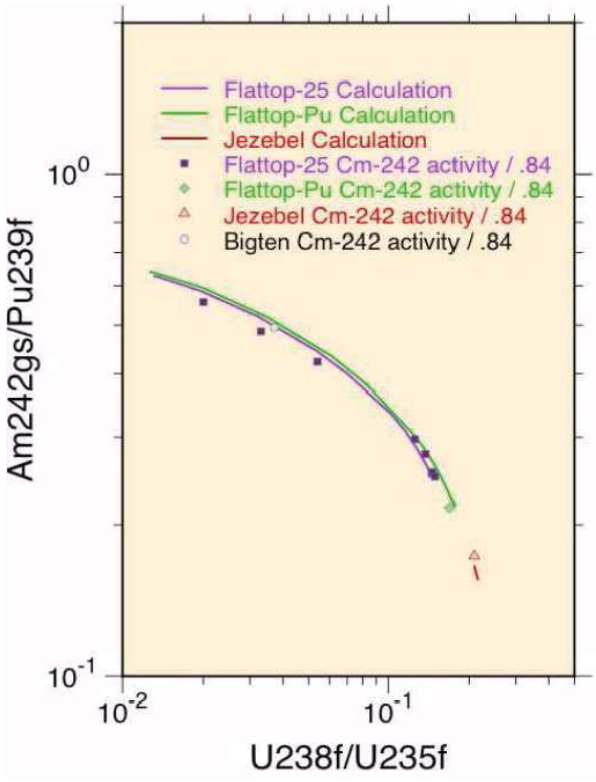

FIG. 108: The integral ^{241}Am neutron capture rate (divided by the ^{239}Pu fission rate) as a function of spectral index for different critical assembly locations. In this case the measurements, which detect the ^{241}Cm are divided by 0.84 to account for the fraction of ^{241}Am that beta decays to ^{241}Cm.

Finally, in Fig. 109 we show some important reaction rates for iridium: the ^{193}Ir(n,n') cross section for creating the isomer, and the ^{191}Ir(n,γ) cross section. A new evaluation for the iridium cross sections has been recently completed. The good integral testing performance shown in this figure provides some confidence in the accuracy of the new iridium cross sections. Again, the fact that the calculation predicts reasonably well the shape of the (n,n') isomer reaction provides confidence in the energy-dependence obtained from the recent T-16/LANSCE cross section evaluations incorporated into ENDF/B-VII.0.

For the reaction rates for fission at the center of various Los Alamos fast critical assemblies, we present our calculated results using ENDF/B-VII.0 data, in ratio to the ^{235}U fission rate. Such fission rate ratios are known as spectral indices, and when the numerator is for a threshold fissioner, such as ^{238}U or ^{237}Np, the ratio is a measure of the hardness of the neutron spectrum within the assembly. For example, the 238Uf/235Uf spectral index is higher at the center of Jezebel (0.21) than at the center of Godiva (0.16), reflecting a hotter neutron spectrum in a plutonium assembly compared to a HEU assembly. Table XXIX compares our calculated spectral indices with measured data. The measurements are typically made using either fission chambers that detect the recoiling fission fragments, or with activation methods that count fission products using radiochemical methods (the former method being more precise). Providing experimental values for fission rate ratios enables these spectral indices to be measured rather precisely, typically to 1-2%.

Comparisons between calculation and measurement provides a test of the cross sections and of the critical assembly calculated neutron spectrum (and its energy dependence) as calculated by MCNP. It is evident from Table XXIX that the calculated values agree with measurement very well, often within the (small) experimental uncertainties quoted. A notable exception is for Godiva, where the 238Uf/235Uf spectral index is calculated 4% low (over three standard deviations). Since these cross sections in the fast range are thought to be accurate to about a percent or better in the fast range, this discrepancy is hard to understand. A possible explanation is that it reflects deficiencies in the calculated neutron spectrum in HEU, the calculated spectrum being possibly too soft - and since ^{238}U has a fission threshold of about 1 MeV, such a deficiency would lead to an underpredicted spectral index. This would then point to future work needed to improve the ^{235}U cross sections that influence the HEU assembly neutron spectrum, such as the inelastic scattering cross sections or the prompt fission spectrum energy dependence. The same issues can be seen for the 237Npf/235Uf spectral index in Godiva - ^{237}Np

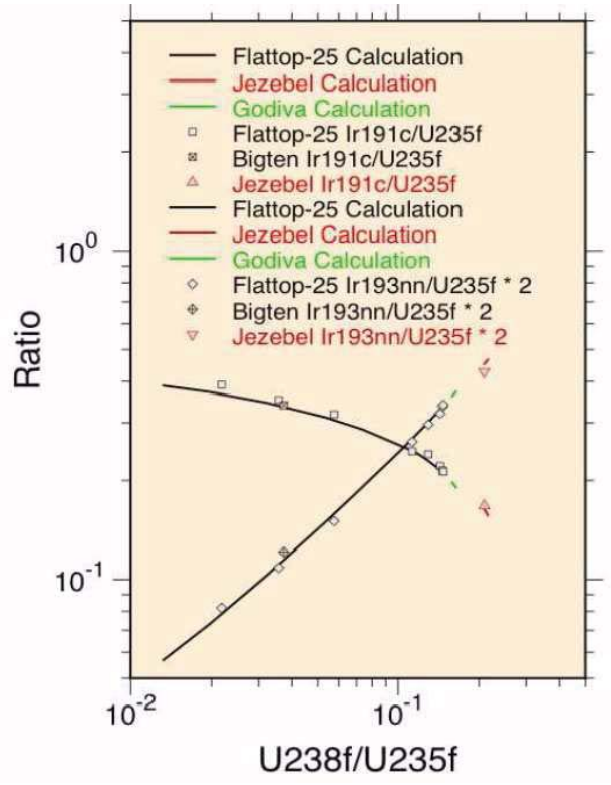

FIG. 109: The integral ^{193}Ir(n,n')^{193m}Ir isomer production rate (divided by the ^{239}Pu fission rate), as well as the ^{191}Ir(n,γ)^{192}Ir production rate (divided by the ^{239}Pu fission rate), as a function of spectral index, for different critical assembly locations. The former (n,n') rate is for the upward sloping curve in the figure, the latter (capture) is for the downward slope. The raw (n,n') measured data are multiplied by a factor of 2, to account for the detector efficiency here.

is another threshold fissioner, with a threshold of about 0.6 MeV.

In Table XXX we provide some other calculated reaction rates in ratio to the ^{239}Pu fission rate, at the center of Jezebel (a sphere of plutonium) and of Flattop-Pu (a smaller plutonium sphere made critical by a ^{238}U reflector shell. Rates are given for $(n, 2n)$ reactions and for (n, γ) reactions. Most of these values are unmeasured, except for the ^{241}Am capture rate to the ^{242}Am ground state that is then measured as curium following its beta decay. The agreement between calculation and experiment here is fairly good (given that capture cross sections are known less well than fission cross sections) - 6% for Jezebel and less than 1% for Flattop-Pu; comparisons at other locations in critical assemblies with softer neutron spectra can be seen in Fig. 108. We provide calculated values for the other rates in XXX as predictions, in the hope that future measurements can be made in fast critical assemblies to test our cross sections.

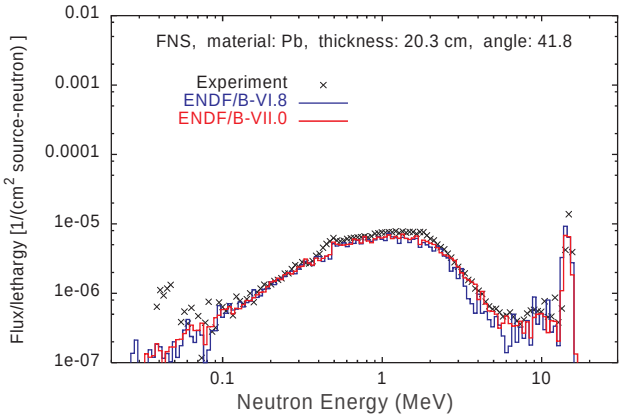

FIG. 110: Simulation of 14 MeV neutron transmission through 20 cm Pb, at 42.8 degrees [277].

E. Shielding and pulsed-sphere testing

In a companion paper [277] Steven van der Marck presents extensive data testing results that show comparisons of MCNP simulation predictions that use our ENDF/B-VII.0 cross sections and measured data, for neutron transmission (shielding) benchmarks. Here, we show some illustrative examples from that paper, focusing on validation benchmarks that test 14 MeV evaluations that have changed between ENDF/B-VI.8 and ENDF/B-VII.0 (e.g. ^{235,238}U, ^{238}Pu, Pb, Li, and Be). These comparisons test the accuracy of the secondary emission spectra of neutrons following nuclear reactions. The thinner target benchmarks test mainly the 14 MeV incident energy evaluations; thicker target benchmarks integrate the effects for a 14 MeV energy together with reactions induced by lower incident-energy neutrons produced in the target.

Fig. 110 shows an example from Van der Marck's companion paper for the FNS (Fusion Neutronics Source) benchmark corresponding to 14 MeV neutrons transmitted through 20 cm lead, at an angle of 42.8 degrees. The agreement between simulation and the FNS data is seen to be good (amd shows an improvement on the earlier ENDF/B-VI.8 data), and provides support for the accuracy of the new ^{208}Pb evaluation by P.G. Young, described in Section III.G.1. The modern GNASH-ECIS caculational analysis by Young led to the improvements in the secondary ejected neutrons in the 3 - 9 MeV region in Fig. 110. This can be contrasted with the poorer quality of comparison with data, *e.g.*, for tungsten isotopes shown in Ref. [275], where ENDF/B-VII.0 has carried over an old evaluation. Similar comparisons are shown for beryllium in Fig. 111 and for lithium-6 (Fig. 112) where in this case the differences between ENDF/B-VII.0 and ENDF/B-VI.8 are small.

Additional figures testing the ENDF/B-VII.0 data for these, and other, materials are given in Ref. [277].

Numerous high-energy pulsed-sphere experiments [282, 283] have been performed in which small, medium,

TABLE XXIX: Comparison of calculated spectra indices for ENDF/B-VII.0 with measured values in the center of various Los Alamos critical assemblies. 238Uf/235Uf refers to the ^{238}U fission rate divided by the ^{235}U fission rate, *etc.* Because ^{238}U and ^{237}Np are threshold fissioners, the spectral indices for these isotopes (in ratio to ^{235}U) measure the hardness of the neutron spectrum in the asssembly. Exp-A refers to experimental data as documented in the CSEWG Fast Reactor Benchmark Compilation, BNL 19302 (June 1973); Exp-B refers to the same measurements, but as reanalyzed by G. Hansen, one of the lead experimentalists, and transmitted to R. MacFarlane in 1984. The C/E ratios are based on the Hansen values where available.

Assembly	Quantity	238Uf/235Uf	237Npf/235Uf	233Uf/235Uf	239Puf/235Uf
Godiva	Calc	0.15774	0.83002	1.56884	1.38252
(HMF001)	Exp-B	0.1643 ±0.0018	0.8516±0.012		1.4152 ± 0.014
	Exp-A	0.1642 ±0.0018	0.837 ±0.013	1.59±0.03	1.402±0.025
	Calc/Exp	C/E=0.9601	C/E=0.9747	C/E=0.9867	C/E=0.9769
Jezebel	Calc	0.20854	0.97162	1.55632	1.42453
(PMF001)	Exp-B	0.2133 ±0.0023	0.9835 ±0.014		1.4609 ± 0.013
	Exp-A	0.2137 ±0.0023	0.962 ±0.016	1.578 ±0.027	1.448 ±0.029
	Calc/Exp	C/E=0.9777	C/E=0.9879	C/E=0.9863	C/E=0.9751
Jezebel-23	Calc	0.21065	0.98111		
(UMF001)	Exp-B	0.2131 ±0.0026	0.9970 ±0.015		
	Exp-A	0.2131 ±0.0023	0.977 ±0.016		
	Calc/Exp	C/E=0.9885	C/E=0.9841		
Flattop-25	Calc	0.14443	0.77114	1.56725	1.35918
(HMF028)	Exp-B	0.1492 ±0.0016	0.7804 ±0.01	1.608 ±0.003	1.3847 ±0.012
	Exp-A	0.149 ±0.002	0.76 ±0.01	1.60 ±0.003	1.37 ±0.02
	Calc/Exp	C/E=0.9681	C/E=0.9881	C/E=0.9747	C/E=0.9816
Flattop-Pu	Calc	0.17703	0.85254		
(PMF006)	Exp-B	0.1799 ±0.002	0.8561 ±0.012		
	Exp-A	0.180 ±0.003	0.84 ±0.01		
	Calc/Exp	C/E=0.9840	C/E=0.9958		
Flattop-23	Calc	0.18691	0.90801		
(UMF006)	Exp-B	0.1916 ±0.0021	0.9103 ±0.013		
	Exp-A	0.191 ±0.003	0.89 ±0.01		
	Calc/Exp	C/E=0.9755	C/E=0.9975		

TABLE XXX: MCNP calculations for ENDF/B-VII.0 of various $(n,2n)$ and (n,γ) reaction rates in ratio to the ^{239}Pu fission rate, at the center of Jezebel and of Flattop-Pu. The only measurements available (Barr, 1971) are for the ^{241}Am capture rate creating the ground state of ^{241}Am, which then decays to curium with a branching ratio of 0.84 (this factor is included into the tabulated calculated values below). Data at other positions in Flattop-Pu are compared with calculations in Fig. 108.

Assembly	Quantity	^{239}Pu$(n,2n)$/ ^{239}Pu(n,f)	^{239}Pu(n,γ)/ ^{239}Pu(n,f)	^{241}Am$(n,2n)$/ ^{239}Pu(n,f)	^{241}Am(n,γ)241Cm/ ^{239}Pu(n,f)
Jezebel	Calc	0.0021	0.033	0.0007	0.1373
	Exp				0.1463
Flattop-Pu	Calc	0.00186	0.044	0.0006	0.1825
	Exp				0.1818

and large spheres of 32 different materials were pulsed with a burst of high-energy (14 MeV) neutrons at Lawrence Livermore National Laboratory's ICT (Insulated Core Transformer) accelerator facility. Measured time-dependent neutron fluxes at collimated detectors located at a distance of 7 - 10 meters provide a benchmark by which various neutron transport codes and cross-section libraries may be evaluated. Fig. 113 shows an example geometry for the 0.7 mfp sphere of ^{235}U. Various types of neutron detectors were located in the 26°, 30°, and 120° beamlines, external to the 2-m-thick concrete vault walls. Time-of-flight neutron measurements were typically made in 2-ns time bins from about 100 to several hundred nanoseconds after a pulse, approximately corresponding to 2-15 MeV in neutron energy. The results can be seen in Figs. 114-116. There, the peak on the left hand side corresponds to the transmission of the 14 MeV transmission of source neutrons; the broad peak further right (lower energies) corresponds to the neutrons created through compound nucleus and fission mechanisms.

Numerous improvements [284–287] to the simulations have been made since the early implementations of these benchmarks. Simulations were performed comparing the measured data with calculated results using ENDF/B-VI.6 or ENDF/B-VII.0 data with MCNP for the smallest spheres of ^{235}U, ^{238}U, and ^{239}Pu. With the improvements in the modeling of the pulsed sphere experiments, problems with down-scattering from 14-MeV to the 8-12 MeV energy region had been noted especially for ^{235}U

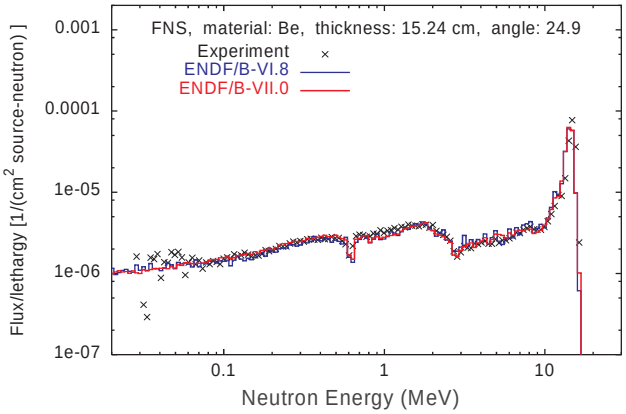

FIG. 111: Simulation of 14 MeV neutron transmission through 15 cm Be, at 24.9 degrees [277].

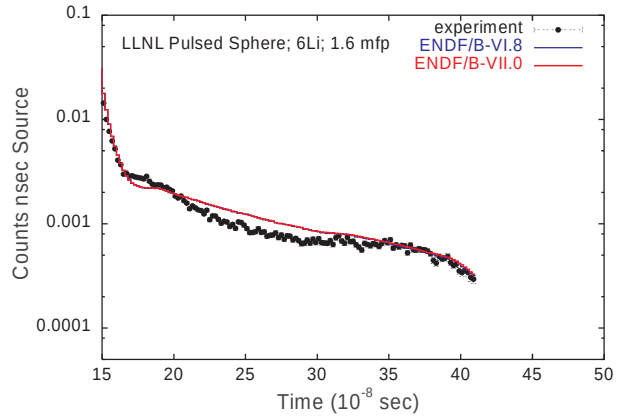

FIG. 112: Simulation of 14 MeV neutron transmission through 1.6 mfp ^{6}Li at 30 degrees [277].

and ^{239}Pu. Recent efforts by Los Alamos National Laboratory to improve the evaluated data for inelastic scattering at these higher incident neutron energies have been incorporated into the ENDF/B-VII.0 evaluations, as described in Sections III.B.2-4.

As shown in Figs. 114-116, the ENDF/B-VII.0 library improves the treatment of inelastic scattering for ^{235}U and ^{239}Pu showing much better agreement with the measured data. The improvements in modeling these integral transmission data experiments in the minimum region around 20 shakes[8] can be directly related to the cross section improvements in the fundamental data for an incident energy of 14 MeV and 8-12 MeV emission energies, see Figs. 25 and 34 in Section III.

[8] A shake is an informal unit of time used in nuclear science, 10^{-8} seconds. The word comes from the expression "two shakes of a lamb's tail" to mean a very short time interval.

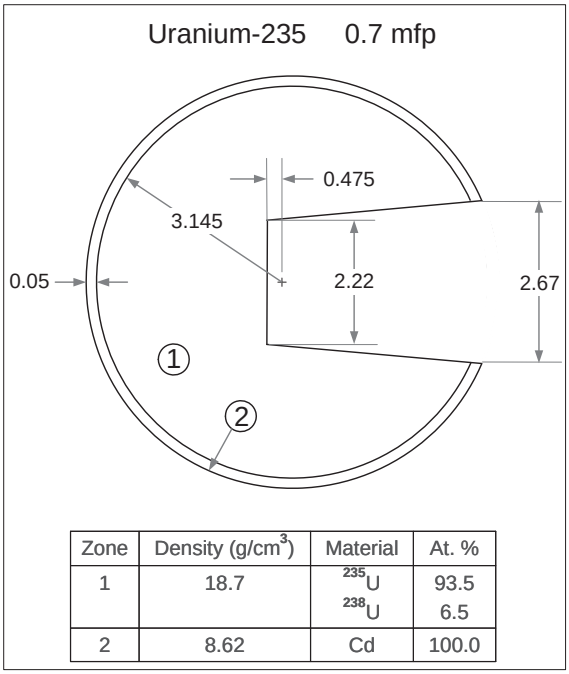

Zone	Density (g/cm^3)	Material	At. %
1	18.7	^{235}U ^{238}U	93.5 6.5
2	8.62	Cd	100.0

FIG. 113: Example sphere of ^{235}U with a radius of 0.7 mean-free-path (mfp).

F. Other data testing

Here, we discuss some other data testing activities that provided useful insight about the ENDF/B-VII.0 library.

1. *Thermal capture, resonance integrals*

Some important quantities at low neutron energies are thermal capture cross sections and capture resonance integrals. These quantities can be extracted from the ENDF/B-VII.0 files and compared with the data in the recently published Atlas of Neutron Resonances.

Ratios of capture cross sections at thermal energies are shown in Fig. 117. Ratios for capture resonances integrals can be seen in Fig. 118. The experimental values reported in the Atlas [30] were used for this comparison.

Overall, there is a fairly good agreement between the values in ENDF/B-VII.0 and the Atlas, although in several instances there are notable discrepancies. In the case of resonance integrals for ^{136}Xe, ^{142}Nd, ^{152}Gd, and ^{232}U the ratios in Fig. 118 deviate from unity since there are inconsistencies between resonance parameters and resonance integral measurements reported in Ref.[30] and the evaluators adopted resonance parameters rather than the experimental integrals. In the extreme case of ^{166m}Ho the experiment is deemed doubtful due to the cadmium cut-off because of the low energy resonance at 0.274 eV. In ^{158}Dy the resolved resonance range is very limited (up to 86 eV) and extrapolation of the unresolved region to such low energies might not be reliable (in particular,

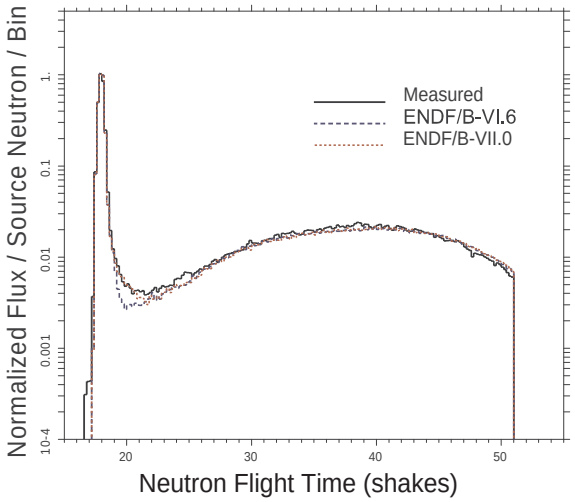

FIG. 114: Comparison of the simulated results using ENDF/B-VI.6 and ENDF/B-VII.0 data for the 0.7 mfp ^{235}U sphere. The experiment used a NE-213 detector biased at 1.6 MeV and located 9.455 m along the 26 degree flightpath. See the footnote for the definition of shake. Note the improved simulation predictions in the minimum region ($E_n \approx 8$ - 12 MeV), where preequilibrium and direct inelastic scattering are present.

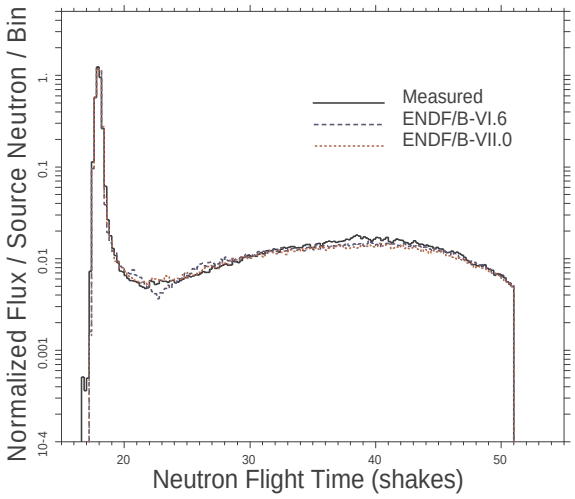

FIG. 115: Comparison of the simulated results using ENDF/B-VI.6 and ENDF/B-VII.0 data for the 0.8 mfp ^{238}U sphere. The experiment used a NE-213 detector biased at 1.6 MeV and located 9.455 m along the 26 degree flightpath.

exact position of the lower boundary might play a significant role).

The remaining outliers (^{31}P, ^{46}Ca, ^{58}Co, ^{176}Hf, ^{204}Hg, ^{244}Pu) are real discrepancies. These are old evaluations that will have to be updated in future releases of the ENDF/B library. The thermal region in ^{232}Pa was revised for ENDF/B-VII.0 by R.Q. Wright (ORNL) leading to the thermal capture nearly 3 times bigger than the one reported in the Atlas. Origin of this discrepancy is

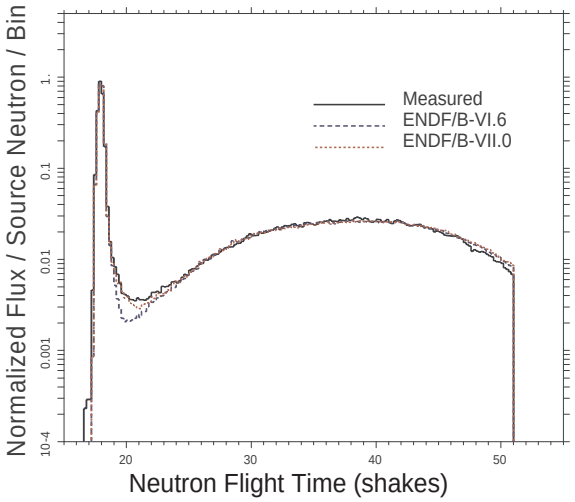

FIG. 116: Comparison of the simulated results using ENDF/B-VI.6 and ENDF/B-VII.0 data for the 0.7 mfp ^{239}Pu sphere. The experiment used a NE-213 detector biased at 1.6 MeV and located 9.455 m along the 26 degree flightpath.

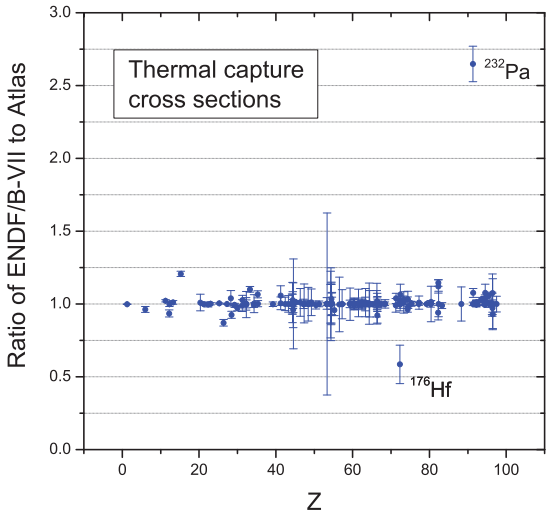

FIG. 117: Thermal neutron capture cross sections in ENDF/B-VII.0 compared to the Atlas of Neutron Resonances [30].

not clear and should be addressed in future.

2. *Unresolved resonance region for ^{235}U*

The graphite-moderated Zeus experiments, HEU-MET-INTER-006 were designed specifically to test the accuracy of ^{235}U cross sections in the intermediate energy range. In those experiments, thin HEU platters were separated by much thicker graphite platters for modera-

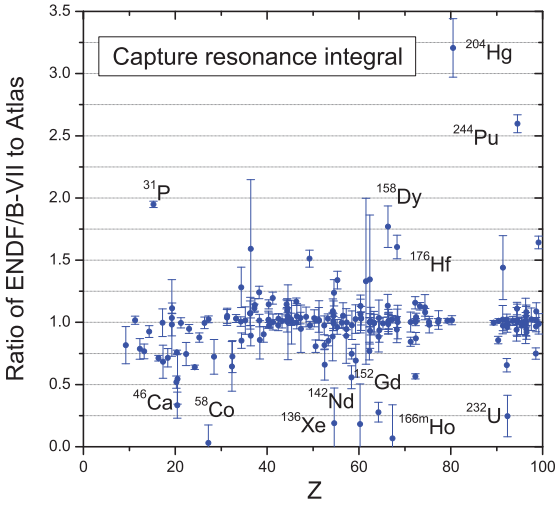

FIG. 118: Neutron capture resonance integrals in ENDF/B-VII.0 compared to the Atlas of Neutron Resonances [30].

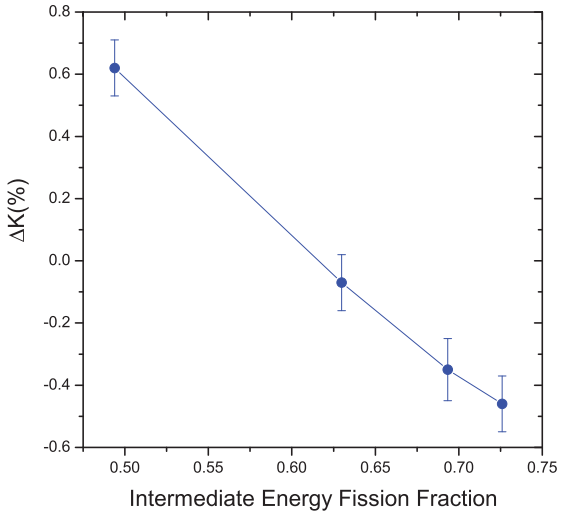

FIG. 119: Reactivity bias for graphite-moderated Zeus benchmarks.

tion. The cylindrical core was surrounded on all sides by a thick copper reflector. The amount of graphite between adjacent HEU platters was reduced from one experiment to the next in order to shift the energy spectrum.

As Fig. 119 illustrates, the bias between the benchmark values for $k_{\rm eff}$ and the values computed with ENDF/B-VII.0 decreases monotonically as the fraction of fissions in the intermediate energy range increases. This behavior, which also was observed with ENDF/B-VI, strongly suggests an energy-dependent bias in the ^{235}U cross sections over that range, which therefore requires further study in the future.

3. Fast neutron cross sections on Cu

The unmoderated Zeus experiment, HMF-73, represents an upper-energy endpoint for the Zeus experiments discussed above (Section X.F.2). It contains no moderator and therefore produces a fast spectrum. ENDF/B-VII.0 calculations for this benchmark overpredict $k_{\rm eff}$ by more than 1%. However, when ENDF/B-V cross sections for copper are used, the calculated value for $k_{\rm eff}$ is well within the experimental uncertainty for the benchmark. No such changes are seen for the graphite-moderated benchmarks, which have intermediate spectra. Consequently, this behavior strongly suggests that improvements are still needed in the copper cross sections in the fast neutron energy range.

XI. CONCLUSIONS AND FUTURE WORK

The new ENDF/B-VII.0 library provides the next generation of evaluated nuclear data recommended for both the nuclear science and nuclear technology communities. The library was produced by the CSEWG collaboration and represents a common achievement by numerous US laboratories. The library also benefited from appreciable input from the international nuclear data community.

A considerable effort has been dedicated to the verification and validation of the library, scanning for any deviations from the ENDF-6 format, providing various consistency checks, and performing "integral" data testing. These activities resulted in numerous corrections to the individual files during their development. We believe that the most significant errors have been detected and removed. We are aware, however, of a number of minor deficiencies that were not fixed, being deemed to be of a marginal importance and not worthy of diverting resources from more important tasks. These minor deficiencies include imprecision in the energy balance (kerma), incompleteness of the ^{253}Es evaluation, problems with some angular distributions, inaccurate matching between resonance and fast neutron regions, and several discrepancies between ENDF/B-VII.0 and recent evaluation of resonance parameters by Mughabghab [30] that have to be investigated. While these deficiencies should be addressed in future releases of the library, they had no negative impact on the critical assembly benchmark calculations.

The library has been carefully validated against integral critical assembly and shielding neutron transmission data. Its overall performance is very good, noticeably better than the earlier ENDF/B-VI library ini-

tially released in 1990, and its most recent upgrade, the ENDF/B-VI.8 library released in 2001.

But despite these successes, there are considerable challenges to be addressed in the future. Probably the most important challenge is to produce quality covariance data for neutron reactions. CSEWG intends to make this one of its priorities for the next couple of years.

Another important development is new requirements for improved cross sections required to design the next generation of nuclear power reactors and advanced fuel cycle technologies, especially for minor actinides.

Among other issues is the need to address deficiencies in several important materials such as Cu, Zr and Pd. Missing evaluations should be produced, such as isotopic evaluations for Zn. Also, the remaining elemental evaluations (C, V and Zn) should be replaced by isotopic evaluations.

Below we list some other specific areas where more work is needed:

- Plutonium thermal solution criticality benchmarks are modeled poorly. Our work for ENDF/B-VII.0 focused only on fast neutrons, not thermal (except for prompt neutron spectrum work). Future work on ^{239}Pu is needed, especially at low and intermediate energies.

- We think that the inelastic scattering, and possibly prompt fission neutron spectra, for ^{235}U and ^{239}Pu need to be improved, based on our data testing of spectral indices in fast critical assemblies. Specifically, in Godiva and Jezebel we underpredict the measured ^{238}U fission rate / ^{235}U fission rate (commonly known as the spectral index, as this provides an integral measure of the hardness of the neutron spectrum in the critical assembly). This underprediction with MCNP is possibly due to fundamental cross section data deficiencies for ^{235}U and ^{239}Pu, which may be representing the secondary neutron spectra with a secondary energy dependence that is too soft. We also note that this deficiency was not found for ^{233}U (Jezebel-23), where the data is based on a recent GNASH and ECIS evaluation. The ^{239}Pu and ^{235}U ENDF/B-VII.0 evaluations in the fast region were carried over from earlier ENDF evaluations, and therefore could benefit from a modern reanalysis. This same issue could result in an improvement in modeling the LANL Np-U composite critical assembly, which currently calculates a little low ($k_{\rm eff}$ = 0.9954). A hotter ^{235}U driver spectrum would increase the composite assembly criticality since ^{237}Np is a threshold fissioner.

- The ^{235}U capture cross section in the 30 keV - 1 MeV region is about 10 % lower than the JENDL-3.3 evaluation. This difference needs to be understood and resolved. The ENDF/B-VII.0 evaluation was carried over from ENDF/B-VI.8, and matches the capture/fission (α) data of Corvi, whereas JENDL-3.3 matches the Karlsruhe data by Beer.

- The n+D scattering angular distributions in the 1-3 MeV range were changed some years ago, for the ENDF/B-VI.4 release, and have been carried over into our new ENDF/B-VII.0 evaluation. These were based upon EDA R-matrix simulations that included p+D measured data in the analysis. However, some integral data testing results for heavy-water HEU reflected spherical assemblies show poorer agreement with data (though others involving unreflected cylinders show improvements). Further work is needed to better understand this. It may be that some fundamental "few-body" nuclear reaction theory predictions could help solve this problem through high-precision predictions.

- A number of calculations of integral critical assembly benchmarks, that involve reflection, point to deficiencies in scattering cross sections. Although some improvements have been seen based on our new ^{208}Pb evaluation, Pb reflected assemblies still show problems in some cases. Likewise, some of the data testing for Cu, and for polyethylene, show poor results. We made some changes to the beryllium scattering distributions to improve the fast beryllium reflected benchmarks, and although some of our results improved (and a bias based on the thickness of the beryllium reflector was largely removed), others comparisons did not improve. This is to be contrasted with our experience with ^{238}U reflected assemblies - the Flattop experiments. Here, our changes to the ^{238}U evaluation led to improvements in the predicted criticality, with the earlier reflection bias largely removed. A common problem with reflectors such as Fe, Cu, Pb and U is the effect of resonance-potential-interference minima in the scattering cross section. These lead to deep penetration into reflectors which impact on the effectiveness of such reflectors. Unfortunately, most cross section measurements have concentrated on the peak cross sections and not on the minima; measurements focused on the minima, such as transmission measurements through thick filters of the reflector, can serve to reduce these uncertainties.

- The poor agreement of calculations of the ZPR6-10 experiment support the need for future work on ^{239}Pu in the lower energy range and also indicate the need for improvement in the data for chromium and manganese in the same energy range.

Acknowledgments

The quality and extent of the ENDF/B-VII.0 library could not have been achieved without important contributions from two international organizations, several non-US evaluation projects and a number of non-CSEWG scientists. It would be next to impossible to mention all contributions and to list all names. The nuclear data international community is highly organized and intertwinned, making it sometimes very difficult to acknowledge in full all those who contributed to specific evaluations, modeling, measurements or validation.

The OECD Nuclear Energy Agency (NEA, Paris) was instrumental in organizing the international collaboration WPEC (Working Party on Evaluation Cooperation) which, with CSEWG scientists, produced a major improvement in the long-standing problem of underpredicting $k_{\rm eff}$ in low-enriched uranium light-water reactor systems (A. Courcelle, coordinator of this project, became a co-author of the present paper). The NEA WPEC collaboration, including CSEWG researchers, produced yet another important result adopted by ENDF/B-VII.0, namely creation of the library of evaluated neutron cross sections for fission products, where T. Nakagawa, JAEA, Japan should be highlighted for important contributions. Limited space prohibits us from listing all other scientists who contributed to these successful projects.

The Nuclear Data Section, International Atomic Energy Agency (IAEA, Vienna) organized an international effort that, with CSEWG, produced the new neutron standards cross sections (V. Pronyaev, its scientific secretary, became a co-author of the present paper), as well as the first version of the photonuclear library. Also, the IAEA organized an international project to improve evaluations for the Th-U cycle, where A. Trkov and R. Capote, IAEA, and M. Sin, Bucharest should be highlighted for the new ^{232}Th evaluation. Space prohibits us from listing many other scientists who contributed to these successful projects.

KAERI, S. Korea should be acknowledged for its contributions to new fission product evaluations produced in collaboration with BNL. In particular, Hyeong-Il Kim made a considerable contribution to the final evaluations, while S.-Y. Oh, J.-H. Chang and Y.-D. Lee were involved in preliminary evaluations. Yet another important contribution by KAERI was made by Yong-Ouk Lee, who evaluated an impressive amount of materials under the IAEA photonuclear project.

The Japanese JENDL-3.3 library was used as a source for a considerable number of evaluations, primarily in the fission product region and minor actinides. It would be difficult to list all evaluators to whom we should express our thanks, but H. Nakamura and S. Chiba deserve a special mention.

Several important evaluations, including several isotopes of Ca and Pb, were adopted from the European JEFF-3.1 project. We would like to highlight an outstanding contribution by Arjan Koning, NRG Petten.

Anatoly Ignatyuk, IPPE Obninsk should be acknowledged for numerous useful discussions and for a comparison of several ENDF/B-VII.0 evaluations with new data produced for the forthcoming BROND-3 library.

R.Q. Wright, ORNL, performed a useful review of almost 30 minor actinides. D. Ridikas, CEA Saclay and M.C. Brady Raap, PNNL should be thanked for useful feedback on our delayed neutron evaluation. We acknowledge collaborative work with D. Ridikas ond M. Giacri on our new actinide photonuclear evaluations. Osamu Iwamoto, JAEA, Japan, contributed to evaluations of Ge isotopes, and B. Sarer, Turkey, to evaluations of rare fission products. We would like to thank Michael MacInnes of LANL for providing the reaction rate critical assembly data. We are grateful to John Rowlands for providing useful peer review of the delayed netron, and the fission energy release, work.

Of crucial importance for quality assurance was the validation of the library. We want to acknowledge an impressive European effort (S. van der Mark became a co-author of the present paper), including the work by Jean-Christophe Sublet, CEA Cadarache, that provided an independent check of the library. A. Trkov, Ljubljana should be highlighted for ^{232}Th and ^{233}U benchmarking. A. Aronson, BNL and R. Zajac, STU Bratislava were instrumental in the Phase 1 testing of the new library.

We would like to express our appreciation for continuing support to several sponsors. In particular to Dennis Kovar, DOE-SC, Office of Nuclear Physics (US Nuclear Data Program), Dimitri Kusnezov, DOE-NNSA (Advanced Simulations and Computing Program), and Jim Felty, DOE-NNSA (Nuclear Criticality Safety Program).

Work at Los Alamos National Laboratory was carried out under the auspices of the National Nuclear Security Agency of the U.S. Department of Energy under Contract No. DE-AC52-06NA25396. Work at Brookhaven National Laboratory was sponsored by the Office of Nuclear Physics, Office of Science of the U.S. Department of Energy under Contract No. DE-AC02-98CH10886 with Brookhaven Science Associates, LLC. Work at Argonne National Laboratory was supported mainly by DOE-SC, Office of Nuclear Physics (US Nuclear Data Program) and DOE-NNSA (Nuclear Criticality Safety Program).

This work was performed under the auspices of the U. S. Department of Energy by University of California, Lawrence Livermore National Laboratory under contract W-7405-Eng-48.

[1] C. Dunford, "A CSEWG retrospective: 35th anniversary, Cross Section Evaluation Working Group," Tech. Rep. BNL-52675, Brookhaven National Laboratory, November 2001.

[2] CSEWG-Collaboration, "Evaluated Nuclear Data File ENDF/B-VI.8." www.nndc.bnl.gov/endf, released in October 2001.

[3] C. Dunford, "Some CSEWG recollections," Tech. Rep. In Report BNL-52675 [1], p.29, Brookhaven National Laboratory, November 2001.

[4] M. Herman, "ENDF-6 Formats Manual: Data Formats and Procedures for the Evaluated Nuclear Data File ENDF/B-VI and ENDF/B-VII," Tech. Rep. BNL-NCS-44945-05-Rev, Document ENDF-102, Brookhaven National Laboratory, June 2005.

[5] M. Chadwick, P. Obložinský, A. Blokhin, T. Fukahori, Y. Han, Y.-O. Lee, M. Martins, S. Mughabghab, V. Varlamov, B. Yu, and J. Zhang, "Handbook on Photonuclear Data for Applications: Cross-sections and Spectra," Tech. Rep. IAEA-TECDOC-1178, International Atomic Energy Agency, October 2000.

[6] M. Mattes and J. Keinert, "Thermal neutron scattering data for the moderator materials H_2O, D_2O, and ZrH_x in ENDF-6 format and as ACE library for MCNP(X) codes," report INDC(NDS)-0470, IAEA, April 2005.

[7] V. G. Pronyaev, S. A. Badikov, A. D. Carlson, Z. Chen, E. V. Gai, G. M. Hale, F.-J. Hambsch, H. M. Hofmann, N. M. Larson, D. L. Smith, S.-Y. Oh, S. Tagesen, and H. Vonach, "An international evaluation of the neutron cross section standards," tech. rep., International Atomic Energy Agency, 2006. to be published as an IAEA Technical Report.

[8] "SCALE: A modular code system for performing standardized computer analysis for licensing evaluation." NUREG/CR-0200, Rev. 6 (ORNL/NUREG/CSD-2/R6), Vols. I, II, and III, May 2000. Available from the Radiation Safety Information Computational Center at Oak Ridge National Laboratory as CCC-545, 2000.

[9] R. E. MacFarlane and D. W. Muir, "The NJOY nuclear data processing system, version 91," Tech. Rep. LA-12740-M, Los Alamos National Laboratory, NM, 1994.

[10] R. MacFarlane, "NJOY nuclear data processing code, version 2006." Nuclear Data Sheets, to be published.

[11] RSICC, "Webpage, Radiation Safety Information Computational Center." www-rsicc.ornl.gov, 2006.

[12] NEA, "Webpage, Nuclear Energy Agency Data Bank." www.nea.fr/html/databank/, 2006.

[13] LANL, "Webpage, T-2 Information Service, Los Alamos National Laboratory." t2.lanl.gov, 2006.

[14] K. Kosako, "Covariance Data Processing Code: ERRORJ," in *the Specialists' Meeting of Reactor Group Constants* (J. Katakura, ed.), JAERI, Tokai, Japan, February 22-23, 2001. JAERI-Conf 2001-009.

[15] D. Wiarda and M. Dunn, "PUFF-IV: Code System to Generate Multigroup Covariance Matrices from ENDF/B-VI Uncertainty Files ." Oak Ridge National Laboratory, Radiation Safety Information Computational Center (RSICC) Code Package PSR-534, 2006.

[16] M. Dunn and N. Greene, "AMPX-2002: A Cross Section Processing System for Generating Nuclear Data for Criticality Safety Applications," Tech. Rep. Trans. Am. Nucl. Soc., ORNL, 2002.

[17] C. Dunford, "ENDF Utility Codes, version 7.02." www.nndc.bnl.gov/nndcscr/endf/endf-util-7.02/, 2005.

[18] X5-MCNP-Team, "MCNP - A General Monte Carlo N-Particle Transport Code, Version 5, Volume I: Overview and Theory," Tech. Rep. LA-UR-03-1987, Los Alamos National Laboratory, April 2003.

[19] J. Briesmeister *et al.*, "MCNP - A general Monte Carlo N-particle transport code, version 4C," Tech. Rep. LA-13709-M, Los Alamos National Laboratory, 2000.

[20] "MCNPX Transport Code for Charged Particles." mcnpx.lanl.gov, 2006.

[21] B. Pritychenko *et al.*, "Nuclear reaction and structure data services of the National Nuclear Data Center," *Ann. Nucl. Energy*, vol. 33, p. 390, 2006.

[22] P. G. Young, E. D. Arthur, and M. B. Chadwick, "Comprehensive nuclear model calculations: Introduction to the theory and use of the GNASH code," Tech. Rep. LA-12343-MS, Los Alamos National Laboratory, Los Alamos, NM, 1992.

[23] P. G. Young and E. D. Arthur, "GNASH: A preequilibrium statistical nuclear model code for calculations of cross sections and esmission spectra," Tech. Rep. LA-6947, Los Alamos National Laboratory, Los Alamos, NM, 1977.

[24] P. G. Young, E. D. Arthur, and M. B. Chadwick, "Comprehensive nuclear model calculations: Theory and use of the GNASH code," in *Proc. of the IAEA Workshop on Nuclear Reaction Data and Nuclear Reactors - Physics, Design, and Safety* (A. Gandini and G. Reffo, eds.), (Singapore), pp. 227–404, Trieste, Italy, April 15 - May 17, 1996, World Scientific Publishing, Ltd., 1998.

[25] M. Herman *et al.*, "Neutron reaction evaluation methodology at the NNDC," *under preparation*, 2006.

[26] J. Raynal, *Notes on ECIS*. CEA-N-2772, Commissariat à l'Energie Atomique, 1994.

[27] N. M. Larson, "Updated users' guide for SAMMY: Multilevel R-matrix fits to neutron data using Bayes' equations," Tech. Rep. ORNL/TM-9179/R7, Document ENDF-364, Oak Ridge National Laboratory, TN, 2006.

[28] G. M. Hale, "Use of R-matrix methods for light element evaluations," in *Proc. of the Conference on Nuclear Data Evaluation Methods and Procedures* (B. Magurno and S. Pearlstein, eds.), pp. 509–531, Brookhaven National Laboratory, Upton, NY, BNL-NCS-51363, 1981.

[29] S. Oh, J. Chang, and S. F. Mughabghab, "Neutron cross section evaluations of fission products below the fast neutron region," Tech. Rep. BNL-NCS-67469, Brookhaven National Lab., 2000.

[30] S. F. Mughabghab, *Atlas of Neutron Resonances: Thermal Cross Sections and Resonance Parameters*. Amsterdam: Elsevier, 2006.

[31] H. M. Hofmann, "Models and methods in few-body physics," in *Models and Methods in Few-Body Physics* (L. S. Ferreira *et al.*, ed.), vol. 273 of *Lecture Notes in Physics*, Heidelberg: Springer, 1987.

[32] H. M. Hofmann and G. M. Hale, "Microscopic calculation of the ^{4}He system," *Nuclear Physics*, vol. A 613, pp. 69–106, January 1997.

[33] A. Ignatyuk, P. Obložinský, M. Chadwick, T. Fukahori, S. Kailas, G. Molnar, G. Reffo, Z. Su, M. Uhl, and

P. Young, "Handbook for calculations of nuclear reaction data: Reference Input Parameter Library," Technical report IAEA-TECDOC-1034, International Atomic Energy Agency, Vienna, Austria, 1998.

[34] P. Young, M. Herman, P. Obložinský, T. Belgya, O. Bersillon, R. Capote, T. Fukahori, G. Zhigang, S. Goriely, A. Ignatyuk, S. Kailas, A. Koning, and V. Plujko, "Handbook for calculations of nuclear reaction data, RIPL-2," TECDOC in press, IAEA, Vienna, 2006.

[35] N. Larson and K. Volev, "Validation of multiple-scattering corrections in the analysis code SAMMY," in *International Conference on the New Frontiers of Nuclear Technology: Reactor Physics, Safety and High-Performance Computing (Physor 2002)*, p. A0203, Seoul, South Korea, 2002.

[36] N. Larson, "On the efficient treatment of data covariance matrices," in *71st Annual Meeting of the Southeastern Section of the APS*, Oak Ridge, TN, November 11 - 13, 2004, American Institute of Physics.

[37] N. Larson, "Treatment of data uncertainties," in *Proc. of the International Conference on Nuclear Data for Science and Technology* (R. Haight, M. Chadwick, T. Kawano, and P. Talou, eds.), (New York, USA), p. 374, Santa Fe, Sept 26 - Oct 1, 2004, American Institute of Physics, 2005.

[38] F. Fröhner, B. Goel, and U. Fischer, "FITACS computer code," Tech. Rep. Report ANL-83-4, p.116, Kernforschungszentrum Karslruhe, 1982. Note: Presented at Specialists' Meeting on Fast Neutron Capture Cross Sections, ANL.

[39] S. F. Mughabghab, M. Divadeenam, and N. E. Holden, *Neutron Cross Sections: Z=1-60*, vol. 1A. New York: Academic Press, 1981.

[40] S. F. Mughabghab, *Neutron Cross Sections: Z=61-100*, vol. 1B. New York: Academic Press, 1984.

[41] J. B. Garg, "Neutron widths and level spacings of ^{64}Zn+n," *Phys. Rev.*, vol. C 23, p. 671, 1981.

[42] L. M. Bollinger and G. E. Thomas, "p-Wave Resonances of ^{238}U," *Phys. Rev.*, vol. 171, p. 1293, 1968.

[43] S. T. Perkins and G. E. Gyulassy, "An Integrated System for Production of Neutronics and Photonics Calculational Constants," Tech. Rep. UCRL-50400, Vol. 12, Univ. of California, 1972.

[44] C. E. Porter and R. G. Thomas, "Fluctuations of Nuclear Reaction Widths," *Phys. Rev.*, vol. 104, pp. 483–491, Oct 1956.

[45] P. Axel, "Electric dipole ground state transition width strength function and 7 MeV photon interaction," *Physical Review*, vol. 126, p. 671, 1962.

[46] D. M. Brink, *Unpublished*. D. Phil. thesis, Oxford University, 1955.

[47] J. Kopecky and M. Uhl, "Test of gamma-ray strength functions in nuclear-reaction model-calculations," *Phys. Rev. C*, vol. 41, pp. 1941–1955, 1990.

[48] S. F. Mughabghab and C. L. Dunford, "A dipole-quadrupole interaction term in E1 photon transitions," *Phys. Lett.*, vol. B 487, p. 155, 2000.

[49] V. Plujko and M. Herman, *Handbook for calculations of nuclear reaction data, RIPL-2*, ch. Chapter 7: Gamma-ray strength functions, p. 120. No. in press, IAEA, Vienna, 2006.

[50] P. A. Moldauer, "Evaluation of the fluctuation enhancement factor," *Phys. Rev. C*, vol. 14, pp. 764–766, Aug 1976.

[51] H. M. Hofmann, J. Richert, J. W. Tepel, and H. A. Weidenmüller, "Direct reactions and Hauser-Feshbach theory," *Ann. Phys.*, vol. 90, p. 403, 1975.

[52] H. Nishioka, J. J. M. Verbaarschot, H. A. Weidenmüller, and S. Yoshida, "Statistical theory of precompound reactions: The multistep compound process," *Ann. Phys.*, vol. 172, p. 67, 1986.

[53] C. Dunford, "Compound nuclear analysis programs COMNUC and CASCADE," Tech. Rep. T1-707-130-013, Atomics International, 1971.

[54] H. M. Hofmann, T. Mertelmeier, M. Herman, and J. W. Tepel, "Calculation in the Presence of Weakly Absorbing Channels with Special Reference to the Elastic Enhancement Factor and Factorization Assumption," *Z. Physik*, vol. A 297, p. 153, 1980.

[55] C. Kalbach, "Systematics of continuum angular distributions: Extensions to higher energies," *Phys. Rev. C*, vol. 37, pp. 2350–2370, 1988.

[56] H. Feshbach, A. Kerman, and S. Koonin, "The statistical theory of multi-step compound and direct reactions," *Ann. Phys. (N.Y.)*, vol. 125, pp. 429–476, 1980.

[57] E. Běták and P. Obložinský, "Code PEGAS: Preequilibrium exciton model with spin conservation and gamma emission," Tech. Rep. INDC(SLK)-001, IAEA/Slovak Academy of Sciences, 1993. Note: DEGAS is an extended version of the code PEGAS using two-parameteric p-h level densities.

[58] M. Blann, "New precompound decay model," *Phys. Rev. C*, vol. 54, p. 1341, 1996.

[59] M. Blann and M. B. Chadwick, "New precompound model: Angular distributions," *Phys. Rev. C*, vol. 57, p. 233, 1998.

[60] M. Blann and M. B. Chadwick, "Precompound Monte-Carlo model for cluster induced reactions," *Phys. Rev. C*, vol. 6203, p. 4604, 2000.

[61] M. B. Chadwick, P. G. Young, D. C. George, and Y. Watanabe, "Multiple preequilibrium emission in Feshbach-Kerman-Koonin analyses," *Phys. Rev. C*, vol. 50, p. 996, Aug 1994.

[62] T. Tamura, T. Udagawa, and H. Lenske, "Multistep direct reaction analysis of continuum spectra in reactions induced by light ions," *Phys. Rev.*, vol. C26, p. 379, 1982.

[63] M. Herman, G. Reffo, and H. A. Weidenmüller, "Multistep-compound contribution to precompound reaction cross section," *Nucl.Phys.*, vol. A536, p. 124, 1992.

[64] C. Kalbach and F. M. Mann, "Phenomenology of continuum angular distributions. I. Systematics and parametrization," *Phys. Rev. C*, vol. 23, pp. 112–123, Jan 1981.

[65] A. Iwamoto and K. Harada, "Mechanism of cluster emission in nucleon-induced preequilibrium reactions," *Phys. Rev. C*, vol. 26, pp. 1821–1834, Nov 1982.

[66] K. Sato, A. Iwamoto, and K. Harada, "Pre-equilibrium emission of light composite particles in the framework of the exciton model," *Phys. Rev. C*, vol. 28, pp. 1527–1537, Oct 1983.

[67] J. S. Zhang and X. G. Shi *et al.*, "The Formulation of UNIFY Code for the Calculation of Fast Neutron Data for Structural Materials," Report INDC(CPR)-014, IAEA, Vienna, 1989.

[68] J. S. Zhang *et al.*, "Formation and Emission of

Light Particles in Fast Neutron-induced Reaction - A Unified Compound Pre-equilibrium Model," Report INDC(NDS)-193, IAEA, Vienna, 1988. p. 21.

[69] D. G. Madland and J. R. Nix, "New calculation of prompt fission neutron-spectra and average prompt neutron multiplicities," *Nucl. Sci. and Eng.*, vol. 81, pp. 213–271, 1982.

[70] NRDC-Network, "CSISRS/EXFOR library of experimental cross sections." www.nndc.bnl.gov/exfor, 2006.

[71] C. Lubitz, "A modification in ENDF/B-VI ^{235}U to increase epithermal alpha and k1," in *Proceedings of the International Conference on Nuclear Data for Science and Technology*, Gatlinburg, USA, 1994.

[72] H. Weigmann, J. Hambsch, W. Mannhart, Mamoru Baba, Liu Tingjin, N. Kornilov, D. Madland, and P. Staples, "Fission neutron spectra of uranium-235," Report NEA/WPEC-9, OECD, 2003.

[73] G. Boykov *et al. Sov. J. Nucl. Phys.*, vol. 53, p. 392, 1991.

[74] W. Younes and J. A. Becker, "The ^{225}U$(n, 2n)$ Cross Section: Preliminary Calculations," Tech. Rep. UCRL-ID-137718, Lawrence Livermore National Laboratory, CA, 1999.

[75] L. C. Leal, H. Derrien, N. M. Larson, and A. Courcelle, "An Unresolved Resonance Evaluation for ^{235}U," in *PHYSOR Conference*, Chicago, Illinois, April 25-29, 2004.

[76] J. A. Harvey, "High Resolution Neutron Transmission Measurements on ^{235}U, ^{239}Pu and ^{238}U," in *Proc. of the International Conference on Nuclear Data for Science and Technology*, (Mito, Japan), JAERI, 1988.

[77] H. Derrien, J. A. Harvey, N. M. Larson, L. C. Leal, and R. Q. Wright, "Neutron Total Cross Sections of ^{235}U from Transmission Measurements in the Energy Range 2 keV to 300 keV and Statistical Model Analysis of the Data," tech. rep., Oak Ridge National Laboratory, 2000.

[78] L. W. Weston and J. H. Todd, "Subthreshold Fission Cross Section of ^{240}Pu and the Fission Cross Sections of ^{235}U and ^{239}Pu," *Nucl. Sci. Eng.*, vol. 88, p. 567, 1984.

[79] L. W. Weston, G. d. Saussure, and R. Gwin, "Ratio of Capture to Fission in ^{235}U at keV Neutron Energies," *Nucl. Sci. Eng.*, vol. 20, p. 80, 1964.

[80] J. Frehaut, "Coherent evaluation of nu-bar (prompt) for ^{235,238}U and ^{239}Pu," Tech. Rep. JEFDOC-17, NEA, JEFF project, 2000.

[81] M. Baba, H. Wakabayashi, N. Ito, K. Maeda, and N. Hirakawa, "Measurement of double-differential neutron emission spectra from uranium-238," *J. Nucl. Sci. Tech.*, vol. 27, pp. 601–616, 1990.

[82] G. Lovchikova *et al.* XIV international Workshop on Nuclear Fission Physics, 2000.

[83] T. Ethvignot *et al. Phys. Lett. B*, vol. 575, p. 221, 2003.

[84] Y. Kanda and M. Baba, "WPEC-SG4 Report: ^{238}U capture and related cross sections," Tech. Rep. WPEC/SG4, NEA Paris.

[85] J. B. Briggs *et al.*, "International handbook of evaluated criticality safety benchmark experiments," Tech. Rep. NEA/NSC/DOC(95)04/I, Nuclear Energy Agency, Paris, France, 2004.

[86] M. Moxon and M. Sowerby, "Summary of the work of the NEANDC task force on ^{238}U," Tech. Rep. NEANDC-313U, OECD Nuclear Energy Agency, Paris, 1994.

[87] A. Courcelle, "First conclusions of the WPEC Subgroup-22," in *Proc. of the International Conference on Nuclear Data for Science and Technology* (R. Haight, M. Chadwick, T. Kawano, and P. Talou, eds.), (New York, USA), pp. 462–467, Santa Fe, Sept 26 - Oct 1, 2004, American Institute of Physics, 2005.

[88] H. Derrien, A. Courcelle, L. Leal, N. M. Larson, and A. Santamarina, "Evaluation of ^{238}U Resonance Parameters from 0 to 20 keV," in *Proc. of the International Conference on Nuclear Data for Science and Technology* (R. Haight, M. Chadwick, T. Kawano, and P. Talou, eds.), (New York, USA), pp. 276–281, Santa Fe, Sept 26 - Oct 1, 2004, American Institute of Physics, 2005.

[89] G. de Saussure, "Measurement of the Uranium-238 Capture Cross Section for Incident Neutron Energies up to 100 keV," *Nucl. Sci. Eng.*, vol. 5, p. 385, 1973.

[90] D. K. Olsen, G. d. Saussure, R. B. Perez, E. G. Silver, F. Difilippo, R. W. Ingle, and H. Weaver, "Precise Measurement and Analysis of Neutron Transmission Through Uranium-238," *Nucl. Sci. Eng.*, vol. 62, p. 479, 1977.

[91] D. K. Olsen, "Measurement and resonance analysis of neutron transmission through Uranium-238," *Nucl. Sci. Eng.*, vol. 479, pp. 202–222, 1979.

[92] H. Kitazawa and Y. Harima, "High Energy Resolution Measurement of the ^{238}U Neutron Capture Yield in the Energy Region Between 1 and 100 keV," in *Proc. of the International Conference on Nuclear Data for Science and Technology*, (Mito, Japan), JAERI, 1988.

[93] A. Trkov *et al.*, "Revisiting the ^{238}U thermal capture cross-section and gamma emission probabilities from ^{239}Np decay," *Nucl. Sci. Eng.*, vol. 150, pp. 336–348, 2005.

[94] F. H. Fröhner, "Evaluation of the Unresolved Resonance Range of ^{238}U," *Nucl. Sci. Eng.*, vol. 103, pp. 119–128, 1988.

[95] P. Staples *et al. Nucl. Phys. A*, vol. 591, pp. 41–60, 1995.

[96] R.W. Lougheed *et al.* , "^{239}Pu and ^{241}Am (n,2n) cross section measurements near 14 MeV," Tech. Rep. UCRL-ID-145592, Lawrence Livermore National Laboratory, CA, 2001.

[97] M. B. Chadwick, P. G. Young, and D. McNabb, "Evaluation of the ^{239}Pu$(n, 2n)$ cross section," Tech. Rep. Memorandum T-16-MBC00/10, Los Alamos National Laboratory, Los Alamos, NM (2000), October 2, 2000.

[98] L. A. Bernstein, J. A. Becker, P. E. Garrett, W. Younes, D. P. McNabb, D. E. Archer, C. A. McGrath, H. Chen, W. E. Ormand, M. A. Stoyer, R. O. Nelson, M. B. Chadwick, G. D. Johns, W. S. Wilburn, M. Devlin, D. M. Drake, and P. G. Young *Physical Review*, vol. C6502, p. 1601, 2002.

[99] L. C. Leal, H. Derrien, J. A. Harvey, K. H. Guber, N. M. Larson, and R. R. Spenser, "R-Matrix Resonance Analysis and Statistical Properties of the Resonance Parameters of ^{233}U in the Neutron Energy Range from Thermal to 600 eV," Tech. Rep. ORNL/TM-2000, ENDF-365, Oak Ridge National Laboratory, Oak Ridge, TN, 2001.

[100] L. C. Leal, H. Derrien, N. M. Larson, and A. Courcelle, "An Unresolved Resonance Evaluation ^{233}U from 600 eV to 40 keV," *Trs. Am. Nucl. Sci.*, vol. 92, 2005.

[101] K. H. Guber, R. R. Spencer, L. C. Leal, P. E. Koehler, J. A. Harvey, R. O. Sayer, H. Derrien, T. E. Valentine, D. E. Pierce, V. M. Cauley, and T. A. Lewis, "High-Resolution Transmission Measurements of ^{233}U Using a

Cooled Sample at the Temperature T = 11^{o}K," *Nucl. Sci. Eng.*, vol. 139, pp. 111–117, 2001.

[102] L. W. Weston, R. Gwin, G. D. Saussure, R. R. Fullwood, and R. W. Hockenbury, "Measurement of the Neutron Fission and Capture Cross Sections for ^{233}U in the Energy Region 0.4 to 2000 eV," *Nucl. Sci. Eng*, vol. 34, pp. 1–12, 1968.

[103] J. C. Hopkins and B. C. Diven, "Neutron Capture to Fission Ratios in ^{233}U, ^{235}U, ^{239}Pu," *Nucl. Sci. Eng.*, vol. 12, pp. 169–177, 1962.

[104] W. Younes and H. C. Britt, "Neutron-induced fission cross sections simulated from (t,pf) results," *Physical Review C*, vol. 67, no. 2, p. 024610, 2003.

[105] C. Plettner, H. Ai, C. W. Beausang, L. A. Bernstein, L. Ahle, H. Amro, M. Babilon, J. T. Burke, J. A. Caggiano, R. F. Casten, J. A. Church, J. R. Cooper, B. Crider, G. Gurdal, A. Heinz, E. A. McCutchan, K. Moody, J. A. Punyon, J. Qian, J. J. Ressler, A. Schiller, E. Williams, and W. Younes, "Estimation of (n,f) cross sections by measuring reaction probability ratios," *Physical Review C*, vol. 71, no. 5, p. 051602, 2005.

[106] H. Derrien and G. de Saussure, "R-matrix analysis of the ^{241}Pu neutron cross-sections in the thermal to 300-ev energy range," *Nuc. Sci. Eng.*, vol. 106, pp. 415–433, 1990.

[107] C. Wagemans, P. Schillebeeckx, A. Deruyter, and R. Barthelemy, "Measurement of the subthermal neutron induced fission cross-section of ^{241}Pu," in *Proceedings Nuclear Data for Science and Technology* (S. Qaim, ed.), Jülich, Germany, May 13-17, 1991, Springer-Verlag, 1992.

[108] H. Derrien, "Revision of the ^{241}Pu Reich-Moore resonance parameters by comparison with recent fission cross-section measurements," tech. rep., JAERI, 1994.

[109] C. Chabert, A. Santamarina, and P. Bioux, "Trends in nuclear data derived from integral experiments in thermal and epithermal reactors," in *Proc. of the International Conference on Nuclear Data for Science and Technology*, Tsukuba, 2002.

[110] H. Derrien, L. Leal, A. Courcelle, and A. Santamarina, "Re-evaluation and validation of the ^{241}Pu resonance parameters in the energy range thermal to 20 eV.," *Nuc. Sci. Eng.*, vol. 150, pp. 109–114, 2005.

[111] D. Rochman, M. Herman, and P.Obložinský, "Modeling and fission cross sections for Americium," *accepted for publication in Nucl. Sci. Eng.*, 2006.

[112] P. Talou, T. Kawano, P. Young, M. Chadwick, and R. MacFarlane, "Improved evaluations of neutron-induced reactions on Americium isotopes," *accepted for publication in Nucl. Sci. Eng.*, 2006.

[113] S. Ohki, K. Yokoyama, K. Numata, and T. Jin, "Target accuracy of Am nuclear data and progress in validation by post irradiation experiments with the fast reactor JOYO," in *Proc. of the 2003 Symposium on Nuclear Data*, p. 40, 2004. Nov. 27-28, 2003, JAERI, Tokai, Japan.

[114] G. Perdikakis *et al.*, "Meaurements of the ^{241}Am(n,2n) reaction cross sections using the activation method," *Phys. Rev. C*, vol. 73, p. 067601, 2006.

[115] W. Younes, H.C.Britt, and J.A.Becker, "Estimated (n,f) cross sections for ^{236,236m,237,238}Np, ^{237,237m}Pu, and ^{240,241,242,242m,243,244,244m}Am isotopes," Livermore Report UCRL-TR-201913, LLNL, 2004.

[116] S. Bjornholm and J. E. Lynn, "The double-humped fission barrier," *Rev.Mod.Phys.*, vol. 52, p. 725, 1980.

[117] A. Trkov, "2nd IAEA Research Co-ordination Meeting on Evaluated Nuclear Data for Thorium-Uranium Fuel Cycle," Technical report INDC(NDS)-447, IAEA, Vienna, 2003.

[118] A. Trkov, "Evaluated Nuclear Data for Th-U Fuel Cycle Summary Report of the Third Research Coordination Meeting," Technical report INDC(NDS)-494, IAEA, Vienna, 2006.

[119] L. Leal and H. Derrien, "Evaluation of the resonance parameters for ^{232}Th in the energy range 0 to 4 keV," technical report, Oak Ridge National Laboratory, 2006. In preparation.

[120] D. Olsen and R. Ingle, "Measurement of Neutron Transmission Spectra through ^{232}Th from 8 MeV to 4 keV," Report ORNL/TM-7661(ENDF-307), Oak Ridge National Laboratory, 1981.

[121] G. Morogovskij and L. A. Bakhanovich, "Evaluation of the resolved resonance region for Pa-233," *Series: Nuclear Constants*, no. 1-2, 2003. Translated in INDC(CCP)-440, International Atomic Energy Agency, Vienna September 2004.

[122] I. Sirakov, P. Schillebeeckx, R. Capote, and A. Trkov, "^{232}Th: Evaluation of the average resonance parameters and their covariances in the unresolved resonance region from 4 to 100 keV." Private Communication, September 2006.

[123] V. Maslov, M. Baba, A. Hasegawa, N. Kornilov, A. Kagalenko, and N. Tetereva, "Neutron Data Evaluation of ^{231}Pa," Technical report INDC(BLR)-19, IAEA, Vienna, 2004.

[124] V. Maslov, M. Baba, A. Hasegawa, N. Kornilov, A. Kagalenko, and N. Tetereva, "Neutron Data Evaluation of ^{233}Pa," Tech. Rep. INDC(BLR)-20, IAEA, Vienna, 2004.

[125] R. Capote, M. Sin, and A. Trkov, "Evaluation of fast neutron induced reactions on ^{232}Th and ^{231,233}Pa up to 60 MeV." to be published.

[126] M. Herman, P. Obložinský, R. Capote, M. Sin, A. Trkov, A. Ventura, and V. Zerkin, "Recent developments of the nuclear reaction model code EMPIRE," in *Proc. of the International Conference on Nuclear Data for Science and Technology* (R. Haight, M. Chadwick, T. Kawano, and P. Talou, eds.), (New York, USA), p. 1184, Santa Fe, Sept 26 - Oct 1, 2004, American Institute of Physics, 2005.

[127] M. Sin, R. Capote, M. Herman, P. Obložinský, A. Ventura, and A. Trkov, "Improvement of the fission channel in the EMPIRE code," in *Proc. of the International Conference on Nuclear Data for Science and Technology* (R. Haight, M. Chadwick, T. Kawano, and P. Talou, eds.), (New York, USA), p. 1249, Santa Fe, Sept 26 - Oct 1, 2004, American Institute of Physics, 2005.

[128] E. S. Soukhovitskii, R. Capote, J. M. Quesada, and S. Chiba, "Dispersive coupled-channel analysis of nucleon scattering from ^{232}Th up to 200 MeV," *Phys.Rev. C*, vol. 72, p. 024604, 2005.

[129] W. Hauser and H. Feshbach, "The inelastic scattering of neutrons," *Phys. Rev.*, vol. 87, pp. 366–373, 1952.

[130] M. Sin, R., A. Ventura, M. Herman, and P. Obložinský, "Fission of light actinides: ^{232}Th(n,f) and ^{231}Pa(n,f) reactions," *Physical Review C*, vol. 74, no. 1, p. 014608, 2006.

[131] G. Aerts and the n-TOF Collaboration, "Neutron capture cross section of ^{232}Th measured at the n-TOF facility at CERN in the unresolved resonance region up to 1 MeV," *Phys.Rev. C*, vol. 73, p. 054610, 2006.

[132] A. Ignatyuk, V. Lunev, Y. Shubin, E. Gai, and N. Titarenko, "Evaluation of n + ^{232}Th cross sections for the energy range up to 150 MeV." Provided to the IAEA CRP on Th-U cycle, 2006.

[133] D. Madland, "Total prompt energy release in the neutron-induced fission of ^{235}U, ^{238}U, and ^{239}Pu," *Nucl. Phys.*, vol. A772, p. 113, 2006.

[134] ICRU-Report-63, in *Nuclear Data for Neutron and Proton Radiotherapy and for Radiation Protection*, Bethesda, MD: International Commission on Radiation Units and Measurements, 2000.

[135] D. Muir, "Gamma rays, Q-values and kerma factors," Tech. Rep. LA-6258-MS, Los Alamos National Laboratory, Los Alamos, NM, 1976.

[136] J. Rowlands, "The incident neutron energy dependence of the prompt energy yield in fission," SERCO document CCU0516 SA/NST/17729/W001, Issue 2, August 2006.

[137] G. Rudstam, P. Fink, A. Filip, A. D'Angelo, and R. McKnight, "Delayed neutron data for the major actinides," Tech. Rep. NEA/WPEC-6, Paris, 2002.

[138] K.-L. Kratz and G. Herrmann, "Systematics of neutron emission probabilities from delayed neutron precursors," *Z. Physik*, vol. 363, pp. 435–442, 1973.

[139] F. Mann, C.Dunn, and R. Schenter, "Beta decay properties using a statistical model," *Phys. Rev.*, vol. C25, pp. 524–526, 1982.

[140] M. Brady, "Evaluation and application of delayed neutron precursor data," Tech. Rep. LA-11534-T, Los Alamos National laboratory, Los Alamos, NM, 1989.

[141] T. England and B. Rider, "Nuclear modeling of the ^{239}Pu(n, xn) excitation function," Tech. Rep. LA-UR-94-3106 ENDF-349, Los Alamos National laboratory, Los Alamos, NM, 1993.

[142] W. Wilson and T. England, "Delayed neutron study using ENDF/B-VI basic nuclear data," *Prog. Nucl. Energy*, vol. 41, pp. 71–107, 2002.

[143] B. Pfeiffer, K.-L. Kratz, and P.Moller, "Status of delayed-neutron data: half-lives and neutron emission probabilities," *Prog. Nucl. Energy*, vol. 41, pp. 39–69, 2002.

[144] G. Audi, O. Bersillon, J. Blachot, and A. Wapstra, "The NUBASE evaluation of nuclear and decay properties," *Nucl. Phys.*, vol. A729, p. 3, 2003.

[145] P.Moller, B. Pfeiffer, and K.-L. Kratz, "New calculations of gross beta decay properties for astrophysical applications: Speeding up the classical r-process," *Phys. Rev.*, vol. C67, p. 055802, 2003.

[146] P. Moller, J. R. Nix, W. D. Myers, and W. J. Swiatecki, "Nuclear ground-state masses and deformations," *Atomic Data Nucl. Data Tables*, vol. 59, pp. 185–381, 1995.

[147] P. Moller, J. Nix, and K.-L. Kratz, "Nuclear properties for astrophysical and radioactive-ion-beam applications," *At. Data Nucl. Data Tables*, vol. 66, p. 131, 1997.

[148] M. Brady and T. England, "Delayed neutron data and group parameters for 43 fissioning systems," *Nucl. Sci. Eng.*, vol. 103, pp. 129–149, 1989.

[149] G. Keepin. New York: Addison-Wesley, 1965.

[150] J. Conant and P. Palmedo, "Delayed neutron data," *Nuc. Sci. Eng.*, vol. 44, p. 173, 1971.

[151] R. Tuttle, "Delayed neutron data," *Nuc. Sci. Eng.*, vol. 56, p. 37, 1975.

[152] T. Ohsawa and T. Oyama, "Possible fluctuations in delayed neutron yields in the resonance region of U-235," in *Proceedings of the Specialists' Meeting on Delayed Neutron Nuclear Data* (J. Katakura, ed.), (Tokai-mura, Naga-kun, Ibaraki-ken, Japan), p. 43, JAERI, American Institute of Physics, 1999.

[153] T. Ohsawa and F.-J. Hambsch, "An interpretation of energy-dependence of delayed neutron yields in the resonance region for ^{235}U and ^{239}Pu," *Nuc. Sci. Eng.*, vol. 148, p. 50, 2004.

[154] K. Nakajima, "Re-evaluation of the effective delayed neutron fraction measured by the substitution technique for a light water moderated low-enriched uranium core," *J. Nucl. Sci. Techn.*, vol. 38, pp. 1120–1125, 2001.

[155] T. Sakurai and S. Okajima, "Adjustment of delayed neutron yields in jendl-3.2," *J. Nuc. Sci. Tech.*, vol. 39, pp. 19–30, 2002. Analyzed β-effective in the JAERI Tank Critical Assembly (TCA, 2.6% enriched) and recommended 0.01586 $\pm$ 1.8%, the value adopted for JENDL-3.3.

[156] S. van der Marck, "Benchmarking ENDF/B-VII beta1." CSEWG 2005 meeting report, www.nndc.bnl.gov/csewg/, 2005. Analyzed TCA, IPEN/MB-01, Stacy, Winco, and Proteus thermal β-effective measurements and found JENDL-3.3 to be superior to ENDF/B-VI.8.

[157] Y. Chao. Westinghouse, Private Communication, 2006.

[158] M. Brady. PNNL, Private Communication, 2006.

[159] J. Pruet, M.-A. Descalle, J. Hall, B. Pohl, and S. Prussin, "Neutron and photon transport in sea-going cargo containers," *J. Appl. Phys.*, vol. 97, p. 094908, 2005.

[160] J. Pruet, J. Hall, M.-A. Descalle, and S. Prussin, "Monte Carlo models for the production of β-delayed gamma-rays following fission of special nuclear materials," *Nuclear Instruments and Methods*, vol. B 222, p. 403, 2004.

[161] D. Brown, J. Pruet, G. Hedstrom, J. Hall, and M.-A. Descalle, "Proposal for ENDF formats that describe emission of post-fission β-delayed photons," Report UCRL-TR-206607, Lawrence Livermore National Laboratory, 2004.

[162] D. Brown, "Translating post-fission β-delayed γ data for ^{239}Pu into ENDF format," Tech. Rep. UCRL-TR-223148, Lawrence Livermore National Laboratory, 2006.

[163] R. Q. Wright and R. E. MacFarlane, "Review of ENDF/B-VI fission-product cross sections," Tech. Rep. ORNL/TM-13723, Oak Ridge National Laboratory, Oak Ridge, TN, 2000.

[164] P. Obložinský *et al.*, "WPEC Subgroup 23: Creation of neutron cross section library for fission products." www.nndc.bnl.gov/sg23, 2006.

[165] M. D. DeHart, "Sensitivity and parametric evaluations of significant aspects of burnup credit for PWR spent fuel packages," Tech. Rep. ORNL/TM-12973, Oak Ridge National Laboratory, 1995.

[166] Y. D. Lee, J. Chang, and P. Obložinský, "Neutron cross section evaluations of fission products in the fast energy region," in *Proc. of the International Conference on Nuclear Data for Science and Technology*, p. 168, Tsukuba, 2002.

[167] Y. D. Lee and J. H. Chang, "Fission product evaluations for the selected nuclei," (New York, USA), p. 378, Santa Fe, Sept 26 - Oct 1, 2004, American Institute of Physics, 2005.

[168] H.-I. Kim, M. Herman, S. F. Mughabghab, P. Obložinský, and D. Rochman, "Evaluation of neutron induced reactions on 33 fission products for ENDF/B-VII.0," Tech. Rep. in preparation, Brookhaven National Laboratory, 2007.

[169] D. Rochman, M. Herman, S. Mughabghab, and P. Obložinský, "New evaluation of the ^{99}Tc neutron-induced cross sections for the ENDF/B-VII.0 library," Tech. Rep. BNL-75892-2006-JA-R1, Brookhaven National Laboratory, 2006.

[170] O. Iwamoto, M. Herman, S. Mughabghab, and P. Obložinský, "Neutron cross-section evaluations for 70,72,73,74,76-Ge," in *Proc. of the International Conference on Nuclear Data for Science and Technology* (R. Haight, M. Chadwick, T. Kawano, and P. Talou, eds.), (New York, USA), p. 434, Santa Fe, Sept 26 - Oct 1, 2004, American Institute of Physics, 2005.

[171] D. Rochman *et al.*, "Evaluation of neutron induced reactions on 8 isotopes of Gd for ENDF/B-VII.0," Tech. Rep. in preparation, Brookhaven National Laboratory, 2007.

[172] D. Rochman, M. Herman, P. Obložinský, S. Mughabghab, T. Kawano, and L. Leal, "Evaluation of covariance data for Gd isotopes." to be published, 2007.

[173] R. Capote. Dispersive Optical Potential for ^{103}Rh, Private communication, 2006.

[174] R. Capote, E. S. Soukhovitskii, J. M. Quesada, and S. Chiba, "Is a global coupled-channel dispersive optical model potential for actinides feasible?," *Physical Review C*, vol. 72, no. 6, p. 064610, 2005.

[175] E. S. Soukhovitskii, R. Capote, J. M. Quesada, and S. Chiba, "Dispersive coupled-channel analysis of nucleon scattering from ^{232}Th up to 200 MeV," *Physical Review C*, vol. 72, no. 2, p. 024604, 2005.

[176] P. Obložinský *et al.*, "WPEC Subgroup 21: Assessment of neutron cross section evaluations for fission products." www.nndc.bnl.gov/sg21, 2005.

[177] P. Obložinský, M. Herman, S. Mughabghab, I. Sirakov, J. Chang, T. Nakagawa, K. Shibata, M. Kawai, A. Ignatyuk, V. Pronyaev, V. Zerkin, S. Qingbiao, and Z. Youxiang, "Assessment of neutron cross-section evaluations for the bulk of fission products," Tech. Rep. NEA/WPEC-21, OECD Nuclear Energy Agency, Paris, 2005.

[178] M. B. Chadwick, P. G. Young, S. Chiba, S. Frankle, G. M. Hale, H. G. Hughes, A. J. Koning, R. C. Little, R. E. MacFarlane, R. E. Prael, and L. S. Waters, "Cross section evaluations to 150 MeV for accelerator-driven systems and implementation in MCNPX," *Nucl. Sci. Eng.*, vol. 131, pp. 293–328, 1999.

[179] D. Cokinos and E. Melkonian, "Measurement of the 2200 m/sec neutron-proton capture cross section," *Phys. Rev.*, vol. C15, p. 1636, 1977.

[180] K. Schoen *et al.*, "Precision neutron interferometric measurements and updated evaluations of the n-p and n-d coherent neutron scattering lengths," *Phys. Rev.*, vol. C67, p. 044005, 2003.

[181] T. L. Houk, "Neutron-proton scattering cross section at a few electron Volts and charge independence," *Phys. Rev.*, vol. C3, p. 1886, 1971.

[182] W. Dilg, "Measurement of the neutron-proton total cross section at 132 eV," *Phys. Rev.*, vol. C11, p. 103, 1975.

[183] N. Boukharaba *et al.*, "Measurement of the n-p elastic scattering angular distribution at $E_n = 10$ MeV," *Phys. Rev.*, vol. C65, p. 014004, 2002.

[184] W. Buerkle and G. Mertens, "Measurement of the neutron-proton differential cross section at 14.1 MeV," *Few Body Systems*, vol. 22, p. 11, 1997.

[185] G. M. Hale *et al.*, "Neutron-triton cross sections and scattering lengths obtained from p-^{3}He scattering," *Phys. Rev.*, vol. C42, p. 438, 1990.

[186] D. Rochman, M. Herman, and P. Obložinský, "New evaluation of ^{51}V(n, np+pn) and (n, t) cross sections for the ENDF/B-VII library," *Fusion Engineering and Design*, vol. 81, pp. 2109–2113, August 2006.

[187] S. Grimes *et al.*, "Charged particle-producing reactions of 15-MeV neutrons on ^{51}V and ^{93}Nb," *Phys. Rev. C*, vol. 17, p. 508, 1978.

[188] O. Kokoo, I. Murata, and A. Takahashi, "Measurements of double-differential cross sections of charged-particle emission reactions for several structural elements of fusion power reactors by 14.1-MeV incident neutrons," *Nuclear Science and Engineering*, vol. 132, p. 16, 1999.

[189] R. Woelfle *et al. Radiochimica Acta*, vol. 50, p. 5, 1990.

[190] T. Kawano *et al.*, "Production of isomers by neutron-induced inelastic scattering on ^{193}Ir and influence of spin distribution in the preequilibrium process," *Nucl. Instr. Meth.*, vol. 562, p. 774, 2006.

[191] A. J. Koning and J. P. Delaroche, "Local and global nucleon optical models from 1 keV to 200 MeV," *Nucl.Phys.*, vol. A713, p. 231, 2003.

[192] A. Koning, S. Hilaire, and M. Duijvestijn, "TALYS: Comprehensive nuclear reaction modeling," in *Proc. of the International Conference on Nuclear Data for Science and Technology* (R. Haight, M. Chadwick, T. Kawano, and P. Talou, eds.), (New York, USA), pp. 1154–1159, Santa Fe, Sept 26 - Oct 1, 2004, American Institute of Physics, 2005.

[193] D. L. Smith, *Probability, Statistics, and Data Uncertainties in Nuclear Science and Technology*. American Nuclear Society, 1991.

[194] R. Kinsey, "ENDF-201: ENDF/B Summary Documentation," Tech. Rep. BNL-NCS-17541, National Nuclear Data Center, BNL, July 1979. Note: 3^{rd} Edition, ENDF/B-V Library.

[195] B. Magurno, R. Kinsey, and F. Scheffel, "Guidebook for the ENDF/B-V Nuclear Data Files," Tech. Rep. EPRI NP-2510, BNL-NCS-31451, ENDF-328, Brookhaven National Laboratory and Electric Power Research Institute, July 1982.

[196] M. Ishikawa, "Recent Application of Nuclear Data to Fast Reactor Core Analysis and Design in Japan," (New York, USA), p. 1405, Santa Fe, Sept 26 - Oct 1, 2004, American Institute of Physics, 2005.

[197] M. Ishikawa, K. Sugino, W. Sato, and K. Numata, "Development of a Unified Cross-section Set ADJ2000 Based on Adjustment Technique for Fast Reactor Analysis," *J. Nucl. Sci. Technol.*, p. 1073, 2002. Suppl. 2.

[198] CSEWG-Collaboration: Evaluated Nuclear Data File, ENDF/B-VI, released in 1990, unpublished.

[199] V. McLane, "ENDF-201: ENDF/B-VI summary documentation," Tech. Rep. BNL-NCS-17541, Ed. 4, **Suppl.**

1 , Brookhaven National Laboratory, National Nuclear Data Center, Upton, NY, 1996.

[200] K. Kosako and N. Yanano, "Preparation of a covariance processing system for the evaluated nuclear data file, JENDL," Tech. Rep. JNC TJ-9440, 99-003, JAERI, 1999. (in Japanese).

[201] T. Kawano, T. Ohsawa, K. Shibata, and H. Nakashima, "Evaluation of Covariance for Fission Neutron Spectra," Tech. Rep. 99-009, JAERI, 1999. (in Japanese).

[202] H. Derrien, L. C. Leal, and N. M. Larson, "Evaluation of ^{232}Th Neutron Resonance Parameters in the Energy Range 0 to 4 keV," Tech. Rep. ORNL/TM-2006/53, Oak Ridge National Laboratory, 2006.

[203] D. Smith, "Covariance matrices for nuclear cross sections derived from nuclear model calculations," report ANL/NDM-159 November, Argonne National Laboratory, 2004.

[204] A. Trkov, "Summary report of the IAEA technical meeting," INDC(NDS)-471, IAEA, Vienna, 2005.

[205] R. E. MacFarlane, "New thermal neutron scattering files for ENDF/B-VI release 2," Tech. Rep. LA-12639-MS (1994), Los Alamos National Laboratory, Los Alamos, NM, 1994.

[206] J. Koppel and D. Houston, "Reference manual for ENDF thermal neutron scattering data," report GA-8774 revised and reissued as ENDF-269 by the National Nuclear Data Center, General Atomic, July 1978.

[207] J. Keinert and J. Sax, "Investigation of neutron scattering dynamics in liquid hydrogen and deuterium for cold neutron sources," *Kerntechnik*, vol. 51, p. 19, 1987.

[208] J. A. Young and J. U. Koppel, "Slow neutron scattering by molecular hydrogen and deuterium," *Phys. Rev.*, vol. 135, pp. A603–A611, Aug 1964.

[209] G. H. Vineyard, "Frequency factors and isotope effects in solid state rate processes," *Journal of Physics and Chemistry of Solids*, vol. 3, no. 1-2, pp. 121–127, 1957.

[210] R. Stedman, L. Almqvist, and G. Nilsson, "Phonon-frequency distributions and heat capacities of Aluminum and Lead," *Phys. Rev.*, vol. 162, pp. 549–557, Oct 1967.

[211] B. N. Brockhouse, H. E. Abou-Helal, and E. D. Hallman, "Lattice vibrations in iron at 296°K," *Solid State Commun.*, vol. 5, p. 211, 1967.

[212] W. P. Poenitz and S. E. Aumeier, "The simultaneous evaluation of the standards and other cross sections of importance for technology," Tech. Rep. ANL/NDM-139, Argonne National Laboratory, Argonne, IL, 1997.

[213] F.-J. Hambsch, A. D. Carlson, and H. Vonach, "Status of the neutron cross section standards database," in *Proc. of the International Conference on Nuclear Data for Science and Technology* (R. Haight, M. Chadwick, T. Kawano, and P. Talou, eds.), (New York, USA), pp. 826–829, Santa Fe, Sept 26 - Oct 1, 2004, American Institute of Physics, 2005.

[214] R. Gwin, R. R. Spencer, and R. W. Ingle, "Measurements of the Energy Dependence of Prompt Neutron Emission from ^{233,235}U and ^{239,241}Pu for En=0.005 to 10 eV Relative to Emission from Spontaneous Fission of ^{252}Cf," *Nucl. Sci. Eng.*, vol. 87, pp. 381–404, 1984.

[215] M. Arif, H. Kaiser, S. A. Werner, and J. O. Willis, "Precison Measurement of the Bound-Coherent-Neutron Scattering Length of ^{235}U," *Phys. Rev.*, vol. A35, p. 2810, 1987.

[216] N. Boukharouba, F. B. Bateman, C. E. Brient, A. Carlson, S. M. Grimes, R. C. Haight, T. N. Massey, and O. A. Wasson, "Measurement of the n-p elastic scattering angular distribution at E_n = 10 MeV," *Phys. Rev. C*, vol. 65, p. 014004, 2002.

[217] A. D. Carlson, G. M. Hale, and V. Pronyaev, "Summary report of the first research coordination meeting on improvement of the standard cross sections for light elements," Tech. Rep. INDC(NDS)-438, International Atomic Energy Agency, Vienna, 2003.

[218] S. Chiba and D. L. Smith, "A suggested procedure for resolving an anomaly in least-squares data analysis known as Peelle's pertinent puzzle and the general implications for nuclear data evaluation," Tech. Rep. ANL/NDM-121, Argonne National Laboratory, Argonne, Illinois, 1991.

[219] W. P. Poenitz, "Data interpretation, objective, evaluation procedures and mathematical technique for the evaluation of energy-dependent ratio, shape and cross section data," in *Proc. of the Conference on Nuclear Data Evaluation Methods and Procedures* (B. Magurno and S. Pearlstein, eds.), pp. 249–289, Brookhaven National Laboratory, Upton, NY, BNL-NCS-51363, 1981.

[220] A. D. Carlson, W. P. Poenitz, G. M. Hale, R. W. Peelle, D. C. Dodder, and C. Y. Fu, "The ENDF/B-VI neutron cross section measurement standards," Tech. Rep. ENDF-351, Brookhaven National Laboratory, National Nuclear Data Center, Upton, NY, 1993.

[221] Z. P. Chen, "Reduced R-matrix analysis for ^{17}O system," *Atomic Energy Science and Technology*, vol. 29, No. 4, pp. 366–371, 1995.

[222] S. Tagesen and D. M. Hetrick, "Enhancements to the generalized least-squares cross-section evaluation code GLUCS," in *Proc. of the International Conference on Nuclear Data for Science and Technology* (J. K. Dickens, ed.), (La Grange Park, IL), pp. 589–591, Gatlinburg, TN, 1994, American Nuclear Society, 1994.

[223] T. Kawano, H. Matsunobu, T. Murata, A. Zukeran, Y. Nakajima, M. Kawai, O. Iwamoto, K. Shibata, T. Nakagawa, T. Ohsawa, M. Baba, and T. Yoshida, "Evaluation of Fission Cross Sections and Covariances for ^{233}U, ^{235}U, ^{238}U, ^{239}Pu, ^{240}Pu, and ^{241}Pu," Tech. Rep. JAERI-Research-2000-004, Japan Atomic Energy Research Institute, Tokai, Japan, 2000.

[224] S. A. Badikov, E. V. Gai, M. A. Guseynov, and N. S. Rabotnov, "Nuclear data processing, analysis, transformation and storage with Pade-approximants," in *Proceedings Nuclear Data for Science and Technology* (S. Qaim, ed.), (New York, NY), pp. 182–187, Jülich, Germany, May 13-17, 1991, Springer-Verlag, 1992.

[225] E. J. Axton, "Evaluation of the Thermal Constants of ^{233}U, ^{235}U, ^{239}Pu and ^{241}Pu, and the Fission Neutron Yield of ^{252}Cf," Tech. Rep. CBNM (IRMM) Report GE/PH/01/86, IRMM, Geel, 1986.

[226] V. M. Maslov, "Uranium symmetric/asymmetric nucleon-induced fission up to 200 MeV," *Eur. Phys. J.*, vol. A21, pp. 281–286, 2004.

[227] J. Hardy. Private Communication, Memo dated 18 June, 1985.

[228] S. S. Dietrich and B. L. Berman, "Atlas of photonuetron cross sections obtained with monoenergetic photons," *Atomic Data and Nuclear Data Tables*, vol. 38, pp. 199–338, 1988.

[229] E. G. Fuller and H. Gerstenberg, "Photonuclear data - abstract sheets 1955-1982," Tech. Rep. Reports of the

US National Bureau of Standards, NBSIR 83-2742, vol. I-XV (1983-1986), National Institute for Standards and Technology, Gaithersburg, MD, 1983-1986.

[230] A. V. Varlamov, V. V. Varlamov, D. S. Rudenko, and M. E. Stepanov, "Atlas of giant dipole resonance paramaters and graphs of photonuclear reaction cross sections," Tech. Rep. INDC (NDS)-394 (1999), International Atomic Energy Agency, Vienna, Austria, 1999.

[231] B. L. Berman, R. E. Pywell, S. S. Dietrich, M. N. Thompson, K. G. McNeill, and J. W. Jury, "Absolute photoneutron cross-sections for Zr, I, Pr, Au, and Pb," *Physical Review*, vol. 36, pp. 1286–1292, 1987.

[232] E. Wolynec, A. R. V. Martinez, P. Gouffon, Y. Miyao, V. A. Serrao, and M. N. Martins, "Comment on photoneutron cross-sections," *Phys. Rev. C*, vol. 29, pp. 1137–1139, 1984.

[233] P. Obložinský and M. Chadwick, "Photonuclear Data on ^{14}N for Gamma Resonance Technology." Unpublished BNL report, December 2002.

[234] F. Ajzenberg-Selove, "Energy Levels of Light Nuclei A = 13-15," *Nucl. Phys.*, vol. A253, pp. 1 – 196, 1991.

[235] M. B. Chadwick, P. G. Young, R. E. MacFarlane, M. C. White, and R. C. Little, "Photonuclear physics in radiation transport: I. Cross sections and spectra photonuclear cross section evaluations to 150 MeV," *Nucl. Sci. Eng.*, vol. 144, pp. 157–173, 2003.

[236] M. L. Giacri, M. B. Chadwick, D. Ridikas, P. G. Young, and W. B. Wilson, "Photonuclear physics in radiation transport: III. Photofission cross sections," *Nucl. Sci. Eng.*, vol. 153, pp. 33–40, 2006.

[237] M. White, R. Little, M. Chadwick, P. Young, and R. MacFarlane, "Photonuclear physics in radiation transport-II: Implementation," *Nucl. Sci. Eng.*, vol. 144, pp. 174–189, 2003.

[238] J. T. Caldwell, E. J. Dowdy, B. L. Berman, R. A. Alvarez, and P. Meyer, "Giant resonance for the actinide nuclei: Photoneutron and photofission cross sections for ^{235}U, ^{236}U, ^{238}U, and ^{232}Th," *Phys. Rev. C*, vol. 21, pp. 1215–1231, Apr 1980.

[239] P. Young and M. B. Chadwick *to be published*, 2007.

[240] W. C. Barber and W. D. George, "Neutron Yields from Targets Bombarded by Electrons," *Phys.Rev.*, vol. 116, pp. 1551–1559, 1959.

[241] M. White, R. Little, M. Chadwick, P. Moller, W. Wilson, M. Nieto, M. Giacri, C. Moss, H. Trellue, G. McKinney, and D. Mashnik, "Photofission delayed neutron detection of HEU for nonproliferation," Tech. Rep. LA-UR-03-7724, Los Alamos National Laboratory, NM, 2003.

[242] G. M. Hale and T. L. Talley, "Cross sections and spectra for charged-particle induced reactions," in *Proc. of the International Conference on Nuclear Data for Science and Technology* (J. K. Dickens, ed.), (La Grange Park, IL), p. 403, Gatlinburg, TN, 1994, American Nuclear Society, 1994.

[243] J. Lohr and W. Haeberli, "Elastic Scattering of 9-13 MeV Vector Polarized Deuterons," *Nucl. Phys.*, vol. A232, p. 381, 1974.

[244] L. McFadden and G. R. Satchler, "Optical model analyses of the scattering of 24.7 MeV alpha particles," *Nucl. Phys.*, vol. 84, pp. 177–200, 1966.

[245] F. D. Becchetti and G. W. Greenlees, "Polarization Phenomena in Nuclear Reactions," in *Proc. of the Conference on Polarization Phenomena in Nuclear Reactions* (H. Barschall and W. Haeberli, eds.), (University of Wisconsin), p. 682, University of Wisconsin Press, 223, 1971.

[246] D. G. Madland, "Recent results in the development of a global medium-energy nucleon-nucleus optical model potential," in *Proc. of a Specialists Meeting on Preequilibrium Reactions in Semmering, Austria* (B. Strohmaier, ed.), no. NEANDC-245, pp. 103–116, OECD Nuclear Energy Agency, Paris, 1988.

[247] A. J. Koning, J. J. van Wijk, and J.-P. Delaroche, "ECISVIEW: An interactive toolbox for optical model development," in *Proc. of a Specialists Meeting on the Nucleon-Nucleus Optical Model up to 200 MeV*, (Paris, France), pp. 111–120, Bruyeres-le-Chatel France, 13-15 November, OECD Nuclear Energy Agency, 1996.

[248] A. V. Ignatyuk, G. N. Smirenkin, and A. Tishin, "Phenomenological description of the energy dependence of the level density parameter," *Sov. J. Nucl. Phys.*, vol. 21, pp. 255–257, 1975.

[249] J. L. Cook, H. Ferguson, and A. R. Musgrove, "Nuclear level densities for intermediate and heavy nuclei," *Aus. J. Phys.*, vol. 20, pp. 477–487, 1967.

[250] C. Kalbach, "The Griffin Model, complex particles and direct nuclear reactions," *Z. Physik*, vol. A283, pp. 401–411, 1977.

[251] C. Kalbach, "PRECO-D2: Program for calculating preequilibrium and direct reaction double differential cross sections," report LA-10248-MS, Los Alamos National Laboratory, 1985.

[252] H. Trellue and M. Chadwick, "Modifications to High-Energy Neutron and Proton Sublibraries (LA150)," Tech. Rep. LA-UR-06-3091, Los Alamos National Laboratory, 2005.

[253] N. Jarmie, R. E. Brown, and R. A. Hardekopf, "Fusion-energy reaction $^2H(t,\alpha)n$ from $E_t = 12.5$ *to* 117 keV," *Phys. Rev. C*, vol. 29, pp. 2031–2046, Jun 1984.

[254] C. H. Poppe, C. H. Holbrow, and R. R. Borchers, "Neutrons from D + T and D + H," *Phys. Rev.*, vol. 129, pp. 733–739, Jan 1963.

[255] M. Drosg, "Improved evaluation of the differential cross sections of the ^{3}H(d,n)^{4}He reaction for deuteron energies between 3 and 7 MeV," *Zeitschrift für Physik A, Hadrons and Nuclei*, vol. 300, pp. 315 – 317, Dec 1981.

[256] D. M. Holm and H. V. Argo, "t-t elastic scattering from 1.6 to 2.0 MeV," *Phys.Rev.*, vol. 101, p. 1772, 1956.

[257] C. Wong, J. D. Anderson, and J. W. McClure, "Neutron spectrum from the t+t reaction," *Nucl.Phys.*, vol. 71, p. 106, 1965.

[258] D. B. Smith, N. Jarmie, and A. M. Lockett, "He^3 + t Reactions," *Phys.Rev.*, vol. 129, p. 785, 1963.

[259] S. Barshay and G. M. Temmer, "Geometric test of the isospin multiplet nature of nuclear analog states," *Phys. Rev. Lett.*, vol. 12, pp. 728–730, Jun 1964.

[260] NSDD-Network, "ENSDF, Evaluated Nuclear Structure Data File." www.nndc.bnl.gov/ensdf, 2006.

[261] J. Tuli, "Nuclear Wallet Cards." Electronic version, www.nndc.bnl.gov/wallet, 2006.

[262] R. Greenwood, R. Helmer, M. Putnam, and K. Watts, "Measurement of β- decay intensity distributions of several fission-product isotopes using a total absorption γ-ray spectrometer," *Nucl.Instrum.Methods Phys.Res.*, vol. A390, p. 95, 1997.

[263] N. Hagura, T. Yoshida, and T. Tachibana, "Reconsideration of the theoretical supplementation of decay data

in fission-product decay heat summation calculations," *Journal of Nucl. Science and Tech. (to be published)*, 2006.

[264] I. Band, M. Trzhaskovskaya, C. Nestor Jr., P. Tikkanen, and S. Raman, "Dirac-Fock internal conversion coefficients," *At. Data Nucl. Data Tables*, vol. 81, p. 1, 2002.

[265] P. Cassette, "SPEBETA programme de calcul du spectre en energie des electros emis par des radionucleides emetterus beta," Tech. Rep. CEA Technical Note LPRI/92/307/J, CEA Saclay, 1992.

[266] A. Tobias and R. Mills. (private communication), 1989.

[267] T. England and B. Rider, "Evaluation and compilation of fission product yields," Tech. Rep. ENDF-349, Los Alamos National Laboratory, 1992.

[268] D. E. Cullen, J. H. Hubbell, and L. Kissel, "EPDL97: The Evaluated Photon Data Library, '97 Version," Tech. Rep. UCRL-50400, Vol.6, Rev.5, Lawrence Livermore National Laboratory, September 1997.

[269] S. T. Perkins, D. E. Cullen, and S. M. Seltzer, "Tables and Graphs of Atomic Subshell and Relaxation Data Derived from the LLNL Evaluated Electron Data Library (EEDL), Z = 1-100," Tech. Rep. UCRL-50400, Vol.30, Lawrence Livermore National Laboratory, October 1991.

[270] S. T. Perkins, D. E. Cullen, and S. M. Seltzer, "Tables and Graphs of Electron Interaction Cross Sections from 10 eV to 100 GeV Data Derived from the LLNL Evaluated Electron Data Library (EEDL), Z = 1-100," Tech. Rep. UCRL-50400, Vol.31, Lawrence Livermore National Laboratory, October 1991.

[271] D. E. Cullen, "ENDF/B-VI Coupled Photon-Electron Data for Use in Radiation Shielding Applications," Tech. Rep. UCRL-JC-148180, Lawrence Livermore National Laboratory, 2002.

[272] J. Both *et al.*, "TRIPOLI-4 Monte Carlo method particle transport computer code," Tech. Rep. CEA-R-6044, CEA Saclay, 2003.

[273] T. Sutton *et al.*, "The physical models and statistical procedures used in the RACER Monte Carlo code," Tech. Rep. KAPL-4840 (DOE/TIC-4500-R75), Knolls Atomic Power Laboratory, 1999.

[274] F. Brown, "Vectorization of 3-D General Geometry Monte Carlo," *Trans. Am. Nucl. Soc.*, vol. 53, p. 283, 1986.

[275] L. Ondis, L. Tyburski, and B. Moskowitz, "RCP01 - a Monte Carlo program for solving neutron and photon transport problems in three-dimensinal geometry with detailed energy desription and depletion capability," Tech. Rep. B-TM-1638, Bechtel Bettis, 2000.

[276] R. Blomquist, "VIM continous energy Monte Carlo transport code," in *Proc. Inter. Conf. on Mathematics, Computations, Reactor Physics and Environmental Analysis*, (Portland, OR), April 30 - May 4 1995.

[277] S.C. van der Marck, "Benchmarking ENDF/B-VII.0." Nuclear Data Sheets, the present issue.

[278] A. dos Dantos, R. Diniz, L. Fanaro, R. Jerez, G. de Andrade e Silva, and M. Yamaguchi, "The experimental determination of the effective delayed neutron parameters of the IPEN/MB-01 reactor," (Chicago), PHYSOR-2004.

[279] S. Okajima, T. Sakurai, J. Lebrat, V. Averlant, and M. M., "Summary on international benchmark experiments for effective delayed neutron fraction," *Progress in Nuclear Energy*, vol. 41, p. 285301, 2002.

[280] R. Klein Meulekamp and S. van der Marck, "Re-evaluation of the effective delayed neutron fraction measured by the substitution technique for a light water moderated low-enriched uranium core," *Nucl. Sci. Eng.*, vol. 152, pp. 142–148, 2006.

[281] S. van der Marck, R. Klein Meulekamp, A. Hogenbirk, and A. Koning, "Benchmark results for delayed neutron data," (New York, USA), pp. 531–534, Santa Fe, Sept 26 - Oct 1, 2004, American Institute of Physics, 2005.

[282] W. Webster *et al.*, "Measurements of the neutron emission spectra from spheres of N, O, W, U-235, U-238, and Pu-239, pulsed by 14 MeV neutrons," Tech. Rep. UCID-17332, 1976.

[283] C. Wong *et al.*, "Livermore pulsed sphere program: Program summary through July 1971," Tech. Rep. UCRL-51144, Rev I, and Addendum (1973), Lawrence Livermore National Laboratory, Livermore, CA, 1972.

[284] A. Marchetti and G. Hedstrom, "New Monte Carlo simulations of the LLNL pulsed-sphere experiments," Tech. Rep. UCRL-ID-131461, Lawrence Livermore National Laboratory, Livermore, CA, 1998.

[285] S. Frankle, "LLNL pulsed-sphere measurements and detector response functions," Tech. Rep. X-5:SCF-04-004 and LA-UR-05-5878, Los Alamos National Laboratory, Livermore, CA, 2004.

[286] S. Frankle, "Possible impact of additional collimators on the LLNL pulsed-sphere experiments," Tech. Rep. X-5:SCF-04-001 and LA-UR-05-5877, Los Alamos National Laboratory, Livermore, CA, 2004.

[287] J. Bucholz and S. Frankle, "Improving the LLNL pulsed-sphere experiments database and MCNP models," *Trans. Am. Nucl. Soc.*, pp. 433–435, 2002.

APPENDIX A: ENDF-6 FORMAT, ABBREVIATIONS

For convenience, we summarize several basic terms and quantities frequently used in the ENDF-6 format. This is shown in Table XXXI where we explain selected file numbers and section numbers. The file number, MF identifies type of information stored in the file, while the section number, MT identifies reaction channel (type of reaction). In Table XXXII we explain some abbreviations used throughout the present paper.

TABLE XXXI: Terms and quantities frequently used in the ENDF-6 format. See ENDF-6 Formats Manual [4] for more details.

File number	Section number	Quantity
MF=1		General information
MF=1	MT=451	Text information
	MT=452	Number of neutrons per fission, $\bar{\nu}$ ($\bar{\nu} = \bar{\nu}_d + \bar{\nu}_p$)
	MT=455	Number of delayed neutrons per fission, $\bar{\nu}_d$
	MT=456	Number of prompt neutrons per fission, $\bar{\nu}_p$
	MT=458	Energy release in fission for incident neutrons
MF=2		Resonance parameters
MF=2	MT=151	Resolved resonance parameters, flag=1
	MT=151	Unresolved resonance parameters, flag=2
MF=3		Reaction cross sections
MF=3	MT=1	Total cross sections
	MT=2	Elastic cross sections
	MT=4	Inelastic cross sections; (n,n') lumped cross sections
	MT=5	Sum of cross sections for all reaction channels not given explicitly under other MT
	MT=16	(n,2n) cross sections
	MT=18	Total fission cross sections
	MT=19	First chance fission cross sections
	MT=51	(n,n'$_1$) cross sections; inelastic scattering to the 1^{st} excited level
	MT=52	(n,n'$_2$) cross sections; inelastic scattering to the 2^{nd} excited level
	MT=102	(n,γ) cross sections
	MT=103	(n,p) cross sections
	MT=105	(n,t) cross sections
	MT=107	(n,α) cross sections
MF=4		Angular distributions of emitted particles
MF=5		Energy distributions (spectra) of emitted particles
MF=6		Energy-angle distributions of emitted particles
MF=7		Thermal neutron scattering
MF=8		Radioactivity and fission-product yields
MF=12		Multiplicities for photon production
MF=13		Cross sections for photon production
MF=31		Covariances for nubar ($\bar{\nu}$)
MF=32		Covariances for resonance parameters
MF=33		Covariances for cross sections
MF=33	MT=1	Covariances for total cross sections
	MT=2	Covariances for elastic cross sections
	MT=851-870	Covariances for cross sections of lumped channels
MF=34		Covariances for angular distributions of emitted particles
MF=35		Covariances for energy spectra of emitted particles
MF=40		Covariances for production of radioactive nuclei

TABLE XXXII: Some abbreviations used in the present paper.

Abbreviation	Meaning
CSEWG	Cross Section Evaluation Working Group
CRP	IAEA Coordinated Research Project
CSISRS	Cross Section Information Storage and Retrieval System, see also EXFOR
DOE-NNSA	U.S. Department of Energy, National Nuclear Security Agency
DOE-SC	U.S. Department of Energy, Office of Science
ENDF	Evaluated Nuclear Data File
EXFOR	EXchange FORmat, library of experimental cross sections, also known as CSISRS
HEU	High-enriched uranium

HMF	High-enriched uranium, metal fuel, fast neutron spectrum (type of benchmark experiment)
IAEA	International Atomic Energy Agency, headquarters located in Vienna
ICSBEP	International Criticality Safety Benchmark Evaluation Project
IMF	Intermediate-enriched uranium, metal fuel, fast neutron spectrum (type of benchmark experiment)
LCT	Low-enriched uranium, compound fuel, thermal neutron spectrum (type of benchmark experiment)
LEU	Low-enriched uranium
NEA	OECD Nuclear Energy Agency, headquarters located in Paris
NNDC	National Nuclear Data Center
PMF	Plutonium, metal fuel, fast neutron spectrum (type of benchmark experiment)
RIPL	Reference Input Parameter Library
USNDP	U.S. Nuclear Data Program
WPEC	NEA Working Party on International Nuclear Data Evaluation Cooperation

APPENDIX B: CONTENTS OF THE ENDF/B-VII.0 LIBRARY

The contents of the ENDF/B-VII.0 library is summarized in the form of lists of evaluated materials. First, in Table XXXIII we show 14 sublibraries constituting the ENDF/B-VII.0 library ordered by their sublibrary numbers (NSUB) as defined by the ENDF-6 format.

Then, we tabulate complete list of evaluated materials for each sublibrary. Given in the tables is the sequence number, followed by the name of the material (isotope or element), laboratory that produced the evaluation, date of the evaluation, authors of the evaluation, and MAT number that uniquely identifies the material in the sublibrary.

TABLE XXXIII: List of 14 sublibraries contained in ENDF/B-VII.0. NSUB identifies the sublibrary in the ENDF-6 format.

No.	**NSUB**	**Sublibrary name**	**Number of materials**
1	0	Photonuclear reactions	163
2	3	Photo-atomic data	100
3	4	Radioactive decay data	3830
4	5	Spontaneous fission yields	9
5	6	Atomic relaxation data	100
6	10	Neutron reactions	393
7	11	Neutron-induced fission yields	31
8	12	Thermal neutron scattering	20
9	19	Neutron cross section standards	8
10	113	Electro-atomic data	100
11	10010	Proton reactions	48
12	10020	Deuteron reactions	5
13	10030	Triton reactions	3
14	20030	^{3}He reactions	2
		Full library	**4812**

TABLE XXXIV: Photonuclear sublibrary (NSUB = 0)

Num.	Material	Lab.	Date	Authors	MAT
1)	1-H - 2	LANL	Jan05	G.M. Hale	128
2)	4-Be- 9	CNDC	Dec98	B.Yu, J.Zhang, Y.Han	425
3)	6-C - 12	LANL	Oct99	M.Chadwick,P.Young	625
4)	6-C - 13	KAERI	Dec99	Y.Han,Y.-O.Lee	628
5)	7-N - 14	KAERI	Dec05	Han,Lee,Oblozinsky,Chadwick	725
6)	7-N - 15	KAERI	Dec99	Y.Han,Y.-O.Lee	728
7)	8-O - 16	LANL	Nov99	M.Chadwick,P.Young	825
8)	8-O - 17	KAERI	Dec99	Y.Han,Y.-O.Lee	828
9)	8-O - 18	KAERI	Dec99	Y.Han,Y.-O.Lee	831
10)	11-Na- 23	KAERI	Dec99	Y.Han,Y.-O.Lee	1125
11)	12-Mg- 24	KAERI	Dec99	Y.Han,Y.-O.Lee	1225
12)	12-Mg- 25	KAERI	Dec99	Y.Han,Y.-O.Lee	1228
13)	12-Mg- 26	KAERI	Dec99	Y.Han,Y.-O.Lee	1231
14)	13-Al- 27	LANL	Dec99	M.Chadwick,P.Young	1325
15)	14-Si- 28	LANL	Nov99	M.Chadwick,P.Young	1425
16)	14-Si- 29	KAERI	Dec99	Y.Han,Y.-O.Lee	1428

TABLE XXXIV: Photonuclear sublibrary (NSUB = 0)

Num.	Material	Lab.	Date	Authors	MAT
17)	14-Si- 30	KAERI	Dec99	Y.Han,Y.-O.Lee	1431
18)	16-S - 32	KAERI	Dec99	Y.Han,Y.-O.Lee	1625
19)	16-S - 33	KAERI	Dec99	Y.Han,Y.-O.Lee	1628
20)	16-S - 34	KAERI	Dec99	Y.Han,Y.-O.Lee	1631
21)	16-S - 36	KAERI	Dec99	Y.Han,Y.-O.Lee	1637
22)	17-Cl- 35	KAERI	Dec99	Y.Han,Y.-O.Lee	1725
23)	17-Cl- 37	KAERI	Dec99	Y.Han,Y.-O.Lee	1731
24)	18-Ar- 36	KAERI	Dec99	Y.Han,Y.-O.Lee	1825
25)	18-Ar- 38	KAERI	Dec99	Y.Han,Y.-O.Lee	1831
26)	18-Ar- 40	KAERI	Dec99	Y.Han,Y.-O.Lee	1837
27)	20-Ca- 40	LANL	Dec98	M.Chadwick,P.Young	2025
28)	20-Ca- 42	KAERI	Dec99	Y.Han,Y.-O.Lee	2031
29)	20-Ca- 43	KAERI	Dec99	Y.Han,Y.-O.Lee	2034
30)	20-Ca- 44	KAERI	Dec99	Y.Han,Y.-O.Lee	2037
31)	20-Ca- 46	KAERI	Dec99	Y.Han,Y.-O.Lee	2043
32)	20-Ca- 48	KAERI	Dec99	Y.Han,Y.-O.Lee	2049
33)	22-Ti- 46	KAERI	Dec99	Y.Han,Y.-O.Lee	2225
34)	22-Ti- 47	KAERI	Dec99	Y.Han,Y.-O.Lee	2228
35)	22-Ti- 48	KAERI	Dec99	Y.Han,Y.-O.Lee	2231
36)	22-Ti- 49	KAERI	Dec99	Y.Han,Y.-O.Lee	2234
37)	22-Ti- 50	KAERI	Dec99	Y.Han,Y.-O.Lee	2237
38)	23-V - 51	CNDC	Apr98	B.Yu, Y,Han, J.Zhang	2328
39)	24-Cr- 50	KAERI	Dec99	Y.Han,Y.-O.Lee	2425
40)	24-Cr- 52	KAERI	Dec99	Y.Han,Y.-O.Lee	2431
41)	24-Cr- 53	KAERI	Dec99	Y.Han,Y.-O.Lee	2434
42)	24-Cr- 54	KAERI	Dec99	Y.Han,Y.-O.Lee	2437
43)	25-Mn- 55	KAERI	Dec99	Y.Han,Y.-O.Lee	2525
44)	26-Fe- 54	KAERI	Dec99	Y.Han,Y.-O.Lee	2625
45)	26-Fe- 56	LANL	Sep98	M.Chadwick,P.Young	2631
46)	26-Fe- 57	KAERI	Dec99	Y.Han,Y.-O.Lee	2634
47)	26-Fe- 58	KAERI	Dec99	Y.Han,Y.-O.Lee	2637
48)	27-Co- 59	KAERI	Dec99	Y.Han,Y.-O.Lee	2725
49)	28-Ni- 58	KAERI	Dec99	Y.Han,Y.-O.Lee	2825
50)	28-Ni- 60	KAERI	Dec99	Y.Han,Y.-O.Lee	2831
51)	28-Ni- 61	KAERI	Dec99	Y.Han,Y.-O.Lee	2834
52)	28-Ni- 62	KAERI	Dec99	Y.Han,Y.-O.Lee	2837
53)	28-Ni- 64	KAERI	Dec99	Y.Han,Y.-O.Lee	2843
54)	29-Cu- 63	LANL	Dec99	M.Chadwick,P.Young	2925
55)	29-Cu- 65	KAERI	Dec99	Y.Han,Y.-O.Lee	2931
56)	30-Zn- 64	KAERI	Dec99	Y.Han,Y.-O.Lee	3025
57)	30-Zn- 66	KAERI	Dec99	Y.Han,Y.-O.Lee	3031
58)	30-Zn- 67	KAERI	Dec99	Y.Han,Y.-O.Lee	3034
59)	30-Zn- 68	KAERI	Dec99	Y.Han,Y.-O.Lee	3037
60)	30-Zn- 70	KAERI	Dec99	Y.Han,Y.-O.Lee	3043
61)	32-Ge- 70	KAERI	Dec99	Y.Han,Y.-O.Lee	3225
62)	32-Ge- 72	KAERI	Dec99	Y.Han,Y.-O.Lee	3231
63)	32-Ge- 73	KAERI	Dec99	Y.Han,Y.-O.Lee	3234
64)	32-Ge- 74	KAERI	Dec99	Y.Han,Y.-O.Lee	3237
65)	32-Ge- 76	KAERI	Dec99	Y.Han,Y.-O.Lee	3243
66)	38-Sr- 84	KAERI	Dec99	Y.Han,Y.-O.Lee	3825
67)	38-Sr- 86	KAERI	Dec99	Y.Han,Y.-O.Lee	3831
68)	38-Sr- 87	KAERI	Dec99	Y.Han,Y.-O.Lee	3834
69)	38-Sr- 88	KAERI	Dec99	Y.Han,Y.-O.Lee	3837
70)	38-Sr- 90	KAERI	Dec99	Y.Han,Y.-O.Lee	3843
71)	40-Zr- 90	KAERI	Dec99	Y.Han,Y.-O.Lee	4025
72)	40-Zr- 91	KAERI	Dec99	Y.Han,Y.-O.Lee	4028
73)	40-Zr- 92	KAERI	Dec99	Y.Han,Y.-O.Lee	4031
74)	40-Zr- 93	KAERI	Dec99	Y.Han,Y.-O.Lee	4034
75)	40-Zr- 94	KAERI	Dec99	Y.Han,Y.-O.Lee	4037
76)	40-Zr- 96	KAERI	Dec99	Y.Han,Y.-O.Lee	4043
77)	41-Nb- 93	KAERI	Dec99	Y.Han,Y.-O.Lee	4125

TABLE XXXIV: Photonuclear sublibrary (NSUB = 0)

Num.	Material	Lab.	Date	Authors	MAT
78)	41-Nb- 94	KAERI	Dec99	Y.Han,Y.-O.Lee	4128
79)	42-Mo- 92	KAERI	Dec99	Y.Han,Y.-O.Lee	4225
80)	42-Mo- 94	KAERI	Dec99	Y.Han,Y.-O.Lee	4231
81)	42-Mo- 95	KAERI	Dec99	Y.Han,Y.-O.Lee	4234
82)	42-Mo- 96	KAERI	Dec99	Y.Han,Y.-O.Lee	4237
83)	42-Mo- 97	KAERI	Dec99	Y.Han,Y.-O.Lee	4240
84)	42-Mo- 98	KAERI	Dec99	Y.Han,Y.-O.Lee	4243
85)	42-Mo-100	KAERI	Dec99	Y.Han,Y.-O.Lee	4249
86)	46-Pd-102	KAERI	Dec99	Y.Han,Y.-O.Lee	4625
87)	46-Pd-104	KAERI	Dec99	Y.Han,Y.-O.Lee	4631
88)	46-Pd-105	KAERI	Dec99	Y.Han,Y.-O.Lee	4634
89)	46-Pd-106	KAERI	Dec99	Y.Han,Y.-O.Lee	4637
90)	46-Pd-107	KAERI	Dec99	Y.Han,Y.-O.Lee	4640
91)	46-Pd-108	KAERI	Dec99	Y.Han,Y.-O.Lee	4643
92)	46-Pd-110	KAERI	Dec99	Y.Han,Y.-O.Lee	4649
93)	47-Ag-107	KAERI	Dec99	Y.Han,Y.-O.Lee	4725
94)	47-Ag-108	KAERI	Dec99	Y.Han,Y.-O.Lee	4728
95)	47-Ag-109	KAERI	Dec99	Y.Han,Y.-O.Lee	4731
96)	48-Cd-106	KAERI	Dec99	Y.Han,Y.-O.Lee	4825
97)	48-Cd-108	KAERI	Dec99	Y.Han,Y.-O.Lee	4831
98)	48-Cd-110	KAERI	Dec99	Y.Han,Y.-O.Lee	4837
99)	48-Cd-111	KAERI	Dec99	Y.Han,Y.-O.Lee	4840
100)	48-Cd-112	KAERI	Dec99	Y.Han,Y.-O.Lee	4843
101)	48-Cd-113	KAERI	Dec99	Y.Han,Y.-O.Lee	4846
102)	48-Cd-114	KAERI	Dec99	Y.Han,Y.-O.Lee	4849
103)	48-Cd-116	KAERI	Dec99	Y.Han,Y.-O.Lee	4855
104)	50-Sn-112	KAERI	Dec99	Y.Han,Y.-O.Lee	5025
105)	50-Sn-114	KAERI	Dec99	Y.Han,Y.-O.Lee	5031
106)	50-Sn-115	KAERI	Dec99	Y.Han,Y.-O.Lee	5034
107)	50-Sn-116	KAERI	Dec99	Y.Han,Y.-O.Lee	5037
108)	50-Sn-117	KAERI	Dec99	Y.Han,Y.-O.Lee	5040
109)	50-Sn-118	KAERI	Dec99	Y.Han,Y.-O.Lee	5043
110)	50-Sn-119	KAERI	Dec99	Y.Han,Y.-O.Lee	5046
111)	50-Sn-120	KAERI	Dec99	Y.Han,Y.-O.Lee	5049
112)	50-Sn-122	KAERI	Dec99	Y.Han,Y.-O.Lee	5055
113)	50-Sn-124	KAERI	Dec99	Y.Han,Y.-O.Lee	5061
114)	51-Sb-121	KAERI	Dec99	Y.Han,Y.-O.Lee	5125
115)	51-Sb-123	KAERI	Dec99	Y.Han,Y.-O.Lee	5131
116)	52-Te-120	KAERI	Dec99	Y.Han,Y.-O.Lee	5225
117)	52-Te-122	KAERI	Dec99	Y.Han,Y.-O.Lee	5231
118)	52-Te-123	KAERI	Dec99	Y.Han,Y.-O.Lee	5234
119)	52-Te-124	KAERI	Dec99	Y.Han,Y.-O.Lee	5237
120)	52-Te-125	KAERI	Dec99	Y.Han,Y.-O.Lee	5240
121)	52-Te-126	KAERI	Dec99	Y.Han,Y.-O.Lee	5243
122)	52-Te-128	KAERI	Dec99	Y.Han,Y.-O.Lee	5249
123)	52-Te-130	KAERI	Dec99	Y.Han,Y.-O.Lee	5255
124)	53-I -127	KAERI	Dec99	Y.Han,Y.-O.Lee	5325
125)	53-I -129	KAERI	Dec99	Y.Han,Y.-O.Lee	5331
126)	55-Cs-133	KAERI	Dec99	Y.Han,Y.-O.Lee	5525
127)	55-Cs-135	KAERI	Dec99	Y.Han,Y.-O.Lee	5531
128)	55-Cs-137	KAERI	Dec99	Y.Han,Y.-O.Lee	5537
129)	59-Pr-141	KAERI	Dec99	Y.Han,Y.-O.Lee	5925
130)	62-Sm-144	KAERI	Dec99	Y.Han,Y.-O.Lee	6225
131)	62-Sm-147	KAERI	Dec99	Y.Han,Y.-O.Lee	6234
132)	62-Sm-148	KAERI	Dec99	Y.Han,Y.-O.Lee	6237
133)	62-Sm-149	KAERI	Dec99	Y.Han,Y.-O.Lee	6240
134)	62-Sm-150	KAERI	Dec99	Y.Han,Y.-O.Lee	6243
135)	62-Sm-151	KAERI	Dec99	Y.Han,Y.-O.Lee	6246
136)	62-Sm-152	KAERI	Dec99	Y.Han,Y.-O.Lee	6249
137)	62-Sm-154	KAERI	Dec99	Y.Han,Y.-O.Lee	6255
138)	65-Tb-158	KAERI	Dec99	Y.Han,Y.-O.Lee	6522

TABLE XXXIV: Photonuclear sublibrary (NSUB = 0)

Num.	Material	Lab.	Date	Authors	MAT
139)	65-Tb-159	KAERI	Dec99	Y.Han,Y.-O.Lee	6525
140)	67-Ho-165	KAERI	Dec99	Y.Han,Y.-O.Lee	6725
141)	73-Ta-181	LANL	Apr99	M.Chadwick,P.Young	7328
142)	74-W -180	CNDC	Dec97	B.Yu, Y,Han, J.Zhang	7425
143)	74-W -182	CNDC	Dec97	B.Yu, Y,Han, J.Zhang	7431
144)	74-W -183	CNDC	Dec97	B.Yu, Y,Han, J.Zhang	7434
145)	74-W -184	LANL	Apr98	M.Chadwick,P.Young	7437
146)	74-W -186	CNDC	Dec97	B.Yu, Y,Han, J.Zhang	7443
147)	79-Au-197	KAERI	Dec99	Y.Han,Y.-O.Lee	7925
148)	82-Pb-206	LANL	Dec98	M.Chadwick,P.Young	8231
149)	82-Pb-207	LANL	Dec98	M.Chadwick,P.Young	8234
150)	82-Pb-208	LANL	Sep98	M.Chadwick,P.Young	8237
151)	83-Bi-209	KAERI	Dec99	Y.Han,Y.-O.Lee	8325
152)	90-Th-232	CJD	Feb98	Blokhin A.I.,+	9025
153)	92-U -233	CJD	Feb98	Blokhin A.I.,+	9222
154)	92-U -234	CJD	Feb99	Blokhin A.I.,+	9225
155)	92-U -235	LANL	Aug05	M.Giacri,D.Ridikas,M.Chadwick	9228
156)	92-U -236	CJD	Feb99	Blokhin A.I. et al.	9231
157)	92-U -238	LANL	Aug05	M.Giacri,D.Ridikas,M.Chadwick	9237
158)	93-Np-237	LANL	Aug05	M.Giacri, D.Ridikas, M.Chadwick	9346
159)	94-Pu-238	CJD	Feb99	Blokhin A.I.,+	9434
160)	94-Pu-239	LANL	Nov05	M.Giacri, D.Ridikas, M.Chadwick	9437
161)	94-Pu-240	LANL	Jun05	M.Giacri, D.Ridikas, M.Chadwick	9440
162)	94-Pu-241	CJD	Feb99	Blokhin A.I.,+	9443
163)	95-Am-241	LANL	Sep05	M.Giacri, D.Ridikas, M.Chadwick	9543

TABLE XXXV: Neutron sublibrary (NSUB = 10)

Num.	Material	Lab.	Date	Authors	MAT
1)	1-H - 1	LANL	EVAL-Oct05	G.M.Hale	125
2)	1-H - 2	LANL	EVAL-Feb97	P.G.Young,G.M.Hale,M.B.Chadwick	128
3)	1-H - 3	LANL	EVAL-Nov01	G.M.Hale	131
4)	2-He- 3	LANL	EVAL-May90	G.Hale,D.Dodder,P.Young	225
5)	2-He- 4	LANL	EVAL-Oct73	Nisley,Hale,Young	228
6)	3-Li- 6	LANL	EVAL-Apr06	G.M.Hale, P.G.Young	325
7)	3-Li- 7	LANL	EVAL-Aug88	P.G.Young	328
8)	4-Be- 7	LANL	EVAL-Jun04	P.R.Page	419
9)	4-Be- 9	LLNL,LANL	EVAL-Jan86	Perkins,Plechaty,Howerton,Frankle	425
10)	5-B - 10	LANL	EVAL-Apr06	G.M.Hale,P.G.Young	525
11)	5-B - 11	LANL	EVAL-May89	P.G.Young	528
12)	6-C - 0	LANL,ORNL	EVAL-Jun96	M.B.Chadwick, P.G.Young, C.Y. Fu	600
13)	7-N - 14	LANL	EVAL-Jun97	M.B.Chadwick,P.G.Young	725
14)	7-N - 15	LANL	EVAL-Sep83	E.Arthur,P.Young,G.Hale	728
15)	8-O - 16	LANL	EVAL-Dec05	Hale,Young,Chadwick,Caro,Lubitz	825
16)	8-O - 17	BNL	EVAL-Jan78	B.A.Magurno	828
17)	9-F - 19	CNDC,ORNL	EVAL-Oct03	Z.X.Zhao,C.Y.Fu,D.C.Larson, Leal+	925
18)	11-Na- 22	NEA	EVAL-Jun83	Scientific Co-ordination Group	1122
19)	11-Na- 23	ORNL	EVAL-Dec77	D.C.Larson	1125
20)	12-Mg- 24	DEC,NEDAC	EVAL-Mar87	M.Hatchya(DEC),T.Asami(NEDAC)	1225
21)	12-Mg- 25	DEC,NEDAC	EVAL-Mar87	M.Hatchya(DEC),T.Asami(NEDAC)	1228
22)	12-Mg- 26	DEC,NEDAC	EVAL-Mar87	M.Hatchya(DEC),T.Asami(NEDAC)	1231
23)	13-Al- 27	LANL,ORNL	EVAL-Feb01	M.B.Chadwick+,Derrien+	1325
24)	14-Si- 28	LANL,ORNL	EVAL-Dec02	M.B.Chadwick,P.G.Young,D.Hetrick	1425
25)	14-Si- 29	LANL,ORNL	EVAL-Jun97	M.B.Chadwick,P.G.Young,D.Hetrick	1428
26)	14-Si- 30	LANL,ORNL	EVAL-Jun97	M.B.Chadwick,P.G.Young,D.Hetrick	1431
27)	15-P - 31	LANL,LLNL	EVAL-Dec97	M.Chadwick,P.Young,R.Howerton	1525
28)	16-S - 32	FUJI E.C.	EVAL-May87	H.Nakamura	1625
29)	16-S - 33	FUJI E.C.	EVAL-May87	H.Nakamura	1628
30)	16-S - 34	FUJI E.C.	EVAL-May87	H.Nakamura	1631
31)	16-S - 36	FUJI E.C.	EVAL-May87	H.Nakamura	1637

TABLE XXXV: Neutron sublibrary (NSUB = 10)

Num.	Material	Lab.	Date	Authors	MAT
32)	17-Cl- 35	ORNL,LANL	EVAL-Oct03	Sayer,Guber,Leal,Larson,Young+	1725
33)	17-Cl- 37	ORNL,LANL	EVAL-Oct03	Sayer,Guber,Leal,Larson,Young+	1731
34)	18-Ar- 36	NEA	EVAL-Jun83	Scientific Co-ordination Group	1825
35)	18-Ar- 38	NEA	EVAL-Jun83	Scientific Co-ordination Group	1831
36)	18-Ar- 40	KHI	EVAL-Mar94	T.Watanabe	1837
37)	19-K - 39	FUJI E.C.	EVAL-May87	H.Nakamura	1925
38)	19-K - 40	FUJI E.C.	EVAL-May87	H.Nakamura	1928
39)	19-K - 41	FUJI E.C.	EVAL-May87	H.Nakamura	1931
40)	20-Ca- 40	NRG	EVAL-Oct04	A.J. Koning	2025
41)	20-Ca- 42	NRG	EVAL-Oct04	A.J. Koning	2031
42)	20-Ca- 43	NRG	EVAL-Oct04	A.J. Koning	2034
43)	20-Ca- 44	NRG	EVAL-Oct04	A.J. Koning	2037
44)	20-Ca- 46	NRG	EVAL-Oct04	A.J. Koning	2043
45)	20-Ca- 48	NRG	EVAL-Oct04	A.J. Koning	2049
46)	21-Sc- 45	ANL,LLNL	EVAL-Jul92	A.B.Smith,R.J.Howerton	2125
47)	22-Ti- 46	KUR	EVAL-Sep88	K.Kobayashi(KUR),H.Hashikura(TOK)	2225
48)	22-Ti- 47	KUR	EVAL-Sep88	K.Kobayashi(KUR),H.Hashikura(TOK)	2228
49)	22-Ti- 48	KUR	EVAL-Sep88	K.Kobayashi(KUR),H.Hashikura(TOK)	2231
50)	22-Ti- 49	KUR	EVAL-Sep88	K.Kobayashi(KUR),H.Hashikura(TOK)	2234
51)	22-Ti- 50	KUR	EVAL-Sep88	K.Kobayashi(KUR),Hashikura(TOK)	2237
52)	23-V - 0	ANL,LLNL,+	EVAL-Jun88	A.Smith,D.Smith+	2300
53)	24-Cr- 50	LANL,ORNL	EVAL-Oct97	S.Chiba,M.Chadwick,D.Hetrick	2425
54)	24-Cr- 52	LANL,ORNL	EVAL-Oct97	S.Chiba,M.Chadwick,D.Hetrick	2431
55)	24-Cr- 53	LANL,ORNL	EVAL-Oct97	S.Chiba,M.Chadwick,K.Shibata	2434
56)	24-Cr- 54	LANL,ORNL	EVAL-Oct97	S.Chiba,M.Chadwick,D.Hetrick	2437
57)	25-Mn- 55	JAERI,ORNL	EVAL-Mar88	K.Shibata	2525
58)	26-Fe- 54	LANL,ORNL	EVAL-Sep96	M.B.Chadwick,P.G.Young,D.Hetrick	2625
59)	26-Fe- 56	LANL,ORNL	EVAL-Sep96	M.B.Chadwick,P.G.Young,C.Y.Fu	2631
60)	26-Fe- 57	LANL,ORNL	EVAL-Sep96	M.B.Chadwick,P.G.YOung,D.Hetrick	2634
61)	26-Fe- 58	ORNL	EVAL-Nov89	Hetrick,Fu,N.M.Larson	2637
62)	27-Co- 58	NEA	EVAL-Jun83	Scientific Co-ordinating Group	2722
63)	27-Co- 58M	NEA	EVAL-Jun82	Scientific Co-ordination Group	2723
64)	27-Co- 59	ANL,ORNL	EVAL-Jul89	A.Smith+,G.Desaussure+	2725
65)	28-Ni- 58	LANL,ORNL	EVAL-Sep97	S.Chiba,M.B.Chadwick,Larson	2825
66)	28-Ni- 59	NEA,ECN	EVAL-Nov87	Gruppelaar,VD.Kamp,Kopecky,Nierop	2828
67)	28-Ni- 60	LANL,ORNL	EVAL-Sep97	S.Chiba,M.B.Chadwick,Larson	2831
68)	28-Ni- 61	LANL,ORNL	EVAL-Sep97	S.Chiba,M.B.Chadwick,Hetrick	2834
69)	28-Ni- 62	LANL,ORNL	EVAL-Sep97	S.Chiba,M.B.Chadwick,Hetrick	2837
70)	28-Ni- 64	LANL,ORNL	EVAL-Sep97	S.Chiba,M.B.Chadwick,Hetrick	2843
71)	29-Cu- 63	LANL,ORNL	EVAL-Feb98	A.Koning,M.Chadwick,Hetrick	2925
72)	29-Cu- 65	LANL,ORNL	EVAL-Feb98	A.Koning,M.Chadwick,Hetrick	2931
73)	30-Zn- 0	FEI	EVAL-Dec89	M.N.Nikolaev, S.V.Zabrodskaja	3000
74)	31-Ga- 69	KHI,BNL	EVAL-Jan05	T.Watanabe, Mughabghab	3125
75)	31-Ga- 71	CNDC	EVAL-Oct98	Song-Bai Zhang,B.S.Yu,Z.J.Zhang	3131
76)	32-Ge- 70	BNL,JAERI	EVAL-Aug04	Iwamoto,Herman,Mughabghab+	3225
77)	32-Ge- 72	BNL,JAERI	EVAL-Aug04	Iwamoto,Herman,Mughabghab+	3231
78)	32-Ge- 73	BNL,JAERI	EVAL-Aug04	Iwamoto,Herman,Mughabghab+	3234
79)	32-Ge- 74	BNL,JAERI	EVAL-Aug04	Iwamoto,Herman,Mughabghab+	3237
80)	32-Ge- 76	BNL,JAERI	EVAL-Aug04	Iwamoto,Herman,Mughabghab+	3243
81)	33-As- 74	LANL	EVAL-Feb06	D.A.Brown, H.I.Kim, S.Mughabghab	3322
82)	33-As- 75	LLNL	EVAL-Feb06	D.A.Brown, Pruet, H.I.Kim	3325
83)	34-Se- 74	JNDC	EVAL-Mar90	JNDC FP Nuclear Data W.G.	3425
84)	34-Se- 76	JNDC	EVAL-Mar90	JNDC FP Nuclear Data W.G.	3431
85)	34-Se- 77	JNDC	EVAL-Mar90	JNDC FP Nuclear Data W.G.	3434
86)	34-Se- 78	JNDC	EVAL-Mar90	JNDC FP Nuclear Data W.G.	3437
87)	34-Se- 79	JNDC	EVAL-Mar90	JNDC FP Nuclear Data W.G.	3440
88)	34-Se- 80	JNDC	EVAL-Mar90	JNDC FP Nuclear Data W.G.	3443
89)	34-Se- 82	JNDC,BNL	EVAL-Jan05	JNDC FPND W.G., Mughabghab	3449
90)	35-Br- 79	JNDC	EVAL-Mar90	JNDC FP Nuclear Data W.G.	3525
91)	35-Br- 81	JNDC,BNL	EVAL-Jan05	JNDC FPND W.G., Mughabghab	3531
92)	36-Kr- 78	JNDC,BNL	EVAL-Feb05	JNDC FPND W.G., Mughabghab	3625

TABLE XXXV: Neutron sublibrary (NSUB = 10)

Num.	Material	Lab.	Date	Authors	MAT
93)	36-Kr- 80	JNDC	EVAL-Mar90	JNDC FP Nuclear Data W.G.	3631
94)	36-Kr- 82	JNDC,BNL	EVAL-Feb05	JNDC FPND W.G., Mughabghab	3637
95)	36-Kr- 83	CNDC	EVAL-Jun99	You-Xiang Zhuang, Chong-Hai Cai	3640
96)	36-Kr- 84	JNDC,BNL	EVAL-Jan05	JNDC FPND W.G., Mughabghab	3643
97)	36-Kr- 85	BNL	EVAL-Mar06	Herman,Oblozinsky,Mughabghab	3646
98)	36-Kr- 86	JNDC,BNL	EVAL-Jan05	JNDC FPND W.G., Mughabghab	3649
99)	37-Rb- 85	JNDC	EVAL-Mar90	JNDC FPND WG + S.F. Mughabghab	3725
100)	37-Rb- 86	BNL	EVAL-Mar06	Herman,Oblozinsky,Mughabghab	3728
101)	37-Rb- 87	JNDC	EVAL-Mar90	JNDC FP Nuclear Data W.G.	3731
102)	38-Sr- 84	BNL	EVAL-Mar06	Herman,Oblozinsky,Mughabghab	3825
103)	38-Sr- 86	JNDC,BNL	EVAL-Feb05	JNDC FPND W.G., Mughabghab	3831
104)	38-Sr- 87	JNDC	EVAL-Mar90	JNDC FP Nuclear Data W.G.	3834
105)	38-Sr- 88	CNDC,BNL	EVAL-Feb05	Zhuang,Cai, Mughabghab	3837
106)	38-Sr- 89	CNDC	EVAL-Sep01	Yin-Lu Han,C.H.Cai,Y.X.Zhuang	3840
107)	38-Sr- 90	JNDC	EVAL-Mar90	JNDC FP Nuclear Data W.G.	3843
108)	39-Y - 89	BNL-LANL	EVAL-Aug06	Rochman,Chadwick,Herman,Kawano+	3925
109)	39-Y - 90	BNL	EVAL-Mar06	Herman,Oblozinsky,Mughabghab	3928
110)	39-Y - 91	JNDC	EVAL-Mar90	JNDC FP Nuclear Data W.G.	3931
111)	40-Zr- 90	BNL	EVAL-Sep06	Herman,Rochman,Oblozinsky	4025
112)	40-Zr- 91	JNDC,BNL	EVAL-Feb05	JNDC FPND W.G., Mughabghab	4028
113)	40-Zr- 92	JNDC	EVAL-Aug89	JNDC FP Nuclear Data W.G.	4031
114)	40-Zr- 93	JNDC,BNL	EVAL-Mar05	JNDC FPND W.G., Mughabghab	4034
115)	40-Zr- 94	JNDC,BNL	EVAL-MAR05	JNDC FPND W.G., Mughabghab	4037
116)	40-Zr- 95	JNDC	EVAL-Mar90	JNDC FP Nuclear Data W.G.	4040
117)	40-Zr- 96	JNDC,BNL	EVAL-Feb05	JNDC FPND W.G., Mughabghab	4043
118)	41-Nb- 93	LANL,ANL	EVAL-Dec97	M.Chadwick,P.Young,D.L.Smith	4125
119)	41-Nb- 94	JNDC	EVAL-Mar90	JNDC FP Nuclear Data W.G.	4128
120)	41-Nb- 95	JNDC	EVAL-Mar90	JNDC FP Nuclear Data W.G.	4131
121)	42-Mo- 92	JNDC	EVAL-Aug89	JNDC FP Nuclear Data W.G.	4225
122)	42-Mo- 94	JNDC,BNL	EVAL-Feb05	JNDC FPND W.G., Mughabghab	4231
123)	42-Mo- 95	BNL,KAERI	EVAL-Feb06	Kim,Herman,Oh,Mughabghab+	4234
124)	42-Mo- 96	JNDC	EVAL-Aug89	JNDC FP Nuclear Data W.G.	4237
125)	42-Mo- 97	JNDC,BNL	EVAL-Feb05	JNDC FPND W.G., Mughabghab	4240
126)	42-Mo- 98	JNDC	EVAL-Aug89	JNDC FP Nuclear Data W.G.	4243
127)	42-Mo- 99	JNDC	EVAL-Mar90	JNDC FP Nuclear Data W.G.	4246
128)	42-Mo-100	CNDC	EVAL-Aug00	Chong-Hai Cai and Qi-Chang Liang	4249
129)	43-Tc- 99	BNL-LANL	EVAL-May06	Oblozinsky,Rochman,Herman,Mughab+	4325
130)	44-Ru- 96	JNDC	EVAL-Mar90	JNDC FP Nuclear Data W.G.	4425
131)	44-Ru- 98	JNDC	EVAL-Mar90	JNDC FP Nuclear Data W.G.	4431
132)	44-Ru- 99	JNDC	EVAL-Mar90	JNDC FP Nuclear Data W.G.	4434
133)	44-Ru-100	JNDC,BNL	EVAL-Mar05	JNDC FPND W.G., Mughabghab	4437
134)	44-Ru-101	BNL,KAERI	EVAL-Feb06	Kim,Herman,Oh,Mughabghab+	4440
135)	44-Ru-102	CNDC,BNL	EVAL-Feb05	Qi-Chang Liang+, Mughabghab	4443
136)	44-Ru-103	CNDC,BNL	EVAL-Feb05	Z.G.Ge+, Mughabghab	4446
137)	44-Ru-104	CNDC	EVAL-Jun99	Z.J.Zhang,Q.C.Liang,Q.Shen,X.Sun	4449
138)	44-Ru-105	CNDC	EVAL-Jun00	Qi-Chang Liang,Z.J.Zhang,X.Q.Sun	4452
139)	44-Ru-106	JNDC	EVAL-Mar90	JNDC FP Nuclear Data W.G.	4455
140)	45-Rh-103	BNL,KAERI	EVAL-Feb06	Kim,Herman,Chang,Mughabghab+	4525
141)	45-Rh-105	CNDC	EVAL-Dec99	X.Sun,Z.Zhang,Q.Shen,J.Zhao,W.Su	4531
142)	46-Pd-102	LANL,BNL	EVAL-MAR05	P. G. Young, Mughabghab	4625
143)	46-Pd-104	LANL,BNL	EVAL-Mar05	P. G. Young, Mughabghab	4631
144)	46-Pd-105	BNL,KAERI	EVAL-Feb06	Kim,Herman,Oh,Mughabghab+	4634
145)	46-Pd-106	LANL,BNL	EVAL-Mar05	P.G.Young, Mughabghab	4637
146)	46-Pd-107	JNDC	EVAL-Mar90	JNDC FP Nuclear Data W.G.	4640
147)	46-Pd-108	LANL,BNL	EVAL-Mar05	P.G.Young, Mughabghab	4643
148)	46-Pd-110	LANL,BNL	EVAL-Mar05	P.G.Young, Mughabghab	4649
149)	47-Ag-107	JAERI,BNL	EVAL-Mar05	Liu+, Mughabghab	4725
150)	47-Ag-109	BNL,KAERI	EVAL-Feb06	Kim,Herman,Oh,Mughabghab+	4731
151)	47-Ag-110M	JNDC,BNL	EVAL-Mar05	JNDC FPND W.G., Mughabghab	4735
152)	47-Ag-111	BNL	EVAL-Mar06	Herman,Oblozinsky,Mughabghab	4737
153)	48-Cd-106	JNDC,BNL	EVAL-Mar05	JNDC FPND W.G., Mughabghab	4825

TABLE XXXV: Neutron sublibrary (NSUB = 10)

Num.	Material	Lab.	Date	Authors	MAT
154)	48-Cd-108	UA,ANL,BNL	EVAL-Mar05	J.McCabe, A.B. Smith, Mughabghab	4831
155)	48-Cd-110	UA,ANL,BNL	EVAL-Mar05	J.McCabe, A.B. Smith, Mughabghab	4837
156)	48-Cd-111	JNDC,BNL	EVAL-Mar05	JNDC FPND W.G., Mughabghab	4840
157)	48-Cd-112	UA,ANL,BNL	EVAL-MAR05	J.McCabe, A.B. Smith, Mughabghab	4843
158)	48-Cd-113	CNDC,BNL	EVAL-Mar05	J.W.Zhao+, Mughabghab	4846
159)	48-Cd-114	UA,ANL, +	EVAL-Aug94	J.McCabe, A.B. Smith, +	4849
160)	48-Cd-115M	BNL	EVAL-Mar06	Herman,Oblozinsky,Mughabghab	4853
161)	48-Cd-116	UA,ANL,BNL	EVAL-Mar05	J.McCabe, A.B. Smith, Mughabghab	4855
162)	49-In-113	JNDC,BNL	EVAL-Mar05	JNDC FPND W.G., Mughabghab	4925
163)	49-In-115	JNDC,BNL	EVAL-Mar05	JNDC FPND W.G., Mughabghab	4931
164)	50-Sn-112	JNDC,BNL	EVAL-Dec04	JNDC FPND W.G., Mughabghab	5025
165)	50-Sn-113	BNL	EVAL-Mar06	Herman,Oblozinsky,Mughabghab	5028
166)	50-Sn-114	JNDC,BNL	EVAL-Dec04	JNDC FPND W.G., Mughabghab	5031
167)	50-Sn-115	JNDC,BNL	EVAL-Dec04	JNDC FPND W.G., Mughabghab	5034
168)	50-Sn-116	JNDC,BNL	EVAL-Dec04	JNDC FPND W.G., Mughabghab	5037
169)	50-Sn-117	JNDC,BNL	EVAL-Dec04	JNDC FPND W.G., Mughabghab	5040
170)	50-Sn-118	JNDC,BNL	EVAL-Dec04	JNDC FPND W.G., Mughabghab	5043
171)	50-Sn-119	JNDC,BNL	EVAL-Dec04	JNDC FPND W.G., Mughabghab	5046
172)	50-Sn-120	JNDC,BNL	EVAL-Dec04	JNDC FPND W.G., Mughabghab	5049
173)	50-Sn-122	JNDC,BNL	EVAL-Dec04	JNDC FPND W.G., Mughabghab	5055
174)	50-Sn-123	JNDC	EVAL-Mar90	JNDC FP Nuclear Data W.G.	5058
175)	50-Sn-124	JNDC,BNL	EVAL-Dec04	JNDC FPND W.G., Mughabghab	5061
176)	50-Sn-125	BNL	EVAL-Mar06	Herman,Oblozinsky,Mughabghab	5064
177)	50-Sn-126	JNDC	EVAL-Mar90	JNDC FP Nuclear Data W.G.	5067
178)	51-Sb-121	CNDC,BNL	EVAL-Dec04	Zhao+, Mughabghab	5125
179)	51-Sb-123	CNDC,BNL	EVAL-Dec04	Zhang+, Mughabghab	5131
180)	51-Sb-124	JNDC	EVAL-Mar90	JNDC FP Nuclear Data W.G.	5134
181)	51-Sb-125	JNDC	EVAL-Mar90	JNDC FP Nuclear Data W.G.	5137
182)	51-Sb-126	BNL	EVAL-Mar06	Herman,Oblozinsky,Mughabghab	5140
183)	52-Te-120	JNDC	EVAL-Mar90	JNDC FP Nuclear Data W.G.	5225
184)	52-Te-122	JNDC,BNL	EVAL-Mar90	JNDC FPND W.G., Mughabghab	5231
185)	52-Te-123	JNDC,BNL	EVAL-Dec04	JNDC FPND W.G., Mughabghab	5234
186)	52-Te-124	JNDC,BNL	EVAL-Dec04	JNFP W.G., Mughabghab	5237
187)	52-Te-125	JNDC,BNL	EVAL-DEC04	JNDC FPND W.G., Mughabghab	5240
188)	52-Te-126	JNDC,BNL	EVAL-Dec04	JNDC FPND W.G., Mughabghab	5243
189)	52-Te-127M	JNDC	EVAL-Mar90	JNDC FP Nuclear Data W.G.	5247
190)	52-Te-128	JNDC,BNL	EVAL-Dec04	JNDC FPND W.G., Mughabghab	5249
191)	52-Te-129M	JNDC	EVAL-Mar90	JNDC FP Nuclear Data W.G.	5253
192)	52-Te-130	CNDC	EVAL-Dec04	W.N.Su+, Mughabghab	5255
193)	52-Te-132	BNL	EVAL-Mar06	Herman,Oblozinsky,Mughabghab	5261
194)	53-I -127	LANL,BNL	EVAL-Jan05	Young, MacFarlane, Mughabghab	5325
195)	53-I -129	JNDC,BNL	EVAL-Jan05	JNDC FPND W.G., Mughabghab	5331
196)	53-I -130	BNL	EVAL-Mar06	Herman,Oblozinsky,Mughabghab	5334
197)	53-I -131	JNDC	EVAL-Mar90	JNDC FP Nuclear Data W.G.	5337
198)	53-I -135	CNDC,BNL	EVAL-Jan05	Q.Shen,X.Sun,Z.Zhang,W.Su,J.Zhao	5349
199)	54-Xe-123	CNDC	EVAL-Oct00	Qing-Biao Shen	5422
200)	54-Xe-124	CNDC,BNL	EVAL-Jan05	Yu, Shen, Mughabghab	5425
201)	54-Xe-126	JNDC,BNL	EVAL-Jan05	JNDC FPND W.G., Mughabghab	5431
202)	54-Xe-128	JNDC,BNL	EVAL-Jan05	JNDC FPND W.G., Mughabghab	5437
203)	54-Xe-129	JNDC,BNL	EVAL-Jan05	JNDC FPND W.G., Mughabghab	5440
204)	54-Xe-130	BNL	EVAL-Jan05	M.R.Bhat+, Mughabghab	5443
205)	54-Xe-131	BNL,KAERI	EVAL-Feb06	Kim,Herman,Oh,Mughabghab+	5446
206)	54-Xe-132	CNDC,BNL	EVAL-Jan05	B.S.Yu+, Mughabghab	5449
207)	54-Xe-133	JNDC	EVAL-Mar90	JNDC FP Nuclear Data W.G.	5452
208)	54-Xe-134	CNDC,BNL	EVAL-Jan05	B.S.Yu+, Mughabghab	5455
209)	54-Xe-135	JNDC	EVAL-Mar90	JNDC FP Nuclear Data W.G.	5458
210)	54-Xe-136	CNDC,BNL	EVAL-Jan05	Q.B.Shen+, Mughabghab	5461
211)	55-Cs-133	BNL,KAERI	EVAL-Feb06	Kim,Herman,Oh,Mughabghab+	5525
212)	55-Cs-134	JNDC,BNL	EVAL-Jan05	JNDC FPND W.G., Mughabghab	5528
213)	55-Cs-135	JNDC,BNL	EVAL-Jan05	JNDC FPND W.G., Mughabghab	5531
214)	55-Cs-136	JNDC	EVAL-Mar90	JNDC FP Nuclear Data W.G.	5534

TABLE XXXV: Neutron sublibrary (NSUB = 10)

Num.	Material	Lab.	Date	Authors	MAT
215)	55-Cs-137	JNDC	EVAL-Mar90	JNDC FP Nuclear Data W.G.	5537
216)	56-Ba-130	JNDC,BNL	EVAL-Jan05	JNDC FPND W.G., Mughabghab	5625
217)	56-Ba-132	JNDC,BNL	EVAL-Jan05	JNDC FPND W.G., Mughabghab	5631
218)	56-Ba-133	BNL	EVAL-Mar06	Herman,Oblozinsky,Mughabghab	5634
219)	56-Ba-134	JNDC,BNL	EVAL-Jan05	JNDC FPND W.G., Mughabghab	5637
220)	56-Ba-135	JNDC,BNL	EVAL-Jan05	JNDC FPND W.G., Mughabghab	5640
221)	56-Ba-136	JNDC,BNL	EVAL-Jan05	JNDC FPND W.G., Mughabghab	5643
222)	56-Ba-137	JNDC,BNL	EVAL-Jan05	JNDC FPND W.G., Mughabghab	5646
223)	56-Ba-138	CNDC,BNL	EVAL-Jan05	W.N.Su+, Mughabghab	5649
224)	56-Ba-140	NEA	EVAL-Jul82	H.Gruppelaar,E.Menapace	5655
225)	57-La-138	JNDC	EVAL-Mar90	JNDC FP Nuclear Data W.G.	5725
226)	57-La-139	CNDC,BNL	EVAL-Jan05	J.W.Zhao+, Mughabghab	5728
227)	57-La-140	BNL	EVAL-Mar06	Herman,Oblozinsky,Mughabghab	5731
228)	58-Ce-136	BNL	EVAL-Mar06	Herman,Oblozinsky,Mughabghab	5825
229)	58-Ce-138	BNL	EVAL-Mar06	Herman,Oblozinsky,Mughabghab	5831
230)	58-Ce-139	BNL	EVAL-Mar06	Herman,Oblozinsky,Mughabghab	5834
231)	58-Ce-140	JNDC,BNL	EVAL-Jan05	JNDC FPND W.G., Mughabghab	5837
232)	58-Ce-141	CNDC,BNL	EVAL-Jan05	Zhang+, Mughabghab	5840
233)	58-Ce-142	JNDC,BNL	EVAL-Jan05	JNDC FPND W.G., Mughabghab	5843
234)	58-Ce-143	BNL	EVAL-Mar06	Herman,Oblozinsky,Mughabghab	5846
235)	58-Ce-144	JNDC	EVAL-Mar90	JNDC FP Nuclear Data W.G.	5849
236)	59-Pr-141	BNL,KAERI	EVAL-Feb06	Kim,Mughabghab,Herman,Oblozinsky	5925
237)	59-Pr-142	BNL	EVAL-Mar06	Herman,Oblozinsky,Mughabghab	5928
238)	59-Pr-143	JNDC,BNl	EVAL-Jan05	JNDC FPND W.G., Mughabghab	5931
239)	60-Nd-142	BNL,KAERI	EVAL-Feb06	Kim,Mughabghab,Herman,Oblozinsky	6025
240)	60-Nd-143	BNL,KAERI	EVAL-Feb06	Kim,Herman,Chang,Mughabghab+	6028
241)	60-Nd-144	BNL,KAERI	EVAL-Feb06	Kim,Mughabghab,Herman,Oblozinsky	6031
242)	60-Nd-145	BNL,KAERI	EVAL-Feb06	Kim,Herman,Chang,Mughabghab+	6034
243)	60-Nd-146	BNL,KAERI	EVAL-Feb06	Kim,Mughabghab,Herman,Oblozinsky	6037
244)	60-Nd-147	BNL,KAERI	EVAL-Feb06	Kim,Mughabghab,Herman,Oblozinsky	6040
245)	60-Nd-148	BNL,KAERI	EVAL-Feb06	Kim,Mughabghab,Herman,Oblozinsky	6043
246)	60-Nd-150	BNL,KAERI	EVAL-Feb06	Kim,Mughabghab,Herman,Oblozinsky	6049
247)	61-Pm-147	JNDC	EVAL-Mar90	JNDC FP Nuclear Data W.G.	6149
248)	61-Pm-148	JNDC	EVAL-Mar90	JNDC FP Nuclear Data W.G.	6152
249)	61-Pm-148M	CNDC	EVAL-Sep01	You-Xiang Zhuang, Qing-Biao Shen	6153
250)	61-Pm-149	JNDC	EVAL-Mar90	JNDC FP Nuclear Data W.G.	6155
251)	61-Pm-151	BNL	EVAL-Mar06	Herman,Oblozinsky,Mughabghab	6161
252)	62-Sm-144	BNL,KAERI	EVAL-Feb06	Kim,Mughabghab,Herman,Oblozinsky	6225
253)	62-Sm-147	BNL,KAERI	EVAL-Feb06	Kim,Mughabghab,Herman,Oblozinsky	6234
254)	62-Sm-148	BNL,KAERI	EVAL-Feb06	Kim,Mughabghab,Herman,Oblozinsky	6237
255)	62-Sm-149	BNL,KAERI	EVAL-Feb06	Kim,Mughabghab,Herman,Oblozinsky	6240
256)	62-Sm-150	BNL,KAERI	EVAL-Feb06	Kim,Mughabghab,Herman,Oblozinsky	6243
257)	62-Sm-151	BNL,KAERI	EVAL-Feb06	Kim,Mughabghab,Herman,Oblozinsky	6246
258)	62-Sm-152	BNL,KAERI	EVAL-Feb06	Kim,Mughabghab,Herman,Oblozinsky	6249
259)	62-Sm-153	BNL,KAERI	EVAL-Feb06	Kim,Mughabghab,Herman,Oblozinsky	6252
260)	62-Sm-154	BNL,KAERI	EVAL-Feb06	Kim,Mughabghab,Herman,Oblozinsky	6255
261)	63-Eu-151	CNDC,BNL	EVAL-Jan05	Ge+, Mughabghab	6325
262)	63-Eu-152	JNDC,ORNL	EVAL-Mar05	JNDC FPND W.G., R.Q.Wright	6328
263)	63-Eu-153	BNL,KAERI	EVAL-Sep02	Oblozinsky,Herman,Rochman,Chang,+	6331
264)	63-Eu-154	CNDC,BNL	EVAL-Jan05	Ge+, Mughabghab	6334
265)	63-Eu-155	CNDC	EVAL-Feb99	You-Xiang Zhuang and Zhi-Gang Ge	6337
266)	63-Eu-156	JNDC	EVAL-Mar90	JNDC FP Nuclear Data W.G.	6340
267)	63-Eu-157	BNL	EVAL-Mar06	Herman,Oblozinsky,Mughabghab	6343
268)	64-Gd-152	BNL,ORNL+	EVAL-Apr06	Rochman,Mughabghab,Leal,Kawano+	6425
269)	64-Gd-153	BNL,ORNL+	EVAL-Apr06	Rochman,Mughabghab,Leal,Kawano+	6428
270)	64-Gd-154	BNL,ORNL+	EVAL-Apr06	Rochman,Mughabghab,Leal,Kawano+	6431
271)	64-Gd-155	BNL,ORNL+	EVAL-Apr06	Rochman,Mughabghab,Leal,Kawano+	6434
272)	64-Gd-156	BNL,ORNL+	EVAL-Apr06	Rochman,Mughabghab,Leal,Kawano+	6437
273)	64-Gd-157	BNL,ORNL+	EVAL-Apr06	Rochman,Mughabghab,Leal,Kawano+	6440
274)	64-Gd-158	BNL,ORNL+	EVAL-Apr06	Rochman,Mughabghab,Leal,Kawano+	6443
275)	64-Gd-160	BNL,ORNL+	EVAL-Apr06	Rochman,Mughabghab,Leal,Kawano+	6449

TABLE XXXV: Neutron sublibrary (NSUB = 10)

Num.	Material	Lab.	Date	Authors	MAT
276)	65-Tb-159	JNDC,BNL	EVAL-Jan05	JNDC FPND W.G., Mughabghab	6525
277)	65-Tb-160	BNL	EVAL-Mar06	Herman,Oblozinsky,Mughabghab	6528
278)	66-Dy-156	BNL,KAERI	EVAL-Feb06	Kim,Mughabghab,Herman,Oblozinsky	6625
279)	66-Dy-158	BNL,KAERI	EVAL-Feb06	Kim,Mughabghab,Herman,Oblozinsky	6631
280)	66-Dy-160	BNL,KAERI	EVAL-Feb06	Kim,Herman,Oh,Oblozinsky	6637
281)	66-Dy-161	BNL,KAERI	EVAL-Feb06	Kim,Herman,Oh,Oblozinsky	6640
282)	66-Dy-162	BNL,KAERI	EVAL-Feb06	Kim,Herman,Oh,Oblozinsky	6643
283)	66-Dy-163	BNL,KAERI	EVAL-Feb06	Kim,Herman,Oh,Oblozinsky	6646
284)	66-Dy-164	BNL,KAERI	EVAL-Feb06	Kim,Herman,Oh,Oblozinsky	6649
285)	67-Ho-165	LANL,BNL	EVAL-Jan05	P.G.Young+, Mughabghab	6725
286)	67-Ho-166M	BNL	EVAL-Mar06	Herman,Oblozinsky,Mughabghab	6729
287)	68-Er-162	TIT	EVAL-Sep00	A.K.M. Harun-Ar-Rashid+	6825
288)	68-Er-164	TIT	EVAL-Sep00	A.K.M. Harun-Ar-Rashid+	6831
289)	68-Er-166	TIT,BNL	EVAL-Jan05	Harun-Ar-Rashid+, Mughabghab	6837
290)	68-Er-167	TIT,BNL	EVAL-Jan05	Harun-Ar-Rashid+, Mughabghab	6840
291)	68-Er-168	TIT,BNL	EVAL-Jan05	Harun-Ar-Rashid+, Mughabghab	6843
292)	68-Er-170	TIT,BNL	EVAL-Jan05	Harun-Ar-Rashid+, Mughabghab	6849
293)	71-Lu-175	ORNL,BNW	EVAL-Mar98	R.Q.Wright, Leonard-Stewart	7125
294)	71-Lu-176	ORNL,BNW	EVAL-Mar98	R.Q.Wright, Leonard-Stewart	7128
295)	72-Hf-174	ORNL,SAI,+	EVAL-Apr76	R.Q.Wright, M.K.Drake+	7225
296)	72-Hf-176	ORNL,SAI,+	EVAL-Apr76	R.Q.Wright, M.K.Drake+	7231
297)	72-Hf-177	ORNL,SAI,+	EVAL-Apr76	R.Q.Wright, M.K.Drake+	7234
298)	72-Hf-178	ORNL,SAI,+	EVAL-Aug76	R.Q.Wright, M.K.Drake+	7237
299)	72-Hf-179	ORNL,SAI,+	EVAL-Apr76	R.Q.Wright, M.K.Drake+	7240
300)	72-Hf-180	ORNL,SAI,+	EVAL-Apr76	R.Q.Wright, M.K.Drake+	7243
301)	73-Ta-181	LLNL	EVAL-Jan72	Howerton, Perkins, MacGregor	7328
302)	73-Ta-182	AI	EVAL-Apr71	J.Otter,C.Dunford and E.Ottewitte	7331
303)	74-W -182	LANL,ANL	EVAL-Oct96	M.B.Chadwick,P.G.Young,E.Arthur	7431
304)	74-W -183	LANL,ANL	EVAL-Oct96	M.B.Chadwick,P.G.Young,Arthur	7434
305)	74-W -184	LANL,ANL	EVAL-Oct96	M.B.Chadwick,P.G.Young,Arthur	7437
306)	74-W -186	LANL,ANL	EVAL-Oct96	M.B.Chadwick,P.G.Young,Arthur	7443
307)	75-Re-185	ORNL,LANL	EVAL-Mar90	L.W.Weston and P.G.Young	7525
308)	75-Re-187	ORNL,LANL	EVAL-Mar90	L.W.Weston and P.G.Young	7531
309)	77-Ir-191	LANL,BNL	EVAL-Aug06	Talou,Kawano,Chadwick,Rochman+	7725
310)	77-Ir-193	LANL,BNL	EVAL-Aug06	Rochman,Chadwick,Talou,Kawano+	7731
311)	79-Au-197	LANL	EVAL-Jan84	P.G.Young	7925
312)	80-Hg-196	LANL	EVAL-Feb98	S.Chiba, M.Chadwick,P.Young	8025
313)	80-Hg-198	LANL	EVAL-Oct04	M.Chadwick,S.Chiba,P.Young	8031
314)	80-Hg-199	LANL	EVAL-Oct04	S.Chiba, M.Chadwick,P.Young	8034
315)	80-Hg-200	LANL	EVAL-Oct04	M.Chadwick,S.Chiba,P.Young	8037
316)	80-Hg-201	LANL	EVAL-Oct04	S.Chiba,M.Chadwick,P.Young	8040
317)	80-Hg-202	LANL	EVAL-Oct04	M.Chadwick,S.Chiba,P.Young	8043
318)	80-Hg-204	LANL	EVAL-Oct05	S.Chiba,M.Chadwick,P.Young	8049
319)	82-Pb-204	NRG	EVAL-Dec04	A.J. Koning	8225
320)	82-Pb-206	NRG	EVAL-Dec04	A.J. Koning	8231
321)	82-Pb-207	NRG	EVAL-Dec04	A.J. Koning	8234
322)	82-Pb-208	LANL,ORNL	EVAL-Aug06	M.B.Chadwick, P.G.Young, C.Y.Fu	8237
323)	83-Bi-209	LANL,ANL	EVAL-Jul98	M.Chadwick,P.Young,A.Smith	8325
324)	88-Ra-223	TIT	EVAL-Aug88	N.Takagi	8825
325)	88-Ra-224	TIT	EVAL-Aug88	N.Takagi	8828
326)	88-Ra-225	TIT	EVAL-Aug88	N.Takagi	8831
327)	88-Ra-226	TIT	EVAL-Aug88	N.Takagi	8834
328)	89-Ac-225	TIT	EVAL-Aug88	N.Takagi	8925
329)	89-Ac-226	TIT	EVAL-Aug88	N.Takagi	8928
330)	89-Ac-227	TIT	EVAL-Aug88	N.Takagi	8931
331)	90-Th-227	TIT	EVAL-Aug88	N.Takagi	9025
332)	90-Th-228	KINKI U.	EVAL-Jun87	T.Ohsawa	9028
333)	90-Th-229	TIT	EVAL-Aug88	N.Takagi	9031
334)	90-Th-230	HEDL	EVAL-Nov77	Mann	9034
335)	90-Th-232	IAEA	EVAL-Feb06	CRP/Th-U Co-ordinator A. Trkov	9040
336)	90-Th-233	KINKI U.	EVAL-Jul87	T.Ohsawa	9043

TABLE XXXV: Neutron sublibrary (NSUB = 10)

Num.	Material	Lab.	Date	Authors	MAT
337)	90-Th-234	KINKI U.	EVAL-Jul87	T.Ohsawa	9046
338)	91-Pa-231	IAEA	EVAL-Feb06	CRP/Th-U Co-ordinator A. Trkov	9131
339)	91-Pa-232	ORNL,TIT	EVAL-Oct05	R.Q.Wright, N.Takagi	9134
340)	91-Pa-233	IAEA	Eval-MAR06	CRP/Th-U Co-ordinator A. Trkov	9137
341)	92-U -232	ORNL,LANL+	EVAL-Apr05	M.B.Chadwick, P.G.Young	9219
342)	92-U -233	LANL,ORNL	EVAL-Sep06	Young,Chadwick,Talou,Leal,Derrien	9222
343)	92-U -234	ORNL,LANL+	EVAL-Apr06	Young,Kawano,Chadwick,MacFarlane	9225
344)	92-U -235	ORNL,LANL,+	EVAL-Sep06	Young,Chadwick,Talou,Madland,Leal	9228
345)	92-U -236	LANL	EVAL-Feb05	Young,Chadwick,MacFarlane+	9231
346)	92-U -237	LANL	EVAL-Feb06	P.G.Young, M.B.Chadwick	9234
347)	92-U -238	ORNL,LANL+	EVAL-Sep06	Young,Chadwick,Derrien,Courcelle	9237
348)	92-U -239	LANL	EVAL-Aug06	P.G.Young, M.B.Chadwick	9240
349)	92-U -240	LANL	EVAL-Feb05	Young,Chadwick,MacFarlane+	9243
350)	92-U -241	LANL	EVAL-Feb05	P.G.Young, M.B.Chadwick	9246
351)	93-Np-235	JAERI	EVAL-Mar95	T.Nakagawa	9340
352)	93-Np-236	ORNL,JAERI	EVAL-Dec99	R.Q. Wright, T.Nakagawa	9343
353)	93-Np-237	LANL	EVAL-Mar06	P.Young,E.Arthur,F.Mann,T.Kawano	9346
354)	93-Np-238	JAERI	EVAL-Mar93	T.Nakagawa	9349
355)	93-Np-239	ORNL	EVAL-Dec88	R.Q.Wright	9352
356)	94-Pu-236	JAERI	EVAL-Feb02	O.Iwamoto	9428
357)	94-Pu-237	HEDL	EVAL-Apr78	Mann and Schenter	9431
358)	94-Pu-238	HEDL,AI,+	EVAL-Apr78	Mann,Schenter,Alter,Dunford+	9434
359)	94-Pu-239	LANL	EVAL-Sep06	Young,Chadwick,MacFarlane,Derrien	9437
360)	94-Pu-240	ORNL	EVAL-Aug86	L.W. Weston and E. D. Arthur	9440
361)	94-Pu-241	ORNL	EVAL-Oct03	L.Weston,R.Wright,H.Derrien +	9443
362)	94-Pu-242	HEDL,SRL,+	EVAL-Oct78	Mann,Benjamin,Madland,Howerton,+	9446
363)	94-Pu-243	SRL,LLNL	EVAL-Jul76	Benjamin,McCrosson,Howerton	9449
364)	94-Pu-244	HEDL,SRL	EVAL-Apr78	Mann,Schenter,Benjamin,McCrosson	9452
365)	94-Pu-246	JAERI	EVAL-Mar95	T.Nakagawa	9458
366)	95-Am-241	LANL	EVAL-Mar06	Kawano,Chadwick	9543
367)	95-Am-242	LANL	EVAL-Dec04	Talou,Young,Kawano	9546
368)	95-Am-242M	LANL	EVAL-Sep05	Talou,Young,Kawano	9547
369)	95-Am-243	LANL,ORNL	EVAL-Jan06	P.G.Young, L.W.Weston, P.Talou	9549
370)	95-Am-244	JAERI	EVAL-Mar88	T.Nakagawa	9552
371)	95-Am-244M	JAERI	EVAL-Mar88	T.Nakagawa	9553
372)	96-Cm-241	HEDL	EVAL-Apr78	Mann and Schenter	9628
373)	96-Cm-242	HEDL,SRL,+	EVAL-Apr78	Mann,Benjamin,Howerton,+	9631
374)	96-Cm-243	MINSK	EVAL-Jul95	V.Maslov,+	9634
375)	96-Cm-244	JAERI	EVAL-Oct95	T.Nakagawa and T.Liu	9637
376)	96-Cm-245	MINSK,BYEL	EVAL-Nov95	V.M. Maslov, +	9640
377)	96-Cm-246	MINSK	EVAL-Nov95	V.Maslov, +	9643
378)	96-Cm-247	JAERI,ORNL	EVAL-Oct05	R.Q. Wright, T.Nakagawa, T.Liu	9646
379)	96-Cm-248	HEDL,SRL,+	EVAL-Apr78	Mann,Benjamin,Howerton, +	9649
380)	96-Cm-249	JAERI	EVAL-Oct95	T.Nakagawa and T.Liu	9652
381)	96-Cm-250	JAERI	EVAL-Oct95	T.Nakagawa and T.Liu	9655
382)	97-Bk-249	CNDC	EVAL-Jun86	Zhou Delin, +	9752
383)	97-Bk-250	JAERI	EVAL-Mar87	T.Nakagawa	9755
384)	98-Cf-249	CNDC	EVAL-Apr89	Zhou Delin, Su Zhongdi, +	9852
385)	98-Cf-250	SRL,LLNL+	EVAL-Jul76	Benjamin,McCrosson,Howerton,+	9855
386)	98-Cf-251	SRL,LLNL+	EVAL-Jul76	Benjamin,McCrosson,Howerton,+	9858
387)	98-Cf-252	SRL,LLNL+	EVAL-Jul76	Benjamin,McCrosson,Howerton,+	9861
388)	98-Cf-253	SRL	EVAL-Dec75	Benjamin and McCrosson	9864
389)	98-Cf-254	TIT	EVAL-Aug87	N.Takagi	9867
390)	99-Es-253	BNL,SRL	EVAL-Jul76	Kinsey,Benjamin, and McCrosson	9913
391)	99-Es-254	TIT	EVAL-Aug87	N.Takagi	9914
392)	99-Es-255	TIT	EVAL-Aug87	N.Takagi	9915
393)	100-Fm-255	TIT	EVAL-Aug87	N.Takagi	9936

TABLE XXXVI: Proton sublibrary (NSUB = 10010)

Num.	Material	Lab.	Date	Authors	MAT
1)	1-H - 1	LANL	Feb98	G.Hale	125
2)	1-H - 2	LANL	Feb97	P.G.Young,G.M.Hale,M.B.Chadwick	128
3)	1-H - 3	LANL	Sep01	G.M.Hale	131
4)	2-He- 3	LANL	Oct83	G.Hale	225
5)	3-Li- 6	LANL	Aug01	G.M.Hale	325
6)	3-Li- 7	LANL	Jun04	P.R.Page	328
7)	4-Be- 9	LANL	Nov88	P.G.Young, E.D.Arthur	409
8)	5-B - 10	LANL	Aug05	P.R.Page	525
9)	6-C - 12	LANL	Jun96	M.B.Chadwick And P.G.Young	625
10)	6-C - 13	LANL	Dec04	P.R.Page	628
11)	7-N - 14	LANL	Aug97	M.B.Chadwick and P.G.Young	725
12)	8-O - 16	LANL	Jun96	M.B.Chadwick and P.G.Young	825
13)	13-Al- 27	LANL	Feb97	M.B.Chadwick and P.G.Young	1325
14)	14-Si- 28	LANL	Jun97	M.B.Chadwick and P.G.Young	1425
15)	14-Si- 29	LANL	Jun97	M.B.Chadwick and P.G.Young	1428
16)	14-Si- 30	LANL	Jun97	M.B.Chadwick and P.G.Young	1431
17)	15-P - 31	LANL	Dec97	M.Chadwick,P.Young	1525
18)	20-Ca- 40	LANL	Mar97	M.B.Chadwick and P.G.Young	2025
19)	24-Cr- 50	LANL	Oct97	S.Chiba,M.Chadwick,P.Young	2425
20)	24-Cr- 52	LANL	Oct97	S.Chiba,M.Chadwick,P.Young	2431
21)	24-Cr- 53	LANL	Oct97	S.Chiba,M.Chadwick,P.Young	2434
22)	24-Cr- 54	LANL	Oct97	S.Chiba,M.Chadwick,P.Young	2437
23)	26-Fe- 54	LANL	Oct96	M.B.Chadwick,P.G.Young,A.J.Koning	2625
24)	26-Fe- 56	LANL	Oct96	M.B.Chadwick,P.G.Young,A.J.Koning	2631
25)	26-Fe- 57	LANL	Oct96	M.B.Chadwick,P.G.Young,A.J.Koning	2634
26)	28-Ni- 58	LANL	Sep97	Chiba,Chadwick,Young,Koning	2825
27)	28-Ni- 60	LANL	Sep97	Chiba,Chadwick,Young,Koning	2831
28)	28-Ni- 61	LANL	Sep97	Chiba,Chadwick,Young,Koning	2834
29)	28-Ni- 62	LANL	Sep97	Chiba,Chadwick,Young,Koning	2837
30)	28-Ni- 64	LANL	Sep97	Chiba,Chadwick,Young,Koning	2843
31)	29-Cu- 63	LANL	Feb98	A.Koning,M.Chadwick,P.Young	2925
32)	29-Cu- 65	LANL	Feb98	A.Koning,M.Chadwick,P.Young	2931
33)	41-Nb- 93	LANL	Dec97	M.Chadwick,P.Young	4125
34)	74-W -182	LANL	Oct96	M.B.Chadwick,P.G.Young	7431
35)	74-W -183	LANL	Oct96	M.B.Chadwick,P.G.Young	7434
36)	74-W -184	LANL	Oct96	M.B.Chadwick,P.G.Young	7437
37)	74-W -186	LANL	Oct96	M.B.Chadwick,P.G.Young	7443
38)	80-Hg-196	LANL	Feb98	S.Chiba, M.Chadwick,P.Young	8025
39)	80-Hg-198	LANL	Feb98	S.Chiba, M.Chadwick,P.Young	8031
40)	80-Hg-199	LANL	Feb98	M.Chadwick,S.Chiba,P.Young	8034
41)	80-Hg-200	LANL	Feb98	M.Chadwick,S.Chiba,P.Young	8037
42)	80-Hg-201	LANL	Feb98	S.Chiba,M.Chadwick,P.Young	8040
43)	80-Hg-202	LANL	Feb98	M.Chadwick,S.Chiba,P.Young	8043
44)	80-Hg-204	LANL	Feb98	S.Chiba,M.Chadwick,P.Young	8049
45)	82-Pb-206	LANL	Oct96	M.B.Chadwick,P.G.Young,A.J.Koning	8231
46)	82-Pb-207	LANL	Oct96	M.B.Chadwick,P.G.Young,A.J.Koning	8234
47)	82-Pb-208	LANL	Oct96	M.B.Chadwick,P.G.Young,A.J.Koning	8237
48)	83-Bi-209	LANL	Jul98	M.B.Chadwick,P.G.Young	8325

TABLE XXXVII: Thermal neutron scattering sublibrary (NSUB = 12)

Num.	Material	Lab.	Date	Authors	MAT
1)	H(H2O)	IKE,LANL	Mar06	MacFarlane, Keinert, Mattes	1
2)	para-H	LANL	Apr93	MacFarlane	2
3)	ortho-H	LANL	Apr93	MacFarlane	3
4)	H(ZrH)	LANL	Apr93	MacFarlane	7
5)	D(D2O)	LANL	Mar06	MacFarlane, Mattes, Keinert	11
6)	para-d	LANL	Apr93	MacFarlane	12
7)	ortho-d	LANL	Apr93	MacFarlane	13
8)	Be metal	LANL	Apr93	MacFarlane	26

TABLE XXXVII: Thermal neutron scattering sublibrary (NSUB = 12)

Num.	Material	Lab.	Date	Authors	MAT
9)	Be(BeO)	LANL	Jul05	MacFarlane	27
10)	O(BeO)	LANL	Jul05	MacFarlane	28
11)	graphite	LANL	Apr93	MacFarlane	31
12)	l-ch4	LANL	Apr93	MacFarlane	33
13)	s-ch4	LANL	Apr93	MacFarlane	34
14)	H(CH2)	GA	Dec69	Koppel, Houston, Sprevak	37
15)	BENZINE	GA	Dec69	Koppel, Houston, Borgonovi	40
16)	13-Al- 27	LANL	Oct05	MacFarlane	45
17)	26-Fe- 56	LANL	Oct05	MacFarlane	56
18)	Zr(ZrH)	LANL	Apr93	MacFarlane	58
19)	O(UO2)	LANL	Feb05	MacFarlane	75
20)	U(UO2)	LANL	Feb05	MacFarlane	76

TABLE XXXVIII: Neutron cross section standards sublibrary (NSUB = 19)

Num.	Material	Lab.	Date	Authors	MAT
1)	1-H - 1	LANL	Oct05	G.M.Hale	125
2)	2-He- 3	LANL	May90	G.Hale, D.Dodder, P.Young	225
3)	3-Li- 6	IAEA	Sep05	IAEA-CRP, NEA-WPEC(SG7), CSEWG	325
4)	5-B - 10	IAEA	Sep05	IAEA-CRP, NEA-WPEC(SG7), CSEWG	525
5)	6-C - 0	LANL,ORNL	Jun96	M.B. Chadwick, P.G. Young, C.Y. Fu	600
6)	79-Au-197	IAEA	Sep05	IAEA-CRP, NEA-WPEC(SG7), CSEWG	7925
7)	92-U -235	IAEA	Sep05	IAEA-CRP, NEA-WPEC(SG7), CSEWG	9228
8)	92-U -238	IAEA	Sep05	IAEA-CRP, NEA-WPEC(SG7), CSEWG	9237

TABLE XXXIX: Deuteron sublibrary (NSUB = 10020)

Num.	Material	Lab.	Date	Authors	MAT
1)	1-H - 2	LANL	Sep01	G.M. Hale	128
2)	1-H - 3	LANL	Jan95	G.M. Hale and M. Drosg	131
3)	2-He- 3	LANL	Feb01	G.M. Hale	225
4)	3-Li- 6	LANL	Jun04	P.R. Page	325
5)	3-Li- 7	LANL	Mar03	G.M. Hale	328

TABLE XL: Triton sublibrary (NSUB = 10030)

Num.	Material	Lab.	Date	Authors	MAT
1)	1-H - 3	LANL	Feb01	G.M. Hale	131
2)	2-He- 3	LANL	Aug01	G.M. Hale	225
3)	3-Li- 6	LANL	Sep01	G.M. Hale	325

TABLE XLI: ^{3}He sublibrary (NSUB = 20030)

Num.	Material	Lab.	Date	Authors	MAT
1)	2-He- 3	LANL	Aug01	G.M. Hale	225
2)	3-Li- 6	LANL	Nov02	G.M. Hale	325

TABLE XLII: Electro-atomic sublibrary (NSUB = 113)

Num.	Material	Lab.	Date	Authors	MAT
1)	1-H -0	LLNL	Dec89	D.E. Cullen	100
2)	2-He-0	LLNL	Dec89	D.E. Cullen	200
3)	3-Li-0	LLNL	Dec89	D.E. Cullen	300
4)	4-Be-0	LLNL	Dec89	D.E. Cullen	400
5)	5-B -0	LLNL	Dec89	D.E. Cullen	500

TABLE XLII: Electro-atomic sublibrary (NSUB = 113)

Num.	Material	Lab.	Date	Authors	MAT
6)	6-C -0	LLNL	Dec89	D.E. Cullen	600
7)	7-N -0	LLNL	Dec89	D.E. Cullen	700
8)	8-O -0	LLNL	Dec89	D.E. Cullen	800
9)	9-F -0	LLNL	Dec89	D.E. Cullen	900
10)	10-Ne-0	LLNL	Dec89	D.E. Cullen	1000
11)	11-Na-0	LLNL	Dec89	D.E. Cullen	1100
12)	12-Mg-0	LLNL	Dec89	D.E. Cullen	1200
13)	13-Al-0	LLNL	Dec89	D.E. Cullen	1300
14)	14-Si-0	LLNL	Dec89	D.E. Cullen	1400
15)	15-P -0	LLNL	Dec89	D.E. Cullen	1500
16)	16-S -0	LLNL	Dec89	D.E. Cullen	1600
17)	17-Cl-0	LLNL	Dec89	D.E. Cullen	1700
18)	18-Ar-0	LLNL	Dec89	D.E. Cullen	1800
19)	19-K -0	LLNL	Dec89	D.E. Cullen	1900
20)	20-Ca-0	LLNL	Dec89	D.E. Cullen	2000
21)	21-Sc-0	LLNL	Dec89	D.E. Cullen	2100
22)	22-Ti-0	LLNL	Dec89	D.E. Cullen	2200
23)	23-V -0	LLNL	Dec89	D.E. Cullen	2300
24)	24-Cr-0	LLNL	Dec89	D.E. Cullen	2400
25)	25-Mn-0	LLNL	Dec89	D.E. Cullen	2500
26)	26-Fe-0	LLNL	Dec89	D.E. Cullen	2600
27)	27-Co-0	LLNL	Dec89	D.E. Cullen	2700
28)	28-Ni-0	LLNL	Dec89	D.E. Cullen	2800
29)	29-Cu-0	LLNL	Dec89	D.E. Cullen	2900
30)	30-Zn-0	LLNL	Dec89	D.E. Cullen	3000
31)	31-Ga-0	LLNL	Dec89	D.E. Cullen	3100
32)	32-Ge-0	LLNL	Dec89	D.E. Cullen	3200
33)	33-As-0	LLNL	Dec89	D.E. Cullen	3300
34)	34-Se-0	LLNL	Dec89	D.E. Cullen	3400
35)	35-Br-0	LLNL	Dec89	D.E. Cullen	3500

TABLE XLII: Electro-atomic sublibrary (NSUB = 113)

Num.	Material	Lab.	Date	Authors	MAT
36)	36-Kr-0	LLNL	Dec89	D.E. Cullen	3600
37)	37-Rb-0	LLNL	Dec89	D.E. Cullen	3700
38)	38-Sr-0	LLNL	Dec89	D.E. Cullen	3800
39)	39-Y -0	LLNL	Dec89	D.E. Cullen	3900
40)	40-Zr-0	LLNL	Dec89	D.E. Cullen	4000
41)	41-Nb-0	LLNL	Dec89	D.E. Cullen	4100
42)	42-Mo-0	LLNL	Dec89	D.E. Cullen	4200
43)	43-Tc-0	LLNL	Dec89	D.E. Cullen	4300
44)	44-Ru-0	LLNL	Dec89	D.E. Cullen	4400
45)	45-Rh-0	LLNL	Dec89	D.E. Cullen	4500
46)	46-Pd-0	LLNL	Dec89	D.E. Cullen	4600
47)	47-Ag-0	LLNL	Dec89	D.E. Cullen	4700
48)	48-Cd-0	LLNL	Dec89	D.E. Cullen	4800
49)	49-In-0	LLNL	Dec89	D.E. Cullen	4900
50)	50-Sn-0	LLNL	Dec89	D.E. Cullen	5000
51)	51-Sb-0	LLNL	Dec89	D.E. Cullen	5100
52)	52-Te-0	LLNL	Dec89	D.E. Cullen	5200
53)	53-I -0	LLNL	Dec89	D.E. Cullen	5300
54)	54-Xe-0	LLNL	Dec89	D.E. Cullen	5400
55)	55-Cs-0	LLNL	Dec89	D.E. Cullen	5500
56)	56-Ba-0	LLNL	Dec89	D.E. Cullen	5600
57)	57-La-0	LLNL	Dec89	D.E. Cullen	5700
58)	58-Ce-0	LLNL	Dec89	D.E. Cullen	5800
59)	59-Pr-0	LLNL	Dec89	D.E. Cullen	5900
60)	70-Nd-0	LLNL	Dec89	D.E. Cullen	6000
61)	71-Pm-0	LLNL	Dec89	D.E. Cullen	6100
62)	72-Sm-0	LLNL	Dec89	D.E. Cullen	6200
63)	73-Eu-0	LLNL	Dec89	D.E. Cullen	6300
64)	74-Gd-0	LLNL	Dec89	D.E. Cullen	6400
65)	75-Tb-0	LLNL	Dec89	D.E. Cullen	6500
66)	76-Dy-0	LLNL	Dec89	D.E. Cullen	6600
67)	77-Ho-0	LLNL	Dec89	D.E. Cullen	6700
68)	78-Er-0	LLNL	Dec89	D.E. Cullen	6800
69)	79-Tm-0	LLNL	Dec89	D.E. Cullen	6900
70)	70-Yb-0	LLNL	Dec89	D.E. Cullen	7000
71)	71-Lu-0	LLNL	Dec89	D.E. Cullen	7100
72)	72-Hf-0	LLNL	Dec89	D.E. Cullen	7200
73)	73-Ta-0	LLNL	Dec89	D.E. Cullen	7300
74)	74-W -0	LLNL	Dec89	D.E. Cullen	7400
75)	75-Re-0	LLNL	Dec89	D.E. Cullen	7500
76)	76-Os-0	LLNL	Dec89	D.E. Cullen	7600
77)	77-Ir-0	LLNL	Dec89	D.E. Cullen	7700
78)	78-Pt-0	LLNL	Dec89	D.E. Cullen	7800
79)	79-Au-0	LLNL	Dec89	D.E. Cullen	7900
80)	80-Hg-0	LLNL	Dec89	D.E. Cullen	8000
81)	81-Tl-0	LLNL	Dec89	D.E. Cullen	8100
82)	82-Pb-0	LLNL	Dec89	D.E. Cullen	8200
83)	83-Bi-0	LLNL	Dec89	D.E. Cullen	8300
84)	84-Po-0	LLNL	Dec89	D.E. Cullen	8400
85)	85-At-0	LLNL	Dec89	D.E. Cullen	8500
86)	86-Rn-0	LLNL	Dec89	D.E. Cullen	8600
87)	87-Fr-0	LLNL	Dec89	D.E. Cullen	8700
88)	88-Ra-0	LLNL	Dec89	D.E. Cullen	8800
89)	89-Ac-0	LLNL	Dec89	D.E. Cullen	8900
90)	90-Th-0	LLNL	Dec89	D.E. Cullen	9000
91)	91-Pa-0	LLNL	Dec89	D.E. Cullen	9100
92)	92-U -0	LLNL	Dec89	D.E. Cullen	9200
93)	93-Np-0	LLNL	Dec89	D.E. Cullen	9300
94)	94-Pu-0	LLNL	Dec89	D.E. Cullen	9400
95)	95-Am-0	LLNL	Dec89	D.E. Cullen	9500
96)	96-Cm-0	LLNL	Dec89	D.E. Cullen	9600

TABLE XLII: Electro-atomic sublibrary (NSUB = 113)

Num.	Material	Lab.	Date	Authors	MAT
97)	97-Bk-0	LLNL	Dec89	D.E. Cullen	9700
98)	98-Cf-0	LLNL	Dec89	D.E. Cullen	9800
99)	99-Es-0	LLNL	Dec89	D.E. Cullen	9900
100)	100-Fm-0	LLNL	Dec89	D.E. Cullen	9920

TABLE XLIII: Photo-atomic sublibrary (NSUB = 3)

Num.	Material	Lab.	Date	Authors	MAT
1)	1-H -0	LLNL	Jul97	D.E. Cullen	100
2)	2-He-0	LLNL	Jul97	D.E. Cullen	200
3)	3-Li-0	LLNL	Jul97	D.E. Cullen	300
4)	4-Be-0	LLNL	Jul97	D.E. Cullen	400
5)	5-B -0	LLNL	Jul97	D.E. Cullen	500
6)	6-C -0	LLNL	Jul97	D.E. Cullen	600
7)	7-N -0	LLNL	Jul97	D.E. Cullen	700
8)	8-O -0	LLNL	Jul97	D.E. Cullen	800
9)	9-F -0	LLNL	Jul97	D.E. Cullen	900
10)	10-Ne-0	LLNL	Jul97	D.E. Cullen	1000
11)	11-Na-0	LLNL	Jul97	D.E. Cullen	1100
12)	12-Mg-0	LLNL	Jul97	D.E. Cullen	1200
13)	13-Al-0	LLNL	Jul97	D.E. Cullen	1300
14)	14-Si-0	LLNL	Jul97	D.E. Cullen	1400
15)	15-P -0	LLNL	Jul97	D.E. Cullen	1500
16)	16-S -0	LLNL	Jul97	D.E. Cullen	1600
17)	17-Cl-0	LLNL	Jul97	D.E. Cullen	1700
18)	18-Ar-0	LLNL	Jul97	D.E. Cullen	1800
19)	19-K -0	LLNL	Jul97	D.E. Cullen	1900
20)	20-Ca-0	LLNL	Jul97	D.E. Cullen	2000
21)	21-Sc-0	LLNL	Jul97	D.E. Cullen	2100
22)	22-Ti-0	LLNL	Jul97	D.E. Cullen	2200
23)	23-V -0	LLNL	Jul97	D.E. Cullen	2300
24)	24-Cr-0	LLNL	Jul97	D.E. Cullen	2400
25)	25-Mn-0	LLNL	Jul97	D.E. Cullen	2500
26)	26-Fe-0	LLNL	Jul97	D.E. Cullen	2600
27)	27-Co-0	LLNL	Jul97	D.E. Cullen	2700
28)	28-Ni-0	LLNL	Jul97	D.E. Cullen	2800
29)	29-Cu-0	LLNL	Jul97	D.E. Cullen	2900
30)	30-Zn-0	LLNL	Jul97	D.E. Cullen	3000
31)	31-Ga-0	LLNL	Jul97	D.E. Cullen	3100
32)	32-Ge-0	LLNL	Jul97	D.E. Cullen	3200
33)	33-As-0	LLNL	Jul97	D.E. Cullen	3300
34)	34-Se-0	LLNL	Jul97	D.E. Cullen	3400
35)	35-Br-0	LLNL	Jul97	D.E. Cullen	3500
36)	36-Kr-0	LLNL	Jul97	D.E. Cullen	3600
37)	37-Rb-0	LLNL	Jul97	D.E. Cullen	3700
38)	38-Sr-0	LLNL	Jul97	D.E. Cullen	3800
39)	39-Y -0	LLNL	Jul97	D.E. Cullen	3900
40)	40-Zr-0	LLNL	Jul97	D.E. Cullen	4000
41)	41-Nb-0	LLNL	Jul97	D.E. Cullen	4100
42)	42-Mo-0	LLNL	Jul97	D.E. Cullen	4200
43)	43-Tc-0	LLNL	Jul97	D.E. Cullen	4300
44)	44-Ru-0	LLNL	Jul97	D.E. Cullen	4400
45)	45-Rh-0	LLNL	Jul97	D.E. Cullen	4500
46)	46-Pd-0	LLNL	Jul97	D.E. Cullen	4600
47)	47-Ag-0	LLNL	Jul97	D.E. Cullen	4700
48)	48-Cd-0	LLNL	Jul97	D.E. Cullen	4800
49)	49-In-0	LLNL	Jul97	D.E. Cullen	4900
50)	50-Sn-0	LLNL	Jul97	D.E. Cullen	5000
51)	51-Sb-0	LLNL	Jul97	D.E. Cullen	5100
52)	52-Te-0	LLNL	Jul97	D.E. Cullen	5200

TABLE XLIII: Photo-atomic sublibrary (NSUB = 3)

Num.	Material	Lab.	Date	Authors	MAT
53)	53-I -0	LLNL	Jul97	D.E. Cullen	5300
54)	54-Xe-0	LLNL	Jul97	D.E. Cullen	5400
55)	55-Cs-0	LLNL	Jul97	D.E. Cullen	5500
56)	56-Ba-0	LLNL	Jul97	D.E. Cullen	5600
57)	57-La-0	LLNL	Jul97	D.E. Cullen	5700
58)	58-Ce-0	LLNL	Jul97	D.E. Cullen	5800
59)	59-Pr-0	LLNL	Jul97	D.E. Cullen	5900
60)	70-Nd-0	LLNL	Jul97	D.E. Cullen	6000
61)	71-Pm-0	LLNL	Jul97	D.E. Cullen	6100
62)	72-Sm-0	LLNL	Jul97	D.E. Cullen	6200
63)	73-Eu-0	LLNL	Jul97	D.E. Cullen	6300
64)	74-Gd-0	LLNL	Jul97	D.E. Cullen	6400
65)	75-Tb-0	LLNL	Jul97	D.E. Cullen	6500
66)	76-Dy-0	LLNL	Jul97	D.E. Cullen	6600
67)	77-Ho-0	LLNL	Jul97	D.E. Cullen	6700
68)	78-Er-0	LLNL	Jul97	D.E. Cullen	6800
69)	79-Tm-0	LLNL	Jul97	D.E. Cullen	6900
70)	70-Yb-0	LLNL	Jul97	D.E. Cullen	7000
71)	71-Lu-0	LLNL	Jul97	D.E. Cullen	7100
72)	72-Hf-0	LLNL	Jul97	D.E. Cullen	7200
73)	73-Ta-0	LLNL	Jul97	D.E. Cullen	7300
74)	74-W -0	LLNL	Jul97	D.E. Cullen	7400
75)	75-Re-0	LLNL	Jul97	D.E. Cullen	7500
76)	76-Os-0	LLNL	Jul97	D.E. Cullen	7600
77)	77-Ir-0	LLNL	Jul97	D.E. Cullen	7700
78)	78-Pt-0	LLNL	Jul97	D.E. Cullen	7800
79)	79-Au-0	LLNL	Jul97	D.E. Cullen	7900
80)	80-Hg-0	LLNL	Jul97	D.E. Cullen	8000
81)	81-Tl-0	LLNL	Jul97	D.E. Cullen	8100
82)	82-Pb-0	LLNL	Jul97	D.E. Cullen	8200
83)	83-Bi-0	LLNL	Jul97	D.E. Cullen	8300
84)	84-Po-0	LLNL	Jul97	D.E. Cullen	8400
85)	85-At-0	LLNL	Jul97	D.E. Cullen	8500
86)	86-Rn-0	LLNL	Jul97	D.E. Cullen	8600
87)	87-Fr-0	LLNL	Jul97	D.E. Cullen	8700
88)	88-Ra-0	LLNL	Jul97	D.E. Cullen	8800
89)	89-Ac-0	LLNL	Jul97	D.E. Cullen	8900
90)	90-Th-0	LLNL	Jul97	D.E. Cullen	9000
91)	91-Pa-0	LLNL	Jul97	D.E. Cullen	9100
92)	92-U -0	LLNL	Jul97	D.E. Cullen	9200
93)	93-Np-0	LLNL	Jul97	D.E. Cullen	9300
94)	94-Pu-0	LLNL	Jul97	D.E. Cullen	9400
95)	95-Am-0	LLNL	Jul97	D.E. Cullen	9500
96)	96-Cm-0	LLNL	Jul97	D.E. Cullen	9600
97)	97-Bk-0	LLNL	Jul97	D.E. Cullen	9700
98)	98-Cf-0	LLNL	Jul97	D.E. Cullen	9800
99)	99-Es-0	LLNL	Jul97	D.E. Cullen	9900
100)	100-Fm-0	LLNL	Jul97	D.E. Cullen	9920

TABLE XLIV: Atomic relaxation sublibrary (NSUB = 6)

Num.	Material	Lab.	Date	Authors	MAT
1)	1-H -0	LLNL	Dec90	D.E. Cullen	100
2)	2-He-0	LLNL	Dec90	D.E. Cullen	200
3)	3-Li-0	LLNL	Dec90	D.E. Cullen	300
4)	4-Be-0	LLNL	Dec90	D.E. Cullen	400
5)	5-B -0	LLNL	Dec90	D.E. Cullen	500
6)	6-C -0	LLNL	Dec90	D.E. Cullen	600
7)	7-N -0	LLNL	Dec90	D.E. Cullen	700
8)	8-O -0	LLNL	Dec90	D.E. Cullen	800

TABLE XLIV: Atomic relaxation sublibrary (NSUB = 6)

Num.	Material	Lab.	Date	Authors	MAT
9)	9-F -0	LLNL	Dec90	D.E. Cullen	900
10)	10-Ne-0	LLNL	Dec90	D.E. Cullen	1000
11)	11-Na-0	LLNL	Dec90	D.E. Cullen	1100
12)	12-Mg-0	LLNL	Dec90	D.E. Cullen	1200
13)	13-Al-0	LLNL	Dec90	D.E. Cullen	1300
14)	14-Si-0	LLNL	Dec90	D.E. Cullen	1400
15)	15-P -0	LLNL	Dec90	D.E. Cullen	1500
16)	16-S -0	LLNL	Dec90	D.E. Cullen	1600
17)	17-Cl-0	LLNL	Dec90	D.E. Cullen	1700
18)	18-Ar-0	LLNL	Dec90	D.E. Cullen	1800
19)	19-K -0	LLNL	Dec90	D.E. Cullen	1900
20)	20-Ca-0	LLNL	Dec90	D.E. Cullen	2000
21)	21-Sc-0	LLNL	Dec90	D.E. Cullen	2100
22)	22-Ti-0	LLNL	Dec90	D.E. Cullen	2200
23)	23-V -0	LLNL	Dec90	D.E. Cullen	2300
24)	24-Cr-0	LLNL	Dec90	D.E. Cullen	2400
25)	25-Mn-0	LLNL	Dec90	D.E. Cullen	2500
26)	26-Fe-0	LLNL	Dec90	D.E. Cullen	2600
27)	27-Co-0	LLNL	Dec90	D.E. Cullen	2700
28)	28-Ni-0	LLNL	Dec90	D.E. Cullen	2800
29)	29-Cu-0	LLNL	Dec90	D.E. Cullen	2900
30)	30-Zn-0	LLNL	Dec90	D.E. Cullen	3000
31)	31-Ga-0	LLNL	Dec90	D.E. Cullen	3100
32)	32-Ge-0	LLNL	Dec90	D.E. Cullen	3200
33)	33-As-0	LLNL	Dec90	D.E. Cullen	3300
34)	34-Se-0	LLNL	Dec90	D.E. Cullen	3400
35)	35-Br-0	LLNL	Dec90	D.E. Cullen	3500
36)	36-Kr-0	LLNL	Dec90	D.E. Cullen	3600
37)	37-Rb-0	LLNL	Dec90	D.E. Cullen	3700
38)	38-Sr-0	LLNL	Dec90	D.E. Cullen	3800
39)	39-Y -0	LLNL	Dec90	D.E. Cullen	3900
40)	40-Zr-0	LLNL	Dec90	D.E. Cullen	4000
41)	41-Nb-0	LLNL	Dec90	D.E. Cullen	4100
42)	42-Mo-0	LLNL	Dec90	D.E. Cullen	4200
43)	43-Tc-0	LLNL	Dec90	D.E. Cullen	4300
44)	44-Ru-0	LLNL	Dec90	D.E. Cullen	4400
45)	45-Rh-0	LLNL	Dec90	D.E. Cullen	4500
46)	46-Pd-0	LLNL	Dec90	D.E. Cullen	4600
47)	47-Ag-0	LLNL	Dec90	D.E. Cullen	4700
48)	48-Cd-0	LLNL	Dec90	D.E. Cullen	4800
49)	49-In-0	LLNL	Dec90	D.E. Cullen	4900
50)	50-Sn-0	LLNL	Dec90	D.E. Cullen	5000
51)	51-Sb-0	LLNL	Dec90	D.E. Cullen	5100
52)	52-Te-0	LLNL	Dec90	D.E. Cullen	5200
53)	53-I -0	LLNL	Dec90	D.E. Cullen	5300
54)	54-Xe-0	LLNL	Dec90	D.E. Cullen	5400
55)	55-Cs-0	LLNL	Dec90	D.E. Cullen	5500
56)	56-Ba-0	LLNL	Dec90	D.E. Cullen	5600
57)	57-La-0	LLNL	Dec90	D.E. Cullen	5700
58)	58-Ce-0	LLNL	Dec90	D.E. Cullen	5800
59)	59-Pr-0	LLNL	Dec90	D.E. Cullen	5900
60)	70-Nd-0	LLNL	Dec90	D.E. Cullen	6000
61)	71-Pm-0	LLNL	Dec90	D.E. Cullen	6100
62)	72-Sm-0	LLNL	Dec90	D.E. Cullen	6200
63)	73-Eu-0	LLNL	Dec90	D.E. Cullen	6300
64)	74-Gd-0	LLNL	Dec90	D.E. Cullen	6400
65)	75-Tb-0	LLNL	Dec90	D.E. Cullen	6500
66)	76-Dy-0	LLNL	Dec90	D.E. Cullen	6600
67)	77-Ho-0	LLNL	Dec90	D.E. Cullen	6700
68)	78-Er-0	LLNL	Dec90	D.E. Cullen	6800
69)	79-Tm-0	LLNL	Dec90	D.E. Cullen	6900

TABLE XLIV: Atomic relaxation sublibrary (NSUB = 6)

Num.	Material	Lab.	Date	Authors	MAT
70)	70-Yb-0	LLNL	Dec90	D.E. Cullen	7000
71)	71-Lu-0	LLNL	Dec90	D.E. Cullen	7100
72)	72-Hf-0	LLNL	Dec90	D.E. Cullen	7200
73)	73-Ta-0	LLNL	Dec90	D.E. Cullen	7300
74)	74-W -0	LLNL	Dec90	D.E. Cullen	7400
75)	75-Re-0	LLNL	Dec90	D.E. Cullen	7500
76)	76-Os-0	LLNL	Dec90	D.E. Cullen	7600
77)	77-Ir-0	LLNL	Dec90	D.E. Cullen	7700
78)	78-Pt-0	LLNL	Dec90	D.E. Cullen	7800
79)	79-Au-0	LLNL	Dec90	D.E. Cullen	7900
80)	80-Hg-0	LLNL	Dec90	D.E. Cullen	8000
81)	81-Tl-0	LLNL	Dec90	D.E. Cullen	8100
82)	82-Pb-0	LLNL	Dec90	D.E. Cullen	8200
83)	83-Bi-0	LLNL	Dec90	D.E. Cullen	8300
84)	84-Po-0	LLNL	Dec90	D.E. Cullen	8400
85)	85-At-0	LLNL	Dec90	D.E. Cullen	8500
86)	86-Rn-0	LLNL	Dec90	D.E. Cullen	8600
87)	87-Fr-0	LLNL	Dec90	D.E. Cullen	8700
88)	88-Ra-0	LLNL	Dec90	D.E. Cullen	8800
89)	89-Ac-0	LLNL	Dec90	D.E. Cullen	8900
90)	90-Th-0	LLNL	Dec90	D.E. Cullen	9000
91)	91-Pa-0	LLNL	Dec90	D.E. Cullen	9100
92)	92-U -0	LLNL	Dec90	D.E. Cullen	9200
93)	93-Np-0	LLNL	Dec90	D.E. Cullen	9300
94)	94-Pu-0	LLNL	Dec90	D.E. Cullen	9400
95)	95-Am-0	LLNL	Dec90	D.E. Cullen	9500
96)	96-Cm-0	LLNL	Dec90	D.E. Cullen	9600
97)	97-Bk-0	LLNL	Dec90	D.E. Cullen	9700
98)	98-Cf-0	LLNL	Dec90	D.E. Cullen	9800
99)	99-Es-0	LLNL	Dec90	D.E. Cullen	9900
100)	100-Fm-0	LLNL	Dec90	D.E. Cullen	9920

TABLE XLV: Spontaneous fission yields sublibrary (NSUB = 5)

Num.	Material	Lab.	Date	Authors	MAT
1)	92-U -238	LANL	Jul89	T.R. England,+	9237
2)	96-Cm-244	LANL	Jul89	T.R. England,+	9637
3)	96-Cm-246	LANL	Jul89	T.R. England,+	9643
4)	96-Cm-248	LANL	Jul89	T.R. England,+	9649
5)	98-Cf-250	LANL	Jul89	T.R. England,+	9855
6)	98-Cf-252	LANL	Jul89	T.R. England,+	9861
7)	99-Es-253	LANL	Jul89	T.R. England,+	9913
8)	100-Fm-254	LANL	Jul89	T.R. England,+	9935
9)	100-Fm-256	LANL	Jul89	T.R. England,+	9937

TABLE XLVI: Neutron-induced fission yields sublibrary (NSUB = 11)

Num.	Material	Lab.	Date	Authors	MAT
1)	90-Th-227	LANL	Jul89	T.R. England,+	9025
2)	90-Th-229	LANL	Jul89	T.R. England,+	9031
3)	90-Th-232	LANL	Jul89	T.R. England,+	9040
4)	91-Pa-231	LANL	Jul89	T.R. England,+	9131
5)	92-U -232	LANL	Jul89	T.R. England,+	9219
6)	92-U -233	LANL	Jul89	T.R. England,+	9222
7)	92-U -234	LANL	Jul89	T.R. England,+	9225
8)	92-U -235	LANL	Jul89	T.R. England,+	9228
9)	92-U -236	LANL	Jul89	T.R. England,+	9231
10)	92-U -237	LANL	Jul89	T.R. England,+	9234
11)	92-U -238	LANL	Jul89	T.R. England,+	9237
12)	93-Np-237	LANL	Jul89	T.R. England,+	9346
13)	93-Np-238	LANL	Jul89	T.R. England,+	9349
14)	94-Pu-238	LANL	Jul89	T.R. England,+	9434
15)	94-Pu-239	LANL	Jul89	T.R. England,+	9437
16)	94-Pu-240	LANL	Jul89	T.R. England,+	9440
17)	94-Pu-241	LANL	Jul89	T.R. England,+	9443
18)	94-Pu-242	LANL	Jul89	T.R. England,+	9446
19)	95-Am-241	LANL	Jul89	T.R. England,+	9543
20)	95-Am-242M	LANL	Jul89	T.R. England,+	9547
21)	95-Am-243	LANL	Jul89	T.R. England,+	9549
22)	96-Cm-242	LANL	Jul89	T.R. England,+	9631
23)	96-Cm-243	LANL	Jul89	T.R. England,+	9634
24)	96-Cm-244	LANL	Jul89	T.R. England,+	9637
25)	96-Cm-245	LANL	Jul89	T.R. England,+	9640
26)	96-Cm-246	LANL	Jul89	T.R. England,+	9643
27)	96-Cm-248	LANL	Jul89	T.R. England,+	9649
28)	98-Cf-249	LANL	Jul89	T.R. England,+	9852

TABLE XLVI: Neutron-induced fission yields sublibrary (NSUB = 11)

Num.	Material	Lab.	Date	Authors	MAT
29)	98-Cf-251	LANL	Jul89	T.R. England,+	9858
30)	99-Es-254	LANL	Jul89	T.R. England,+	9914
31)	100-Fm-255	LANL	Jul89	T.R. England,+	9936

TABLE XLVII: Radioactive decay data sublibrary (NSUB = 4). Given is the atomic charge, with corresponding chemical symbol, and the range of atomic mass number with data in this sublibrary. The total number of materials is 3830.

Z	Mass range	Lab.	Date	Author
0 (Neutron)	1	BNL	Apr06	A.A. Sonzogni
1 (H)	1 to 6	BNL	Apr06	A.A. Sonzogni
2 (He)	3 to 10	BNL	Apr06	A.A. Sonzogni
3 (Li)	4 to 12	BNL	Apr06	A.A. Sonzogni
4 (Be)	6 to 16	BNL	Apr06	A.A. Sonzogni
5 (B)	7 to 19	BNL	Apr06	A.A. Sonzogni
6 (C)	9 to 22	BNL	Apr06	A.A. Sonzogni
7 (N)	10 to 25	BNL	Apr06	A.A. Sonzogni
8 (O)	12 to 28	BNL	Apr06	A.A. Sonzogni
9 (F)	14 to 31	BNL	Apr06	A.A. Sonzogni
10 (Ne)	17 to 34	BNL	Apr06	A.A. Sonzogni
11 (Na)	18 to 37	BNL	Apr06	A.A. Sonzogni
12 (Mg)	20 to 40	BNL	Apr06	A.A. Sonzogni
13 (Al)	21 to 42	BNL	Apr06	A.A. Sonzogni
14 (Si)	22 to 44	BNL	Apr06	A.A. Sonzogni
15 (P)	24 to 46	BNL	Apr06	A.A. Sonzogni
16 (S)	26 to 49	BNL	Apr06	A.A. Sonzogni
17 (Cl)	29 to 51	BNL	Apr06	A.A. Sonzogni
18 (Ar)	31 to 53	BNL	Apr06	A.A. Sonzogni
19 (K)	33 to 55	BNL	Apr06	A.A. Sonzogni
20 (Ca)	35 to 57	BNL	Apr06	A.A. Sonzogni
21 (Sc)	38 to 60	BNL	Apr06	A.A. Sonzogni
22 (Ti)	38 to 63	BNL	Apr06	A.A. Sonzogni
23 (V)	42 to 65	BNL	Apr06	A.A. Sonzogni
24 (Cr)	42 to 67	BNL	Apr06	A.A. Sonzogni
25 (Mn)	44 to 69	BNL	Apr06	A.A. Sonzogni
26 (Fe)	45 to 72	BNL	Apr06	A.A. Sonzogni
27 (Co)	49 to 75	BNL	Apr06	A.A. Sonzogni
28 (Ni)	48 to 78	BNL	Apr06	A.A. Sonzogni
29 (Cu)	53 to 80	BNL	Apr06	A.A. Sonzogni
30 (Zn)	55 to 83	BNL	Apr06	A.A. Sonzogni
31 (Ga)	60 to 86	BNL	Apr06	A.A. Sonzogni
32 (Ge)	60 to 89	BNL	Apr06	A.A. Sonzogni
33 (As)	64 to 92	BNL	Apr06	A.A. Sonzogni
34 (Se)	65 to 94	BNL	Apr06	A.A. Sonzogni
35 (Br)	68 to 97	BNL	Apr06	A.A. Sonzogni
36 (Kr)	69 to 100	BNL	Apr06	A.A. Sonzogni
37 (Rb)	72 to 101	BNL	Apr06	A.A. Sonzogni
38 (Sr)	73 to 105	BNL	Apr06	A.A. Sonzogni
39 (Y)	76 to 108	BNL	Apr06	A.A. Sonzogni
40 (Zr)	78 to 110	BNL	Apr06	A.A. Sonzogni
41 (Nb)	81 to 113	BNL	Apr06	A.A. Sonzogni
42 (Mo)	83 to 115	BNL	Apr06	A.A. Sonzogni
43 (Tc)	85 to 118	BNL	Apr06	A.A. Sonzogni
44 (Ru)	87 to 120	BNL	Apr06	A.A. Sonzogni
45 (Rh)	89 to 122	BNL	Apr06	A.A. Sonzogni
46 (Pd)	91 to 124	BNL	Apr06	A.A. Sonzogni
47 (Ag)	93 to 130	BNL	Apr06	A.A. Sonzogni
48 (Cd)	95 to 132	BNL	Apr06	A.A. Sonzogni
49 (In)	97 to 135	BNL	Apr06	A.A. Sonzogni

TABLE XLVII: Radioactive decay data sublibrary (NSUB = 4). Given is the atomic charge, with corresponding chemical symbol, and the range of atomic mass number with data in this sublibrary. The total number of materials is 3830.

Z	Mass range	Lab.	Date	Author
50 (Sn)	99 to 137	BNL	Apr06	A.A. Sonzogni
51 (Sb)	103 to 139	BNL	Apr06	A.A. Sonzogni
52 (Te)	105 to 142	BNL	Apr06	A.A. Sonzogni
53 (I)	108 to 144	BNL	Apr06	A.A. Sonzogni
54 (Xe)	110 to 147	BNL	Apr06	A.A. Sonzogni
55 (Cs)	112 to 151	BNL	Apr06	A.A. Sonzogni
56 (Ba)	114 to 153	BNL	Apr06	A.A. Sonzogni
57 (La)	117 to 155	BNL	Apr06	A.A. Sonzogni
58 (Ce)	119 to 157	BNL	Apr06	A.A. Sonzogni
59 (Pr)	121 to 159	BNL	Apr06	A.A. Sonzogni
60 (Nd)	124 to 161	BNL	Apr06	A.A. Sonzogni
61 (Pm)	126 to 163	BNL	Apr06	A.A. Sonzogni
62 (Sm)	128 to 165	BNL	Apr06	A.A. Sonzogni
63 (Eu)	130 to 167	BNL	Apr06	A.A. Sonzogni
64 (Gd)	134 to 169	BNL	Apr06	A.A. Sonzogni
65 (Tb)	136 to 171	BNL	Apr06	A.A. Sonzogni
66 (Dy)	138 to 173	BNL	Apr06	A.A. Sonzogni
67 (Ho)	140 to 175	BNL	Apr06	A.A. Sonzogni
68 (Er)	143 to 177	BNL	Apr06	A.A. Sonzogni
69 (Tm)	145 to 179	BNL	Apr06	A.A. Sonzogni
70 (Yb)	148 to 181	BNL	Apr06	A.A. Sonzogni
71 (Lu)	150 to 184	BNL	Apr06	A.A. Sonzogni
72 (Hf)	153 to 188	BNL	Apr06	A.A. Sonzogni
73 (Ta)	155 to 190	BNL	Apr06	A.A. Sonzogni
74 (W)	158 to 192	BNL	Apr06	A.A. Sonzogni
75 (Re)	160 to 194	BNL	Apr06	A.A. Sonzogni
76 (Os)	162 to 196	BNL	Apr06	A.A. Sonzogni
77 (Ir)	164 to 199	BNL	Apr06	A.A. Sonzogni
78 (Pt)	166 to 202	BNL	Apr06	A.A. Sonzogni
79 (Au)	169 to 205	BNL	Apr06	A.A. Sonzogni
80 (Hg)	171 to 210	BNL	Apr06	A.A. Sonzogni
81 (Tl)	176 to 212	BNL	Apr06	A.A. Sonzogni
82 (Pb)	178 to 215	BNL	Apr06	A.A. Sonzogni
83 (Bi)	184 to 218	BNL	Apr06	A.A. Sonzogni
84 (Po)	188 to 220	BNL	Apr06	A.A. Sonzogni
85 (At)	193 to 223	BNL	Apr06	A.A. Sonzogni
86 (Rn)	195 to 228	BNL	Apr06	A.A. Sonzogni
87 (Fr)	199 to 232	BNL	Apr06	A.A. Sonzogni
88 (Ra)	202 to 234	BNL	Apr06	A.A. Sonzogni
89 (Ac)	206 to 236	BNL	Apr06	A.A. Sonzogni
90 (Th)	209 to 238	BNL	Apr06	A.A. Sonzogni
91 (Pa)	212 to 240	BNL	Apr06	A.A. Sonzogni
92 (U)	217 to 242	BNL	Apr06	A.A. Sonzogni
93 (Np)	225 to 244	BNL	Apr06	A.A. Sonzogni
94 (Pu)	228 to 247	BNL	Apr06	A.A. Sonzogni
95 (Am)	231 to 249	BNL	Apr06	A.A. Sonzogni
96 (Cm)	234 to 252	BNL	Apr06	A.A. Sonzogni
97 (Bk)	235 to 254	BNL	Apr06	A.A. Sonzogni
98 (Cf)	237 to 256	BNL	Apr06	A.A. Sonzogni
99 (Es)	240 to 258	BNL	Apr06	A.A. Sonzogni
100 (Fm)	242 to 260	BNL	Apr06	A.A. Sonzogni
101 (Md)	245 to 262	BNL	Apr06	A.A. Sonzogni
102 (No)	248 to 264	BNL	Apr06	A.A. Sonzogni
103 (Lr)	251 to 266	BNL	Apr06	A.A. Sonzogni
104 (Rf)	253 to 268	BNL	Apr06	A.A. Sonzogni
105 (Db)	255 to 269	BNL	Apr06	A.A. Sonzogni
106 (Sg)	258 to 273	BNL	Apr06	A.A. Sonzogni
107 (Bh)	260 to 275	BNL	Apr06	A.A. Sonzogni

TABLE XLVII: Radioactive decay data sublibrary (NSUB = 4). Given is the atomic charge, with corresponding chemical symbol, and the range of atomic mass number with data in this sublibrary. The total number of materials is 3830.

Z	Mass range	Lab.	Date	Author
108 (Hs)	263 to 276	BNL	Apr06	A.A. Sonzogni
109 (Mt)	265 to 279	BNL	Apr06	A.A. Sonzogni
110 (Ds)	267 to 281	BNL	Apr06	A.A. Sonzogni
111 (Rg)	272 to 283	BNL	Apr06	A.A. Sonzogni